

# Magnetoreception mechanisms in birds – towards the discovery of the sixth sense

Dissertation  
zur Erlangung des Doktorgrades  
der Naturwissenschaften

vorgelegt beim Fachbereich Physik  
der Johann Wolfgang Goethe–Universität  
in Frankfurt am Main

von  
Ilia A. Solov'yov  
aus St. Petersburg, Russland

Frankfurt am Main  
2008

(D30)

vom Fachbereich Physik der  
Johann Wolfgang Goethe–Universität, Frankfurt am Main, als  
Dissertation angenommen.

Dekan: Prof. Dr. Wolf Aßmus

Gutachter: Prof. Dr. Dr. h.c. mult Walter Greiner, Prof.  
Dr. Klaus Schulten, Prof. Dr. Günther Fleissner

Datum der Disputation: 04.02.2008

for Notes



# Abstract

This work is devoted to the description of mechanisms that might be responsible for avian magnetoreception. Two possible theoretical concepts underlying this phenomenon are formulated and their functionality is proven in realistic geomagnetic fields.

It has been suggested that the “magnetic sense” in birds may be mediated by the blue light receptor protein – cryptochrome – which is known to be localized in the retinas of migratory birds. Cryptochromes are a class of photoreceptor signaling proteins that are found in a wide variety of organisms and which primarily perform regulatory functions, such as the entrainment of circadian rhythm in mammals and the inhibition of hypocotyl growth in plants. Recent experiments have shown that the activity of cryptochrome-1 in *Arabidopsis thaliana* is enhanced by the presence of a weak external magnetic field, confirming the ability of cryptochrome to mediate magnetic field responses. Cryptochrome’s signaling is tied to the photoreduction of an internally bound chromophore, flavin adenine dinucleotide (FAD). The spin chemistry of this photoreduction process, which involves electron transfer from a chain of three tryptophans, is modulated by the presence of a magnetic field in an effect known as the radical pair mechanism. Cryptochrome was suggested as a possible magnetoreceptor for the first time in Ref. [1]. However, no realistic calculations of the magnetic field effect in cryptochrome were performed. One of the goals of the present thesis is computationally to study the electron spin dynamics in cryptochrome and to show the feasibility of a cryptochrome-based compass in birds. In particular, the activation yield of cryptochrome was studied as a function of an external magnetic field and it was shown that the activation of the protein can be influenced by the geomagnetic field. In the work it has also been proven that cryptochrome provides an inclination compass, which is necessary for bird orientation. The evolution of spin densities as a function of time is also discussed.

An alternative mechanism of avian magnetoreception discussed in the thesis is based on the interaction of two iron minerals (magnetite and maghemite) which were

only recently found in subcellular compartments within the sensory dendrites of the upper beak of several bird species. The iron minerals in the beak form platelets of crystalline maghemite and assemblies of magnetite nanoparticles (magnetite clusters). The interaction between these particles can be manipulated by an external magnetic field inducing a primary receptor potential via strain-sensitive membrane channels that lead to a certain bird orientation effect. Various properties of the magnetite/maghemite magnetoreceptor system have been considered: the potential energy surface of the magnetite cluster has been calculated and analyzed as a function of the orientation of an external magnetic field; the forces acting on the magnetite cluster were calculated and analyzed; the force differences caused by the change of the direction of external magnetic field were established; the probability of opening the mechanosensitive ion channel was calculated. Finally it has been demonstrated that the iron-mineral based magnetoreceptor provides a polarity magnetic compass. Various conditions at which the magnetoreception process is violated are outlined.

# Zusammenfassung

Seit langer Zeit fasziniert die Vogelmigration den Menschen. Die Frage, wie Vögel ihren Weg bei ihren halbjährlichen Flügen finden, war schon immer von großem Interesse für amateurhafte Ornitologen wie auch für professionelle Wissenschaftler. Für die Orientierung benutzen die Zugvögel Hinweise aus unterschiedlichen Quellen. Verschiedene Orientierungsversuche mit wildgefangenen und hausgezüchteten Vögeln haben gezeigt, dass sie überirdische und geomagnetische Informationen für die Identifizierung der Migrationsrichtung benutzen (einen Überblick über solche Studien findet man in [2–6]). Der Sonnenkompass zusammen mit der lokalen Zeit, gemessen mit inneren Uhren, ermöglicht den Vögeln die Azimutposition der Sonne während des Tages zu bestimmen [7]. Auch das Muster von polarisiertem Licht, das besonderes gut bei Sonnenaufgang sichtbar ist, spielt eine wichtige Rolle bei der Orientierung [8–10]. Sobald die jungen Vögel durch die Beobachtung des Rotationszentrums des Sternenhimmels die räumliche Verknüpfung zwischen den Sternen erlernt haben, gibt ihnen der Sternenkompass Informationen über die geografische Richtung [11, 12].

Viele Vögel sind auch dann im Stande sich exakt zu orientieren, wenn der Himmel nicht sichtbar ist (zum Beispiel wenn es bewölkt ist). Dies erfordert aber nicht visuelle Informationsquellen. Viele Untersuchungen [13–16] haben bewiesen, dass die Vögel das Erdmagnetfeld fühlen können. Tauben, Rotkehlchen und andere Vögel benutzen das geomagnetische Feld als einen Kompass und sind auch für geringe zeitliche und räumliche Änderungen des magnetischen Feldes, die eventuell zur Festlegung der Position nützlich sind, sensibel.

Nicht nur Vögel haben den magnetischen Sinn. Salamander, Frösche und Schildkröten benutzen das magnetische Feld um sich in Richtung des nächsten Ufers zu orientieren wenn sie zum Beispiel Gefahr spüren [17–20]. Bei den Honigbienen wurde eine Magnetorezeption beim Wabenbau und der Hausorientierung nachgewiesen [21–25]. Bewegung und Orientierung von Organismen relativ zum magnetischen Feld, *Magnetotaxis*, wurde auch bei Bakterien nachgewiesen [26–28].

Aber im Vergleich zu den anderen Sinnen der Tiere wissen wir über die Magne-

torezeptionsmechanismen sehr wenig. Statische magnetische Felder wie das Erdmagnetfeld penetrieren lebendige Materie und der Rezeptor könnte sich fast überall im Körper befinden. Tatsächlich scheint es trotz intensiver Suche kein grosses Organ zu sein, das sich auf die Magnetorezeption spezialisiert hat. Das Hauptproblem dabei ist, dass das Erdmagnetfeld so schwach ist und ein Magnetorezeptor dazu imstande sein sollte, die Absolutgrößen und kleine Variationen des Feldes zu detektieren.

Die Verhaltensversuche [6, 9, 14, 29–32] haben geholfen, die Funktion von Magnetorezeptoren einiger Tiergruppen zu charakterisieren. Die physiologische Untersuchungen [2, 6, 33] haben wertvolle Indizien, wie Tiere das magnetische Feld empfangen, geliefert.

Die Unterschiedlichkeit der existierenden theoretischen Magnetorezeptionsmodelle [1, 34–47] illustriert durch wie viele verschiedene theoretische Vorstellungen die Magnetorezeption funktionieren könnte. Der magnetische Sinn ist das am wenigsten verstandene Sensorsystem der Tiere. Genau das macht es zu Untersuchung interessant.

Schon im Jahr 1855 deutete von Middendorff die Benutzung des magnetischen Feldes durch die Zugvögel an : *”... so liegt der Gedanke nahe, es möge die erstaunliche Unbeirrbarkeit der Zugvögel – trotz Wind und Wetter, trotz Nacht und Nebel – eben darauf beruhen, dass das Geflügel immerwährend der Richtung des Magnetpoles sich bewusst ist, und demzufolge auch seine Zugrichtung genau einzuhalten weiss. Was dem Schiffe die Magnetnadel ist, wäre dann diesen ‘Seglern der Lüfte’ das innere magnetische Gefühl, welches im Zusammenhang mit den galvanisch-magnetischen Strömungen stehen mag, die im Innern des Körpers dieser Tiere, zumal in ihren Bewegungsapparaten, erwiesener Maassen kreisen.”* (siehe [48]). Aber nicht vor 1960 wurde der magnetische Kompass experimentell bei Vögeln nachgewiesen. [13–15].

Die Verhaltens- und physiologischen Untersuchungen deuten zwei Magnetorezeptionsmechanismen in Vögeln an, die unterschiedliche Parameter des Erdmagnetfeldes detektieren: (1) ein lichtabhängiger Prozess, der die Inklinationwinkel der Linien des Erdmagnetfeldes detektiert und eine Art Inklinationskompass darstellt; (2) Ein Magnetit-vermittelter Prozess, der die Information über die magnetische Karte liefert (Kartensinn, für einen Überblick siehe [2, 49–53]).

Das Ziel dieser Arbeit ist zwei kürzlich vorgeschlagene [36–39] mögliche Magnetorezeptionsmechanismen zu untersuchen und ihre Funktionalität unter realistischen Erdmagnetfeldbedingungen zu überprüfen. Es wurden vorgeschlagen:



(i) **Tiermagnetorezeption**, die über das blaues Licht empfangende Protein *Cryptochrom* vermittelt wird. Cryptochrome gehören zu der Klasse von Photorezeptor-signalproteinen, die man in verschiedenen Arten von Tieren und Organismen finden kann, und die hauptsächlich Regulatorfunktion ausüben (wie z.B. Unterhaltung des Zirkadianrhythmus im Säugetier [54,55] und die Inhibition von Hypocotylwachstum in Pflanzen [56].) Die Struktur von Cryptochrom ist schematisch in Abb. 1a gezeigt.

Neuere Versuche [57] haben gezeigt, dass die Aktivität von Cryptochrom in der Pflanze *Arabidopsis thaliana* im Magnetfeld zunimmt, was die Magnetfeld-Abhängigkeit der Cryptochrom-Aktivität belegt. Der Aktivzustand von Cryptochrom ist mit dem Photoreduktionsprozess von Chromophor, *Flavin Adenine Dinucleotide (FAD)* verbunden, der sich im Inneren des Cryptochroms befindet (siehe Abb. 1a). Die Spin-Chemie dieses Photoreduktionsprozesses ist mit dem Elektronübergang zwischen drei Tryptophan-aminosäuren (Trp<sub>324</sub>, Trp<sub>377</sub>, Trp<sub>400</sub>, siehe Abb. 1a) verbunden. Der Elektronübergangsprozess wird durch ein externes Magnetfeld beeinflusst. Der unterliegende Übergangsmechanismus ist als Radikalpaarmechanismus bekannt und wird in dieser Arbeit besprochen.

Cryptochrome wurde als möglicher Magnetorezeptor zum ersten Mal in Ref. [1] vorgeschlagen. Jedoch wurden bis heute keine realistischen Berechnungen von Magnetfeldeffekten in dem Protein durchgeführt. Eines der Ziele dieser Dissertation ist eine numerische Untersuchung der Spindynamik in Cryptochrom durchzuführen, und die Möglichkeit des Cryptochrom-basierten Kompasses im Vogel zu demonstrieren. Insbesondere wird die Aktivierungsrate von Cryptochrom als Funktion des externen Magnetfeldes untersucht. Es wird gezeigt, dass die Aktivierungsrate von Cryptochrom durch schwache Magnetfelder (wie z.B. dem Erdmagnetfeld) beeinflusst werden kann. Die Aktivierungsrate von Cryptochrom wird als Funktion der Richtung des äusseren Magnetfeldes untersucht. Es wird gezeigt, dass Cryptochrom als ein Inklinationskompass dienen kann, der für die Navigation von Vögeln in Frage kommen kann. Des weiteren wird analysiert, wie sich die Spindichte im Cryptochrom mit der Zeit entwickelt.

(ii) Die Vogelmagnetorezeption tritt auf Grund der Wechselwirkung zweier eisenhaltiger Mineralien (Magnetit und Maghemit). Diese Mineralien wurden experimentell in den Sensor-Dendriten des oberen Schnabels von verschiedenen Vogelarten nachgewiesen [58–61]. Die eisenhaltigen Mineralien im Schnabel sind als Maghemitkristallplättchen und kugelähnlichen Formen aus Magnetit-Nanokristallen zu finden

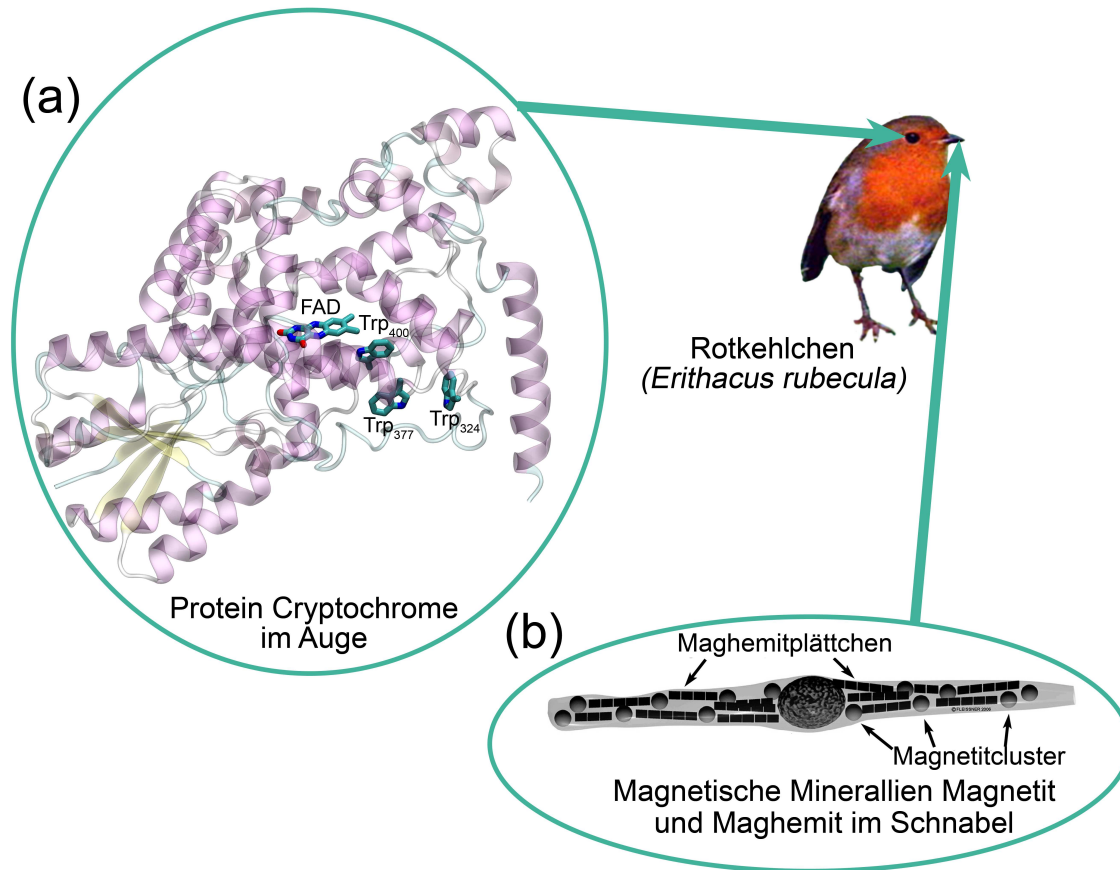


Figure 1: (a) Schematische Darstellung von dem blaues Licht empfangenden Protein Cryptochrom, das sich im Auge von Vögeln, sowie in einige anderen Tieren und Pflanzen befindet. In dieser Dissertation wird Cryptochrom als möglicher Magnetorezeptor vorgeschlagen. Im Teil (b) der Abbildung ist schematisch die Struktur des Sensor dendriten gezeigt, der die magnetischen Mineralien Magnetit und Maghemit enthält. Diese Mineralien wurden experimentell in den Sensor-Dendriten des oberen Schnabels bei verschiedenen Vogelarten nachgewiesen. Das Maghemit/Magnetit bildet einen zweiten Magnetfeldrezeptor, der in diese Arbeit beschrieben wird.

(Magnetitcluster) (siehe Abb. 1b). Die Wechselwirkung zwischen diesen Teilchen kann durch das externe Magnetfeld beeinflusst werden, welches zunächst die Öffnung von mechanosensiblen Ionenkanälen verursacht und letzten Endes zum Orientierungsverhalten der Vögel führt. In der Dissertation wird die potentielle Energie des Magnetitclusters unter verschiedenen Orientierungen des externen Magnetfeldes untersucht. Aus dem potentiellen Energieprofil werden anschließend die

Kräfte berechnet, die auf den Magnetitcluster wirken. Danach werden die Kraftänderungen aufgrund der Änderung der Magnetfeldrichtung berechnet. Als nächstes werden die Wahrscheinlichkeit für die mechanosensible Ionenkanal-Öffnung festgestellt. Als wichtigen Hinweis, den die Experimentatoren prüfen müssen, wird das Fenster für die Magnetfeldintensität innerhalb dessen der Mechanismus funktionieren kann. Zum Schluss wird gezeigt, dass dieser auf Eisenmineralien basierenden Mechanismus sowohl ein Inklinationskompass als auch ein Polarkompass darstellt. Verschiedene Bedingungen, die den Magnetorezeptionsprozess stören könnten, werden ebenfalls beschrieben.

Der Gedanke, dass das Erdmagnetfeld im Vogel durch kleine magnetische Teilchen erkannt wird, wurde schon seit dem Jahre 1970 diskutiert, nachdem experimentell nachgewiesen wurde, dass einige Bakterien lange Magnetketten besitzen [26]. Es wurde gezeigt, dass diese Ketten magnetisch sind und die Bakterien sich deswegen entlang der Feldlinien ausrichten. Verschiedene Modelle der erklären, wie der magnetit-basierte Magnetorezeptor im Vogel funktionieren könnte, wurden in den letzten Jahren vorgeschlagen [40–44]. Der Mechanismus, der in dieser Dissertation besprochen wird, ist anders, weil er Grundlegend zwei magnetische Mineralien beinhaltet. In den oben zitierten Arbeiten spricht man nur über Magnetit, und es wurde vorgeschlagen, dass die Magnetitcluster sich anziehen oder sich abstossen, was zur Deformation der Zellmembrane führt, und die Öffnung der Ionenkanäle steuert. Diese Mechanismen wurden vor fünfzehn Jahren vorgeschlagen [62], als man noch nichts über die Maghemiteplättchen wusste. Wegen der starken magnetischen Eigenschaften des Maghemit (es ist ferrimagnetisch [63]) sollten die Maghemitplättchen eine wichtige Rolle im Magnetorezeptionsmechanismus spielen.

Als die beiden Hypothesen für Vogel-Magnetorezeption vorgeschlagen wurden (nämlich der lichtabhängige Prozess im Auge und die Wechselwirkung von magnetischen Teilchen im Schnabel) hat man sie als zwei konkurrierende Mechanismen betrachtet. Jedoch zeigen viele experimentelle Befunde, dass wenigstens im Vogel beide Mechanismen nebeneinander möglich sind. Vögel und Fische sind die einzigen Gruppen für die es einige Neuroanatomische und Elektrophysiologische Nachweise, die mit Magnetorezeption assoziiert sind, gibt. Verhaltensversuche, die zwischen den zwei Mechanismen unterscheiden, sind nur für Vögel bekannt.

Das Ziel dieser Dissertation ist es, eine umfassende theoretische und numerische Untersuchung der Magnetorezeptionsphänomen durchzuführen. In dieser Arbeit werden als erster grosser Schritt die theoretischen Modelle beschrieben und ihre

Funktionalität unter realistischen Bedingungen für das Erdmagnetfeld überprüft. Die Ergebnisse, die hier beschrieben werden, kann man als Basis für weitere Forschungsprojekte nutzen. Zum Beispiel kann man auf Grund dieser Arbeit untersuchen, wie verschiedene Bedingungen (z.B. die Influenz eines oszillierenden Magnetfeldes, sowie der Flug (die Bewegung) durch elektrische Felder, etc) die Magnetorezeption in Tieren ändern könnte. Ein weiterer grosser Schritt wird sein zu verstehen, wie einige Tiere das Erdmagnetfeld fühlen können, und wie im Vergleich dazu lokale Magnetfelder erzeugt durch Gebäude, Strassen, Autobahnen, Gebirge, Eisenbergwerke und andere magnetische Objekte, registriert werden können. Möglicherweise wird diese Forschung zur Entdeckung eines ähnlichen ("sechsten") Sinnes in vielen Tieren führen und auch im Menschen bedeutsam sein.

# Contents

<b>1</b>	<b>Introduction</b>	<b>1</b>
1.1	Aims of the Thesis . . . . .	2
<b>2</b>	<b>Magnetoreception Mechanisms in Birds</b>	<b>5</b>
2.1	The Geomagnetic Field . . . . .	5
2.2	Inclination and Polarity Compass . . . . .	7
2.3	Magnetoreception Models . . . . .	11
2.3.1	Light-Dependent Magnetic Compass . . . . .	12
2.3.2	Iron-Mineral-Based Magnetic Map . . . . .	15
2.4	Novel Magnetoreception Mechanisms . . . . .	18
2.4.1	Radical-Pair-Based Compass in Cryptochrome . . . . .	18
2.4.2	Iron-Mineral-Based Magnetoreceptor . . . . .	25
<b>3</b>	<b>Theoretical Background</b>	<b>33</b>
3.1	The Radical Pair Mechanism . . . . .	33
3.1.1	The Radical Pair Mechanism: Introduction . . . . .	33
3.1.2	Radical Pair Hamiltonian . . . . .	36
3.1.3	Hyperfine Interaction . . . . .	39
3.1.4	Exchange and Dipolar Interactions . . . . .	41
3.1.5	Density Matrix and the Liouville Equation . . . . .	44
3.1.6	Stochastic Liouville Equation . . . . .	46
3.1.7	Theory of Electron Transfer . . . . .	50
3.1.8	Singlet – Triplet Interconversion Rate . . . . .	54
3.1.9	Cryptochrome Activation Yield . . . . .	58
3.2	Iron-Mineral Based Magnetoreceptor Model . . . . .	59
3.2.1	Magnetic Properties of the Iron-Minerals . . . . .	59
3.2.2	Magnetic Moment of the Maghemite Platelet . . . . .	66

3.2.3	Magnetic Moment of the Magnetite Cluster . . . . .	67
3.2.4	Model of Interacting Point-Like Dipoles . . . . .	70
3.2.5	Model of Interacting Dipoles of Finite Size . . . . .	72
3.3	Summary . . . . .	75
<b>4</b>	<b>Magnetic Field Effect in Cryptochrome</b>	<b>77</b>
4.1	Introduction . . . . .	77
4.2	Hyperfine Coupling . . . . .	77
4.3	Rate Constants for the Electron Transfer Processes in Cryptochrome .	80
4.3.1	Electron Forward Transfer . . . . .	80
4.3.2	Electron Back-Transfer . . . . .	82
4.3.3	Deprotonation Rate . . . . .	83
4.3.4	Rate Constants of Various Processes in Cryptochrome . . . . .	83
4.4	Magnetic Field Dependence of Activation Yield . . . . .	84
4.5	Angular Dependence of Activation Yield . . . . .	89
4.6	Time Dependence of Singlet and Triplet Populations . . . . .	92
<b>5</b>	<b>Iron-Mineral based Magnetoreceptor Model</b>	<b>97</b>
5.1	Introduction . . . . .	97
5.2	Magnetic Properties of the Magnetite Platelets and of the Magnetite Cluster . . . . .	98
5.3	Interaction of Point-Like Dipoles . . . . .	99
5.3.1	Potential Energy Surface of the Magnetite Cluster . . . . .	99
5.3.2	Forces Acting on the Magnetite Cluster . . . . .	103
5.4	Model for a Transducer Mechanism of the Geomagnetic Field . . . . .	107
5.5	Interaction of Dipoles of Finite Size . . . . .	115
5.5.1	Potential Energy Surface of the Magnetite Cluster . . . . .	115
5.5.2	Forces Acting on the Magnetite Cluster . . . . .	118
5.6	Magnetic Window of the Iron-Mineral-Based Magnetoreception Me- chanism . . . . .	120
5.7	The Polarity Compass . . . . .	122
5.8	Magnetoreceptor Unit with Different Number of Platelets . . . . .	127
5.9	Magnetoreceptor Unit in Higher Magnetic Fields . . . . .	135
5.10	Role of the Non-Magnetic Vesicle . . . . .	138
5.11	Further Steps for Experimental Verification . . . . .	139

---

<b>6 Conclusion</b>	<b>143</b>
<b>Acknowledgments</b>	<b>147</b>
<b>Appendix A: Direct Product of Matrices</b>	<b>149</b>
<b>Appendix B: Physical Units</b>	<b>155</b>
<b>Bibliography</b>	<b>159</b>
<b>Biography (Lebenslauf)</b>	<b>181</b>





# Chapter 1

## Introduction

Bird migration has fascinated humans for a long time and the question of how birds can find their way on their biannual migratory flights has been of great interest to amateur ornithologists as well as to professional scientists. Migratory birds use cues of a wide variety of different sources for orientation. Orientational experiments with wild and hand-raised birds have shown that they use celestial and geomagnetic information for identifying their migratory direction (reviews of these studies can be found in [2–6]). The sun compass in association with the local time, measured by their inner clock, allows them to identify the azimuthal position of the sun during the day [7]. Polarized light patterns, most prominently visible at the sky during sunset and sunrise, plays an important role in orientation [8–10]. Once young birds have learned the spatial relationships between stars by observing the center of rotation of the starry sky, the star compass provides them with information about geographic direction [11, 12].

Many birds are also able to accurately orient themselves when the sky is not visible (e.g., cloud cover). This requires non-visual sources of information. Many studies [13–16] have established that birds are sensitive to the Earth’s magnetic field. Pigeons and other birds use the geomagnetic field as a compass, and are also sensitive to slight temporal and spatial variation in the magnetic field that are potentially useful for determining location [3, 44].

Not only do birds have a magnetic sense. Salamanders, frogs and sea turtles use the magnetic field to orient themselves in the direction of the nearest shore when, for example, they sense danger [17–20]. In honeybees magnetoreception is demonstrated by activities such as comb building and homing orientation [21–25]. Movement and orientation of organisms with respect to a magnetic field, magnetotaxis, has also

been shown to exist in bacteria [26–28].

However, despite decades of research, the precise mechanism of magnetoreception is still not well understood. During the last forty years several hypotheses were suggested to explain this phenomenon. The main subject of this thesis is to study two mechanisms underlying animal magnetoreception, which are likely to be co-existing. The main focus of the thesis is made on avian magnetoreception, but the suggested mechanisms are believed to be general and possible in all kinds of animals and even human beings.

## 1.1 Aims of the Thesis

The aim of this work is to describe the two mechanisms which might be responsible for avian magnetoreception. Two theoretical concepts possibly underlying this phenomenon are formulated and their functioning is proven in a realistic geomagnetic fields. It has been proposed that:

1. Animal magnetoreception is mediated by the blue light receptor protein cryptochrome, which was recently found to be localized in the retinas of migratory birds [64]. Cryptochromes are a class of photoreceptor signaling proteins which are found in a wide variety of organisms and which primarily perform regulatory functions, such as the entrainment of circadian rhythm in mammals [54, 55] and the inhibition of hypocotyl growth in plants [56].

Cryptochrome was suggested as a possible magnetoreceptor for the first time in Ref. [1]. However, no realistic calculation of magnetic field effect in cryptochrome were performed. One of the goals of the present thesis is to study computationally the spin dynamics in cryptochrome and to show the feasibility of the cryptochrome-based compass in birds. The analysis is based on the results published in our recent paper [36].

2. The avian magnetoreception mechanism is based on the interaction of two iron minerals (magnetite and maghemite) which were experimentally found in subcellular compartments within sensory dendrites of the upper beak of several bird species [58–61]. The iron minerals in the beak form platelets of crystalline maghemite and assemblies of magnetite nanoparticles. The interaction between these particles can be manipulated by the external magnetic field

inducing a primary receptor potential via strain-sensitive membrane channels leading to a certain bird orientation effect.

The idea that the geomagnetic field is being mediated by tiny magnets in the birds has been discussed since the 1970s, when certain bacteria were discovered to contain chains of single domain magnetite [26] that act as magnets and align the bacteria along the field lines. A variety of models on how such magnetite-based magnetoreceptors might work has been suggested [40–44]. The mechanism discussed in the present thesis is different from the magnetite-based magnetoreception mechanism suggested earlier because it involves two different types of iron-minerals. In the papers cited above, only magnetite was considered. It was suggested that the magnetite clusters, depending on the orientation of the external field, will attract or repel each other, thus deforming the membrane and possible opening or closing the ion channels. This mechanism was suggested about fifteen years ago [62], long before the maghemite platelets were discovered in the beak of birds. Since maghemite has ferrimagnetic nature [63,65–68] and possesses pronounced magnetic properties the maghemite platelets should play an important role in the magnetoreception mechanism.

The second part of the thesis, devoted to the study of the iron-mineral-based magnetoreceptor, is based on our recent publications [37–39].

When it was first suggested, the magnetite hypothesis and the spin-based model were considered alternatives that largely exclude each other. However, an increasing body of evidence indicates that both mechanisms can exist side by side, at least in birds (for review see Refs. [2–6]). Unfortunately, the number of groups that have so far been tested for their magnetoreception mechanisms is still very limited, with birds being by far the best-studied group. Birds and fish are the only groups where some neuroanatomical and electrophysiological evidence associated with magnetoreception is available. Behavioral experiments designed to distinguish between the two models are only known from birds.

The thesis is organized as follows. Chapter 2 gives an overview of magnetoreception mechanisms in birds. The basic facts about the geomagnetic field are presented in section 2.1. In section 2.2 two different magnetic compasses observed in animals are described, namely the polarity compass and the inclination compass. 2.3. The existing magnetoreception models described in literature are overviewed

in section 2.3. In section 2.4 the two novel proposed magnetoreception mechanisms are discussed in detail. The cryptochrome-based mechanism is described in subsection 2.4.1, while the iron-mineral-based magnetoreception mechanism is described in subsection 2.4.2.

The theoretical formalism underlying both magnetoreception mechanisms is described in chapter 3. In section 3.1 the theory of the radical pair mechanism in cryptochrome is discussed. The construction of the radical-pair Hamiltonian is outlined in subsection 3.1.2. In subsections 3.1.3 and 3.1.4 the hyperfine and exchange/dipolar interactions in the radical pairs in cryptochrome are discussed. The density matrix is introduced in subsection 3.1.5. Subsection 3.1.6 discusses the Stochastic Liouville equation, which is used to calculate the activation yield of cryptochrome in external magnetic field. The basics of the electron transfer theory are discussed in subsection 3.1.7, while the rate of the singlet – triplet spin – flip transitions is calculated in subsection 3.1.8. The cryptochrome activation yield is discussed in section 3.1.9.

The theory behind the iron-mineral-based magnetoreception model is outlined in section 3.2. The basic facts about the magnetic properties of magnetite and maghemite are summarized in subsection 3.2.1. The magnetic moments of the maghemite platelets and of the magnetite cluster are estimated in subsections 3.2.2 and 3.2.3 respectively. Further in this section two theoretical models are discussed: in subsection 3.2.4 a model is formulated which neglects the size of the maghemite platelets and of the magnetite cluster and treats them as point-like dipoles; in subsection 3.2.5 a model, which accounts for the finite size of the maghemite platelets and of the magnetite cluster is presented.

Chapters 4-5 discuss the results of the calculation. Chapter 4 discusses the spin chemistry processes in cryptochrome, while chapter 5 discusses the iron-mineral based magnetoreceptor model.

The thesis is summarized in chapter 6.

The present thesis is based on the original results, partly published in leading international journals (see a list of publication).

# Chapter 2

## Magnetoreception Mechanisms in Birds

### 2.1 The Geomagnetic Field

A detailed knowledge of the properties of the geomagnetic field is important when discussing animal magnetoreception, orientation and navigation. The geomagnetic field is a dipole field, that is aligned approximately with the Earth's axis of rotation [69] (see Fig. 2.1). It is generated by a self-sustaining geo-dynamo, where electrically conducting iron material in the outer liquid core is moved across the existing magnetic field [70].

The intensity of the geomagnetic field is maximal at the magnetic poles (being about  $68 \mu\text{T}=0.68 \text{ G}$ ), where the field lines stand vertically to the Earth's surface (inclination angle  $90^\circ$ ) and minimal close to the magnetic equator (being about  $23 \mu\text{T}=0.23 \text{ G}$ ), where the field lines are parallel to the Earth's surface (inclination angle  $0^\circ$ ). Figures 2.1 and 2.2 illustrate this fact.

The Earth's North Magnetic Pole is the wandering point on the Earth's surface at which the Earth's magnetic field points vertically downwards.

As of 2005 the **North Magnetic Pole** lay near *Ellesmere Island* in northern Canada at  $82.7^\circ \text{ N}$ ,  $114.4^\circ \text{ W}$ . [71] Its southern hemisphere counterpart is the **South Magnetic Pole**. As of 2005 the South Magnetic Pole was calculated to lie at  $64.5^\circ \text{ S}$ ,  $137.9^\circ \text{ E}$  [71], just off the coast of Wilkes Land, Antarctica. It is moving north west by about 10 to 15 kilometers per year

Because the Earth's magnetic field is not exactly symmetrical, the North and South Magnetic Poles are not antipodal: a line drawn from one to the other does not pass through the center of the Earth (it actually misses by about 530 km).

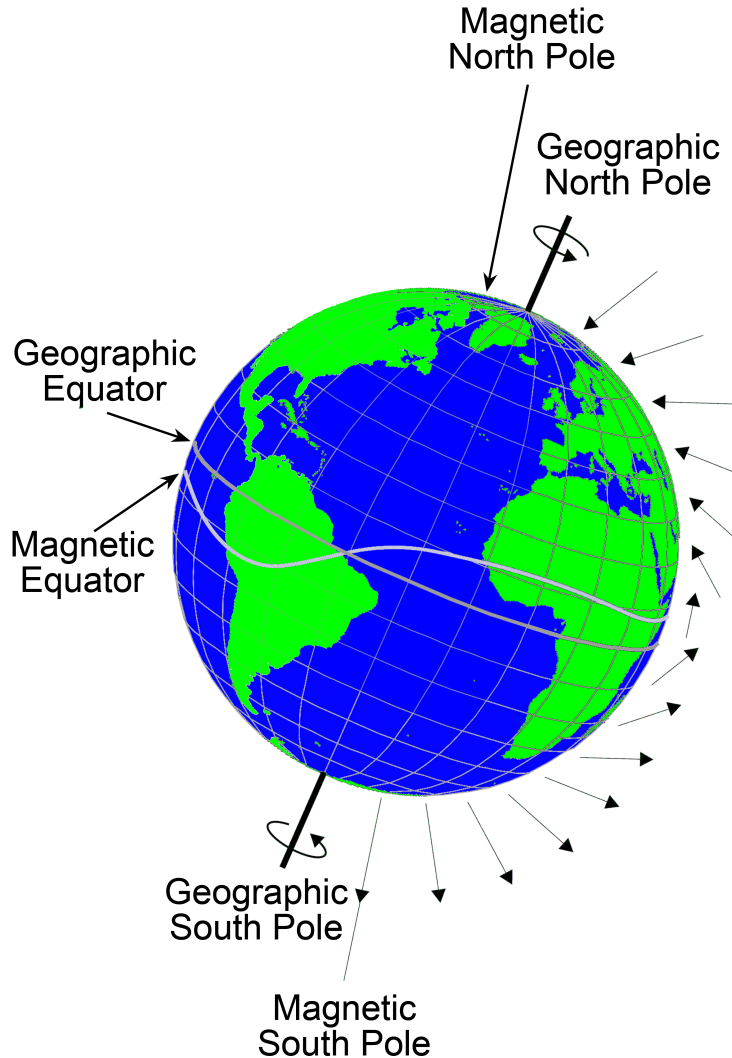


Figure 2.1: Schematic drawing of the Earth's magnetic field (redrawn from [51]). The arrows show the course of the magnetic field lines and their length is drawn relative to the magnetic field intensity at different latitudes. The magnetic field intensity is strongest at the magnetic poles (about  $68 \mu\text{T}=0.68 \text{ G}$ ) and weakest at the magnetic equator (about  $23 \mu\text{T}=0.23 \text{ G}$ ). The steepness of the magnetic field lines relative to the surface of the Earth shows the angle of inclination, which is maximal at the magnetic poles ( $\pm 90^\circ$ ) and minimal ( $0^\circ$ ) at the magnetic equator.

Because of changes in the flow patterns generated in the Earth's liquid outer-core and boundary processes in the core-mantle, the Earth's main magnetic field is constantly drifting [69]. The poles are wandering several tenths of a degree annually

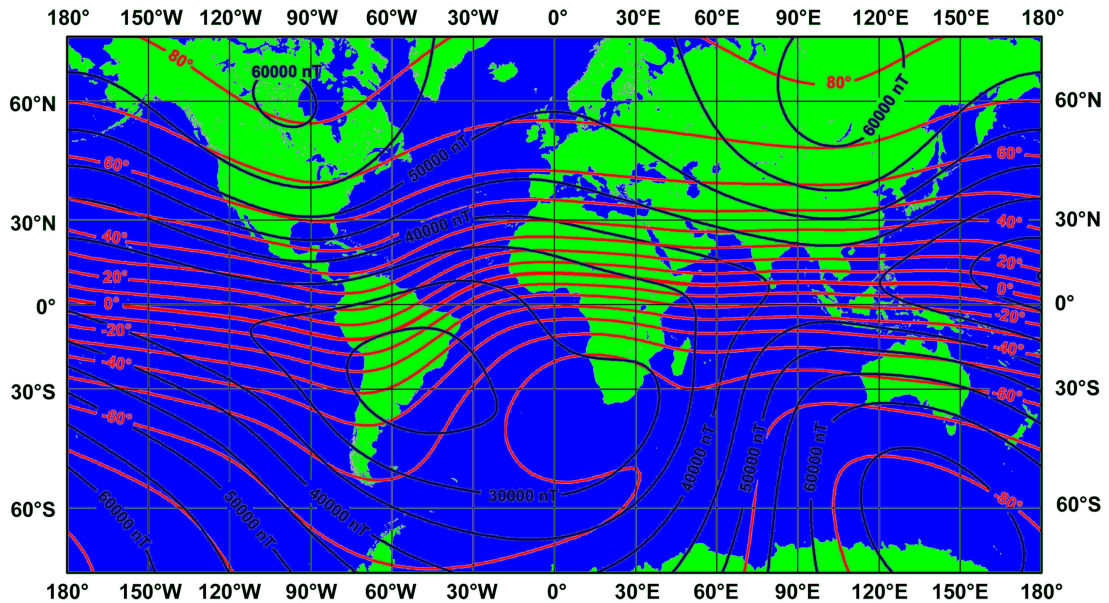


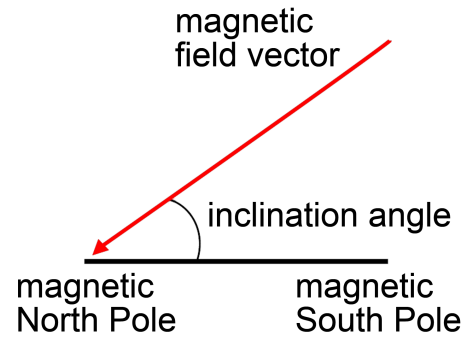
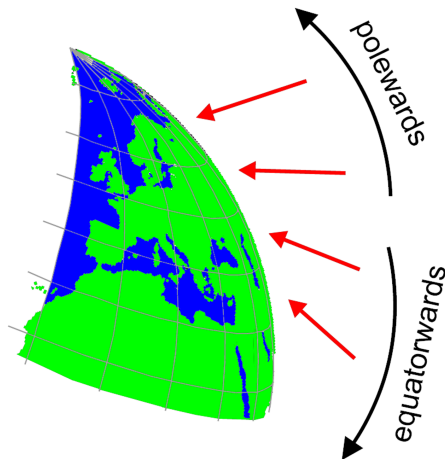
Figure 2.2: Total intensity (dark-blue contour lines) and inclination (red contour lines) of the Earth's magnetic field according to the World Magnetic Model WMM 2000 (<http://geomag.usgs.gov/dod.html>). The total intensity is given in steps of 5000 nT, the inclination in steps of 10°.

(secular variation), such that the total intensity of the Earth's magnetic field has been decreasing by about 10% since 1900. Therefore, these secular variations have to be considered when discussing the evolution of migration routes and the use of geomagnetic maps for navigation in long-living animals. Solar electromagnetic radiation, constantly emitted during solar activity and thunderstorms, also produces a large time-varying magnetic fields in the atmosphere and is especially strong on the sunward side of the Earth [72]. Normal diurnal changes are in the order of 10 nT to 30 nT, but can reach 500 nT during magnetic storms. These diurnal changes can pose substantial difficulties for animals using the geomagnetic field for orientation or navigation at smaller scales and there are indications that animals might calibrate their magnetic compass and map during the magnetically calmer nights [73].

## 2.2 Inclination and Polarity Compass

Two different magnetic compasses have been described in the literature with fundamental differences in their functional characteristics: a **polarity compass** and an **inclination compass** (Fig. 2.3 and Fig. 2.4). The polarity compass is similar to our

## Northern hemisphere



## Southern hemisphere

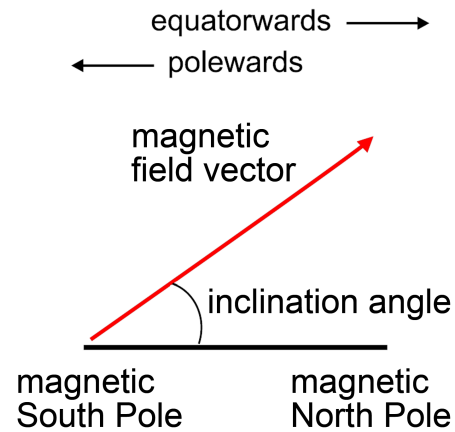
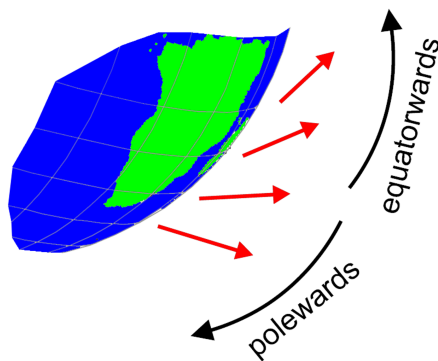


Figure 2.3: The avian inclination compass provides the animals with information on the axial alignment of the magnetic field (direction along the magnetic north-south axis), the direction towards the magnetic pole that lies closer (intersection of magnetic field line with horizon) and the magnetic equator (direction where magnetic field lines and horizon diverge). An inclination compass does not perceive the polarity of the magnetic field vector, as used by our technical compasses.

technical compass, using the polarity of the magnetic field to distinguish between magnetic 'North' and 'South' (see Fig. 2.4a). The inclination compass, in contrast, ignores polarity and relies instead on the axial course of the field lines. It obtains unimodal directional information by interpreting the inclination of the field lines



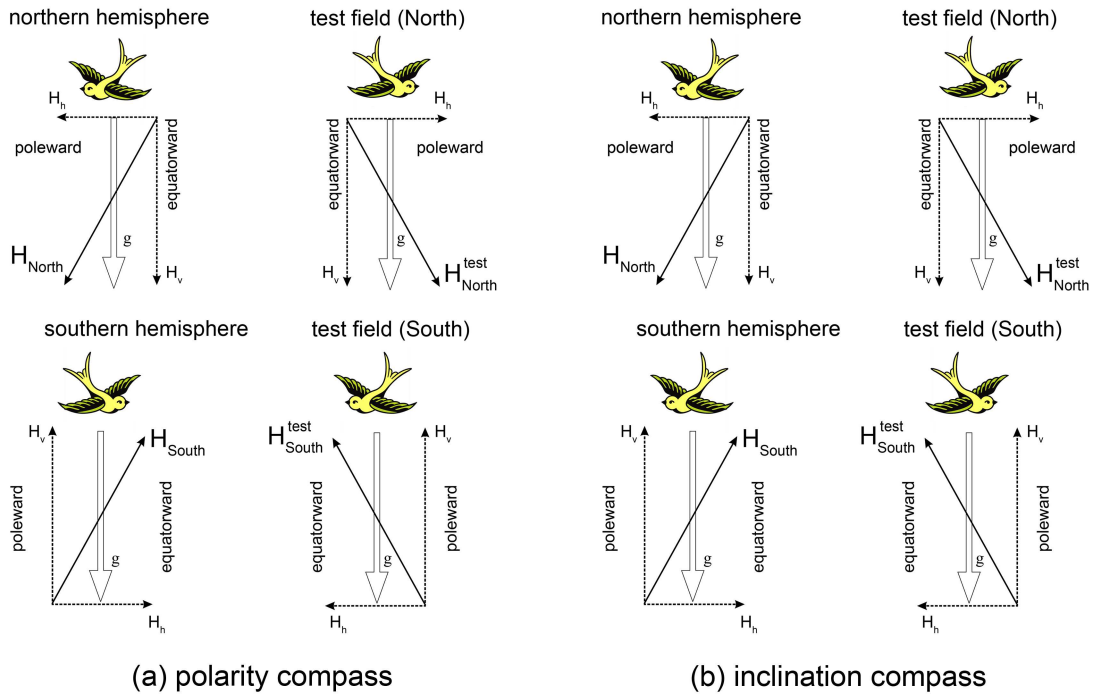


Figure 2.4: Principle of the **polarity compass** (a) and of the **inclination compass** (b), after Wiltschko and Wiltschko [16,74]. In the inclination compass the polarity of the magnetic field vector is irrelevant since birds obtain directional information from the axial course of the lines. That way, birds cannot distinguish between northward and southward, but between poleward and equatorward. In the polarity compass the direction of the magnetic field vector is important.  $g$  represents the gravity vector,  $H_v$  and  $H_h$  are the vertical and horizontal components of the magnetic field.  $H_{North}$  and  $H_{South}$  indicate the Earth magnetic field in the northern and southern hemispheres.  $H_{North}^{test}$  and  $H_{South}^{test}$  indicate the experimental magnetic field in the northern and southern hemisphere, which correspond to the "normal" magnetic field with inverted horizontal component. The images of the bird above each drawing shows the flight direction of a bird during its "poleward" flight program [74].

with respect to up and down.

The magnetic compass was first described for European robins (*Erithacus rubecula*), a passerine species that migrates at night. Captive individuals of migrants become restless in their cages at the times of the year when their free-living conspecifics migrate, and they prefer to stay at the side of their cage pointing towards their migratory direction. This behavior was used to analyze the birds' orientation in the laboratory, where magnetic conditions can easily be changed in a controlled way. The test-bird was put in a funnel-like cage, covered with the scratch-sensitive

tip-Ex paper. The external magnetic field was created by the coils, surrounding the cage. When the magnetic north was rotated by coil systems, while the field's total intensity and inclination were almost unchanged and all other potential directional cues remained the same, the birds altered their directional preferences according to the change in magnetic north. This behavior indicates that they used the magnetic field for direction finding [15].

Analyses of the birds' magnetic compass showed that if the vertical component of the magnetic field vector was inverted: birds heading North in the geomagnetic field reversed their heading, now preferring South (see Fig. 2.4b, top left and Fig. 2.4b, bottom right diagrams). This is how the inclination compass in birds was discovered. The major experiments were performed by Wiltschko *et al.* and published in Refs. [2, 16, 74–76]. Reversing the horizontal component and inverting the vertical component alter the axial course of the field lines in the same way (see Fig. 2.4b, top left and Fig. 2.4b, bottom left diagrams); an animal not perceiving the polarity of the magnetic field will not realize any difference. Hence birds reverse their headings in both situations alike [2, 16, 74, 75].

This means that the avian magnetic compass does not distinguish between magnetic 'north' and 'south', as indicated by polarity, but between 'poleward' (where the field lines run downward) and 'equatorward' (where they run upward), as shown in Fig. 2.4.

The response of animals in a magnetic field with the vertical component inverted (see Fig. 2.4, right) is diagnostic: rodents [77] and spiny lobsters [78] maintain their headings, indicating that their magnetic compass is a polarity compass, while birds [16], salamanders [79] and marine turtles [80] reverse theirs, revealing the use of an inclination compass.

However, the geomagnetic field does not only provide directional information, magnetic intensity and/or inclination can be used to obtain positional information. This is less well documented and the available evidence comes only from a small number of species. When spiny lobsters [81] and marine turtles [18] were tested in magnetic fields characteristic for sites hundreds of kilometers away from the location where they actually stayed, the animals chose headings that would have led them to their home site if they had been displaced to the respective sites. This clearly shows that these animals can use magnetic intensity and inclination to derive information on their position relative to a goal. The same is suggested for birds [82] and salamanders [19].

Total intensity, inclination or a combination of both may also serve as 'sign-posts' or 'triggers' – marking certain regions on the earth where animals must respond in a particular way. Here, specific magnetic parameters elicit orientational responses such as changes in the heading of migratory birds [83,84] and marine turtles [17] as well as physiological responses like gaining body weight [85].

## 2.3 Magnetoreception Models

In contrast with most other senses in animals, we know very little about magnetoreception mechanisms. Static magnetic fields such as the geomagnetic field penetrate living matter and a receptor can thus be located almost anywhere in the body. Indeed, there seems to be no large organ specialized for magnetoreception, despite intense search for it. The main problem of geomagnetic field perception is the fact that the Earth's magnetic field is very weak and that a magnetoreceptor needs to be able to detect absolute values or small variations of such a field. Behavioral experiments [6,14,29–32] have helped to characterize the function of the magnetoreceptors in some animal groups, while physiological studies [2,6,33] have revealed valuable indications of how animals could perceive the geomagnetic field. The variety of magnetoreception models [1,34–47] illustrate in how many different theoretical ways magnetoreception could function.

The magnetic sense is the least understood sensory system in animals and this is what makes it in my opinion so interesting to explore! As early as 1855 did von Middendorff suggest the use of the magnetic field by migrating birds: *"... so liegt der Gedanke nahe, es möge die erstaunliche Unbeirrbarkeit der Zugvögel - trotz Wind und Wetter, trotz Nacht und Nebel - eben darauf beruhen, dass das Geflügel immerwährend der Richtung des Magnetpoles sich bewusst ist, und demzufolge auch seine Zugrichtung genau einzuhalten weiss. Was dem Schiffe die Magnetnadel ist, wäre dann diesen 'Seglern der Lüfte' das innere magnetische Gefühl, welches im Zusammenhang mit den galvanisch-magnetischen Strömungen stehen mag, die im Innern des Körpers dieser Tiere, zumal in ihren Bewegungsapparaten, erwiesener Maassen kreisen."* [48]. Still, not before the 1960's was the magnetic compass experimentally demonstrated in birds [13–15].

Behavioral and physiological studies suggest the presence of two magnetoreception mechanisms in birds that detect different parameters of the geomagnetic field: (1) a light-dependent process detecting the axial course and the inclination angle

of the geomagnetic field lines, providing the birds with magnetic compass information (inclination compass) [2–6] and (2) a magnetite-mediated process, providing magnetic map information (map sense; for reviews see [2, 49–53]).

### 2.3.1 Light-Dependent Magnetic Compass

Several different biophysical magnetoreception models have been proposed to explain the light dependence of the magnetic compass in animals. Leask [86] was the first to propose an "optical pumping model" where magnetoreception might be dependent on light. The currently most discussed model was originally proposed by Klaus Schulten [87, 88] who demonstrated that an external magnetic field can influence photon-induced processes involving bimolecular reactions. In this process, the so-called **radical pairs** are formed by photon excitation through light absorption similar to the photosynthetic reactions. Based on this theory, Schulten and Windemuth [34] proposed a model for a biophysical magnetic compass with photoreceptor-molecules as likely organic reactants and suggested vision as a possible sensory detection system. The animals would perceive the magnetic field as an apparent light intensity or color variation in their visual field.

Ritz *et al.* [1] refined this magnetoreception model and proposed **cryptochromes**, a class of photoreceptors newly discovered in animals [64], as the magnetosensing molecules. It was shown theoretically that magnetic fields with intensities in the range of the geomagnetic field can produce a significant increase of the activation yield, which also depends on the relative orientation between the magnetic field and the radical pairs [1, 35, 36, 89–95]. Magneto-sensitive photoreceptors arranged in an ordered array, like the retina or pineal<sup>1</sup>, would show an increased or decreased response to light, depending on their alignment relative to the magnetic field – hence allowing the animals to "see" the magnetic field lines.

In birds, there is strong evidence that magnetoreception of inclination compass information takes place in the eyes, specifically in the right eye [29, 96]. Recent experiments showed that birds are disoriented when tested with the right eye covered

---

<sup>1</sup>The pineal gland (also called the pineal body, *epiphysis cerebri*, or *epiphysis*) is a small endocrine gland in the brain. It is shaped like a tiny pine cone, and is located near the center of the brain, between the two hemispheres, tucked in a groove where the two rounded thalamic bodies join. It produces structurally simple hormone that communicates information about environmental lighting to various parts of the body. Ultimately, melatonin has the ability to entrain biological rhythms and has important effects on reproductive function of many animals. The light-transducing ability of the pineal gland has led some to call the pineal the "third eye".

with light-proof caps, but were well oriented and reacted to an inversion of the magnetic field when tested with the left eye covered [29, 96]. Recent findings of cryptochrome expression in avian retinas further support this model furthermore [97, 98].

Also extracellular recordings in the nucleus of the basal optic root (nBOR) and in the optic tectum, which are parts of the optic nerve, in pigeons support the involvement of the optical system in magnetoreception. The optic nerve, also called cranial nerve II, is the nerve that transmits visual information from the retina to the brain. The experiments demonstrated response to changes in the direction of the magnetic field [99] and maximal magnetic responsiveness occurred at wavelengths of 503 nm and 582 nm [33]. It will be very valuable to reproduce these recordings and examine the neuronal responses at the wavelengths where behavioral experiments show specific orientation reactions.

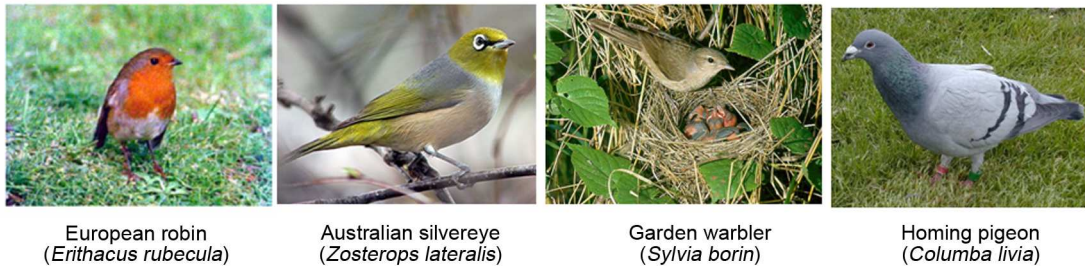


Figure 2.5: Images of European robin (*Erithacus rubecula*), Australian silvereye (*Zosterops lateralis*), Garden warbler (*Sylvia borin*), and homing pigeon (*Columba livia*).

The proposed involvement of light in the transduction mechanism of magnetoreception encouraged homing and orientation experiments under different wavelengths of light. The first experiments were carried out with homing pigeons, *Columba livia domestica*, demonstrating that young, inexperienced birds were disoriented after being displaced in complete darkness or under 660 nm red light, but oriented towards the home direction after being transported to the release site under 565 nm green or full spectrum light [30, 31]. Orientation experiments with passerine migrants under different monochromatic lights gave further support for the involvement of light-sensitive molecules active at specific wavelengths (for a summary, see Fig. 2.6). European robins, Australian silvereyes, Garden warblers and homing pigeons, Fig. 2.5,

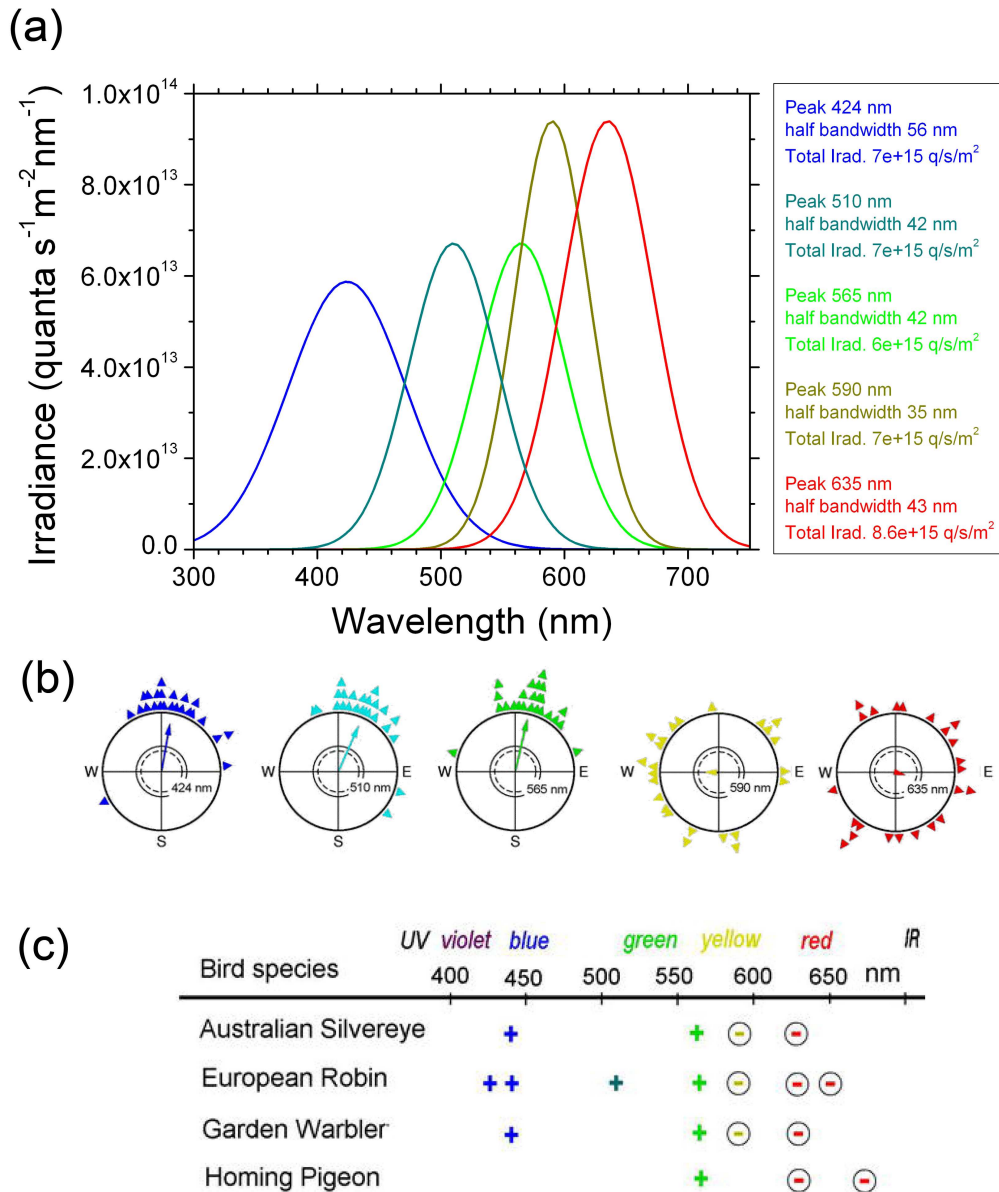


Figure 2.6: Orientation behavior of birds under monochromatic lights produced by light-emitting diodes (LEDs) of various wavelengths, with the peakwavelength indicated. (a): Spectra of the LEDs producing the test lights. (b): Orientation of European robins in spring. Each triangle represents the heading of an individual bird. (c): Responses of four bird species tested under the various wavelengths: Australian silvereeyes, *Zosterops lateralis*, European robins, *Erithacus rubecula*, Garden warblers, *Sylvia borin*, and homing pigeons, *Columba livia*: (+) oriented behavior, (-) disoriented behavior. Figure adapted after Refs. [2, 6].

were tested under light with wavelength in the range between 424 nm (blue) and 635 nm (red) and under different intensities ranging from 0.57 to  $44 \times 10^{15}$  quanta  $\text{s}^{-1}\text{m}^{-2}$  (see Appendix B for more details on light-intensity units). The experiments under low-intensity light showed that both juvenile and adult birds were well oriented into the seasonally expected migratory directions under full spectrum (white), 443 nm (blue), 510 nm (turquoise) and 565 nm (green) light, but disoriented under 590 nm (yellow) and 630 nm (red) light [32, 100–104]. These results indicate that magnetoreception becomes critical under light of peak wavelengths longer than 565 nm.

Light-dependent magnetoreception seems to vary not only between wavelengths, but also between different intensities of light of the same wavelength. Shifts in directions deviating from the expected migratory direction have been reported under higher light intensities for different wavelengths ( $43\text{--}44 \times 10^{15}$  quanta  $\text{s}^{-1}\text{m}^{-2}$ ; [29, 32, 105]). Just recently, Wiltschko et al. [106] showed that birds do not use inclination compass orientation when tested under blue and green lights of such high intensities, i.e. they did not react to an inversion of the vertical component of the magnetic field. Still, they reacted to a shift of the horizontal component, indicating the use of a polarity compass or a fixed alignment along a magnetic direction (see section 2.2 for more details about polarity and inclination compasses).

In early experiments [32, 100–104], migratory birds had shown to be apparently unable to use their magnetic compass under 635 nm red light. However, pre-exposure to red light for 1 hr immediately before the critical tests under red light of  $6\text{--}7 \times 10^{15}$  quanta  $\cdot \text{s}^{-1} \cdot \text{m}^{-2}$  enabled robins to orient in their seasonally appropriate migratory direction in spring as well as in autumn [107]. Pre-exposure to darkness, by contrast, failed to induce orientation under red light. Under green light of  $7 \times 10^{15}$  quanta  $\cdot \text{s}^{-1} \cdot \text{m}^{-2}$ , the birds were oriented in their migratory orientation after both types of preexposure. These findings suggest that the newly gained ability to orient under red light might be based on learning to interpret a novel pattern of activation of the magnetoreceptors and hence, may represent a parallel to the previously described enlargement of the functional window to new magnetic intensities.

### 2.3.2 Iron-Mineral-Based Magnetic Map

The receptor of the avian map sense is proposed to contain magnetic particles and to be situated in the ethmoid region of the upper beak area [58], which is innervated

by the *Ramus ophthalmicus*, a branch of the trigeminal nerve. The localization of putative magnetoreceptors in the beak of homing pigeons is schematically illustrated in Fig. 2.7. For several bird species, magnetic measurements of the head, neck and beak area and histological examinations of the upper beak area indicate the presence of magnetic material [58, 108–114]. When first discovered, these particles have been at least partly identified as single-domain or superparamagnetic magnetite crystals ( $\text{Fe}_3\text{O}_4$ ) [58, 112, 113].

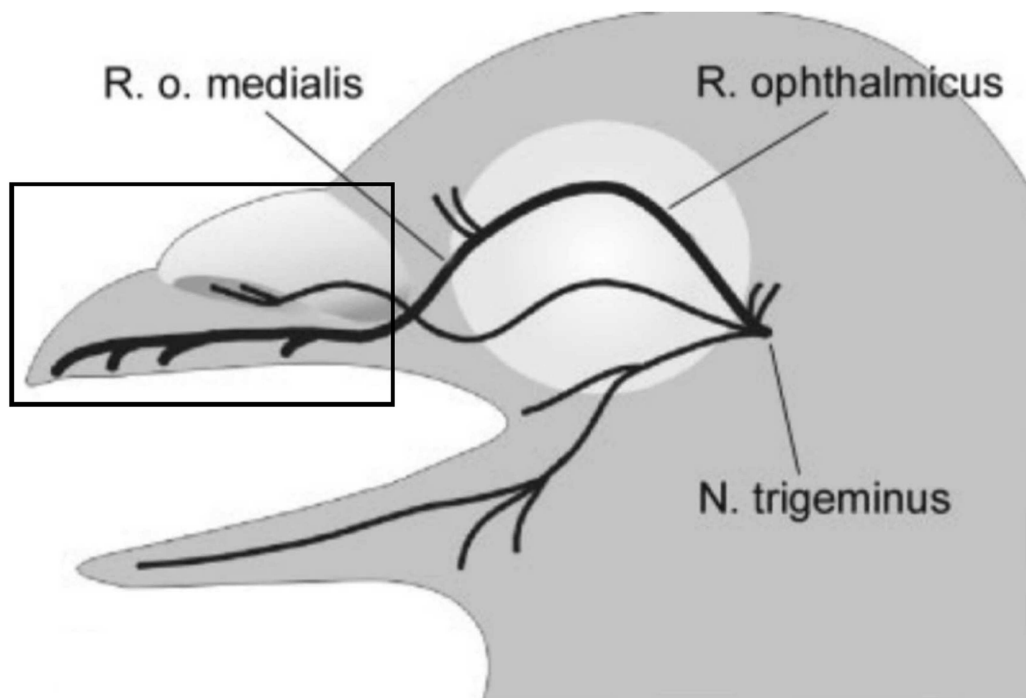


Figure 2.7: Localization of putative magnetoreceptors in the beak of homing pigeons. Scheme of the pigeon skull with the peripheral course of the ophthalmic branch of the trigeminal nerve, that gives rise, by its median branch (R. o. medialis, *Ramus ophthalmicus medialis*) to the entire somatosensory innervation of the tip of the upper beak. The rectangle shows the area where the magnetic iron minerals were detected. Figure adapted after Ref. [58]. *Ramus ophthalmicus* (R. ophthalmicus) is a branch of the trigeminal nerve, *N. trigeminus*, *Nervus trigeminus*. The trigeminal nerve is responsible for sensation in the face. It is similar to the spinal nerves C2–S5 that are responsible for sensation in the rest of the body. Sensory information from the face and body is processed by parallel pathways in the central nervous system.

Magnetoreception models involving both single domain and superparamagnetic magnetite have been proposed. Elongated single domain magnetite particles are



arranged in chain and have a magnetic moment directed towards one of its two ends, that are attached to a transduction mechanism (e.g. a mechanoreceptor in form of a hair cell or a mechanically gated ion channel). It is possible that these particles could elicit a change in membrane conductance when exposed to a torque [40, 43, 45, 115–117]. Alternatively, clusters of the much smaller superparamagnetic magnetite particles (with magnetic moments only in the presence of an external magnetic field) dispersed in a liquid and enclosed by a biological membrane can be deformed by magnetic field strengths as small as the geomagnetic field – resulting in activation of putative mechano-sensitive membrane receptor channels [45]. The magnetic characteristics of both types of magnetoreception models seem to allow sufficient discrimination of both direction and intensity of an ambient magnetic field comparative to the strength of the Earth’s magnetic field, while including small magnetic-field variations necessary for a map sense [43, 112, 113, 115, 118].

In birds, recent findings of superparamagnetic magnetite in homing pigeons in the form of dense clusters embedded in a solid fibrous cup with iron phosphate platelets as putative magnetic field amplifiers suggest that the ambient magnetic field is detected by such structures [58]. They were found in nerve-ending terminals of the ophthalmic nerve. A deformation by the magnetic field would lead to a change in the action potential of mechano-sensitive ion channels and lead to a nerve signal transmitted by the trigeminal nerve to the brain [45, 58, 112, 113].

Both single domain and superparamagnetic magnetite magnetoreceptors can be predictably affected by pulse remagnetization, which involves applying a single, brief directional magnetic pulse to the head of a bird. The application of such high-intensity magnetic pulses of 0.5 T for 4-5 ms was designed to temporarily change the polarity of the magnetite particles and disturb the magnetic map sense. They resulted in disorientation or deflection in the migratory orientation of passerines, which had some migration experience and thus could use a magnetic map [119–123]. Completely inexperienced, juvenile birds were immune to such treatments, agreeing with the assumption that they do not utilize a magnetic map [52, 103].

Electrophysiological recordings from the ophthalmic nerve have shown responses to changes in both the horizontal and vertical component of the magnetic field [110, 124]. Blocking this nerve made adult birds unresponsive to magnetic pulsing, but did not inhibit their orientation [121].

## 2.4 Novel Magnetoreception Mechanisms

The subject of this thesis is to study two, likely co-existing, mechanisms underlying avian magnetoreception. Both mechanisms are motivated by behavioral [6, 14, 29–32], physiological [2, 6, 33] and histological [58–61, 112, 113, 125] studies which were performed during the last several decades. The motivation for and the basic ideas behind these mechanism are discussed in the following subsections.

### 2.4.1 Radical-Pair-Based Compass in Cryptochrome

There are several arguments for the feasibility of the radical-pair-based compass in birds. The avian compass is an inclination compass, sensitive only to the inclination of the Earth's magnetic field lines and not to their polarity [2, 3]. The avian compass is also known to be highly sensitive to the strength of the ambient magnetic field, requiring a period of acclimation before orientation can occur at intensities differing from that of the natural geomagnetic field [126]. Further evidence favoring a radical-pair-based compass is offered by recent experiments probing the effects of low-intensity radio frequency radiation on bird orientational behavior [127, 128]. Furthermore, the avian compass is light-dependent, as first suggested by theory [34, 87], normally requiring light in the blue-green range in order to function properly [32, 100]. It is known to be localized in the right eye of migratory birds [96]. A radical pair model in which a light-driven, magnetic-field-dependent chemical reaction in the eye of the bird modulates the visual sense indeed predicts these properties [1, 34, 87–92, 129, 130]. Finally, a protein harboring blue-light-dependent radical pair formation, cryptochrome, is found localized in the retinas of migratory birds [97, 98, 131, 132] where its effects could intercept the visual pathway.

The radical pair mechanism, in general, involves a process by which a pair of spin-1/2 radicals lead to distinct reaction products for the spins being in either an overall singlet or triplet state. The mechanism has been explored for a variety of model systems [1, 35, 87–89, 92–95, 133]. In such instances, hyperfine coupling, exchange, dipole-dipole, and Zeeman interactions acting on the electron spins can induce magnetic field effects in the reaction yields.

The radical pair mechanism supposedly linked to the avian compass arises in the protein cryptochrome [1], which is a signaling protein found in a wide variety of plants and animals [64, 134, 135], and is highly homologous to DNA photolyase [135, 136]. The role of cryptochrome varies widely among organisms, from the entrainment

of circadian rhythms<sup>2</sup> in vertebrates to the regulation of hypocotyl<sup>3</sup> elongation and anthocyanin production<sup>4</sup> in plants [54–56].

The role of cryptochrome as a magnetic compass as suggested in [1, 36, 57] is however still hypothetical because no direct experimental prove has been made.

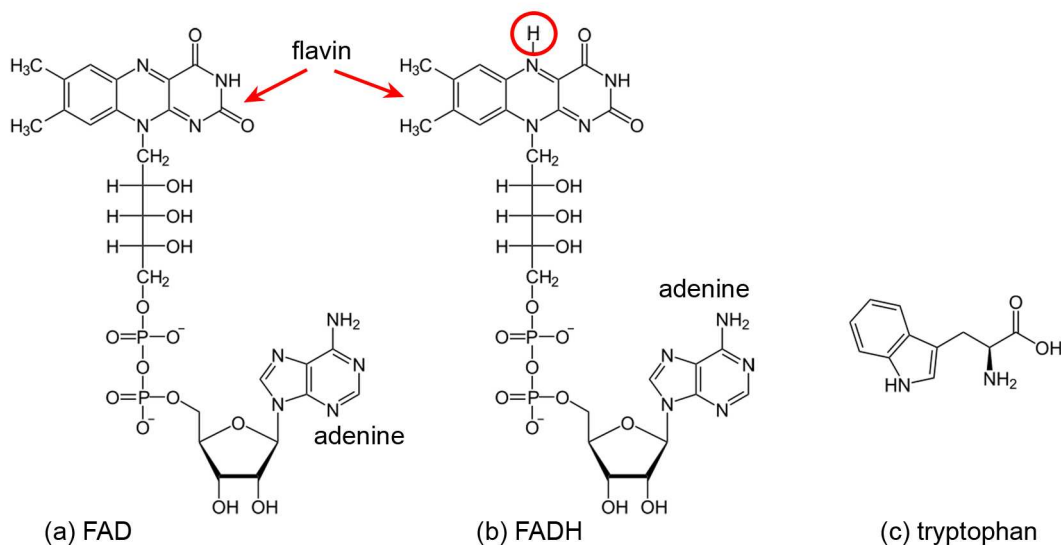


Figure 2.8: (a) Schematic representation of the structure of the flavin adenine dinucleotide complex (FAD) and its semireduced form (FADH) (b). The difference between the two complexes is in the additional hydrogen atom, attached to the nitrogen of the flavin-group (see circle). (c) Schematic representation of the structure of the tryptophan amino acid.

Photolyase and cryptochrome both internally bind the chromophore flavin adenine dinucleotide (FAD). The chemical structure of the FAD is shown if Fig. 2.8a.

<sup>2</sup>A circadian rhythm is a roughly-24-hour cycle in the physiological processes of living beings, including plants, animals, fungi and cyanobacteria. The term "circadian", coined by Franz Halberg, comes from the Latin *circa*, "around", and *dies*, "day", meaning literally "about a day". The formal study of biological temporal rhythms such as daily, weekly, seasonal, and annual rhythms, is called chronobiology.

<sup>3</sup>Hypocotyl is a botanical term for a part of a germinating seedling of a seed plant. As the plant embryo grows at germination, it sends out a shoot called a radicle that becomes the primary root and penetrates down into the soil. After emergence of the radicle, the hypocotyl emerges and lifts the growing tip (usually including the seed coat) above the ground, bearing the embryonic leaves (called cotyledons) and the plumule that gives rise to the first true leaves. The hypocotyl is the primary organ of extension of the young plant and develops into the stem.

<sup>4</sup>Anthocyanins (from Greek *anthos* – flower, and *kyanos* – blue) are water-soluble vacuolar flavonoid pigments that appear red to blue, according to pH. They are synthesized by organisms of the plant kingdom and bacteria, and have been observed to occur in all tissues of higher plants, providing color in leaves, stems, roots, flowers, and fruits.

In photolyase, the presence of FAD in its fully reduced  $\text{FADH}^-$  (see Fig. 2.8b) state is necessary for its DNA repair activity. The FAD cofactor, which typically exists in photolyase in its semireduced FADH form (see Fig. 2.8b), is brought to the  $\text{FADH}^-$  state by a series of light-induced electron transfers involving a chain of three tryptophans (see Fig. 2.8c) that bridge the space between FAD and the protein surface [137–141].

Although little is presently known about the activity of cryptochromes, it has been suggested [142, 143] that a light-induced autophosphorylation reaction is involved in the early stage of cryptochrome’s signaling activity. Recent experiments [144] have shown that light-induced electron transfer from a tryptophan chain conserved from photolyase is the dominant FAD reduction pathway in *Arabidopsis thaliana* (mouse-ear cress) cryptochrome, and that disruption of this photoreduction pathway impedes the protein’s autophosphorylation activity. However, while photolyase seems to be activated when the semireduced FADH form is converted to the fully reduced  $\text{FADH}^-$  form, cryptochrome seems to be activated when the fully oxidized FAD form is converted to the semireduced FADH form [145].

The tryptophan chain in *Arabidopsis* cryptochrome consists of Trp324, Trp377, and Trp400, as shown in Fig. 2.9. Trp324 is located near the periphery of the protein body, and Trp400 is proximal to the flavin cofactor with Trp377 located in between. Before light activation of cryptochrome, the flavin cofactor is present in its fully oxidized FAD state. FAD absorbs blue light photons, being thereby promoted to an excited state,  $\text{FAD}^*$ .  $\text{FAD}^*$  is then protonated, likely from a nearby aspartic acid [146], producing  $\text{FADH}^+$ . Once the electronically excited flavin is in the  $\text{FADH}^+$  state, light-induced electron transfer is initiated. An electron first jumps from the nearby Trp400 into the hole left by the excited electron in  $\text{FADH}^+$ , forming  $\text{FADH} + \text{Trp400}^+$ . An electron then jumps from Trp377 to Trp400, forming  $\text{FADH} + \text{Trp377}^+$ , and subsequently from Trp324 to Trp377, forming  $\text{FADH} + \text{Trp324}^+$ . Finally  $\text{Trp324}^+$  becomes deprotonated to  $\text{Trp324}_{\text{dep}}$ , i.e., forming  $\text{FADH} + \text{Trp324}_{\text{dep}}$  [138], fixing the electron on the FADH cofactor. This scenario is summarized in Fig. 2.10.

However, before the final deprotonation takes place, it is possible for the electron on FADH to back-transfer to one of the tryptophans, which quenches the signaling state. This back-transfer, leading to the formation of  $\text{FADH}^+$ , as shown in Fig. 2.10, can only occur if the spins of the two unpaired electrons are in an overall singlet state. An external magnetic field can influence the overall electron spin state through

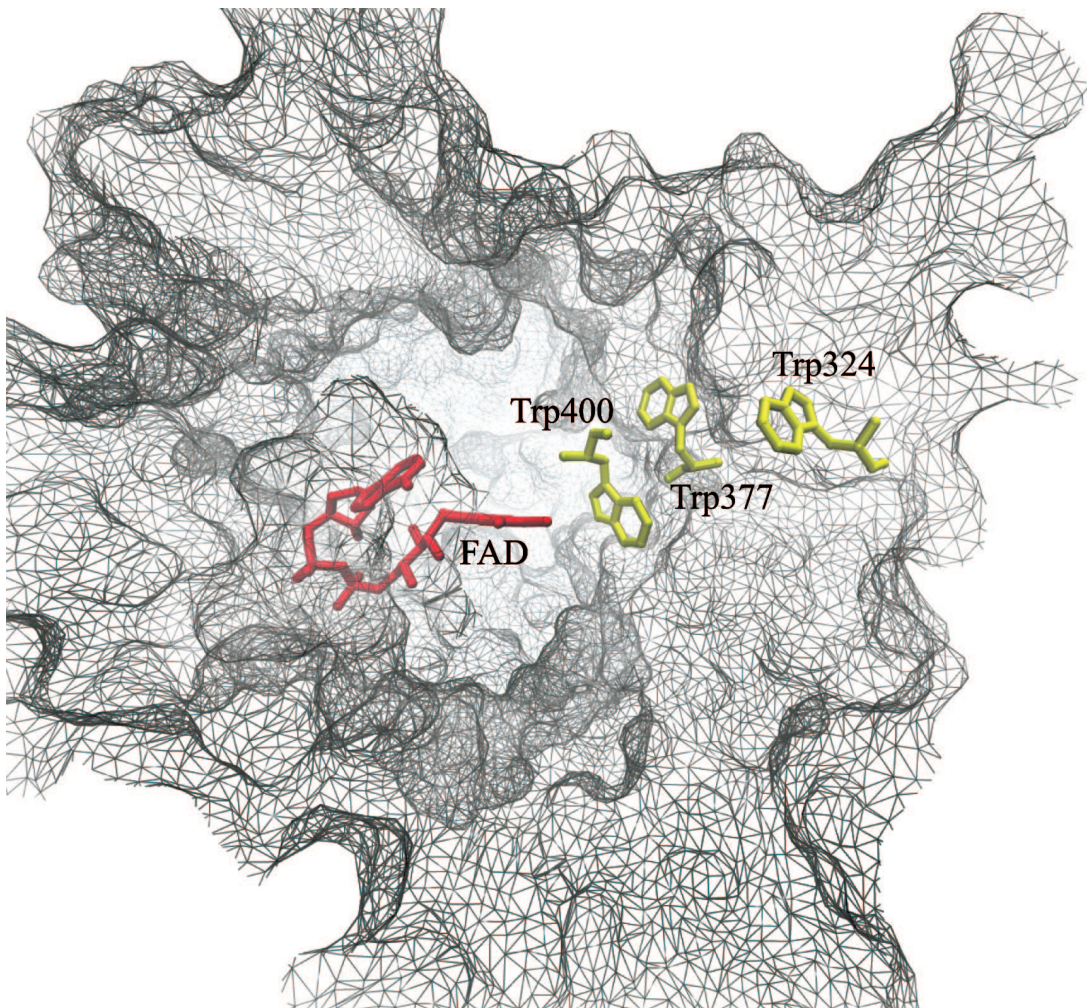


Figure 2.9: FAD cofactor and tryptophan chain in *Arabidopsis thaliana* cryptochrome-1. Cryptochrome is in its signaling state when the FAD cofactor is in the semireduced FADH state. The signaling state is achieved through photoreduction via a chain of three tryptophans (Trp400, Trp377 and Trp324) which bridge the space between FADH and the surface of the protein, followed by deprotonation of Trp324 to Trp324<sub>dep</sub>.

the Zeeman interaction acting jointly with hyperfine coupling to the nuclear spins associated with the hydrogen and nitrogen atoms [93]. If the overall spin state is triplet, electron back-transfer and formation of FADH<sup>+</sup> cannot occur, extending the time, in which cryptochrome stays in its signaling state. This, in turn, could affect the visual perception of a bird as described in [1], permitting the bird to visually discern the magnetic field.

One of the goals of this thesis is computationally to study the electron transfer

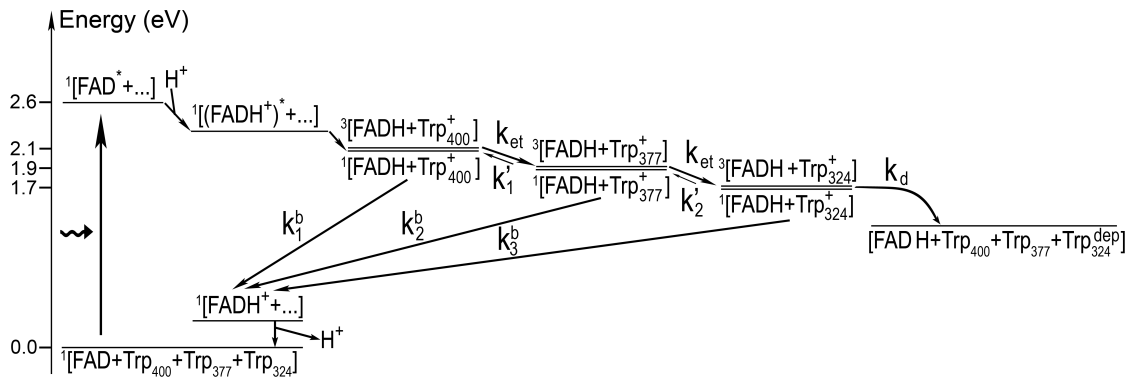


Figure 2.10: Schematic presentation of the radical pair reaction pathway in cryptochrome. After the flavin cofactor in its fully oxidized form, FAD, is excited by a blue photon ( $\text{FAD} \rightarrow \text{FAD}^*$ ) and subsequently protonated ( $\text{FAD}^* \rightarrow (\text{FADH}^+)^*$ ), an electron jumps from the nearby Trp400 to  $\text{FADH}^+$ , creating a radical pair ( $\text{FADH} + \text{Trp400}^+$ ) state. Electron transfer from Trp377 to Trp400 and from Trp324 to Trp377 follows, creating the radical pair state  $\text{FADH} + \text{Trp377}^+$  and then  $\text{FADH} + \text{Trp324}^+$ . For each radical pair state, the spins of the unpaired electrons are in either the singlet or triplet state, as denoted by  $^1[\dots]$  or  $^3[\dots]$ , respectively. Electron back-transfer, the effect of which is to quench the cryptochrome signaling state, is possible only when the two unpaired electron spins of one of the three possible radical pair states form a singlet state  $^1[\dots]$ . If  $\text{Trp324}^+$  becomes deprotonated ( $\text{Trp324}^+ \rightarrow \text{Trp324}_{\text{dep}}$ ), electron back-transfer  $\text{FADH} \rightarrow \text{Trp324}_{\text{dep}}$  is impeded, and cryptochrome is stabilized in its signaling state,  $\text{FADH} + \text{Trp324}_{\text{dep}}$ . Transitions between the three radical pair states, i.e.  $^1,^3[\text{FADH} + \text{Trp400}^+]$ ,  $^1,^3[\text{FADH} + \text{Trp377}^+]$ , and  $^1,^3[\text{FADH} + \text{Trp324}^+]$ , are governed by the rate constant  $k_{\text{et}}$  and correspond to an electron jumping between tryptophans in the direction opposite to that of the arrows shown (the arrows show electron hole transfer). Electron back-transfer from FADH to one of the tryptophans is governed by the rate constant  $k_b$  and deprotonation of the third tryptophan by the rate constant  $k_d$ . The steps denoted by rate constants  $(k_1)'$  and  $(k_2)'$ , correspond to reverse electron transfer in the tryptophan chain and are neglected in the description.

and spin dynamics in cryptochrome as depicted in Fig. 2.10 and to demonstrate the feasibility of a radical-pair-based compass in birds. This requires an atomic-level structure of the protein. Unfortunately, no structure of avian cryptochrome is currently available. The only available structure at this time is that of the *Arabidopsis thaliana* (mouse-ear cress) cryptochrome-1 [135]. However, the cryptochromes of birds and of plants are very similar. A BLAST<sup>5</sup> [147] comparison of *Erithacus*

<sup>5</sup>BLAST stands for Basic Local Alignment Search Tool. In bioinformatics it is an algorithm for comparing primary biological sequence information, such as the amino-acid sequences of different

Sequence Alignment of *Arabidopsis thaliana* cryptochrome-1 with *Erithacus rubecula* cryptochrome-1a and cryptochrome-1b

```

E. rubecula cryla -----MGVNAVHWFRLKRLHDPALRECIAGADTVRCVYILDPFAGSSNVGINR
E. rubecula crylb -----MGVNAVHWFRLKRLHDPALRECIAGADTVRCVYILDPFAGSSNVGINR
A. thaliana cryl  MSGSVSGCGSGGCSIVWFRDLRVEDNPALAAAVR-AGPVIALFVWAPEEGHYHPGRVS
                  ^   ^   ^   ^   ^   ^   ^   ^   ^   ^   ^   ^   ^   ^   ^   ^   ^
E. rubecula cryla WRFLQCLELDLNDANLRKLSRLFVIRG-OPADVPRFLKKEWNIAKLSIEYDSEPFCKERD
E. rubecula crylb WRFLQCLELDLNDANLRKLSRLFVIRG-OPADVPRFLKKEWNIAKLSIEYDSEPFCKERD
A. thaliana cryl  RWLKNLSLAQLDSSLSLGTCLITKRSTDVSLDLDVVKSTGASQIFFNHLYDPLSLVRD
                  ^   ^   ^   ^   ^   ^   ^   ^   ^   ^   ^   ^   ^   ^   ^   ^
E. rubecula cryla AAIKKLASEAGVEIVRISHTLYDLDKIIELNGGQPPLYKRFQTLISR----MEPLEMP
E. rubecula crylb AAIKKLASEAGVEIVRISHTLYDLDKIIELNGGQPPLYKRFQTLISR----MEPLEMP
A. thaliana cryl  HRAKDVLTAGGIAVRSFNADLLYEPWEVTDLGRPFMFPAFWRCLSMYPDPESPLLPP
                  ^   ^   ^   ^   ^   ^   ^   ^   ^   ^   ^   ^   ^   ^   ^   ^
E. rubecula cryla VETITPEVMKKCTTPVFDHDEKYGVPSLEELGFDTDGLPSAVWPGGETEALTRLERHLE
E. rubecula crylb VETITPEVMKKCTTPVFDHDEKYGVPSLEELGFDTDGLPSAVWPGGETEALTRLERHLE
A. thaliana cryl  KKIISGDVSKCVADPLVFEDDSEKGSNALLARAWSPG-----WSNGDKALTTFIN----
                  ^   ^   ^   ^   ^   ^   ^   ^   ^   ^   ^   ^   ^   ^   ^   ^
E. rubecula cryla RKASVANFERPRMNANSLLASPTGLSPYLRFGCCLSCR---LFYFKLTDLYKVKKNSSP
E. rubecula crylb RKASVANFERPRMNANSLLASPTGLSPYLRFGCCLSCR---LFYFKLTDLYKVKKNSSP
A. thaliana cryl  --GPLLEYSKRRKADS--ATTSFLSPLHFGEVSVRKFVHLVRKIQVAVANEGNEAGEE
                  ^   ^   ^   ^   ^   ^   ^   ^   ^   ^   ^   ^   ^   ^   ^   ^
E. rubecula cryla PLSLYGQQLL-WREFFYTAATNNPRFDKMEGNP ICVQIPWDKNPEALAKWAEGRTGFPWID
E. rubecula crylb PLSLYGQQLL-WREFFYTAATNNPRFDKMEGNP ICVQIPWDKNPEALAKWAEGRTGFPWID
A. thaliana cryl  SVNLFKLSIGLREYSRYISFNHPYSHERPLLGHKFFPWAVDENYKAWRQGRTYPLVD
                  ^   ^   ^   ^   ^   ^   ^   ^   ^   ^   ^   ^   ^   ^   ^   ^
E. rubecula cryla AIMGQLRQEGWIHHLARHAVACFLTRGDLWISWEEGMKVFEELLDADWSVNAGSWMWLS
E. rubecula crylb AIMGQLRQEGWIHHLARHAVACFLTRGDLWISWEEGMKVFEELLDADWSVNAGSWMWLS
A. thaliana cryl  AGMRELWATGWLHDIRVIVVSSFFVK-VLQLPWRWGMKYFWDTLDDADLESADLGQYIT
                  ^   ^   ^   ^   ^   ^   ^   ^   ^   ^   ^   ^   ^   ^   ^   ^
E. rubecula cryla -CSSFFQQFFHCYCPVGFGRRTDPNGDYIRRYLPVLRGFPKAYIYDPWNPAPESIQAAKC
E. rubecula crylb -CSSFFQQFFHCYCPVGFGRRTDPNGDYIRRYLPVLRGFPKAYIYDPWNPAPESIQAAKC
A. thaliana cryl  GTLPDSREFDRI DNPQFEGYKFDPNGEYVRRWLPELSRLPTDWIHHWPWNPAPESVLQAAGI
                  ^   ^   ^   ^   ^   ^   ^   ^   ^   ^   ^   ^   ^   ^   ^   ^
E. rubecula cryla IIGVNYPKPMVNHAEASRLNIERMKIYQQLSRYR-----GLGLLATVPSNPNNG
E. rubecula crylb IIGVNYPKPMVNHAEASRLNIERMKIYQQLSRYR-----GLGLLATVPSNPNNG
A. thaliana cryl  ELGSNYPLPIVGLDEAKARLHEALSQMWQLEAASRAIENGSEELGDSAEVEEAPIEFP
                  ^   ^   ^   ^   ^   ^   ^   ^   ^   ^   ^   ^   ^   ^   ^   ^
E. rubecula cryla NGGLMGYSPGESISGCG-----STGGAQLGTGDGHTVVSQCTLGDSHSGTSG---
E. rubecula crylb NGGLMGYSPGESISGCG-----STGGAQLGTGDGHTVVSQCTLGDSHSGTSG---
A. thaliana cryl  RDITMEETEPTRLNPNRRYEDQMVPSITSSLIRPEEDESLSNLRNSVGDSTRAEVPRMNV
                  ^   ^   ^   ^   ^   ^   ^   ^   ^   ^   ^   ^   ^   ^   ^   ^
E. rubecula cryla ----IQQQGYCQASSILHYAHGDNQQSHLLQAGR TALGTGISAGKRPN-----
E. rubecula crylb ----IQQQG-----IMAVPVCGRS-PNACNYGK-----
A. thaliana cryl  NTNQAQQRRRAEPASNQVTAMIPEFNIRIVAESTEDSTAESSSSGRRERSGGIVPEWSPGY
                  ^   ^   ^   ^   ^   ^   ^   ^   ^   ^   ^   ^   ^   ^   ^   ^
E. rubecula cryla ----PEEETQSGVKVQRQSTN-----
E. rubecula crylb ----PDKTSK-----
A. thaliana cryl  SEQFPEENRIGGGSTTSSYLQNHHEILNWRRLSQTG
                  ^

```

^ indicates conserved residue

Figure 2.11: BLAST sequence alignment between *Erithacus rubecula* (European robin) and *Arabidopsis thaliana* (mouse-ear cress) cryptochromes. The alignment shows a high similarity between the bird and plant cryptochromes. *Erithacus rubecula* cryptochrome-1a gives an expectation value of  $3 \times 10^{-38}$  and cryptochrome-1b gives an expectation value of  $2 \times 10^{-37}$  when compared to *Arabidopsis thaliana* cryptochrome-1. Residues conserved between the three cryptochromes are marked with the ^ character.

*rubecula* (European robin) cryptochrome-1a and cryptochrome-1b with *Arabidopsis thaliana* cryptochrome-1 gives expectation values of  $3 \times 10^{-38}$  and  $2 \times 10^{-37}$ , respectively, with 28% sequence identity for each (see Fig. 2.11). Therefore, the computational analysis will be based on the electron transfer and spin dynamics of *Arabidopsis* cryptochrome-1.

With regard to the similarity of avian and plant cryptochromes, a recent experiment on the effect of an external magnetic field on *Arabidopsis thaliana* seedlings [57] is encouraging. It was found that signaling from cryptochrome-1, measured through a hypocotyl inhibition and anthocyanin production assay, is enhanced when seedlings are placed in a magnetic field of 5 G, compared with the assay at an Earth-strength (0.5 G) magnetic field. Mutant seedlings lacking cryptochromes showed no change under different magnetic field strengths. This observation suggests that the plant cryptochrome spends a longer time in its signaling state when placed in an external magnetic field of 5 G than under Earth-strength magnetic field conditions.

Magnetoreception of cryptochrome is studied in chapter 4 of the thesis. The following issues were considered:

- (i) The rate constants for various electron transfer processes (i.e. for the electron tunneling from one tryptophan to another, and electron back-transfer from FADH to one of the tryptophans (see Fig. 2.10)) in cryptochrome were estimated and the corresponding values were compared with experimental observations;
- (ii) The activation yield of cryptochrome was studied as a function of external magnetic field and it was shown that activation of the protein can be influenced by the geomagnetic field;
- (iii) The activation yield of cryptochrome was studied as a function of the direction of the external magnetic field. It was demonstrated that the radical-pair-based compass is an inclination one;
- (iv) The evolution of the singlet and triplet spin densities in cryptochrome were analysed;

---

proteins or the nucleotides of DNA sequences. A BLAST search enables a researcher to compare a query sequence with a library or database of sequences, and identify library sequences that resemble the query sequence above a certain threshold. For example, following the discovery of a previously unknown gene in the mouse, a scientist will typically perform a BLAST search of the human genome to see if humans carry a similar gene; BLAST will identify sequences in the human genome that resemble the mouse gene based on similarity of sequence.



### 2.4.2 Iron-Mineral-Based Magnetoreceptor

The second magnetoreception mechanism studied in the present thesis is the so-called iron-mineral-based magnetoreceptor mechanism. This magnetoreception mechanism is thought to be responsible for sensing the magnetic map [52]. However, this hypothesis has not been verified so-far. In the thesis it is demonstrated that the iron-mineral system, first discovered in the pigeon beak [58, 112] provides a sensitive magnetometer with various interesting properties, which are crucial for bird navigation.

This motivation for the iron-mineral-based magnetoreception mechanism is based on recent experimental findings of Fleissner *et al.*, who demonstrated the presence of the small magnetic particles in the upper part of the beak of homing pigeons (*Columba livia*) [58, 60, 112] and later in several other birds species [125]. With the use of different light and electron microscopic methods combined with X-Ray analysis Fleissner *et al.* concluded that there are two different types of iron compound in the beak. In the later papers [59–61] these compounds were identified using micro-synchrotron X-ray-absorption-near-edge-structure-spectroscopy as two ferrimagnetic materials: magnetite ( $\text{Fe}_3\text{O}_4$ ) and maghemite ( $\gamma\text{-Fe}_2\text{O}_3$ ). It was shown that magnetite forms micro clusters, attached to the cell membrane, while maghemite crystals have a platelet-like structure arranged in chains inside the dendrite.

Based on their experimental findings Fleissner *et al.* suggested a mechanism for an iron-mineral based magnetoreception [60, 61]: namely, in an external magnetic field the maghemite platelets become magnetized and enhance the local magnetic field in the cell by orders of magnitude. Thus the magnetite clusters will experience an attractive (repulsive) force inducing their displacement, which might induce a primary receptor potential via strain-sensitive membrane channels that could possibly lead to a certain orientation effect.

This mechanism is different from the magnetite-based magnetoreception mechanism suggested earlier because it involves two different types of iron-minerals (see e.g. [40–44, 62]). In these papers only magnetite was considered and it was suggested that the magnetite clusters, depending on the orientation of the external magnetic field, will attract or repel each other, deforming the membrane and possibly opening (closing) the ion channels. This mechanism was suggested about fifteen years ago [62], long before the maghemite platelets were discovered in the beak of

birds. Since maghemite has a ferrimagnetic nature [63] and possesses pronounced magnetic properties, the maghemite platelets should play an important role in the magnetoreception mechanism.

So far no direct experimental or theoretical verifications of the magnetoreception mechanism suggested in [59–61] has been reported. In the thesis, this problem is addressed from a theoretical point of view. The studied magnetoreceptor mechanism is based on the magnetoreceptor model introduced in [60,61]. However, it is slightly different because in the suggested mechanism the maghemite platelets have a static magnetic moment rather than an induced one. This assumption is motivated by the size of the platelets and their composition, which clearly show that maghemite platelets should behave like small permanent magnets. In order to explain the iron-mineral based magnetoreceptor model, Fig. 2.12b shows schematically the structure of a single dendrite containing iron minerals. The figure is based on the experimental results discussed in Refs. [58–60].

Histological studies of the upper beak of homing pigeons showed [58–61] that there are six patches in the beak where iron minerals are concentrated, Fig. 2.13a. The iron minerals were found in symmetrical spots near the lateral margin of the skin of the upper beak, inside the dendrites of nerve cells (neuron). This is schematically shown in Fig. 2.12a.

The neuron consists of several dendrites, which induce the nerve signal: an axon – a long fiber – used to transmit the signal; a soma with the cell nucleus and an axon terminal, which transmits the nervous signal. The dendrites act as the nerve signal input interface, while the axon terminal is the signal output interface (see Fig. 2.12a).

The size of the iron mineral patches in dendrites was found to be always about the same, being  $350\ \mu\text{m}$  long and  $200\ \mu\text{m}$  in diameter [58–61] (see Fig. 2.13b and Fig. 2.13c). In every patch the iron-minerals were found parallel to the axon bundles with a certain spatial orientation. It was shown [60] that the dendrites in the frontal, middle and caudal parts of the beak are aligned in three perpendicular directions: the frontal ones have a preferred dorsal-to-ventral direction, the middle a median-to-lateral direction and the caudal a caudal-to-rostral direction. The spatial distribution of iron minerals within the putative magnetoreceptor system, measured in [60], is illustrated in Fig. 2.13.

In addition it was demonstrated that dendrites containing iron also form a regular pattern. Several of them may align side by side but, longitudinally, the distance

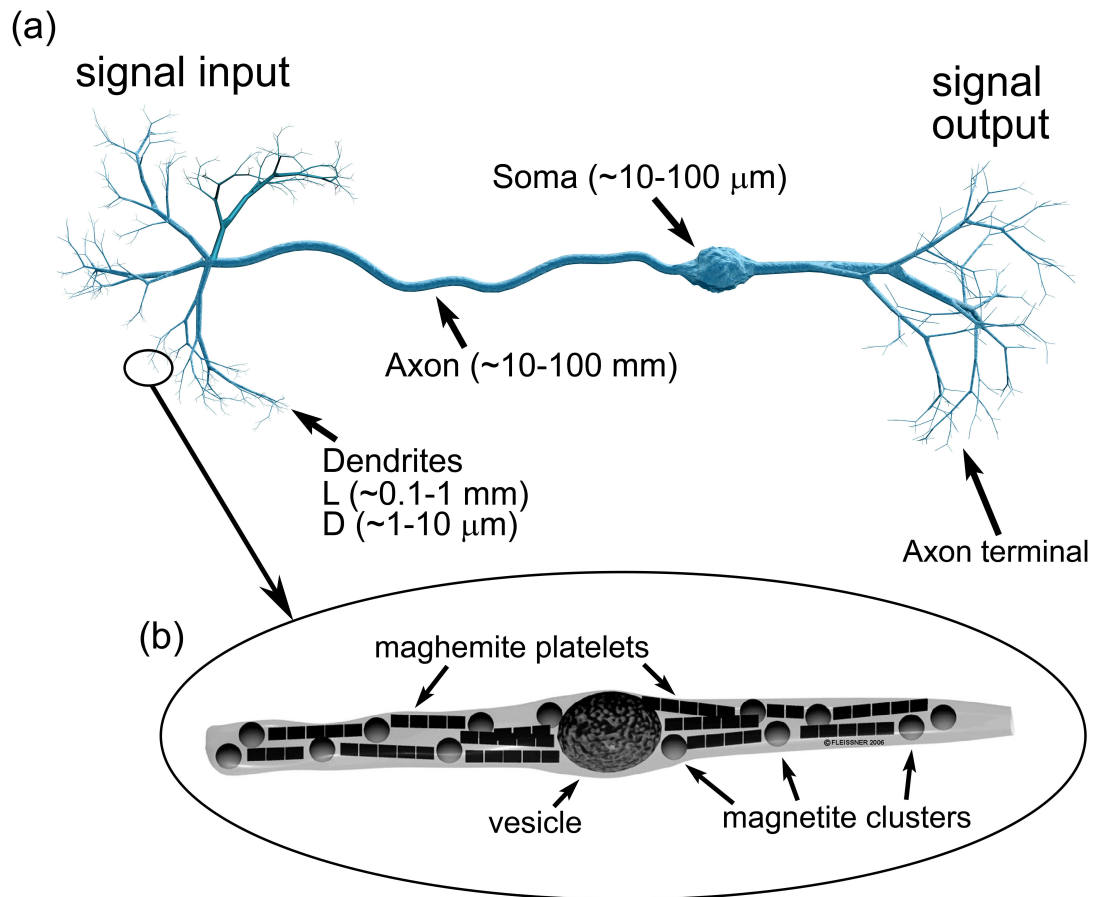


Figure 2.12: Schematic illustration of a nerve cell (neuron) (a). The dendrites form a tree-like structure and are the nerve signal input interface of the neuron, the axon connects the dendrites with the axon terminal, being the signal output interface of the neuron. The cell nucleus is located in the soma. The nucleus contains most of the cell's genetic material, organized as multiple long linear DNA molecules in complex with a large variety of proteins, such as histones, to form chromosomes. The genes within these chromosomes make up the cell's nuclear genome. The function of the nucleus is to maintain the integrity of these genes and to control the activities of the cell by regulating gene expression. The characteristic size of the cell components is indicated (L – length, D – diameter). Plot (b) of the figure shows the characterization and subcellular localization of iron minerals within a dendrite. The drawing shows schematically the structure of a single dendrite as derived from serial ultrathin (approximately 120 nm) sections with the three subcellular components containing iron: chains of maghemite crystals ( $1 \times 0.1 \times 1 \mu\text{m}$ ) magnetite clusters of nanoparticles (diameter about 1  $\mu\text{m}$ ), and the iron-coated vesicle (diameter 3 to 5  $\mu\text{m}$ ). Figure presented by the courtesy of Gerta and Günther Fleissner, Universität Frankfurt am Main.

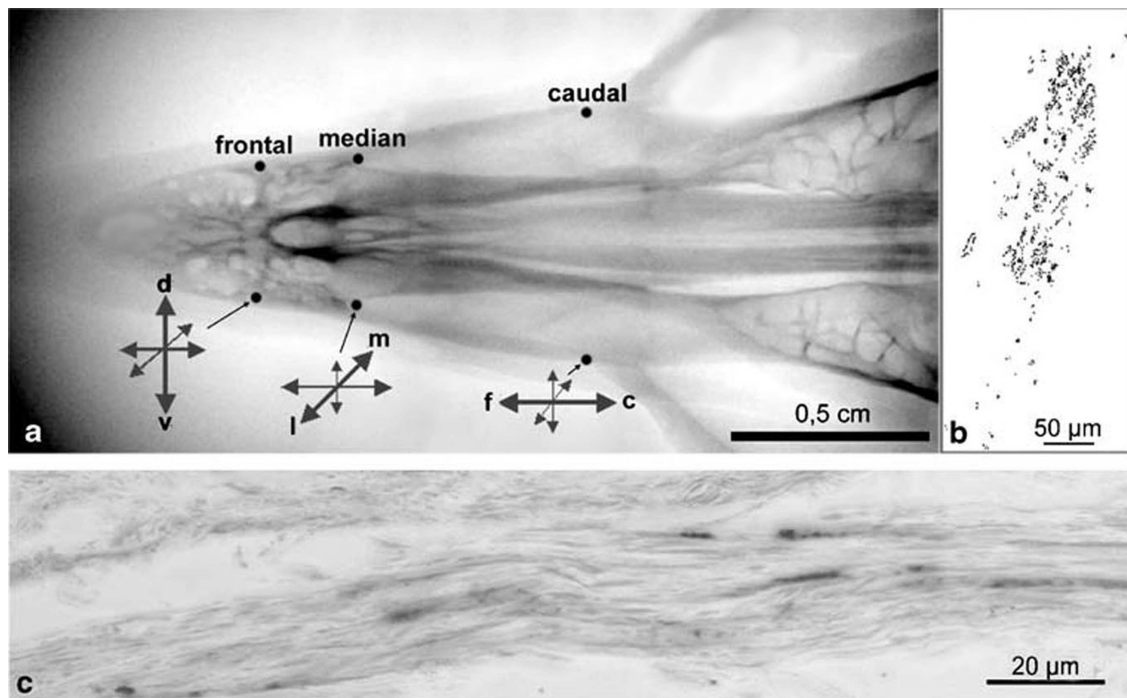


Figure 2.13: Spatial distribution of iron minerals within the putative magnetoreceptor system, measured in [60]. (a) X-ray image of the upper beak showing its six iron-containing areas and the prevailing orientation of their dendritic fields (arrows: *c* – caudal, *d* – dorsal, *f* – frontal, *l* – lateral, *m* – median, *r* – rostral, *v* – ventral). (b) Camera lucida drawing of all Prussian blue reactive 'bullets' (black dots) of one dendritic field as visible in the light microscope. (c) Axon bundle, which carries multiple iron-containing dendrites. The dendrites are aligned in parallel.

between them is about  $100 \mu\text{m}$ . This fact has been independently confirmed in the  $\mu$ -SAXRF-measurements of histologically undisturbed and unstrained material [60].

All dendrites containing iron have a similar structure which is schematically shown in Fig. 2.12b. Note, that in the dendrite there are three different subcellular compartments containing iron-minerals: several magnetite clusters, an iron coated vesicle and maghemite platelets which are marked in Fig. 2.12b. Each dendrite contains 10-15 clusters of magnetite nanocrystals of average size  $5 \text{ nm}$  [46, 47, 60]. The clusters have an average diameter of  $1 \mu\text{m}$  [58–61] and adhere to the cell membrane. The maghemite platelets form bands, which extend through the entire dendrite. The magnetite clusters are usually found at the edges of maghemite bands which include about 5-10 platelets. Each platelet was found to be  $1 \mu\text{m}$  wide and long and less than  $0.1 \mu\text{m}$  thick [58–61]. The vesicle is most often located in the center of the

dendrite and its composition is still not well understood. However, in [58–60,125] it was demonstrated that the vesicle is covered by some non-crystalline iron-substance and has a diameter of about  $5 \mu\text{m}$ .

Note that the particle arrangement in the dendrite presented in Fig. 2.12b is different from what was published in Ref. [58]. This happens because the interpretation of experimental data in [58] was based on low resolution measurements while the quality of experiments has been significantly improved in [60,61]. Thus the spatial orientation of iron-mineral particles in the dendrite has been determined more accurately and differs from the structure presented in [58]. The position of the large vesicle in the middle of the dendrite is also more reasonable than at the edge, as published in Ref. [58] due to symmetry. Two hypotheses explaining the possible roles of the vesicle are given in subsection 5.10.

The idea of the iron-mineral magnetoreception mechanism is rather simple. It is similar to the idea of an earlier magnetite-based magnetoreception mechanisms. However, the nature of the forces acting on the magnetite particles and the force magnitudes are quite different. If the magnetoreceptor unit (Fig. 2.12b) is subject to an external magnetic field, the forces acting on the magnetite clusters in the dendrite should be different at different field orientations.

The primary magnetoreceptor unit is defined as the smallest structure possessing the magnetoreception properties of the whole dendrite. It contains ten maghemite platelets and one magnetite cluster and is shown in Fig. 2.14. It has been chosen to study the forces acting on a single magnetite cluster. Note, that in the dendrite there are about 10-15 of such units (see Fig. 2.12b), which should have similar behavior in the external magnetic field. Therefore, if the entire dendrite is subject to an external magnetic field the repetition of the magnetoreceptory units increases the functional safety of the dendrite magnetoreception.

The geometry of the magnetoreceptor unit is determined from the experimental observations [60]. Thus, the maghemite platelets have the dimensions  $1 \times 0.1 \times 1 \mu\text{m}$ , while the magnetite cluster has the diameter of  $1 \mu\text{m}$ . In order to study the behavior of the magnetoreceptor unit at different orientations of an external magnetic field, it should be considered in a certain coordinate frame: the maghemite platelets are put in the (xz)-plane aligned along the x-axis (see Fig. 2.14). The distance between two neighbouring platelets is equal to  $0.1 \mu\text{m}$ . The platelets are numbered in the positive direction of the x-axis with the first plate having its origin at  $(0.5,0,0) \mu\text{m}$ . The position of the magnetite cluster is defined by the vector  $\vec{R}=(x,y,z)$  (see

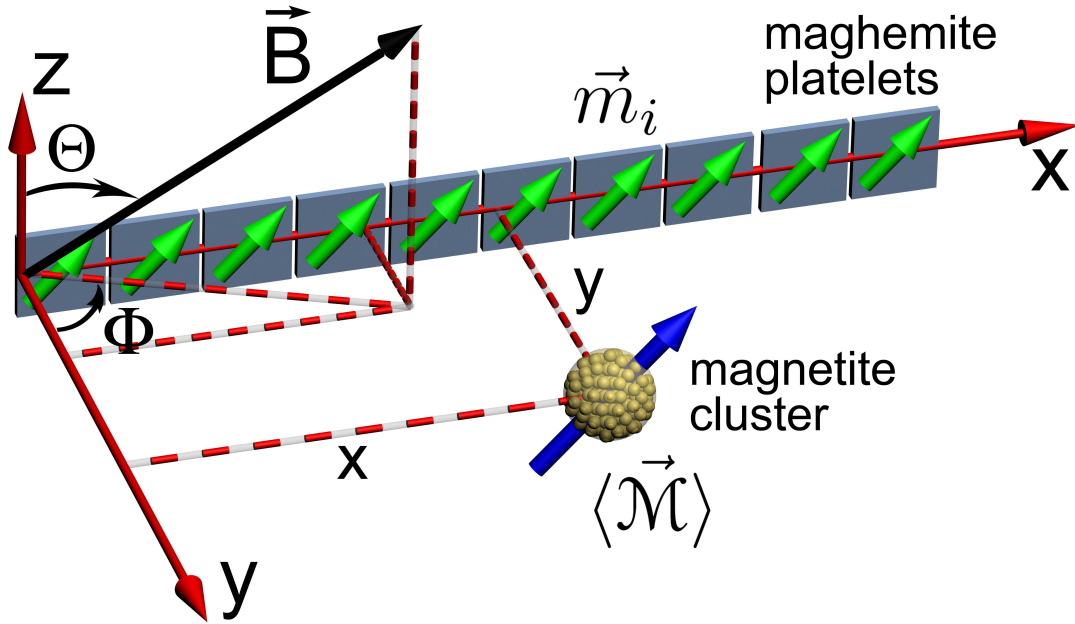


Figure 2.14: Magnetoreceptor unit consisting of ten maghemite platelets (boxes) and a magnetite cluster (sphere). The coordinate frame shown in the figure is used in the computations. The direction of the external magnetic induction vector  $\vec{B}$  is characterized by the polar angle  $\Theta$  and the azimuthal angle  $\Phi$  as shown. The magnetic moments of the  $i$ -th maghemite platelet and of the magnetite cluster are shown with  $\vec{m}_i$  and  $\langle \vec{\mathcal{M}} \rangle$  respectively. This magnetoreceptor unit is used in the most discussions throughout the dissertation, however in section 5.7 the modified magnetoreceptor unit with one, two, three, etc platelets is considered as well as the composition of several magnetoreceptor units of different size.

Fig. 2.14).

It is still unclear if the maghemite platelets are fixed in space or can rotate. There are experimental claims [58–60, 125] that the platelets are fixed, but this fact has not been verified carefully so-far. In the present model it will be assumed that the platelets are quasi-fixed, i.e. they can rotate only in the (xz)-plane. This assumption is governed by the size and spatial arrangement of the platelets in the dendrite. According to the experimental observations [60] chains of maghemite platelets are packed tightly side by side and thus the rotation of platelets in the (xy) or (yz)

planes is difficult. The rotation of platelets in the ( $xz$ )-plane is much more probable and can be excited by the external magnetic field for example directed along the  $z$ -axis. The model of rotating platelets is used in most discussions in the present thesis. However in section 5.7 the fixed platelets are also discussed.

Another important question is the number of platelets in the magnetoreceptor unit. It is assumed that each magnetoreceptor unit has 10 platelets as suggested by the experimental observations [60]. However there might be units with a different number of platelets, i.e. with five, two, one. As will be shown in section 5.8 that such systems might play a very important role in the magnetoreception process. Therefore an experimental determination of the distribution of magnetoreceptor units with different number of platelets is necessary.

The vector of the external magnetic induction,  $\vec{B}$ , is also shown in Fig. 2.14. It is described by an absolute value,  $B_0$ , polar angle  $\Theta$  and azimuthal angle  $\Phi$ .

Chapter 5 of the thesis is devoted to the study of the iron-mineral-based magnetoreceptor mechanism in birds. The following points are emphasized:

- (i) The potential energy surface of the magnetite cluster in magnetoreceptor unit is studied at different orientations of external magnetic field;
- (ii) The forces which act on the magnetite cluster are calculated and analyzed;
- (iii) The force differences caused by the change of the direction of external magnetic field are established;
- (iv) The probability of opening certain mechanosensitive ion channels in the nerve cell membrane is calculated;
- (v) The magnetic field range, i.e. the magnetic functionality window of the iron-mineral-based magnetoreceptor is determined;
- (vi) It is demonstrated that the iron-mineral based magnetoreceptor mechanism provides a polarity compass;
- (vii) The functionality of the magnetoreceptor unit with  $N=1, 2, 3, \dots, 10$  platelets has been considered and it is shown that for  $N=1$  the system provides an inclination compass;
- (viii) The influence of strong magnetic fields on the magnetoreceptor unit has also been analyzed.





# Chapter 3

## Theoretical Background

### 3.1 The Radical Pair Mechanism

In this section the formalism of the radical pair mechanism is discussed. At first the general ideas behind the radical pair mechanism are presented in order to explain the physics behind this mechanism. In the later subsections the formalism of the radical pair mechanism theory is applied to cryptochrome and the calculation of cryptochrome activation and its magnetic field dependence is outlined. This is achieved by incorporating realistic hyperfine coupling tensors for FADH and tryptophan, by including multiple tryptophans in the photoreduction pathway, and by using realistic reaction rate constants for electron forward transfer, electron back-transfer, and tryptophan deprotonation.

#### 3.1.1 The Radical Pair Mechanism: Introduction

Spin populations of diamagnetic<sup>1</sup> and paramagnetic<sup>2</sup> species in the presence of an external magnetic field are usually in thermal equilibrium if no saturation and polarization transfer are present. Chemically Induced Magnetic Polarization is the name

---

<sup>1</sup>Diamagnetism is a weak repulsion from a magnetic field. It is a form of magnetism that is only exhibited by a substance in the presence of an externally applied magnetic field. It results from changes in the orbital motion of electrons. Applying a magnetic field creates a magnetic force on a moving electron in the form of  $F = q\mathbf{v} \times \mathbf{B}$ . This force changes the centripetal force on the electron, causing it to either speed up or slow down in its orbital motion. This changed electron speed modifies the magnetic moment of the orbital in a direction opposing the external field.

<sup>2</sup>Paramagnetism is a form of magnetism which occurs only in the presence of an externally applied magnetic field. Paramagnetic materials are attracted to magnetic fields, hence have a relative magnetic permeability greater than one (or, equivalently, a positive magnetic susceptibility). However, unlike ferromagnets which are also attracted to magnetic fields, paramagnets do not retain any magnetization in the absence of an externally applied magnetic field.

given to the generation of the non-equilibrium nuclear and electron spin levels produced during chemical reactions with the participation of free radicals. The nuclear phenomenon is called Chemically Induced Dynamic Nuclear Polarization (CIDNP).

The explanation of the experimentally observed CIDNP phenomena has been enabled by the appearance and development of the radical pair mechanism theory [148–152]. The vast majority of the CIDNP observations can be treated within this theory.

In chemistry, radicals (often referred to as free radicals) are atomic or molecular species with unpaired electrons on an otherwise open shell configuration. These unpaired electrons are usually highly reactive, so radicals are likely to take part in chemical reactions. Radicals play an important role in combustion, atmospheric chemistry, polymerization, plasma chemistry, biochemistry, and many other chemical processes, including human physiology. The radical pair mechanism requires the participation in a chemical reaction of a pair of short-lived, reactive radicals with the following properties:

(i) The two radicals must be created simultaneously from non-radical precursor molecules. The examples of this process are:

**Unimolecular homolytic cleavage**, i.e. the breaking of a single (two-electron) bond in which one electron remains on each of the atoms. This process is also known as free-radical reaction. The general chemical reaction for this process can be written as:

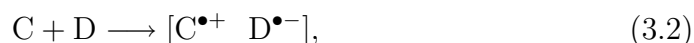


where A-B represents a molecule (for example Br-Br, or CH<sub>3</sub>-CH<sub>3</sub>), while A<sup>•</sup> and B<sup>•</sup> represent the two radicals (i.e. Br<sup>•</sup> in the case of the Br<sub>2</sub> molecule or CH<sub>3</sub><sup>•</sup> in the case of the C<sub>2</sub>H<sub>6</sub> molecule.).

**Intermolecular electron transfer**, i.e. a process by which an electron moves from one atom or molecule to another. Electron transfer is a mechanistic description of the thermodynamic concept of redox, wherein the formal oxidation states of both reaction partners change. Numerous essential processes in biology employ electron transfer reactions, including: oxygen binding/transport, photosynthesis/respiration, metabolic syntheses, and detoxification of reactive species. Additionally, the process of energy transfer can be formalized

as a two electron exchange (two concurrent electron transfer events in opposite directions). Electron transfer reactions commonly involve transition metal complexes, but there are now many examples of electron transfer in organic molecules [137–139, 144, 145, 153–160].

The general chemical reaction for this process can be written as



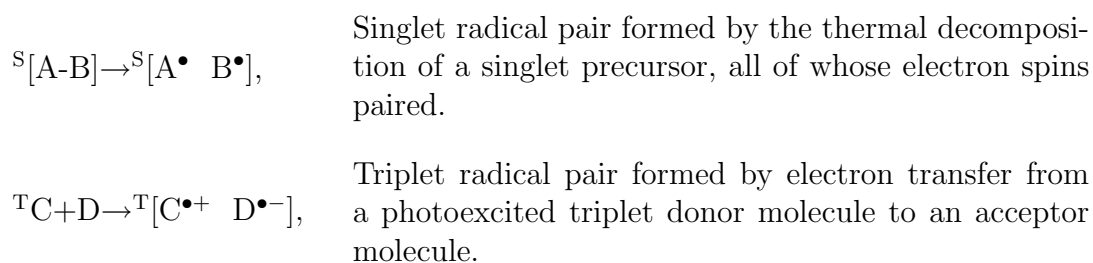
where C and D represent the electron donor and acceptor molecules respectively. The electron transfer process in cryptochrome, described in subsection 2.4.1, is a typical example.

**Intermolecular hydrogen atom transfer**, i.e a process by which a hydrogen atom moves from one molecule, and attaches to another. It can be schematically denoted in the following reaction scheme:



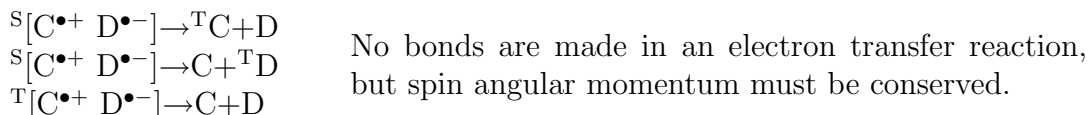
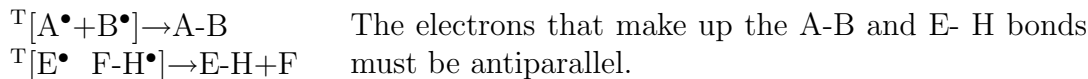
The reactions described above may be induced thermally, photochemically or by ionizing radiation.

(ii) The formation of the radical pair must be such that the two unpaired electrons, one on each radical, have correlated spins. The electron spins of the two radicals must initially be either parallel ( $\uparrow\uparrow$ ) or antiparallel ( $\uparrow\downarrow$ ) to one another. The former is called a triplet state (T) and the latter a singlet state (S). Conservation of spin angular momentum usually ensures that at the moment of its creation the radical pair has the same multiplicity (S or T) as its precursor(s). For example:



(iii) Singlet and triplet radical pairs must have different fates; i.e. the reactivity of the pair must be spin-selective. This usually arises from the requirements that the spin angular momentum is conserved and that the chemical bonds are comprised

of the electrons with antiparallel spins. For example, the following processes are usually forbidden



(iv) At least one of the radicals must have hyperfine couplings. These are intramolecular interactions between the magnetic moments of the unpaired electron and the nuclei of atoms such as hydrogen ( $^1\text{H}$ ), nitrogen ( $^{14}\text{N}$ ) and phosphorus ( $^{31}\text{P}$ ). The hyperfine interaction is discussed in more detail in subsection 3.1.3. Atomic nuclei are magnetic if, like the electron, they possess spin angular momentum. Nuclei of atoms such as carbon ( $^{12}\text{C}$ ) and oxygen ( $^{16}\text{O}$ ) have no spin and hence no magnetism. Almost all radicals have at least one or more hyperfine couplings.

Hyperfine interactions are crucial because they affect the interconversion between the S and T states of a radical pair.  $S\leftrightarrow T$  interconversion is a coherent, oscillatory and quantum mechanical process: radical pairs oscillate between S and T states at frequencies determined by the strength of the hyperfine interactions. Typical hyperfine couplings are in the range 100-1000  $\mu\text{T}$ , corresponding to interconversion frequencies of 3-30 MHz. The timescale of  $S\leftrightarrow T$  interconversion is thus approximately 30-300 ns. In subsection 3.1.8, estimates of the  $S\leftrightarrow T$  interconversion period will be considered.

### 3.1.2 Radical Pair Hamiltonian

The radical pair mechanism is known to operate for radical reactions in solution [93, 161–164] and in solid-like environments [91, 165–167]. We start with the latter, as it is more closely related to the subject of the thesis. The idea of the radical-pair-based compass in birds have been outlined and described in section 2.4.1. It has been proposed that the radical pair mechanism – supposedly linked to the avian compass – arises in the protein cryptochrome.

In the present section, the underlying theory behind the radical pair mechanism in cryptochrome will be outlined. Let us begin by constructing the Hamiltonian for the possible radical pair in cryptochrome.

The Hamiltonian for the intermediate radical pair systems, FADH + Trp400<sup>+</sup>, FADH + Trp377<sup>+</sup>, or FADH + Trp324<sup>+</sup>, is the sum of two Hamiltonians for each radical pair, e.g., a Hamiltonian for FADH and a Hamiltonian for Trp400<sup>+</sup>. In addition, a Hamiltonian  $\hat{H}_{\text{int}}$  accounts for the exchange and dipolar interactions within the radical pair. This part of the Hamiltonian will be discussed in more details in subsection 3.1.4.

The Hamiltonian for one specific pair is denoted generically as

$$\hat{H} = \hat{H}_{\text{FADH}} + \hat{H}_{\text{Trp}} + \hat{H}_{\text{int}} . \quad (3.4)$$

The Hamiltonians  $\hat{H}_{\text{FADH}}$  and  $\hat{H}_{\text{Trp}}$ , as explained in [36, 88], are composed of a Zeeman and a hyperfine coupling interaction term and are respectively written as

$$\hat{H}_j = \mu_B (\vec{B} \cdot \hat{g} \cdot \vec{S}_j) + \mu_B \sum_i (\vec{I}_i \cdot \hat{A}_i \cdot \vec{S}_j) \quad (3.5)$$

where  $j$  denotes the FADH or the tryptophan radical,  $\vec{I}_i = (I_x, I_y, I_z)_i$  is the spin operator of the  $i$ -th nucleus,  $\vec{S}_j = (S_x, S_y, S_z)$  is the electron spin operator,  $\hat{A}_i$  is the hyperfine coupling tensor for nucleus  $i$ ,  $\mu_B = 5.78843 \times 10^{-9}$  eV/Gauss is the Bohr magneton, and

$$\vec{B} = (B_x, B_y, B_z) = (B_0 \sin \Theta \cos \Phi, B_0 \sin \Theta \sin \Phi, B_0 \cos \Theta) \quad (3.6)$$

is the induction vector of the external magnetic field. The sum over  $i$  in Eq. (3.5) is performed over all the nuclei of one radical. The second term in Eq. (3.5) describes the coupling interaction and is discussed in more details in subsection 3.1.3.

The nuclear and electron spins, and the external magnetic field are depicted in Fig. 3.1. As explained in detail in [88, 89], in the semiclassical picture the electrons precess in the local magnetic field corresponding to the term  $\mu_B (\vec{B} + \sum_i \vec{I}_i \cdot \hat{A}_i)$  in Eq. (3.5), with contributions from the external field  $\vec{B}$  and from the nuclear spins  $\vec{I}_i$ . The operator  $\hat{g}$  is the so-called  $g$ -tensor which in an appropriate coordinate system, can be diagonalized with diagonal values called  $g$ -factors:

$$\hat{g} = \begin{pmatrix} g_{xx} & 0 & 0 \\ 0 & g_{yy} & 0 \\ 0 & 0 & g_{zz} \end{pmatrix} . \quad (3.7)$$

In this work an isotropic  $g$ -tensor is assumed, where  $g_{xx} = g_{yy} = g_{zz} = g = 2$ .

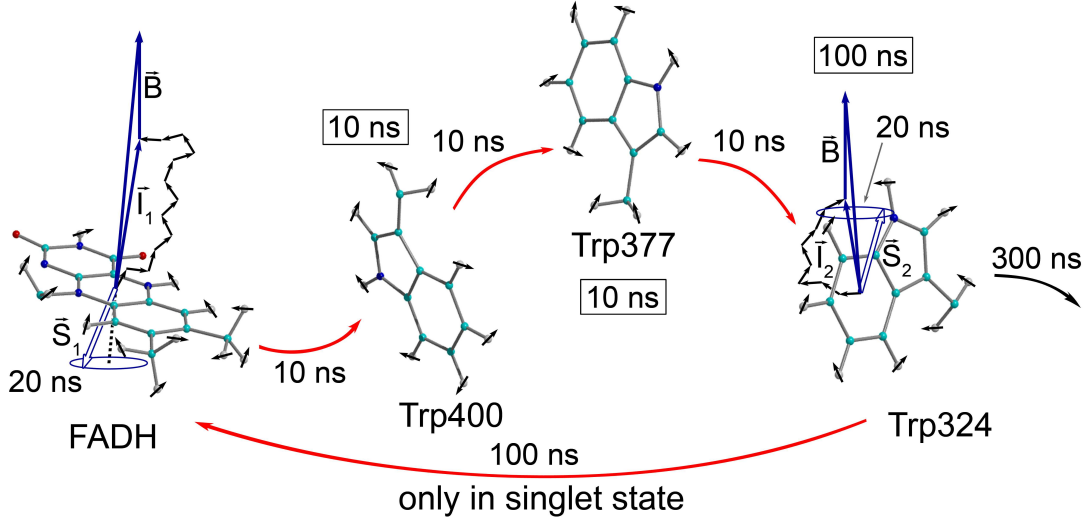


Figure 3.1: Schematic illustration of electron hole transfer and electron spin dynamics in the FADH cofactor and the tryptophan chain. Following photoexcitation of the FADH cofactor, an electron hole propagates outward through the three-tryptophan chain (transfer times 10 ns), forming in sequence the radical pair states  $\text{FADH} + \text{Trp400}^+ \rightarrow \text{FADH} + \text{Trp377}^+ \rightarrow \text{FADH} + \text{Trp324}^+$ . The latter radical pair state is terminated through either electron back-transfer or deprotonation with transition times 100 ns and 300 ns, respectively. The system spends about 100 ns in the  $\text{FADH} + \text{Trp324}^+$  state but only 10 ns the  $\text{FADH} + \text{Trp400}^+$  and  $\text{FADH} + \text{Trp377}^+$  states (radical pair state lifetimes are shown in square boxes), making the  $\text{FADH} + \text{Trp324}^+$  radical pair state the major contributor to the magnetic field effect. Electron hole migration (10 ns), spin precession (20 ns), electron back-transfer (100 ns) and deprotonation of Trp324 (300 ns) are shown with arrows. Also shown are the electronic and nuclear spins in the  $\text{FADH} + \text{Trp324}^+$  radical pair; while in Trp400 and Trp377 only the nuclear spins are shown. The nuclear spins are shown with typical random orientations, and the electron spins are shown in the initial anti-parallel, i.e. singlet, alignment. The picture corresponds to the so-called semi-classical description of electron-nuclear spin dynamics [88,89]. In this description, the electron spins ( $\vec{S}_1$  and  $\vec{S}_2$ ) precess about a local magnetic field produced by the addition of the external magnetic field  $\vec{B}$  and contributions  $\vec{I}_1$  and  $\vec{I}_2$  from the nuclear spins on the two radicals. The spin precession continuously alters the relative spin orientation, causing the singlet (anti-parallel)  $\leftrightarrow$  triplet (parallel) interconversion which underlies the magnetic field effect.

The dimension of the Hamiltonian in Eq. (3.5) is determined by the dimensions of the spin spaces of the nuclei. The spin operator in Eq. (3.5) can be written

$$S_k = \left( \frac{1}{2} \sigma_k \right) \otimes E_{\text{Dim}(I_1)} \otimes E_{\text{Dim}(I_2)} \otimes \dots, \quad k = x, y, z \quad (3.8)$$

where  $(\sigma_x, \sigma_y, \sigma_z)$  are the Pauli spin matrices [168–170]:

$$\sigma_x = \begin{pmatrix} 0 & 1 \\ 1 & 0 \end{pmatrix}, \quad \sigma_y = \begin{pmatrix} 0 & -i \\ i & 0 \end{pmatrix}, \quad \sigma_z = \begin{pmatrix} 1 & 0 \\ 0 & -1 \end{pmatrix} \quad (3.9)$$

$E_n$  in Eq. (3.8) is the identity matrix of dimension  $n$ . The dimension of the identity matrices is determined by the dimension of the spin spaces of the corresponding nuclei, shown in Eq. (3.8) as a subscript to matrices  $E$ . The  $\otimes$  symbol denotes the direct product (see Appendix A for more details regarding the direct product algebra).

The nuclear spin matrices  $\vec{I}$  for spin-1/2 nuclei (i.e. hydrogen  $^1\text{H}$ ) are defined as follows:

$$I_k = \frac{1}{2}\sigma_k, \quad k = x, y, z \quad (3.10)$$

while the spin matrices for spin-1 nuclei (i.e. nitrogen  $^{14}\text{N}$ ) are (see, for example, [169, 171]):

$$I_x = \frac{1}{\sqrt{2}} \begin{pmatrix} 0 & 1 & 0 \\ 1 & 0 & 1 \\ 0 & 1 & 0 \end{pmatrix}, \quad I_y = \frac{1}{\sqrt{2}} \begin{pmatrix} 0 & -i & 0 \\ i & 0 & -i \\ 0 & i & 0 \end{pmatrix}, \quad I_z = \begin{pmatrix} 1 & 0 & 0 \\ 0 & 0 & 0 \\ 0 & 0 & -1 \end{pmatrix}. \quad (3.11)$$

Spin matrices for higher spins are irrelevant here because in the considered radical pairs include only hydrogen and nitrogen are the particles with hyperfine couplings, while for carbon and oxygen it is zero.

### 3.1.3 Hyperfine Interaction

The hyperfine interaction,  $\hat{H}_{HF}$ , is basically a dipolar coupling between an electron and a nuclear spin. It is described by the following Hamiltonian:

$$\hat{H}_{HF} = \mu_B g_e \mu_N g_N \left[ \frac{3(\vec{S}\vec{r})(\vec{I}\vec{r})}{r^5} - \frac{\vec{S}\vec{I}}{r^3} \right] + \frac{8\pi}{3} \mu_B g_e \mu_N g_N \vec{S}\vec{I}\rho(0). \quad (3.12)$$

Here,  $g_e$  and  $g_N$  are the g-factors of the electron and the nucleus respectively.  $\mu_B$  and  $\mu_N$  are the electron and nuclear magnetic moments respectively.  $\rho(0) = |\Psi(0)|^2$  is the unpaired electron density at the site of the nucleus. The first term in Eq. (3.12) describes the pure dipole-dipole interaction between the electron and nuclear spin. For electrons that are not close to the nucleus (such as the p, d or f electrons) this

is the main contribution to the hyperfine interaction. The second term describes the Fermi – contact interaction between the nuclei and the s-electron. Note that in many-electron systems even the p, d or f electrons may have a partial s-character and therefore contributions from Fermi – contact have to be considered. The hyperfine interaction, Eq. (3.12) can be expressed in terms of the hyperfine coupling tensor  $\hat{A}$  as follows:

$$\hat{H}_{HF} = \mu_B \sum_i (\vec{I}_i \cdot \hat{A}_i \cdot \vec{S}_j), \quad (3.13)$$

what corresponds to the second term in Eq. (3.5).

The hyperfine coupling tensor parameterizes the electron-nuclear spin interaction, and can be derived from molecular electronic energy terms that are bilinear in electronic spin and nuclear spin. One can define the hyperfine coupling tensor relative to a magnetic nucleus  $i$  as the second derivative of the molecular electronic energy ( $E$ ) with respect to the total electronic  $\mathbf{S}$ , and nuclear  $\mathbf{I}_i$  spins:

$$A_i = \frac{\partial^2 E}{\partial \mathbf{S} \partial \mathbf{I}_i}. \quad (3.14)$$

Thus, each nuclear spin is coupled to the electron spin by a hyperfine coupling tensor  $\hat{A}_i$ . This hyperfine coupling tensor is split into an isotropic and an anisotropic part:

$$\sum_i (\vec{I}_i \cdot \hat{A}_i \cdot \vec{S}_j) = \sum_i (\vec{I}_i \cdot \hat{A}_i^{(iso)} \cdot \vec{S}_j) + \sum_i (\vec{I}_i \cdot \hat{A}_i^{(aniso)} \cdot \vec{S}_j). \quad (3.15)$$

The isotropic part can be written (for the sake of simplicity the index  $j$  is left out) as

$$\begin{aligned} \sum_i (\vec{I}_i \cdot \hat{A}_i^{(iso)} \cdot \vec{S}) &= \sum_i A_{i_{xx}}^{(iso)} \left[ \left( \frac{1}{2} \sigma_x \right) \otimes \dots \otimes I_x^{(i)} \otimes \dots \right] \\ &+ A_{i_{yy}}^{(iso)} \left[ \left( \frac{1}{2} \sigma_y \right) \otimes \dots \otimes I_y^{(i)} \otimes \dots \right] \\ &+ A_{i_{zz}}^{(iso)} \left[ \left( \frac{1}{2} \sigma_z \right) \otimes \dots \otimes I_z^{(i)} \otimes \dots \right], \end{aligned} \quad (3.16)$$

where

$$A_{i_{xx}}^{iso} = A_{i_{yy}}^{iso} = A_{i_{zz}}^{iso} = a_i^{iso} \quad (3.17)$$

are the isotropic hyperfine coupling constants.



The isotropic part of the hyperfine tensor is diagonal in the same basis as the  $g$ -tensor, but the anisotropic part, in general, is not. The hyperfine axes define the orthonormal basis in which the anisotropic part of the hyperfine tensor is diagonal. In order to compute the inner product  $\vec{I} \cdot \hat{A}^{(aniso)} \cdot \vec{S}$ , the electron and nuclear spins must be rotated into the same basis. If the coordinate frames of the  $g$ -tensor and the anisotropic hyperfine tensor are denoted as  $(x, y, z)$  and  $(x', y', z')$  – corresponding to the unit vectors  $(\vec{i}, \vec{j}, \vec{k})$  and  $(\vec{i}', \vec{j}', \vec{k}')$  respectively – then the anisotropic part of the tensor can be written as

$$\begin{aligned} \sum_i (\vec{I}_i \cdot \hat{A}_i^{(aniso)} \cdot \vec{S}) &= \sum_i A_{i_{xx}}^{(aniso)} \left[ \left( \frac{1}{2} \sigma'_x \right) \otimes \dots \otimes I_x^{(i)} \otimes \dots \right] \\ &+ A_{i_{yy}}^{(aniso)} \left[ \left( \frac{1}{2} \sigma'_y \right) \otimes \dots \otimes I_y^{(i)} \otimes \dots \right] \\ &+ A_{i_{zz}}^{(aniso)} \left[ \left( \frac{1}{2} \sigma'_z \right) \otimes \dots \otimes I_z^{(i)} \otimes \dots \right]. \end{aligned} \quad (3.18)$$

Here the rotated spin matrices are

$$\begin{cases} \sigma'_x = \sigma_x(\vec{i} \cdot \vec{i}') + \sigma_y(\vec{j} \cdot \vec{i}') + \sigma_z(\vec{k} \cdot \vec{i}') \\ \sigma'_y = \sigma_x(\vec{i} \cdot \vec{j}') + \sigma_y(\vec{j} \cdot \vec{j}') + \sigma_z(\vec{k} \cdot \vec{j}') \\ \sigma'_z = \sigma_x(\vec{i} \cdot \vec{k}') + \sigma_y(\vec{j} \cdot \vec{k}') + \sigma_z(\vec{k} \cdot \vec{k}') \end{cases}. \quad (3.19)$$

In this model the three tryptophans are considered to be identical and as such, the orientational differences between them are neglected. Hence each will have an identical Hamiltonian.

Note that the anisotropic hyperfine coupling constants in Eq. (3.18) in general can be different:  $A_{i_{xx}}^{(aniso)} \neq A_{i_{yy}}^{(aniso)} \neq A_{i_{zz}}^{(aniso)}$ .

### 3.1.4 Exchange and Dipolar Interactions

In addition to the Zeeman and hyperfine coupling interaction terms in Eq. (3.5), one also needs to take into account, the electron-electron exchange and dipolar interactions in the radical pair. This is done through the term  $\hat{H}_{\text{int}}$  in Eq. (3.4). These interactions play an important role when the distances between the radicals are small comparing to the characteristic size of the radicals. The part of the Hamiltonian describing the electron-electron exchange and dipolar interactions is

$$\hat{H}_{\text{int}} = \mu_B J(R) \left( \frac{1}{2} + 2\vec{S}_1 \cdot \vec{S}_2 \right) + \mu_B D(R) \left[ \vec{S}_1 \cdot \vec{S}_2 - 3(\vec{S}_1 \cdot \vec{n})(\vec{S}_2 \cdot \vec{n}) \right] \quad (3.20)$$

where  $\vec{S}_1$  and  $\vec{S}_2$  are respectively the unpaired electron spins on the FADH and Trp radicals. The functions  $J(R)$  and  $D(R)$  describe the strength of the exchange and dipolar couplings and are assumed, as is often done (see e.g. Refs. [95,172]), to take the simple functional form

$$J(R) = J_0 \exp[-\beta_0 R] \quad (3.21)$$

$$D(R) = \mu_B / R^3. \quad (3.22)$$

In Eqs. (3.20)-(3.22),  $R$  is the edge-to-edge distance (i.e. the minimal distance) between the radicals,  $J_0$  is the exchange coupling constant,  $\vec{n}$  is the unit vector in the direction of  $\vec{R}$ , and  $\beta_0$  is the range parameter. The exchange and dipolar coupling parameters rapidly decrease with distance between the radicals and can be neglected if the distance is sufficiently large (i.e the distance between the radicals is greater than the characteristic size of the radicals). It is possible to estimate the values of the coupling parameters for a given distance between the FADH and Trp radicals using Eqs. (3.20-3.22). The characteristic distances  $R_{\text{FADH-Trp400}}$ ,  $R_{\text{FADH-Trp377}}$ , and  $R_{\text{FADH-Trp324}}$  are:

$$R_{\text{FADH-Trp400}} = 6.0 \text{ \AA}$$

$$R_{\text{FADH-Trp377}} = 8.9 \text{ \AA}$$

$$R_{\text{FADH-Trp324}} = 13.3 \text{ \AA}.$$

The values for  $J_0$  and  $\beta_0$  are taken (from a study of acyl-ketyl biradicals [95,172]) to be  $J_0 = 7 \times 10^9 \text{ G}$  and  $\beta_0 = 2.14 \text{ \AA}^{-1}$ ; these values are typical for radical pairs in solution. With these values for  $J_0$ ,  $\beta_0$ , and  $R$ , one makes the following estimates for the exchange coupling parameters:

$$J(R_{\text{FADH-Trp400}}) \approx 19000 \text{ G}$$

$$J(R_{\text{FADH-Trp377}}) = 37 \text{ G}$$

$$J(R_{\text{FADH-Trp324}}) = 0.006 \text{ G}.$$

The estimated values for the dipolar coupling parameters are

$$D(R_{\text{FADH-Trp400}}) \approx 43 \text{ G}$$

$$D(R_{\text{FADH-Trp377}}) = 13 \text{ G}$$

$$D(R_{\text{FADH-Trp324}}) = 4 \text{ G}.$$

The estimated exchange interaction in the FADH + Trp400<sup>+</sup> radical pair is significantly larger than the hyperfine interaction, which is characterized by a coupling constant ( $A_i^{iso}$  in Eq. (3.16)) of about 10 G per nucleus (see chapter 4). In the FADH + Trp377<sup>+</sup> radical pair, the exchange interaction is significantly smaller than for the FADH + Trp400<sup>+</sup> pair, but is comparable with the typical hyperfine interaction. In the FADH + Trp324<sup>+</sup> radical pair, the exchange interaction is much smaller than both the typical hyperfine interaction and the external magnetic field. However, it must be stressed that the given estimates are only qualitative and that the real exchange interaction in cryptochrome may be significantly different from the values given above. An accurate calculation of the exchange interaction depends upon knowledge of the constants  $J_0$  and  $\beta_0$ , and the coupling parameter is especially sensitive to the constant  $\beta_0$ . For example, a value of  $\beta_0 = 4.28 \text{ \AA}^{-1}$  [95] produces

$$\begin{aligned} J(R_{\text{FADH-Trp400}}) &\approx 0.05 \text{ G} \\ J(R_{\text{FADH-Trp377}}) &= 2 \times 10^{-7} \text{ G} \\ J(R_{\text{FADH-Trp324}}) &= 4.8 \times 10^{-15} \text{ G}, \end{aligned}$$

all of which are negligible in comparison with the hyperfine interaction.

The estimated dipole-dipole interaction appears to be of the same order of magnitude as the hyperfine interaction term for the FADH+Trp400<sup>+</sup> and FADH+Trp377<sup>+</sup> radical pairs (see the discussion in subsection 4.2), however it is notably smaller than the typical hyperfine interaction for the FADH + Trp324<sup>+</sup> radical pair.

Large values of the exchange or dipolar coupling parameters in the Hamiltonian of a radical pair mean that the singlet-triplet interconversion process in the radical pair will be suppressed [95]. The large estimates for the exchange and dipolar couplings for the FADH + Trp400<sup>+</sup> and FADH + Trp377<sup>+</sup> pairs would then seem problematic for the production of a magnetic field effect. However, because the characteristic rate for electron transfer from Trp377 to Trp400 and from Trp324 to Trp377 is of the same order of magnitude as the singlet-triplet interconversion rate (see discussion on rate constants in subsection 4.3 and on the singlet – triplet interconversion in subsection 3.1.8), neglecting the exchange and dipolar interaction terms for these pairs will not significantly affect the spin dynamics. As is further illustrated in Fig. 3.1, the main contribution to the spin dynamics of the system comes from the FADH + Trp324<sup>+</sup> radical pair due to the disparity in the lifetimes  $\tau(\text{FADH} + \text{Trp400}^+) \approx \tau(\text{FADH} + \text{Trp377}^+) \approx 10 \text{ ns}$  and

$\tau(\text{FADH} + \text{Trp324}^+) \approx 100$  ns. Hence neglecting the exchange and dipolar interaction in the  $\text{FADH} + \text{Trp400}^+$  and  $\text{FADH} + \text{Trp377}^+$  pairs is acceptable. For the  $\text{FADH} + \text{Trp324}^+$  radical pair, the estimates for both the exchange and dipolar couplings are smaller than the typical hyperfine interaction, so the exchange and dipolar interactions may be neglected for this pair as well. For these reasons the term  $H_{\text{int}}$  in Eq. (3.4) is neglected and only the effects of the Zeeman and hyperfine interaction terms are considered.

### 3.1.5 Density Matrix and the Liouville Equation

For the description of spin dynamics in a quantum system (i.e. the time evolution of the radical pair in cryptochrome) one has to solve the Schrödinger equation which describes the evolution of the wavefunction of the system (see e.g. [169, 170]):

$$\hat{H}|\Psi\rangle = i\hbar \frac{\partial |\Psi\rangle}{\partial t}, \quad (3.23)$$

where  $\hat{H}$  is the Hamilton operator (Hamiltonian) and  $|\Psi\rangle$  is the wavefunction of the system, which can be written as:

$$|\Psi\rangle = \sum_n C_n |u_n\rangle, \quad (3.24)$$

where the set of states  $\{|u_n\rangle\}$  is orthonormal and complete, that is

$$\langle u_m | u_n \rangle = \delta_{nm}; \quad \sum_n |u_n\rangle \langle u_n| = 1 \quad (3.25)$$

The time-dependent expansion coefficients  $C_n$  in Eq. (3.24) satisfy the relation

$$\sum_n |C_n|^2 = 1, \quad (3.26)$$

expressing the fact that  $|\Psi\rangle$  is normalized. According to the principles of quantum mechanics, full information regarding the physical system is contained in its wavefunction  $|\Psi(t)\rangle$  being a normalized vector in a certain Hilbert space. Each physical quantity,  $A$ , is described by a corresponding Hermitian operator  $\hat{A}$ . The expectation value of the observable  $A$  in the Schrödinger picture is then given as

$$\langle A \rangle_t = \langle \Psi(t) | \hat{A} | \Psi(t) \rangle \quad (3.27)$$

This statement can be checked only by performing the measurement of observable  $A$  on the ensemble of systems, each prepared in the quantum-mechanical state  $|\Psi\rangle$ . If the measurements are done only on one system it is not possible to predict the result with certainty. Note that the average in (3.27) depends parametrically on time.

Let us now compute the expectation value of the observable  $A$ . Substituting expansion Eq. (3.24) into Eq. (3.27) one obtains:

$$\langle A \rangle_t = \sum_{m,n} C_n^*(t) C_m(t) A_{nm} \quad (3.28)$$

where  $A_{nm}$  denotes the matrix element  $\langle u_n | \hat{A} | u_m \rangle$ . Let us consider the operator  $\rho \equiv |\Psi(t)\rangle\langle\Psi(t)|$ . The operator  $\rho$  is usually referred as the **density operator** [169–171, 173] and its corresponding matrix – the **density matrix**. The density operator is a Hermitian operator, with matrix elements

$$\rho_{mn}(t) = \langle u_m | \rho(t) | u_n \rangle = C_m(t) C_n^*(t). \quad (3.29)$$

Since  $|\Psi(t)\rangle$  is normalized:

$$1 = \sum_n |C_n(t)|^2 = \sum_n \rho_{nn}(t) = \text{Tr}[\rho(t)]. \quad (3.30)$$

Here  $\text{Tr}[A]$  denotes the **trace** of matrix  $A$ . With the use of the density operator it is possible to re-express the expectation value of observable  $A$ :

$$\begin{aligned} \langle A \rangle_t &= \sum_m \sum_n C_m(t) C_n^*(t) A_{mn} = \sum_m \sum_n \rho_{mn}(t) A_{mn} = \\ &= \sum_n [\rho(t) A]_{nn} = \text{Tr}[\rho(t) A]. \end{aligned} \quad (3.31)$$

The time evolution of a quantum state is described by the Schrödinger equation Eq. (3.23). Thus, the time evolution of the density operator may be computed according to:

$$\begin{aligned} \frac{d}{dt} \rho(t) &= \frac{d}{dt} (|\Psi(t)\rangle\langle\Psi(t)|) = |\dot{\Psi}(t)\rangle\langle\Psi(t)| + |\Psi(t)\rangle\langle\dot{\Psi}(t)| = \\ &= -\frac{i}{\hbar} \hat{H} |\Psi(t)\rangle\langle\Psi(t)| + \frac{i}{\hbar} |\Psi(t)\rangle\langle\Psi(t)| \hat{H} = \\ &= -\frac{i}{\hbar} [\hat{H}, \rho(t)]_-. \end{aligned} \quad (3.32)$$

This equation of motion is usually referred to as the Liouville – von Neumann equation for the density operator [169–171, 173]. The notation  $[\hat{H}, \rho(t)]_-$  in Eq. (3.32) denotes the commutator corresponding to  $[\hat{A}, \hat{B}]_- = \hat{A}\hat{B} - \hat{B}\hat{A}$ .

### 3.1.6 Stochastic Liouville Equation

Within the semiclassical approach [174–178] one can describe fluctuating irreversible processes in the system by adding a **non-Hermitian relaxation term**  $-i\hbar\hat{K}(t)$  in the operator  $\hat{H}$ . An example of such process is the electron-hopping process introduced in section 2.4.1. Thus, such fluctuating irreversible processes result in modification of the Liouville equation (3.32). In this case the evolution of the wavefunction is described by the following equation:

$$|\dot{\Psi}\rangle = -\frac{i}{\hbar}\hat{H}_0|\Psi\rangle - \hat{K}|\Psi\rangle. \quad (3.33)$$

Here  $\hat{H}_0$  is the Hermitian part of the Hamiltonian (i.e. the spin Hamiltonian defined in subsection 3.1.2). Thus:

$$\hat{H} = \hat{H}_0 - i\hbar\hat{K}(t). \quad (3.34)$$

The complex conjugate to Eq. (3.33) reads as:

$$\langle\dot{\Psi}| = \frac{i}{\hbar}\langle\Psi|\hat{H}_0 - \langle\Psi|\hat{K}. \quad (3.35)$$

Substituting Eqs. (3.33)-(3.35) in the equation for the time derivative of the density matrix (3.32) one obtains

$$\begin{aligned} \dot{\rho} &= |\dot{\Psi}(t)\rangle\langle\Psi(t)| + |\Psi(t)\rangle\langle\dot{\Psi}(t)| = \\ &= -\frac{i}{\hbar}\hat{H}_0|\Psi(t)\rangle\langle\Psi(t)| + \frac{i}{\hbar}|\Psi(t)\rangle\langle\Psi(t)|\hat{H}_0 \\ &\quad - K|\Psi(t)\rangle\langle\Psi(t)| - |\Psi(t)\rangle\langle\Psi(t)|K. \end{aligned} \quad (3.36)$$

Introducing the anticommutator  $[\hat{A}, \hat{B}]_+$  of two operators  $\hat{A}$  and  $\hat{B}$  as:

$$[\hat{A}, \hat{B}]_+ = \hat{A}\hat{B} + \hat{B}\hat{A} \quad (3.37)$$

Eq. (3.37) can be rewritten as follows:

$$\dot{\rho} = -\frac{i}{\hbar}[\hat{H}_0, \rho(t)]_- - [\hat{K}, \rho(t)]_+. \quad (3.38)$$

This equation of evolution of the density matrix is usually referred as the modified Liouville equation or the **stochastic Liouville equation** [174–178].

In order to describe FAD photoreduction and a radical-pair-based magnetic field effect in cryptochrome, the description in [1] is extended and three intermediate radical pairs, i.e., FADH + Trp400<sup>+</sup>, FADH + Trp377<sup>+</sup>, and FADH + Trp324<sup>+</sup>, are included as shown in Figs. 2.10 and 3.1. The time-evolution of the corresponding spin system is described through a modified stochastic Liouville equation. For this purpose, three density matrices  $\rho_i$  are defined for the states  $1 \leq i \leq 3$  corresponding to FADH + Trp400<sup>+</sup>, FADH + Trp377<sup>+</sup>, and FADH + Trp324<sup>+</sup>. Each density matrix follows a stochastic Liouville equation which describes the spin motion and also takes into account the transitions into and out of a particular state into other states, as illustrated in Fig. 2.10. The equations that govern the evolution of the density matrices  $\rho_i$  are generalizations of Eq. (3) in [1]:

$$\frac{\partial \rho_1(t)}{\partial t} = -\frac{i}{\hbar}[\hat{H}_1, \rho_1]_- - \frac{k_1}{2}[\hat{Q}^S, \rho_1]_+ - \frac{k_1}{2}[\hat{Q}^T, \rho_1]_+ - \frac{k_1^b}{2}[\hat{Q}^S, \rho_1]_+ \quad (3.39)$$

$$\begin{aligned} \frac{\partial \rho_2(t)}{\partial t} &= -\frac{i}{\hbar}[\hat{H}_2, \rho_2]_- - \frac{k_2}{2}[\hat{Q}^S, \rho_2]_+ - \frac{k_2}{2}[\hat{Q}^T, \rho_2]_+ - \frac{k_2^b}{2}[\hat{Q}^S, \rho_2]_+ \quad (3.40) \\ &\quad + \frac{k_1}{2}[\hat{Q}^S, \rho_1]_+ + \frac{k_1}{2}[\hat{Q}^T, \rho_1]_+ \end{aligned}$$

$$\begin{aligned} \frac{\partial \rho_3(t)}{\partial t} &= -\frac{i}{\hbar}[\hat{H}_3, \rho_3]_- - \frac{k_d}{2}[\hat{Q}^S, \rho_3]_+ - \frac{k_d}{2}[\hat{Q}^T, \rho_3]_+ - \frac{k_3^b}{2}[\hat{Q}^S, \rho_3]_+ \quad (3.41) \\ &\quad + \frac{k_2}{2}[\hat{Q}^S, \rho_2]_+ + \frac{k_2}{2}[\hat{Q}^T, \rho_2]_+ . \end{aligned}$$

The operators  $k_i \hat{Q}^S/2$  and  $k_i \hat{Q}^T/2$  (with  $k_i$  equal to  $k_1$ ,  $k_2$ ,  $k_d$ ,  $k_1^b$ ,  $k_2^b$  or  $k_3^b$ ) are the non-Hermitian operators  $\hat{K}$  in Eq. (3.38) [1, 36, 89, 93, 129, 130, 164, 167, 179].  $\hat{Q}^S$  and  $\hat{Q}^T$  are the projection operators onto the singlet and triplet states of the electron spin pair, which are defined as (see for example Refs. [1, 36, 93, 167]):

$$\hat{Q}^S = \frac{1}{4} - \vec{S}_1 \cdot \vec{S}_2 \quad (3.42)$$

$$\hat{Q}^T = \frac{3}{4} + \vec{S}_1 \cdot \vec{S}_2, \quad (3.43)$$

where  $\vec{S}_1$  and  $\vec{S}_2$  denote the spin-matrices which describe the unpaired electron on FADH and Trp respectively.  $\hat{H}_i$  in Eqs. (3.39)-(3.41) is the Hamiltonian associated with the radical pair that consists of FADH and the  $i^{\text{th}}$  tryptophan. Since all tryptophans are assumed to be identical, it then follows that  $\hat{H}_1 = \hat{H}_2 = \hat{H}_3 = \hat{H}$ . The

rate constants associated with the process of electron jumping from one tryptophan to the next are denoted by  $k_1$  and  $k_2$ . The rate constants for electron back-transfer from each of the three tryptophans are denoted  $k_1^b$ ,  $k_2^b$ , and  $k_3^b$ , while  $k_d$  is the rate constant associated with tryptophan deprotonation [138]. The following assumptions and notational conventions will be adopted

$$\begin{aligned} k_1 = k_2 &= k_{et} \\ k_1^b = k_2^b = k_3^b &= k_b . \end{aligned} \quad (3.44)$$

The subscript *et* shows that the corresponding rate constant describes the electron transfer process. These assumptions will be rationalized in the discussion of rate constants in chapter 4, section 4.3. The assumptions Eq. 3.45 reduces the number of parameters in the problem to three:  $k_{et}$ ,  $k_b$  and  $k_d$ . These parameters will be estimated in section 4.3.

To illustrate the derivation of Eqs. (3.39)-(3.41) it will be useful to explain the right-hand-side of Eq. (3.40). The first term describes the electron spin motion; the second and third terms describe the loss of density due to the electron hole transitions  $\text{FADH} + \text{Trp377}^+ \rightarrow \text{FADH} + \text{Trp324}^+$ ; the fourth term describes the electron back-transfer  $\text{FADH} + \text{Trp377}^+ \rightarrow \text{FADH}^+ + \text{Trp377}$ ; the last two terms account for the electron hole transition  $\text{FADH} + \text{Trp400}^+ \rightarrow \text{FADH} + \text{Trp377}^+$ . Terms two, three, five, and six correspond to spin-independent reactions, but term four describes a manifestly spin-dependent reaction, as electron back-transfer is only permitted when the  $\text{FADH} + \text{Trp377}^+$  radical pair is in an overall singlet electron spin pair state.

By using the relationship  $\hat{Q}^T = 1 - \hat{Q}^S$  and collecting terms, Eqs. (3.39)-(3.41) can be re-written as:

$$\frac{\partial \rho_1(t)}{\partial t} = -\frac{i}{\hbar}[\hat{H}, \rho_1]_- - k_{et}\rho_1 - \frac{k_b}{2}(\hat{Q}^S \rho_1 + \rho_1 \hat{Q}^S) \quad (3.45)$$

$$\frac{\partial \rho_2(t)}{\partial t} = -\frac{i}{\hbar}[\hat{H}, \rho_2]_- - k_{et}\rho_2 + k_{et}\rho_1 - \frac{k_b}{2}(\hat{Q}^S \rho_2 + \rho_2 \hat{Q}^S) \quad (3.46)$$

$$\frac{\partial \rho_3(t)}{\partial t} = -\frac{i}{\hbar}[\hat{H}, \rho_3]_- - k_d\rho_3 + k_{et}\rho_2 - \frac{k_b}{2}(\hat{Q}^S \rho_3 + \rho_3 \hat{Q}^S) . \quad (3.47)$$

Simplifying once more, one obtains the final set of coupled differential equations as:



$$\frac{\partial \rho_1(t)}{\partial t} = - \left( \frac{i}{\hbar} \hat{H} + \frac{k_b \hat{Q}^S}{2} \right) \rho_1 + \rho_1 \left( \frac{i}{\hbar} \hat{H} - \frac{k_b \hat{Q}^S}{2} \right) - k_{\text{et}} \rho_1 \quad (3.48)$$

$$\frac{\partial \rho_2(t)}{\partial t} = - \left( \frac{i}{\hbar} \hat{H} + \frac{k_b \hat{Q}^S}{2} \right) \rho_2 + \rho_2 \left( \frac{i}{\hbar} \hat{H} - \frac{k_b \hat{Q}^S}{2} \right) - k_{\text{et}} \rho_2 + k_{\text{et}} \rho_1 \quad (3.49)$$

$$\frac{\partial \rho_3(t)}{\partial t} = - \left( \frac{i}{\hbar} \hat{H} + \frac{k_b \hat{Q}^S}{2} \right) \rho_3 + \rho_3 \left( \frac{i}{\hbar} \hat{H} - \frac{k_b \hat{Q}^S}{2} \right) - k_d \rho_3 + k_{\text{et}} \rho_2 . \quad (3.50)$$

Assuming that the system with the hole on the first tryptophan and with the electron spin pair in the singlet (rather than triplet) state, the initial conditions are:

$$\rho_1(0) = \frac{\hat{Q}^S}{\text{Tr}[\hat{Q}^S]} , \quad (3.51)$$

$$\rho_2(0) = 0 , \quad (3.52)$$

$$\rho_3(0) = 0 . \quad (3.53)$$

This assumption is based on experimental data taken from DNA photolyase [141]. DNA photolyase is the prokaryotic homologous protein of cryptochrome. The similarity of photolyase and cryptochrome has been discussed in subsection 2.4.1. The actual initial state of cryptochrome is not known and might be a triplet state; however, the results of calculation would be qualitatively similar if a triplet state would be chosen for the initial condition.

Note that the possibility of electrons transferring backwards in the tryptophan chain is not included in the model, i.e., electrons undergo the transfers Trp377  $\rightarrow$  Trp400, or Trp324  $\rightarrow$  Trp377, but never the transfers Trp400  $\rightarrow$  Trp377, or Trp377  $\rightarrow$  Trp324. While the latter transfers are feasible, calculations in the Ref. [140] and the estimates presented in the next chapter suggest that the rate constants for electrons transferring backwards in the chain are 2 to 3 orders of magnitude smaller than the rate constants for forward transfer. As will be described in the following section the rate constant of the electron transfer process is determined by the free energy of the reaction, which in the case of electron forward transfer is negative (i.e. the product state is energetically more favorable than the initial state), and is positive in the case of electron backward transfer. This implies that the probability for the electron to transfer backward is small and, therefore, the reverse electron transfer is neglected in the model discussed.

### 3.1.7 Theory of Electron Transfer

Let us consider a unimolecular electron transfer reaction (i.e. an electron transfer in cryptochrome). The general equation of the charge transfer reads as:



The electronic-nuclear coupling is strong and electron transfer is controlled by the nuclear motion. The system moves on diabatic energy surfaces (see Fig. 3.2). Tunneling between reactant and product states occurs when both electronic levels are in resonance and the motion of the nuclei is the driving force needed to achieve this resonance. In Marcus' classical theory the nuclear motion is expressed in terms of harmonic oscillators for the reactant and product states with identical frequency  $\nu$  moving along a generalized reaction coordinate [153–155].<sup>3</sup> The reaction coordinate describes schematically the effect of the protein degrees of freedom on the energy needed to transfer the electron. The two diabatic energy surfaces for the reactant and product states are depicted in Fig. 3.2. The crossing point of the two parabola is called the transition state (TS). In Fig. 3.2b  $\Delta G$  is the (unknown) activation energy,  $\Delta G_0$  is the experimentally available free energy of the reaction (Gibbs) of the transition and  $\lambda$  the reorganization energy. The latter is required to change the positions of all nuclei from the equilibrated reactant state into the equilibrated product state while the electron resides on the donor. In the case of a solvent environment, the reorganization energy of the surrounding molecules has to be added to the intra-molecular reorganization energy and can exceed the latter in the case of polar solvents.

In this description, the electron moves back and forth with the frequency of the harmonic oscillator in the reactant parabola, crossing the transition state twice per period. At the transition state there is a small (weak electronic coupling) probability for a transition to the product state. This is called the non-adiabatic limit. The quantum mechanical description is done in terms of the first order perturbation theory. With a harmonic perturbation, this leads to Fermi's golden rule [169, 171,

---

<sup>3</sup>Marcus Theory is a theory originally developed by Rudolph A. Marcus to explain outer sphere electron transfer, but was later extended to inner sphere electron transfer by Noel Hush. Besides the inner and outersphere applications, Marcus theory has been extended to address heterogeneous electron transfer. Rudolph Marcus received the Nobel Prize in Chemistry in 1992 for this theory. Marcus theory is used in various aspects of chemistry and biology, including photosynthesis, corrosion, certain types of chemiluminescence and more.

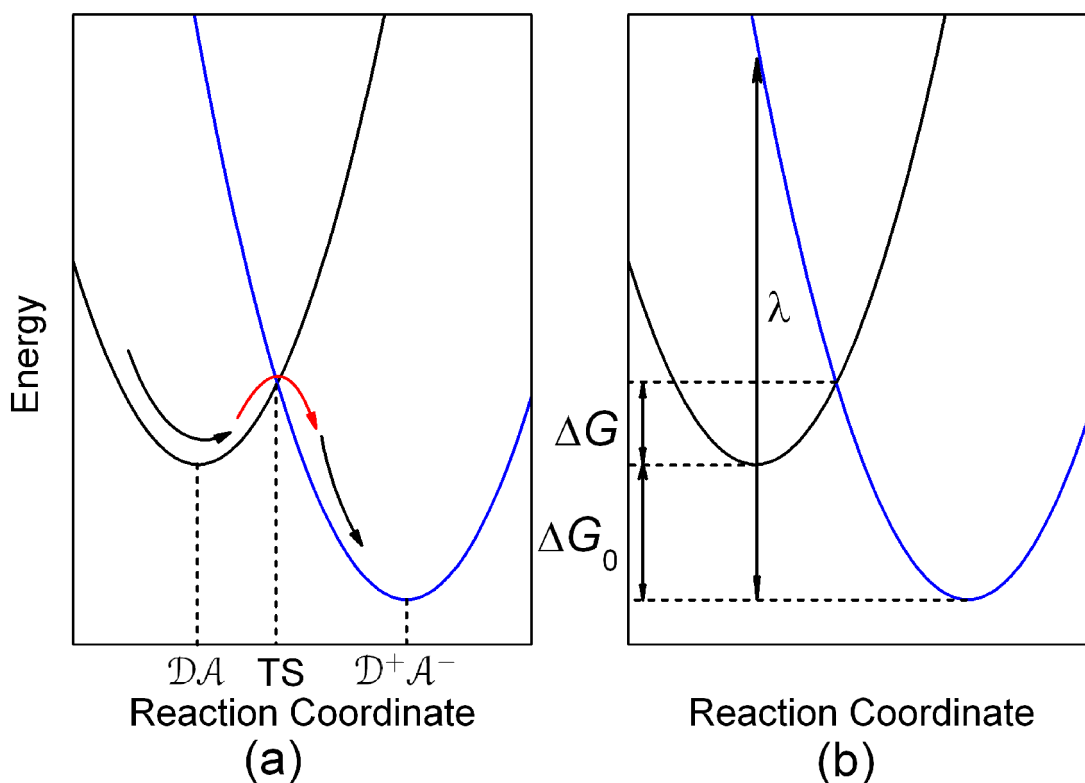


Figure 3.2: (a) Diabatic energy surfaces for the reactant  $\mathcal{D}\mathcal{A}$  and product  $\mathcal{D}^+\mathcal{A}^-$  state along the reaction coordinate. The crossing point of the two energy surfaces correspond to a transition state (TS). (b) Schematic representation of the energetics assumed in electron transfer theory from a donor  $\mathcal{D}$  to an acceptor  $\mathcal{A}$ . The energy,  $\lambda$ , required to reorganize nuclear coordinates upon electron transfer, the activation energy  $\Delta G$ , and the free energy of the reaction  $\Delta G_0$  are indicated.

180]:

$$k_{et} = \frac{2\pi}{\hbar} V_R^2 \text{FC}. \quad (3.55)$$

$V_R$  is the electronic coupling matrix element that is the weak perturbation of the system and FC is the Frank-Condon-weighted density of states. FC is the integrated overlap of reactant and product nuclear wavefunctions of equal energy. Returning to Marcus' classical description [153, 154, 181], FC can be expressed in terms of the probability of overcoming the activation barrier with thermal energy taken from the system. The activation energy is expressed in terms of the reorganization energy and the free energy of the reaction:

$$\text{FC} = \sqrt{\frac{1}{4\pi\lambda kT}} \exp\left(-\frac{\Delta G}{kT}\right), \quad (3.56)$$

where  $\Delta G$  corresponds to the free energy of activation for electron transfer (see Fig. 3.2b),  $k$  is the Boltzmann constant and  $T$  is the temperature.

From analytical geometry of intersecting parabolas, it follows that:

$$\Delta G = \frac{(\lambda + \Delta G_0)^2}{4\lambda}. \quad (3.57)$$

Substituting Eq. (3.57) in Eq. (3.56) one obtains:

$$\text{FC} = \sqrt{\frac{1}{4\pi\lambda kT}} \exp\left(-\frac{(\lambda + \Delta G_0)^2}{4\lambda kT}\right). \quad (3.58)$$

Substituting Eq. (3.58) into Eq. (3.55) one obtains the basic equation of Marcus theory:

$$k_{et} = \frac{2\pi}{\hbar} V_R^2 \sqrt{\frac{1}{4\pi\lambda kT}} \exp\left(-\frac{(\lambda + \Delta G_0)^2}{4\lambda kT}\right). \quad (3.59)$$

Eq. (3.59) indicates that for  $-\Delta G_0 < \lambda$ , an increase of  $-\Delta G_0$  leads to an increase in the electron transfer rate  $k_{et}$ . This is the normal regime (Fig. 3.3a). For  $-\Delta G_0 = \lambda$ ,  $k_{et}$  reaches its maximum (Fig. 3.3b). For  $-\Delta G_0 > \lambda$ , a further increase in  $-\Delta G_0$  causes the electron transfer rate  $k_{et}$  to decrease, hence the inverted regime is obtained (Fig. 3.3c). The effect of decreasing  $k_{et}$  in the inverted regime can be explained physically as follows: increasing the driving force  $-\Delta G_0$  to values larger than the reorganization energy,  $\lambda$ , leads to an increase of the free energy of activation  $\Delta G$ , i.e. barrier of the reaction. This has been verified experimentally for various systems [182, 183].

For the case where the bridge in a donor-bridge-acceptor system has no electronic levels in the vicinity of the relevant transition state, a simple exponential dependence between electron transfer rate and the distance is expected, following the exponential decay of the electronic wavefunctions in the forbidden region occupied by the bridge:

$$V_R^2 = V_0^2 \exp(-\beta R), \quad (3.60)$$

where  $R$  is the length of the bridge,  $\beta$  an exponential coefficient for the decay of the wavefunction, which is proportional to the square root of the barrier height, and  $V_0$

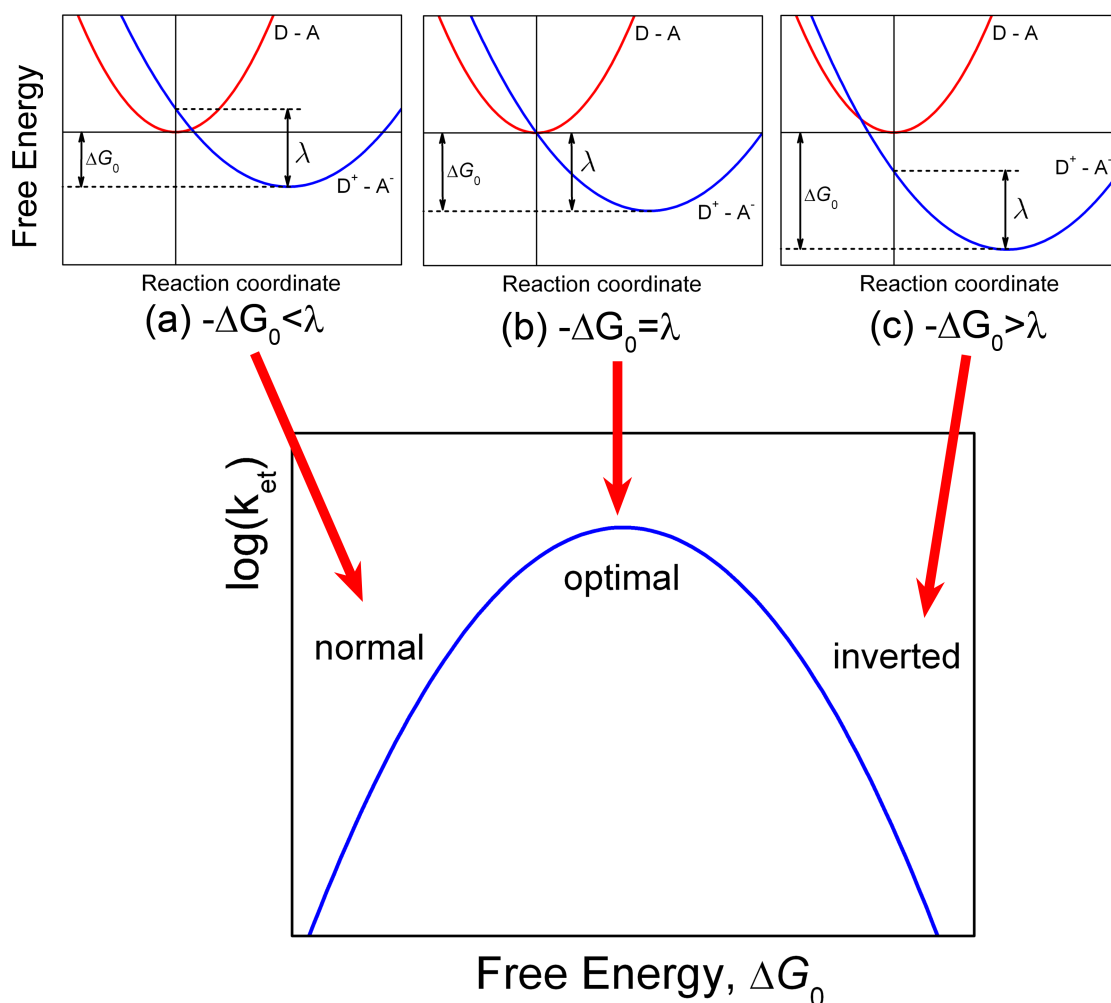


Figure 3.3: Schematic representation of the energetics assumed in electron transfer theory from a donor  $\mathcal{D}$  to an acceptor  $\mathcal{A}$  (top) and the corresponding dependence of the transfer rates on  $\Delta G_0$  (bottom). The energy,  $\lambda$ , required to reorganize nuclear coordinates upon electron transfer, and the driving force,  $\Delta G_0$ , for the electron transfer are indicated. The solvent coordinate describes schematically the effect of the protein degrees of freedom on the energy needed to transfer the electron in the process  $\mathcal{D} - \mathcal{A} \rightarrow \mathcal{D}^+ - \mathcal{A}^-$ . By increasing the free energy of reaction  $-\Delta G_0$ , the activation energy  $\Delta G$  decreases leading to an increase of the electron transfer rate (normal regime). If  $-\Delta G_0 > \lambda$ , increasing further  $-\Delta G_0$  leads to the increasing of  $\Delta G$  and consequently to the decreasing of the electron transfer rate (inverted regime).

the maximum electronic coupling. This exponential relation has been verified for various systems experimentally (see e.g. Refs. [184,185] and references therein).

Thus, the rate constant can be expressed as the product of two factors. The first factor is an electronic term arising from the strength of the coupling of the electron donor/acceptor wavefunctions, leading to a roughly exponential fall-off in the electron tunneling rate with distance through the insulating barrier and, accordingly, is proportional to  $\exp(-\beta R)$ , (see 3.60). The second factor depends on the energy,  $\lambda$ , required to repolarize the protein matrix upon electron transfer, and the driving force,  $\Delta G_0$ , for the electron transfer. These quantities are depicted in the Marcus diagram [153,186] shown in Fig. 3.3.

Electron tunneling between covalently bridged redox centers in synthetic systems ( $\beta \approx 0.9 \text{ \AA}^{-1}$ ) [187] is clearly much faster than tunneling through vacuum ( $\beta \approx 2.8 - 3.5 \text{ \AA}^{-1}$ ) [157,158]. Earlier experimental examination of tunneling in proteins suggested an intermediate value ( $\beta \approx 1.4 \text{ \AA}^{-1}$ ) corresponding to a weighted average of the two extreme  $\beta$  values [157,159]. A simple empirical expression that incorporates an exponential decay of the tunneling rate constant  $k$  (in  $s^{-1}$ ) with an edge-to-edge distance  $R$  (in  $\text{\AA}$ ) and a parabolic dependence of the rate on  $\Delta G_0$  and  $\lambda$  (in eV) is [188]

$$\log_{10} k_{et} = 15 - 0.6R - 3.1 \frac{(\Delta G_0 + \lambda)^2}{\lambda}. \quad (3.61)$$

The coefficient 0.6 corresponds to  $\beta = 1.4 \text{ \AA}^{-1}$  on a common log scale, whereas the coefficient 3.1 collects the room temperature constants for the quantized nuclear term [156], as suggested by extensive studies of photosynthetic reaction centers [157,160,189]. Equation (3.61) has proven to be a useful approximation for electron-transfer rate constants in the absence of a detailed protein structure; however, it neither explicitly addresses the variations in polypeptide structure, nor whether those variations have been naturally selected to influence tunneling rate constants to a physiological advantage.

### 3.1.8 Singlet – Triplet Interconversion Rate

In order to test the feasibility of the singlet-triplet interconversion required to facilitate a magnetic-field-dependent cryptochrome activation, it is necessary to estimate the characteristic time for this process. This time should be of the same order of magnitude (or shorter) than the time needed for forward electron transfer. In this subsection an estimate for the singlet-triplet interconversion<sup>2</sup> time is derived for a

model radical pair with one nucleus and two electrons. In this case the spin Hamiltonian, given by Eq. (3.4) with  $H_{\text{int}}$  neglected, is

$$\hat{H} = \mu_B(\vec{B} \cdot \hat{g}_A \cdot \vec{S}_A) + \mu_B(\vec{B} \cdot \hat{g}_B \cdot \vec{S}_B) + \mu_B(\vec{S}_A \cdot \hat{A} \cdot \vec{I}_D) \quad (3.62)$$

where  $\hat{g}_A$  and  $\hat{g}_B$  are the  $g$ -tensors of the electrons in radicals  $A$  and  $B$ , which comprise the radical pair;  $D$  denotes the spin-1/2 nuclei involved in hyperfine coupling to one of the electron spins.

To describe the spin motion one needs to choose the basis states of the wavefunction. For three spin-1/2 particles, eight basis states are required [168, 190], denoted as  $\psi_i$ ,  $i = 1, 2, \dots, 8$ . If the two electrons of the radical pair are found in the singlet state, then the corresponding basis states are

$$\psi_1 = \psi_S \alpha_D \quad (3.63)$$

$$\psi_2 = \psi_S \beta_D \quad (3.64)$$

where

$$\psi_S = \frac{1}{\sqrt{2}} (\alpha_A \beta_B - \beta_A \alpha_B). \quad (3.65)$$

$\alpha_i$  and  $\beta_i$  are the eigenfunctions of the operator  $S_{iz}$  with eigenvalues 1/2 and -1/2, respectively;  $\alpha_D$  and  $\beta_D$  denote the analogous states for the nuclear spin. The singlet state of a two - spin system is schematically shown in Fig. 3.4a.

Another six states are connected with the triplet states of the radical pair, and are denoted as  $\psi_{T_{+1}}$ ,  $\psi_{T_0}$  and  $\psi_{T_{-1}}$ :

$$\psi_{T_{+1}} = \alpha_A \alpha_B, \quad (3.66)$$

$$\psi_{T_0} = \frac{1}{\sqrt{2}} (\alpha_A \beta_B + \beta_A \alpha_B), \quad (3.67)$$

$$\psi_{T_{-1}} = \beta_A \beta_B. \quad (3.68)$$

The three triplet states are schematically shown in Fig. 3.4b-d with the use of vector model. If the radical pair is found in the triplet state, the total spin of the system can be 1/2 or 3/2. The basis states which describe the state of the system with total spin 1/2 are

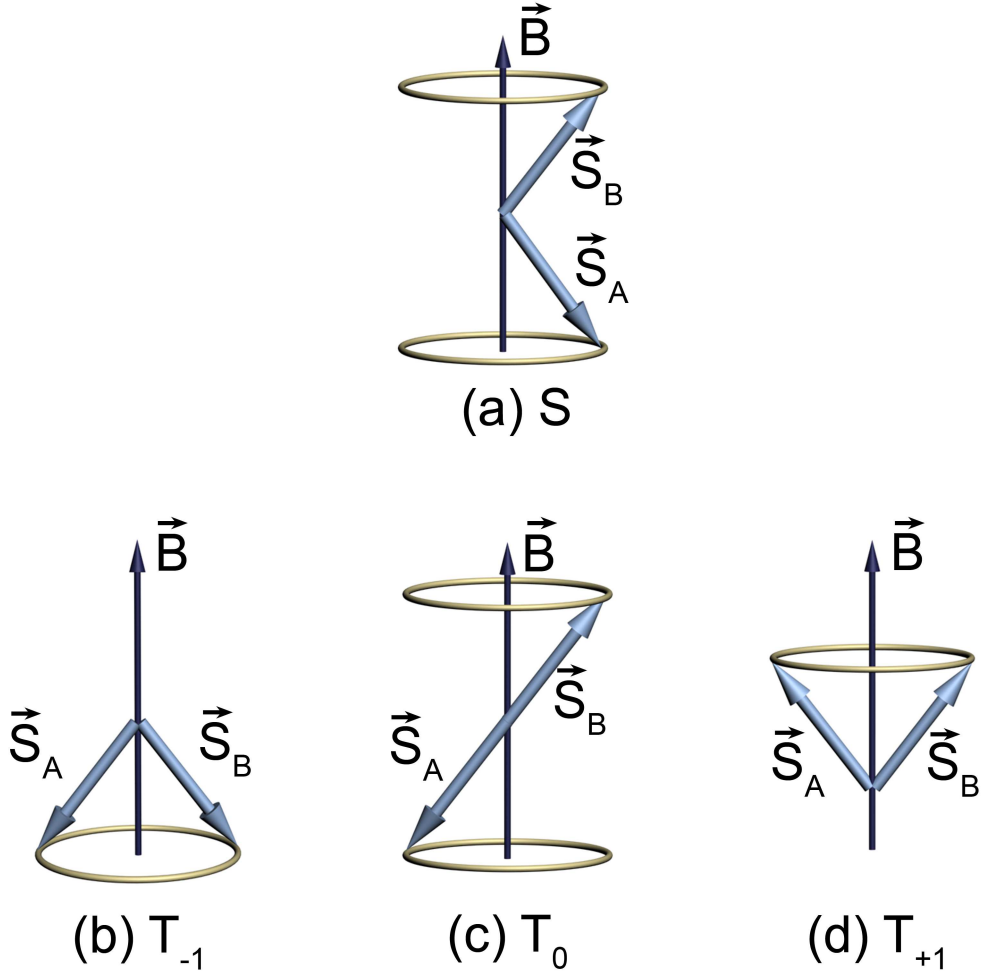


Figure 3.4: Vector model of the spin states of the radical pair. The two spins of the radical pair are denoted as  $\vec{S}_A$  and  $\vec{S}_B$ . The effective magnetic field vector, which includes the external magnetic field and the magnetic field created by the nucleus is denoted as  $\vec{B}$ . The three triplet states are denoted as  $T_{-1}$ ,  $T_0$  and  $T_{+1}$ , while the singlet state is denoted as  $S$ .

$$\psi_3 = \frac{1}{3} \left( \sqrt{2}\psi_{T_{+1}}\beta_D - \psi_{T_0}\alpha_D \right) \quad (3.69)$$

$$\psi_4 = \frac{1}{3} \left( \sqrt{2}\psi_{T_{-1}}\alpha_D - \psi_{T_0}\beta_D \right) \quad (3.70)$$

while the basis states which describe the four states of the system with total spin  $3/2$  are



$$\psi_5 = \psi_{T_{+1}}\alpha_D \quad (3.71)$$

$$\psi_6 = \frac{1}{3} \left( \psi_{T_{+1}}\beta_D + \sqrt{2}\psi_{T_0}\alpha_D \right) \quad (3.72)$$

$$\psi_7 = \frac{1}{3} \left( \psi_{T_{-1}}\alpha_D + \sqrt{2}\psi_{T_0}\beta_D \right) \quad (3.73)$$

$$\psi_8 = \psi_{T_{-1}}\beta_D. \quad (3.74)$$

One can now calculate, for example, the transition probability from a singlet state, e.g., the one described by wavefunction  $\psi_1$ , to a triplet state, e.g., the one described by wavefunction  $\psi_3$ . This transition is possible if the conditions

$$V_{1 \rightarrow 3} = \langle \psi_1 | \hat{H} | \psi_3 \rangle \neq 0 \quad (3.75)$$

$$|V_{1 \rightarrow 3}| \geq |E_1 - E_3| = |\Delta E| \quad (3.76)$$

are met, where  $E_1 = \langle \psi_1 | \hat{H} | \psi_1 \rangle$  and  $E_3 = \langle \psi_3 | \hat{H} | \psi_3 \rangle$  are the energy expectation values of the system in states corresponding to  $\psi_1$  and  $\psi_3$ , respectively. The matrix element for the  $\psi_1 \rightarrow \psi_3$  transition can be evaluated in terms of the parameters specifying the Hamiltonian (3.62). One obtains

$$V_{1 \rightarrow 3} = \frac{1}{2\sqrt{3}}\mu_B B_0(g_A - g_B) - \frac{1}{4\sqrt{3}}\mu_B A_{zz} \quad (3.77)$$

and the energies of states  $\psi_1$  and  $\psi_3$  calculated likewise are

$$E_1 = 0 \quad (3.78)$$

$$E_3 = \frac{1}{3}\mu_B B(g_A + g_B) - \frac{1}{6}\mu_B A_{zz}. \quad (3.79)$$

These expressions have been obtained under the assumption that the hyperfine coupling tensor,  $\hat{A}$  is anisotropic and has the form:

$$\hat{A} = \begin{pmatrix} 0 & 0 & 0 \\ 0 & 0 & 0 \\ 0 & 0 & A_{zz} \end{pmatrix}. \quad (3.80)$$

With  $g_A = g_B = 2$ ,  $A_{zz} = 16$  G,  $B_0 = 0.5$  G,  $\mu_B = 5.78843 \times 10^{-9}$  eV/G, one obtains  $V_{1 \rightarrow 3} = -2.674 \times 10^{-8}$  eV and  $E_3 = -1.158 \times 10^{-8}$  eV, and conditions (3.75) and (3.76) are satisfied.

If the system is initially in state  $\psi_1$ , then the probability to find it in state  $\psi_3$  at a later time  $t$  is

$$p(1 \rightarrow 3) = \frac{4V^2}{4V^2 + \Delta E^2} \sin^2 \left( \frac{(4V^2 + \Delta E^2)^{1/2} t}{2\hbar} \right) \quad (3.81)$$

as long as the other six states ( $\psi_2, \psi_4 - \psi_8$ ) are neglected. Thus, the radical pair oscillates from the singlet to the triplet state with a characteristic frequency of

$$\Omega = \frac{(4V^2 + \Delta E^2)^{1/2}}{\hbar}. \quad (3.82)$$

With the values above, one obtains  $\Omega \approx 8.3 \times 10^7 \text{ s}^{-1}$ , which is indeed of the same order of magnitude as the electron forward transfer rate constant,  $k_{\text{et}} = 1 \times 10^8 \text{ s}^{-1}$  – this will be discussed in chapter 4.

### 3.1.9 Cryptochrome Activation Yield

Once the density matrix has been obtained as a solution of the coupled stochastic Liouville equations (Eqs. (3.48)-(3.53)), observables of interest can be evaluated. The main quantity of interest is the activation yield of cryptochrome. This yield corresponds to the formation of the product  $\text{FADH} + \text{Trp324}_{\text{dep}}$  and depends on the strength and orientation of the magnetic induction (magnetic field), described through  $(B_0, \Theta, \Phi)$  and given by the expression

$$\Upsilon(B_0, \Theta, \Phi) = \int_0^\infty k_d \text{Tr}[\rho_3(t)] dt, \quad (3.83)$$

where  $k_d$  is the deprotonation rate constant (see Fig.2.10). In case the cryptochrome is oriented randomly relative to the external field, the total yield is averaged over  $\theta$  and  $\phi$ ,

$$\bar{\Upsilon}(B_0) = \frac{1}{4\pi} \int_0^{2\pi} d\Phi \int_0^\pi \sin \Theta d\Theta \Upsilon(B_0, \Theta, \Phi). \quad (3.84)$$

The magnetic field dependence of  $\Upsilon(B_0, \Theta, \Phi)$  and  $\bar{\Upsilon}(B_0)$  develops due to the electron back-transfer reaction  $\text{FADH} + \text{Trp}^+ \rightarrow \text{FADH}^+ + \text{Trp}$  (see Fig. 2.10) and, in particular, due to the reaction  $\text{FADH} + \text{Trp324}^+ \rightarrow \text{FADH}^+ + \text{Trp324}$ . This reaction is possible only in the singlet state of the  $\text{FADH} + \text{Trp324}^+$  radical pair and its yield is given by

$$\Upsilon^S(B_0, \Theta, \Phi) = \int_0^\infty k_b \text{Tr}[\hat{Q}^S \rho_3(t)] dt . \quad (3.85)$$

Here  $k_b$  is the electron back-transfer rate constant (see Fig.2.10). One can recognize that the activation yield of cryptochrome is determined by the function  $\text{Tr}[\hat{Q}^S \rho_3(t)]$ . Consequently,  $\text{Tr}[\hat{Q}^S \rho_3(t)]$  and its complement  $\text{Tr}[\hat{Q}^T \rho_3(t)]$  are referred to as the singlet and triplet state populations respectively.

## 3.2 Iron-Mineral Based Magnetoreceptor Model

This section discusses the formalism of the iron-mineral-based magnetoreceptor model. The motivation for this magnetoreception mechanism has been given in section 2.4.2. It was inspired by recent experimental findings of Fleissner *et al.*, who demonstrated the presence of small magnetic particles in the upper part of the beak of homing pigeons (*Columba livia*) [58–61, 112] and later, in several other birds species [125]. With the use of different light and electron microscopic methods combined with X-Ray analysis, Fleissner *et al.* concluded that there are two different types of iron compounds in the beak. These compounds were later identified using micro-synchrotron X-ray-absorption-near-edge-structure-spectroscopy as two ferrimagnetic materials: magnetite ( $\text{Fe}_3\text{O}_4$ ) and maghemite ( $\gamma\text{-Fe}_2\text{O}_3$ ) [59–61]. It has been shown that magnetite forms micro clusters, attached to the cell membrane, while maghemite crystals have a platelet-like structure arranged in chains inside the dendrite.

### 3.2.1 Magnetic Properties of the Iron-Minerals

#### Magnetic Properties of Magnetite

Magnetite has the structural formula  $\text{Fe}^{3+}(\text{Fe}^{2+}\text{Fe}^{3+})\text{O}_4$  and is the most important magnetic mineral on Earth. <sup>4</sup> Crystallographically, it is a cubic mineral with inverse spinel structure, and ferrimagnetic properties. The unit cell has eight tetrahedral sites (i.e. Fe ion is surrounded by four oxygens) filled with  $\text{Fe}^{3+}$  cations and sixteen

<sup>4</sup>Magnetite is the most magnetic of all the naturally occurring minerals on Earth, and its magnetic properties led to lodestone being used as an early form of magnetic compass. Magnetite typically carries the dominant magnetic signature in rocks, and so it has been a critical tool in paleomagnetism, a science important in discovering and understanding plate tectonics. The relationships between magnetite and other iron-rich oxide minerals such as ilmenite, hematite, and ulvospinel have been much studied, as the complicated reactions between these minerals and oxygen influence how and when magnetite preserves records of the Earth's magnetic field.

octahedral sites (i.e. Fe ion is surrounded by six oxygens), half of which are filled with  $\text{Fe}^{2+}$  cations and the other half with  $\text{Fe}^{3+}$  cations. The unit cell of magnetite is schematically shown in Fig. 3.5a, while Fig. 3.5b illustrates its central part. In crystallography one can distinguish between the so-called A-sites and B-sites (A-sublattice and B-sublattice), where A-site denote the tetrahedral position of the atoms, and B-site denotes the octahedral position of the atoms.

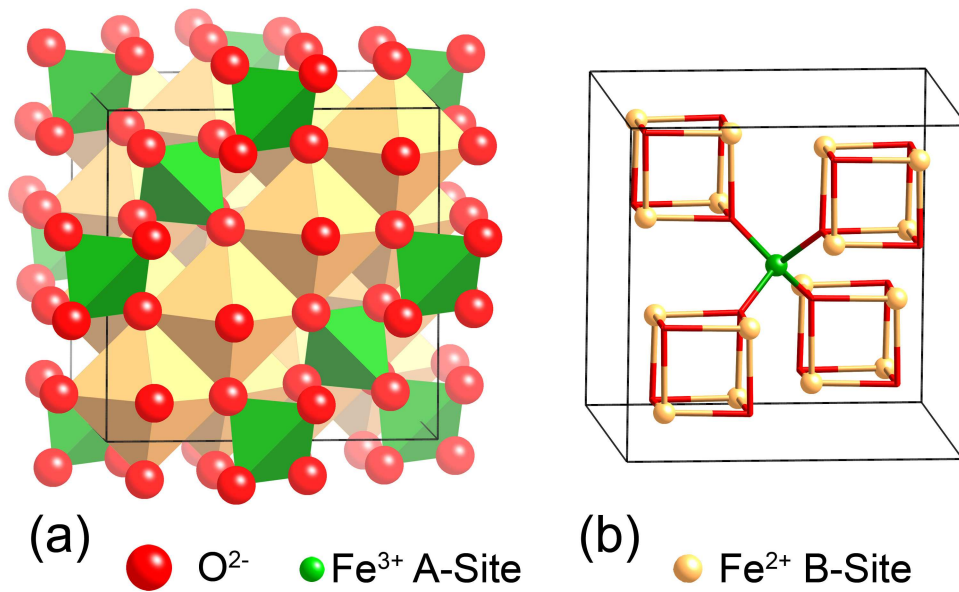


Figure 3.5: Structure of elementary unit cell of magnetite,  $\text{Fe}_3\text{O}_4$  (a) and a schematic illustration of its characteristic central part (b) showing the spatial location of ions in the unit cell. Plot (b) shows the difference between the structure of magnetite and maghemite, whose unit cell is shown in Fig. 3.8. A-sites represent the tetrahedral sites and B-site represent the octahedral sites in the unit cell. Crystal structure data for magnetite was obtained from [66,68,191,192].

**Saturation magnetization** ( $M_s$ ), is a fundamental property of a ferromagnetic and ferrimagnetic materials and is independent of particle size. For magnetite at room temperature,  $M_s \sim 480 \text{ emu/cm}^3$ .  $M_s$  is a function of temperature and pressure. The maximum value of  $M_s$  occurs at  $0^\circ \text{ K}$ . As the sample is heated, the observed magnetization decreases and goes to zero at the Curie point ( $T_c$ ), when the thermal energy ( $kT_c$ , where  $k$  is Boltzmann constant) equals the ferrimagnetic coupling energy. The dependence of the saturation magnetization on temperature measured for magnetite is shown in Fig. 3.6.  $T_c$  is another intrinsic parameter of a

ferrimagnetic material and in the case of magnetite  $T_c \sim 850^\circ$  K. The dependence of  $M_s$  on temperature is a diagnostic property for identifying minerals, since each ferrimagnetic material has a different Curie temperature.

The **magnetic susceptibility** of a material,  $\chi$ , indicates how a material responds to an applied magnetic field, and is defined as the ratio of the magnetization of the material,  $M$ , and the applied magnetic field,  $H$ :

$$\chi = \frac{|\vec{M}|}{|\vec{H}|}. \quad (3.86)$$

The magnetization of a material,  $M$ , is defined as the magnetic moment per unit volume or per unit mass of a material. It is dependent on the individual magnetic dipole moments of its constituent atoms and on the interactions of these dipoles with each other.

Above the Curie temperature there will be a change in the susceptibility as the material becomes paramagnetic, given with the equation:

$$\chi = \frac{C}{T - T_c} = \frac{M}{H}, \quad (3.87)$$

where  $C$  describes the Curie-constant. Equation (3.87) is the Curie-Weiss law [193–195] that describes the ferro – ferrimagnetic  $\leftrightarrow$  paramagnetic phase transition.

**Ferromagnetism** is the "normal" form of magnetism which most people are familiar with, as exhibited in horseshoe magnets and refrigerator magnets, for instance. It is responsible for most of the magnetic behavior encountered in everyday life. The materials in which the spins of electrons align in a regular pattern with neighboring spins pointing in opposite directions are referred as the **antiferromagnetic materials**. Generally, antiferromagnetic materials exhibit antiferromagnetism at a low temperature, and become disordered above a certain temperature; the transition temperature is called the Neel temperature. Above the Neel temperature, the material is typically paramagnetic. A **ferrimagnetic** material is one in which the magnetic moment of the atoms on different sublattices are opposed, as in antiferromagnetism; however, in ferrimagnetic materials, the opposing moments are unequal and a spontaneous magnetization remains. This happens when the sublattices consist of different materials or ions (such as  $\text{Fe}^{2+}$  and  $\text{Fe}^{3+}$ ). **Paramagnetism** is a form of magnetism which occurs only in the presence of an externally applied magnetic field. Paramagnetic materials are attracted to magnetic fields, hence have a relative magnetic permeability greater than one (or, equivalently, a positive magnetic

susceptibility). However, unlike ferromagnets which are also attracted to magnetic fields, paramagnets do not retain any magnetization in the absence of an externally applied magnetic field.

Figure 3.6 shows that the saturation magnetization of magnetite decreases with increasing temperature until it falls to zero at  $T_c$  indicating the point where the material becomes paramagnetic.

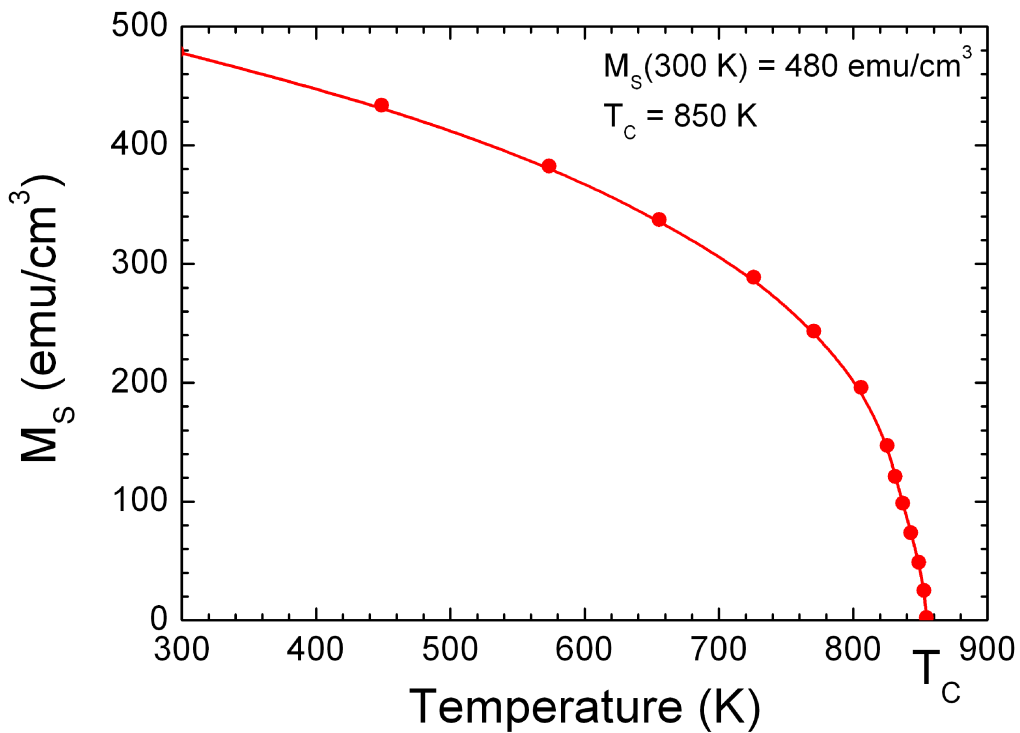


Figure 3.6: Saturation magnetization of magnetite,  $M_s$ , as a function of temperature. The figure has been drawn according to the data presented in Ref. [196]. The saturation magnetization of magnetite at 300 K and the Curie temperature are indicated.

At a temperature ( $T_v$ ) of  $\sim 120^\circ \text{ K}$ , magnetite undergoes an ordered arrangement of  $\text{Fe}^{2+}$  and  $\text{Fe}^{3+}$  ions on the octahedral sublattice, resulting in a slight distortion of the unit cell from a cubic to a **monoclinic** or a **triclinic** structure [197]. At this transition – referred to as the **Verwey transition** after the pioneering work of its discoverer [198] – the electrical conductivity of magnetite drops sharply by a factor of 100, due to a reduction of electron mobility on the B-sublattice [199]. Above  $T_v$ , electrons from the 3d shells move or "hop" between the  $\text{Fe}^{3+}$  and  $\text{Fe}^{2+}$  cations

on the B-sublattice, and magnetite behaves as a moderate electric conductor. This crystallographic transition also affects the saturation magnetization, and is often used to identify magnetite in bulk samples [200].

When studying biogenic magnetite, it is important to establish the size of the particles synthesized by the organism. The main subdivisions, **multi-domain** (MD), **pseudo-single-domain** (PSD), magnetically stable **single-domain** (SD), and **superparamagnetic** (SP), are determined by the number of magnetic domains contained within the particle (the domain state). The domain state determines the magnetic properties which will, in turn, be selected according to physiological requirements and the role the magnetite particles play in the organism. Magnetic domains (they are also sometimes referred as the Weiss domains) are regions within a magnetic particle where the direction of spontaneous magnetization is uniform, although different domains within a single particle may have different directions. Consequently, a MD particle can have zero remanence if the magnetization directions cancel each other on the other hand a magnetically stable SD is always magnetized to saturation and shows a remanent magnetization at room temperature. Finally, due to their small volume, SP particles lose their remanence in time spans of seconds to nano-seconds, and can be considered, for practical reasons, to acquire only an induced magnetization in the presence of a magnetic field [201].

Some magnetic parameters, such as the saturation magnetization,  $M_s$ , remanent magnetization,  $M_r$ , coercive force,  $H_c$  and coercivity of remanence,  $H_r$  are characteristic for every magnetic mineral. The coercivity of remanence is the reverse field which, when applied and then removed, reduces the saturation remanence to zero. It is always larger than the coercive force. The ratios ( $M_r/M_s$  and  $H_r/H_c$ ) serve to define domain states, although the limits between SD, PSD and MD behavior are not well defined, and often the interpretation of these parameters is not straightforward. The parameters  $M_s$ ,  $M_r$ ,  $H_c$  and  $H_r$  are shown in Fig. 3.7, where a typical magnetization pattern of magnetite is shown. The magnetization of ferrimagnetic material (i.e magnetite and maghemite) has a **hysteresis shape** if considered as a function of an external magnetic field or magnetic induction [202, 203].

For the case of uniaxial SD crystals of magnetite, the theoretical values of the remanence ratio and the coercivity ratio are  $M_r/M_s \sim 0.5$  and  $H_r/H_c \sim 1.0$ , respectively [204]. For SD magnetite, these ratios are essentially temperature invariant, except in the blocking range just below  $T_c$ , where  $M_r/M_s$  falls and  $H_r/H_c$  rises steeply [205]. In the case of MD particles,  $M_r/M_s \leq 0.05$  and  $H_r/H_c \geq 4$  [206].

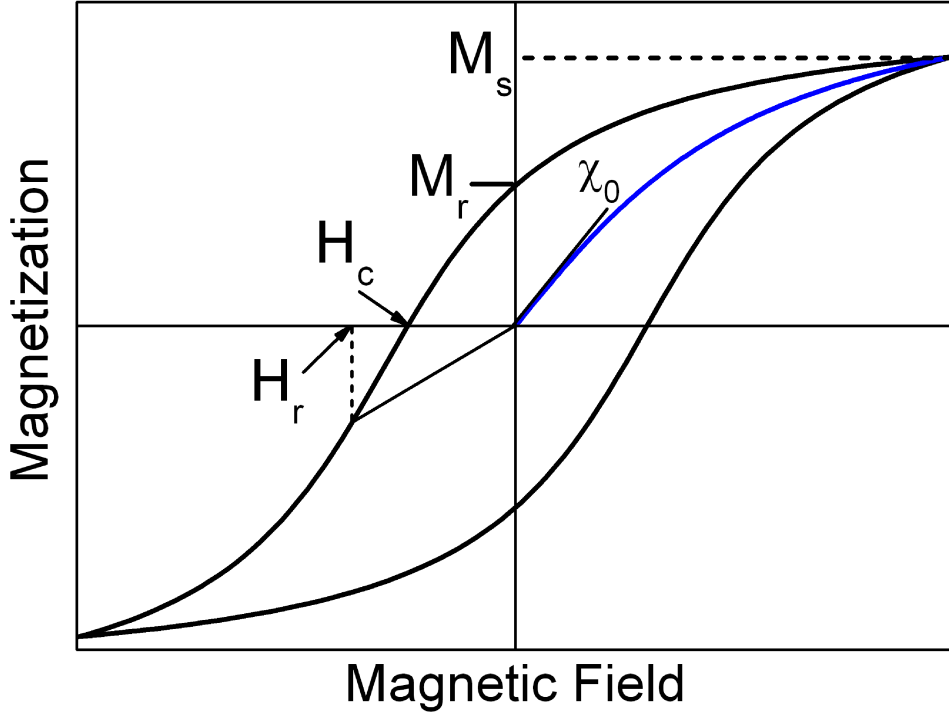


Figure 3.7: Hysteresis profile of magnetization of a ferrimagnet. The remanent magnetization  $M_r$ , saturation magnetization  $M_s$ , coercive force  $H_c$ , coercivity of remanence  $H_r$  and the low field magnetic susceptibility  $\chi_0$  are indicated.

By definition, SP particles have both  $M_r$  and  $H_r = 0$ . However, due to particle interactions or small mixtures of SP and SD particles, finite, albeit low, values for  $M_r$  and  $H_r$  [201, 207, 208] are often given.

The ratios  $M_r/\chi_0$  and  $\chi_0/M_s$  (where  $\chi_0$  is the low field magnetic susceptibility) are also useful in distinguishing SP from non-SP behavior. In SD and MD particles of magnetite,  $M_s/\chi_0$  will vary from  $\sim 2$  to 70 mT, whereas for SP particles  $M_s/\chi_0 < 0.01$  mT [209]. Table 3.1 shows characteristic values and behavior for some magnetic parameters for the different domain states of magnetite particles.

A useful technique in determining the domain state of the magnetite particles is the low-temperature measurement of coercivity, remanence, and low field susceptibility ( $\chi_0$ ). The susceptibility of MD particles is practically invariant between  $T_c$  and  $T_v$  [210]; however near  $T_v$ ,  $\chi_0$  increases and produces a characteristic peak. Elongated SD particles show a slight decrease of  $\chi_0$  with temperature and the peak at 120 K is suppressed. SP particles have the most drastic change in susceptibility



Parameter	SP	SD	MD
$M_r/M_s$	$\ll 0.01$	$\sim 0.5$	$\leq 0.05$
$H_r/H_c$	$\gg 10$	$\sim 1.5$	$\geq 4$
$M_r/\chi_0$	$< 0.01$ mT	2-70 mT	2-70 mT
$\chi_0/M_s$	$> 7 \cdot 10^{-4}$ mT $^{-1}$	$\sim 7 \cdot 10^{-4}$ mT $^{-1}$	$\sim 7 \cdot 10^{-4}$ mT $^{-1}$
$\chi_0(T)$	large increase	small decrease	peak at $\sim 118$ K
$H_c(T)$	large increase	small decrease	peak at decrease 118 K
$M_r(T)$	large increase	small decrease	peak at decrease 118 K

Table 3.1: Characteristic values and behavior for some magnetic parameters for magnetite depending on the domain state. The data taken from Ref. [201].

with temperature. Between 300 K and 4 K,  $\chi_0$  can vary by as much as a factor of 200 [201].

SP grains of magnetite are also characterized by a steep increase of  $M_r$  and  $H_c$  when cooling from 30 K to 5 K. In this temperature range, SP particles behave as stable single domains and are able to acquire relatively large remanences. In contrast, in SD and MD grains,  $M_r$  and  $H_c$  do not display significant variations as temperature decreases. For MD magnetite, as it cools through  $T_v$ , both  $M_r$  and  $H_c$  decrease. In SD particles controlled by shape anisotropy or interacting strongly, both  $M_r$  and  $H_c$  show slight increases associated with the increase in  $M_s$ .

Despite these well established rock magnetic properties, the identification and characterization of biogenic magnetite in natural samples is often a challenging enterprise. The volume concentration of biogenic magnetite particles in natural environments is typically very low, often at the threshold of the instruments, and many instruments used in rock magnetism fail to detect biogenic magnetite particles in the samples. However, during the last years, a number of papers have been devoted to study magnetite of biogenic origin [23, 25, 27, 40, 47, 58, 63, 69, 112] and a variety of different magnetic parameters have been reported (see papers cited above). The differences between those parameters are not discussed in the thesis, though characteristic values for the given particle sizes are used.

### Magnetic Properties of Maghemite

Maghemite ( $\text{Fe}_2\text{O}_3$ ,  $\gamma\text{-Fe}_2\text{O}_3$ ) can be considered as a Fe(II)-deficient magnetite with formula  $(\text{Fe}_8^{\text{III}})_A[\text{Fe}_{40/3}^{\text{III}}\square_{8/3}]_B\text{O}_{32}$  where  $\square$  represents a vacancy,  $A$  indicates tetrahedral positioning and  $B$  octahedral [211]. The structure of the unit cell of maghemite is shown in Fig. 3.8a, while Fig. 3.8b illustrates its central part. Plot (b) in Fig. 3.8

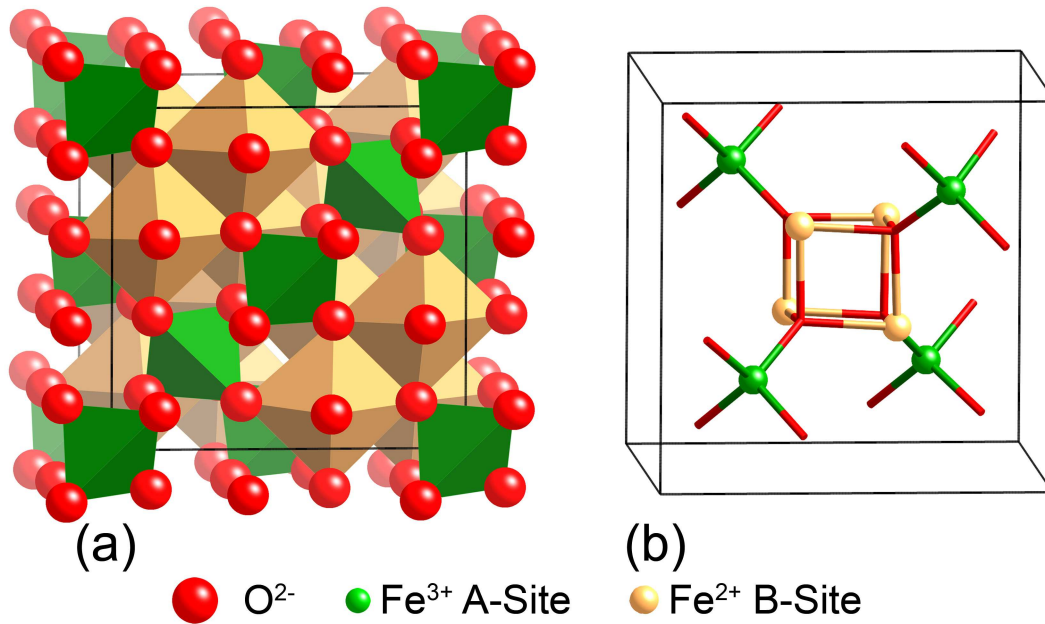


Figure 3.8: Structure of elementary unit cell of maghemite,  $\gamma\text{-Fe}_2\text{O}_3$  (a) and a schematic illustration of its characteristic central part (b) showing the spatial location of ions in the unit cell. A-sites represent the tetrahedral sites and B-site represent the octahedral sites in the unit cell. Crystal structure data for magnetite was obtained from [65–68].

shows the difference between the structure of magnetite and maghemite (compare Fig. 3.5b and Fig. 3.8b).

The magnetic properties of maghemite are similar to the magnetic properties of magnetite since maghemite also belongs to the inverse spinel group, and possesses ferrimagnetic properties.

Crystalline maghemite has a slightly lower value of the saturation magnetization than crystalline magnetite:  $M_s^{maghm} \approx 380 \text{ emu/cm}^3$ , while the saturation magnetization for bulk magnetite  $M_s^{magn} \approx 480 \text{ emu/cm}^3$  [63, 202, 203]. The Curie temperature for maghemite is  $T_c^{maghm} \approx 863 - 948 \text{ K}$  [63], slightly higher than the corresponding value for magnetite.

### 3.2.2 Magnetic Moment of the Maghemite Platelet

Magnetic properties of a ferrimagnetic material vary with size and shape of the particle [43, 46, 47]. In the problem considered here the size of a single maghemite platelet is  $1 \times 0.1 \times 1 \mu\text{m}$  (see discussion in section 2.4.2) which is sufficient for

the formation of a multi-domain structure in the (xz)-plane [43] (see Fig. 2.14). Since maghemite is a ferrimagnetic mineral, the maghemite platelets have a non-zero magnetic moment in this plane even in the absence of an external magnetic field. The magnetic moment of a platelet with index  $i$ ,  $\vec{m}_i$ , is proportional to its volume and, therefore is given by

$$\vec{m}_i = \vec{M}_i V_i = \vec{M}_i l_x l_y l_z, \quad (3.88)$$

where  $\vec{M}_i$  is the volume magnetization of the  $i$ -th platelet,  $V_i$  is its volume and  $l_x$ ,  $l_y$  and  $l_z$  are its dimensions along the x-, y- and z-axes respectively. Since all maghemite platelets are assumed to have identical volume then:

$$V_i = l_x l_y l_z \equiv v. \quad (3.89)$$

The direction of the magnetic moment of a platelet is governed by the projection of the total magnetic field on the (xz)-plane. The total magnetic field at the site of the platelet with index  $i$ ,  $\vec{\mathcal{H}}_i$ , is the sum of the external magnetic field, the magnetic field created by other platelets and by the magnetic field created by the magnetite cluster. Thus, the magnetic moment of a platelet is given by:

$$\vec{m}_i = Mv \frac{1}{\sqrt{\mathcal{H}_{i_x}^2 + \mathcal{H}_{i_z}^2}} (\mathcal{H}_{i_x}, 0, \mathcal{H}_{i_z}), \quad (3.90)$$

The expression for the magnetic field strength is discussed in detail in subsection 3.2.4.

### 3.2.3 Magnetic Moment of the Magnetite Cluster

The magnetite cluster consists of magnetite nanomagnets, which are about 5 nm in diameter [46, 47, 60]. Hence the magnetic properties of the cluster are significantly different from the magnetic properties of bulk magnetite. The nanomagnets behave like dipoles which can rotate freely inside the cluster. Thus the **magnetite cluster** behaves like a **superparamagnet**, i.e. if it is subject to an external magnetic field, then the nanomagnets try to align in the direction of the field, so that the potential energy of each nanomagnet is minimal. In this case all magnetic moments of the nanomagnets add to a total magnetic moment  $\vec{\mathcal{M}}$  of the cluster. On the other hand, at a given temperature the statistical motion of the nanomagnets counteracts the alignment. In the limit of a very high temperature, therefore, all nanomagnets are

statistically distributed, and their magnetic moments cancel each other, so that the total moment  $\vec{\mathcal{M}}$  vanishes. In the case of a finite temperature and a finite magnetic field, the mean total moment  $\langle \vec{\mathcal{M}} \rangle$  is somewhere between these two extreme cases.

In the latest transmission electron view of the nanomagnets inside the magnetite cluster [125], it has been demonstrated that the nanomagnets often assemble in short chains of about 5-10 elements. In the present thesis this fact is neglected and therefore a lower estimate for the magnetic moment of the magnetite cluster is obtained. The fact that the nanomagnets form chains inside the cluster will enhance the magnetic properties of the cluster leading to an increase of its magnetic moment.

As a model of a superparamagnetic cluster a system of  $n$  freely revolvable nanomagnets is considered and their translational motion is neglected. The total number of nanomagnets within a cluster can be estimated from the following relation:

$$n \sim \frac{V_{cluster}}{V_{nanomagnet}} = \frac{R_0^3}{r_0^3}, \quad (3.91)$$

where  $V_{cluster}$  and  $V_{nanomagnet}$  are the volumes of the cluster and the nanomagnet respectively,  $R_0$  and  $r_0$  are their radii. With  $R_0 = 0.5 \mu\text{m}$  and  $r_0 = 2.5 \text{ nm}$  one obtains  $n \approx 8 \cdot 10^6$ .

To calculate the mean total moment of the magnetite cluster one needs to calculate the partition function of a system with energy

$$E = - \sum_{i=1}^n \vec{\mu}_i \cdot \vec{H}, \quad (3.92)$$

where  $\vec{\mu}_i$  is the magnetic moment of the  $i$ -th nanomagnet and  $\vec{H}$  is the magnetic field strength. Assuming that the magnetic field at the site of the cluster is homogeneous, equal to  $\vec{H}$ , and all nanomagnets have magnetic moments of equal magnitude,  $\mu$ , the magnetic moment of the cluster can be estimated. Let us introduce a coordinate system associated with the field vector  $\vec{H}$ . It will be denoted as  $(x_1, y_1, z_1)$  and the field vector  $\vec{H}$  points in the  $z_1$ -direction. The orientation of each dipole can, then be expressed by the polar angles  $\theta_i$  and  $\varphi_i$ .

Each microstate of the system corresponds to a set  $\{\theta_i; \varphi_i\}$  of orientations of all dipoles. The partition function over all microstates depends on the temperature of the system  $T$ , magnetic field strength  $H$  and the number of nanomagnets  $n$ :

$$Z(T, H, n) = \int d\Omega_1 \int d\Omega_2 \dots \int d\Omega_n \exp \left( \frac{\mu H}{kT} \sum_{i=1}^n \cos \theta_i \right), \quad (3.93)$$

where  $k$  is the Boltzmann factor, and  $d\Omega_i = \sin\theta_i d\theta_i d\phi_i$ . The integrals  $\int d\Omega_i$  extend over all spatial angles. The partition function factors, since the individual nanomagnets are assumed non-interacting, and therefore

$$Z(T, H, n) = [Z(T, H, 1)]^n, \quad (3.94)$$

where

$$Z(T, H, 1) = \int d\Omega \exp\left(\frac{\mu H}{kT} \cos\theta\right) = 4\pi \frac{kT}{\mu H} \sinh\left(\frac{\mu H}{kT}\right). \quad (3.95)$$

The probability for a nanomagnet to assume an orientation between  $\theta, \theta + d\theta$  and  $\varphi, \varphi + d\varphi$  is given by

$$\rho(\theta, \varphi) d\Omega = \frac{1}{Z(T, H, 1)} \exp\left(\frac{\mu H \cos\theta}{kT}\right) \sin\theta d\theta d\varphi. \quad (3.96)$$

With the aid of Eq. (3.96), the mean magnetic moment  $\langle \vec{\mu} \rangle$  of a nanomagnet can be calculated:

$$\langle \vec{\mu} \rangle = \frac{\mu}{Z(T, H, 1)} \int \vec{n} \cdot \exp\left(\frac{\mu H \cos\theta}{kT}\right) \sin\theta d\theta d\varphi, \quad (3.97)$$

where  $\vec{n} = (\sin\theta \cos\varphi, \sin\theta \sin\varphi, \cos\theta)$ . From Eq. (3.97) follows that  $\langle \mu_{x_1} \rangle = \langle \mu_{y_1} \rangle = 0$ . The reason is that all orientations of the nanomagnet perpendicular to the  $z_1$ -axis are equally probable. Thus

$$\langle \mu_{z_1} \rangle = \frac{\mu}{Z(T, H, 1)} \int \cos\theta \exp\left(\frac{\mu H \cos\theta}{kT}\right) \sin\theta d\theta d\varphi = \mu \left[ \coth\left(\frac{\mu H}{kT}\right) - \frac{kT}{\mu H} \right], \quad (3.98)$$

and the total mean dipole moment of the magnetite cluster in the  $z_1$ -direction becomes:

$$\langle \mathcal{M}_{z_1} \rangle = n \langle \mu_{z_1} \rangle = n\mu \left[ \coth\left(\frac{\mu H}{kT}\right) - \frac{kT}{\mu H} \right]. \quad (3.99)$$

If  $\mu H \ll kT$  the expression in the square brackets of (3.99) can be expanded, and the expression for the average total magnetic moment of the magnetite cluster is given by

$$\langle \vec{\mathcal{M}} \rangle \approx \frac{n\mu^2}{3kT} \vec{H}. \quad (3.100)$$

From Eq. (3.100) it is clear that the total magnetic moment of the magnetite cluster is proportional to the field strength. The proportionality constant is called the **magnetic susceptibility**, which was defined in Eq. (3.86) and reads as follows:

$$\chi = \frac{n\mu^2}{3kT}. \quad (3.101)$$

The magnetic moment of a nanomagnet reads as follows:

$$\mu = M_s^{mt} \frac{4}{3} \pi r_0^3, \quad (3.102)$$

where  $M_s^{mt}$  is the saturation magnetization of magnetite (see Fig. 3.7).

Dividing the magnetic susceptibility by the volume of the magnetite cluster one obtains the volume susceptibility of the cluster,  $\chi_v$ :

$$\chi_v = \frac{\chi}{\frac{4}{3}\pi R_0^3} = \frac{R_0^3}{r_0^3} \frac{(M_s^{mt} \frac{4}{3} \pi r_0^3)^2}{3kT \frac{4}{3} \pi R_0^3} = \frac{4\pi (M_s^{mt})^2 r_0^3}{9kT} \quad (3.103)$$

### 3.2.4 Model of Interacting Point-Like Dipoles

Let us now consider the potential energy of the magnetite cluster. In this section a model which neglects the size of the maghemite platelets and of the magnetite cluster is discussed. Within this model, the maghemite platelets and the magnetite clusters are treated as point-like dipoles.

The potential energy of the magnetite cluster reads

$$E(\vec{R}) = -\langle \vec{\mathcal{M}} \rangle \vec{H}(\vec{R}) = -\chi_v \frac{4}{3} \pi R_0^3 \left| \vec{H}(\vec{R}) \right|^2, \quad (3.104)$$

where  $\langle \vec{\mathcal{M}} \rangle$  is defined in Eq. (3.100) and  $\chi_v$  is defined in Eq. (3.103),  $\vec{R}$  describes the position of the magnetite cluster (see Fig. 2.14) and  $\vec{H}(\vec{R})$  is the magnetic field vector at the site of the cluster, which is given by

$$\vec{H}(\vec{R}) = \frac{\vec{B}}{\mu_{med}} + \sum_{j=1}^N \vec{H}_j(\vec{R}). \quad (3.105)$$

Here  $\vec{B}$  is the induction vector of the external magnetic field,  $\mu_{med} \approx 1$  is the permeability of the medium,  $N$  is the number of platelets,  $\vec{H}_j(\vec{R})$  is the magnetic field created by the  $j$ -th platelet at the site of the magnetite cluster, which is known to be [212, 213]

$$\vec{H}_j(\vec{R}) = \frac{3 \left( \vec{R} - \vec{r}_j \right) \left( \vec{m}_j \left( \vec{R} - \vec{r}_j \right) \right) - \vec{m}_j \left| \vec{R} - \vec{r}_j \right|^2}{\left| \vec{R} - \vec{r}_j \right|^5}. \quad (3.106)$$

Here  $\vec{r}_j$  describes the position of the  $j$ -th platelet and  $\vec{m}_j$  is its magnetic moment defined in Eq. (3.90). To calculate the magnetic moment of a platelet one needs to know the local magnetic field at its site. The local magnetic field at the site of the  $i$ -th platelet consists of three terms:

$$\vec{\mathcal{H}}_i = \frac{\vec{B}}{\mu_{med}} + \sum_{\substack{j=1 \\ j \neq i}}^N \vec{H}_j(\vec{r}_i) + \frac{3 \left( \vec{r}_i - \vec{R} \right) \left( \langle \vec{\mathcal{M}} \rangle \left( \vec{r}_i - \vec{R} \right) \right) - \langle \vec{\mathcal{M}} \rangle \left| \vec{r}_i - \vec{R} \right|^2}{\left| \vec{r}_i - \vec{R} \right|^5}. \quad (3.107)$$

The first term describes the external magnetic field, the second term describes the magnetic field created by all platelets except the  $i$ -th one and the third term describes the field created by the magnetite cluster. The third term in Eq. (3.107) can be neglected because  $\langle \mathcal{M} \rangle \ll m_i$  (the estimates in subsection 5.2 show that  $m_i \approx 3.121$  eV/G and  $\langle \mathcal{M} \rangle \approx 0.392$  eV/G).

It follows from Eq. (3.107) that the local magnetic field  $\vec{\mathcal{H}}_i$  is determined by the magnetic moments of the platelets. Thus Eqs. (3.90) and (3.107) have to be treated iteratively. In the zeroth-order of approximation all the  $\vec{m}_i$  are assumed to be aligned along the x-axis, which corresponds to the most energetically favorable configuration. The expression for the magnetic moment of a platelet is then given by

$$\vec{m}_i^{(0)} = Mv\vec{\mathbf{i}}, \quad (3.108)$$

where  $\vec{\mathbf{i}}$  is the basis vector of the x-axis. Substituting Eq. (3.108) into Eq. (3.107) one obtains the first-order approximation of the local magnetic field at the site of the  $i$ -th platelet:

$$\vec{\mathcal{H}}_i^{(1)} = \vec{B} + 2Mv\xi_i\vec{\mathbf{i}}, \quad (3.109)$$

where  $x_i$  is the x-coordinate of the  $i$ -th platelet and  $\xi_i = \sum 1/|x_i - x_j|^3$ . Substituting Eq. (3.109) into Eq. (3.90) one yields the first-order approximation for  $\vec{m}_i$ :

$$\vec{m}_i^{(1)} = \frac{Mv}{\sqrt{(B_x + 2Mv\xi_i)^2 + B_y^2 + B_z^2}} (B_x + 2Mv\xi_i, 0, B_z). \quad (3.110)$$

Here  $B_x$ ,  $B_y$  and  $B_z$  are the x-, y- and z-components of the external magnetic induction vector respectively. The iterative procedure should be continued until  $\vec{m}_i$  and  $\vec{\mathcal{H}}_i$  do not change more than a given threshold value. Then the potential energy  $E^{(w)}(\vec{R})$  of the magnetite cluster reads as:

$$E^{(w)}(\vec{R}) = -\chi_v \frac{4}{3} \pi R_0^3 \left| \vec{B} + \sum_{j=1}^N \frac{3 \left( \vec{R} - \vec{r}_j \right) \left( \vec{m}_j^{(w)} \left( \vec{R} - \vec{r}_j \right) \right) - \vec{m}_j^{(w)} \left| \vec{R} - \vec{r}_j \right|^2}{\left| \vec{R} - \vec{r}_j \right|^5} \right|^2, \quad (3.111)$$

where  $(w)$  is the approximation-order of the magnetic moment of a platelet. If  $w = 1$  then the expression for  $\vec{m}_j^{(w)}$  is given in Eq. (3.110). If  $w \neq 1$  then iterative treatment of Eqs. (3.90) and (3.107) has to be continued until the  $w$ -th order of approximation is obtained.

From Eq. (3.111) one can then calculate the force acting on the magnetite cluster according to

$$\vec{F} = -\nabla E(\vec{R}). \quad (3.112)$$

### 3.2.5 Model of Interacting Dipoles of Finite Size

In this subsection the finite size of the maghemite platelets and the magnetite cluster is accounted for. Both platelets and the cluster will be considered as bodies with homogeneous magnetic moments.

By splitting the platelets and the cluster into infinitesimal parts and integrating over their volumes, it is possible to calculate the interaction energy of a magnetite cluster with the platelets in an external field (see Fig. 3.9). The magnetic field created by an infinitesimal part of the maghemite platelet is given by

$$\vec{d}H_j(\vec{R}, \vec{r}_1, \vec{r}_2) = \frac{3(\vec{R} - \vec{r}_j + \vec{r}_1 - \vec{r}_2) \left( \vec{d}m_j^{(w)}(\vec{R} - \vec{r}_j + \vec{r}_1 - \vec{r}_2) \right)}{\left| \vec{R} - \vec{r}_j + \vec{r}_1 - \vec{r}_2 \right|^5} - \frac{\vec{d}m_j^{(w)}}{\left| \vec{R} - \vec{r}_j + \vec{r}_1 - \vec{r}_2 \right|^3}, \quad (3.113)$$

where  $\vec{r}_1$  is the vector from the center of the magnetite cluster to a point inside its volume,  $\vec{r}_2$  is the vector from the center of the platelet to a point inside its volume,



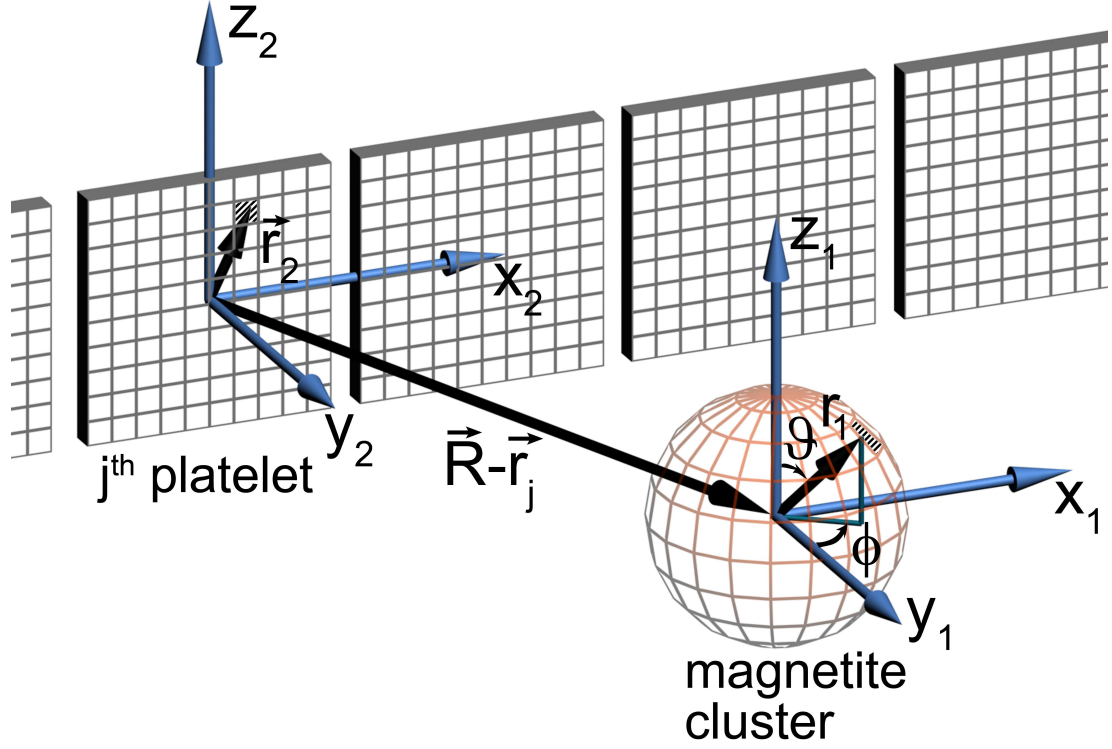


Figure 3.9: Illustration of the integration scheme used in the model of interacting dipoles of finite size. Coordinate frames used for the integration over the volume of the magnetite cluster  $(x_1, y_1, z_1)$  and over the maghemite platelets  $(x_2, y_2, z_2)$  are indicated. The splitting of the platelets and of the cluster into infinitesimal parts is schematically shown. The infinitesimal part inside the cluster is characterized by the vector  $\vec{r}_1 = (r_1 \sin \theta \sin \phi, r_1 \sin \theta \cos \phi, r_1 \cos \theta)$ , while the infinitesimal part inside a platelet is characterized by the vector  $\vec{r}_2 = (x_2, y_2, z_2)$ . The vector  $\vec{R} - \vec{r}_j$  connects the center of the  $j$ -th platelet with the center of the cluster.

$\vec{R} - \vec{r}_j$  is the vector from the center of the  $j$ -th platelet to the center of the cluster (see Fig. 3.9), and  $\vec{d}m_j^{(w)}$  is

$$\vec{d}m_j^{(w)} = \frac{M l_y dx_2 dz_2}{|\vec{\mathcal{H}}_j^{(w)}|} \left( \mathcal{H}_{j_x}^{(w)}, 0, \mathcal{H}_{j_z}^{(w)} \right) = \vec{M}^{(w)} l_y dx_2 dz_2. \quad (3.114)$$

Substituting Eq. (3.114) into Eq. (3.113) and integrating over  $dx_2$  and  $dz_2$  one obtains the field created by a platelet:

$$\vec{H}_j(\vec{R}, \vec{r}_1) = \int_{-l_x/2}^{l_x/2} \int_{-l_z/2}^{l_z/2} \vec{d}H_j(\vec{R}, \vec{r}_1, \vec{r}_2) dx_2 dz_2. \quad (3.115)$$

The integration of Eq. (3.115) in its general form is not trivial. Therefore a reasonable simplification will be made which allows an analytical solution of (3.115):

$$l_x = l_z = l \quad (3.116)$$

$$\vec{M}^{(w)} = (M_x, 0, 0). \quad (3.117)$$

Assumption (3.117) will be discussed in the section 5.3 in more detail. With assumptions Eq. (3.116)-(3.117) the expression for the magnetic field components created by the platelet with index  $j$  at the point defined by the vector  $\vec{R} - \vec{r}_j + \vec{r}_1$  is given by

$$\begin{aligned} H_{j_x}(\vec{R}, \vec{r}_1) = & -\sqrt{2}M_x l_y \left( \frac{(l - 2s_x)(l + 2s_z)}{\left( (l - 2s_x)^2 + 4s_y^2 \right) \sqrt{l^2 - 2(s_x - s_z)l + 2s^2}} \right. \\ & + \frac{(l + 2s_x)(l - 2s_z)}{\left( (l + 2s_x)^2 + 4s_y^2 \right) \sqrt{l^2 + 2(s_x - s_z)l + 2s^2}} \\ & + \frac{(l - 2s_x)(l - 2s_z)}{\left( (l - 2s_x)^2 + 4s_y^2 \right) \sqrt{l^2 - 2(s_x + s_z)l + 2s^2}} \\ & \left. + \frac{(l + 2s_x)(l + 2s_z)}{\left( (l + 2s_x)^2 + 4s_y^2 \right) \sqrt{l^2 + 2(s_x + s_z)l + 2s^2}} \right) \quad (3.118) \end{aligned}$$

$$\begin{aligned} H_{j_y}(\vec{R}, \vec{r}_1) = & 2\sqrt{2}M_x l_y \left( \frac{s_y(l + 2s_z)}{\left( (l - 2s_x)^2 + 4s_y^2 \right) \sqrt{l^2 - 2(s_x - s_z)l + 2s^2}} \right. \\ & + \frac{s_y(2s_z - l)}{\left( (l + 2s_x)^2 + 4s_y^2 \right) \sqrt{l^2 + 2(s_x - s_z)l + 2s^2}} \\ & + \frac{s_y(l - 2s_z)}{\left( (l - 2s_x)^2 + 4s_y^2 \right) \sqrt{l^2 - 2(s_x + s_z)l + 2s^2}} \\ & \left. - \frac{s_y(l + 2s_z)}{\left( (l + 2s_x)^2 + 4s_y^2 \right) \sqrt{l^2 + 2(s_x + s_z)l + 2s^2}} \right) \quad (3.119) \end{aligned}$$

$$\begin{aligned} H_{j_z}(\vec{R}, \vec{r}_1) = & -\sqrt{2}M_x l_y \left( \frac{1}{\sqrt{l^2 - 2(s_x - s_z)l + 2s^2}} + \frac{1}{\sqrt{l^2 + 2(s_x - s_z)l + 2s^2}} \right. \\ & \left. - \frac{1}{\sqrt{l^2 - 2(s_x + s_z)l + 2s^2}} - \frac{1}{\sqrt{l^2 + 2(s_x + s_z)l + 2s^2}} \right), \quad (3.120) \end{aligned}$$

where  $s_x = x - x_j + x_1$ ,  $s_y = y - y_1$ ,  $s_z = z - z_1$  and  $s^2 = s_x^2 + s_y^2 + s_z^2$ . Thus, the potential energy of the magnetite cluster follows as:

$$E(\vec{R}, \vec{r}_1) = - \sum_{i=1}^n \langle \vec{\mu}(\vec{R}, \vec{r}_{1_i}) \rangle \left( \sum_{j=1}^N \vec{H}_j(\vec{R}, \vec{r}_{1_i}) + \vec{B} \right), \quad (3.121)$$

where  $i$  specifies a certain nanomagnet within the magnetite cluster. Here  $n$  denotes the total number of nanomagnets and  $\langle \vec{\mu}(\vec{R}, \vec{r}_{1_i}) \rangle$  is the average magnetic moment of the  $i$ -th nanomagnet defined by vectors  $\vec{R}$  and  $\vec{r}_{1_i}$  (see Fig. 3.9). The sum in Eq. (3.121) can then be replaced by an integration over the volume of the cluster:

$$E(\vec{R}) = - \frac{n}{4/3\pi R_0^3} \int_0^{2\pi} d\phi \int_0^\pi d\vartheta \int_0^{R_0} \langle \vec{\mu}(\vec{R}, \vec{r}_1) \rangle \left( \sum_{j=1}^N \vec{H}_j(\vec{R}, \vec{r}_1) + \vec{B} \right) r_1^2 \sin \vartheta dr_1, \quad (3.122)$$

where  $r_1$ ,  $\vartheta$  and  $\phi$  represent  $\vec{r}_1$  in spherical coordinates (see Fig. 3.9). The average magnetic moment of a nanomagnet is defined as (see Eq. (3.100)):

$$\langle \vec{\mu}(\vec{R}, \vec{r}_1) \rangle = \frac{\chi}{n} \left( \sum_{j=1}^N \vec{H}_j(\vec{R}, \vec{r}_1) + \vec{B} \right). \quad (3.123)$$

Substituting (3.123) into (3.122) yields:

$$E(\vec{R}) = -\chi_v \int_0^{2\pi} d\phi \int_0^\pi d\vartheta \int_0^{R_0} \left| \sum_{j=1}^N \vec{H}_j(\vec{R}, \vec{r}_1) + \vec{B} \right|^2 r_1^2 \sin \vartheta dr_1, \quad (3.124)$$

The force which acts on the cluster can then be calculated according to the general relation (3.112).

### 3.3 Summary

This chapter discusses the theoretical formalism behind the two magnetoreception mechanisms studied in the dissertation. The theory of the radical pair mechanism in cryptochrome was discussed in section 3.1, while the theory behind the iron-mineral-based magnetoreception model was discussed in section 3.2. Note, that the aim of this discussion was to present essential ideas of the methods and give the necessary references, rather than to describe them in all the details. The theory and

methods described in this chapter are used to study spin dynamics in cryptochrome, in chapter 4, and the iron-mineral-based magnetoreception mechanism in chapter 5.

# Chapter 4

## Magnetic Field Effect in Cryptochrome

### 4.1 Introduction

The theory and methods described in chapter 3, in section 3.1 were used to study spin dynamics in cryptochrome. In the present chapter, in section 4.2 of the current chapter, the choice of the hyperfine coupling constants in cryptochrome is explained. In subsection 4.3 the rate constants for various processes are estimated. In section 4.4 the magnetic field dependence of the formation of FADH stabilized by deprotonation of Trp324<sup>+</sup> to Trp324<sub>dep</sub>, averaged over the orientation of the magnetic field, is analyzed by means of the observable  $\bar{\Upsilon}(B_0)$  defined in Eq. (3.84). It is demonstrated that the suggested radical pair mechanism is consistent with a cryptochrome-mediated magnetic field response in *Arabidopsis thaliana*. The dependence of the activation yield  $\Upsilon(B_0, \Theta, \Phi)$ , defined in Eq. (3.83) on the orientation  $(\Theta, \Phi)$  of an external magnetic field is discussed in section 4.5 and it is shown that cryptochrome activation might serve as an inclination compass. Results on the time evolution of the singlet population  $\text{Tr}[\hat{Q}^S \rho_3(t)]$  are presented and discussed in detail in section 4.6.

### 4.2 Hyperfine Coupling

The cryptochrome activation yield is very sensitive to the hyperfine coupling tensors chosen for the FADH and tryptophan radicals. In order for the yield to acquire a dependence on the angle between the magnetic field vector and the radical pair axis, the hyperfine tensor of at least one radical must have significant anisotropy. One

of the improvements made in the model of the FADH-tryptophan radical pair is to use realistic hyperfine coupling tensors for the two radicals, rather than to rely on an order-of-magnitude guess as was done in [1]. Information regarding the hyperfine tensors of nuclei in FADH and tryptophan in photolyase and other molecules has been published [214–216]. The hyperfine tensors for FADH and tryptophan in cryptochrome are assumed to be similar to those exhibited by related systems. Indeed, the possibility for magnetic field effects in photolyase have previously been examined using similar hyperfine tensors [35]. The model discussed in the present thesis differs from those previously considered in that it allows for a more complex reaction mechanism in which electron transfer and back-transfer rate constants are considered.

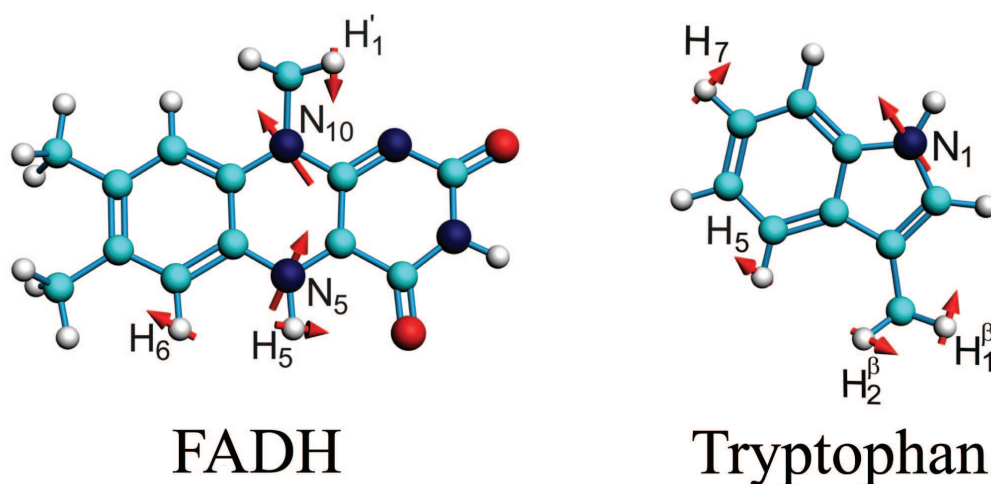


Figure 4.1: FADH and tryptophan shown with those of their nuclei involved in the strongest hyperfine coupling. The numbering of the nuclei in each radical is chosen to be consistent with [35, 214, 215], which is governed by the rules of standard chemical nomenclature.  $\beta$  indicates the  $\beta$ -protons.

The hyperfine coupling constants and principal hyperfine axes used in the calculation are presented in Table 4.1. Because of the computational cost of calculating the activation yield for systems with a high-dimensional Hamiltonian, only up to four nuclei were included in each of the considered models of the FADH-tryptophan radical pair. Several combinations of nuclei in each radical were considered, and the activation yield for each configuration was calculated. However, the dependence of the activation yield on the magnetic field is sensitive to the choice of nuclei and

associated hyperfine coupling constants. Fig. 4.1 shows the labeling used for the nuclei in FADH and tryptophan.  $\beta$  indices indicate the  $\beta$ -protons.<sup>1</sup>

Hyperfine Constants and Axes Chosen for FADH					
Nucleus	$a_{iso}$ (G)	$T_{ii}$ (G)	Hyperfine Axes		
N <sub>5</sub>	3.93	-4.98	0.4380	0.8655	-0.2432
		-4.92	0.8981	-0.4097	0.1595
		0, 9.89*	-0.0384	0.2883	0.9568
H <sub>5</sub>	-7.69	-6.16	0.9819	0.1883	-0.0203
		-1.68	-0.0348	0.2850	0.9579
		7.84	-0.1861	0.9398	-0.2864
Hyperfine Constants and Axes Chosen for Tryptophan					
Nucleus	$a_{iso}$ (G)	$T_{ii}$ (G)	Hyperfine Axes		
H <sub>1</sub> <sup><math>\beta</math></sup>	16	0.00	1.000	0.000	0.000
		0.00	0.000	1.000	0.000
		0.00	0.000	0.000	1.000
H <sub>5</sub>	5	0.00	1.000	0.000	0.000
		0.00	0.000	1.000	0.000
		0.00	0.000	0.000	1.000

Table 4.1: Hyperfine tensors of nuclei in FADH and tryptophan. Information on the hyperfine tensors in photolyase and other molecules has been published previously [214–216]. The hyperfine coupling constants were determined using the ESR and ENDOR spectroscopy techniques. The chosen values listed are similar or identical to those published earlier. The hyperfine coupling constants incorporate the g-value of the electron and are in units of Gauss.

\*The value of 9.89 G was used for radical pair model 1 and 0.00 G for radical pair model 2.

Radical Pair Model	Nuclei in FADH	Nuclei in Tryptophan
1	N <sub>5</sub>	H <sub>5</sub> , H <sub>1</sub> <sup><math>\beta</math></sup>
2	N <sub>5</sub> , H <sub>5</sub>	H <sub>5</sub> , H <sub>1</sub> <sup><math>\beta</math></sup>

Table 4.2: Choices of nuclei for two radical pair models adopted.

In this thesis two representative choices of nuclei were considered. The first choice

<sup>1</sup>The  $\alpha$ -carbon in organic chemistry refers to the first carbon after the carbon that attaches to the functional group (the carbon is attached at the first, or alpha, position). By extension, the second carbon is the  $\beta$ -carbon, and so on. This nomenclature can also be applied to the hydrogen atoms attached to the carbons. A hydrogen attached to an alpha carbon is called an  $\alpha$ -hydrogen, a hydrogen on the  $\beta$ -carbon is a  $\beta$ -hydrogen, and so on.

includes the nuclei  $N_5$  in FADH and  $H_5$  and  $H_1^\beta$  in tryptophan; the second choice includes  $N_5$  and  $H_5$  in FADH and  $H_5$  and  $H_1^\beta$  in tryptophan. The two radical pair models are listed in Table 4.2, and the corresponding hyperfine coupling constants are given in Table 4.1. The chosen nuclei were those having the strongest hyperfine coupling according to the literature [214–216], as the calculated magnetic field dependence of cryptochrome activation proved to be most sensitive to the influence of these nuclei. The hyperfine coupling constants for the tryptophan nuclei were determined using the electron spin resonance (ESR) and electron-nuclear double resonance (ENDOR) spectroscopy techniques.

The coupling constants were then modified from the values reported and the values that gave the largest change in activation upon increase of the magnetic field to 5 G were chosen (as stated, the values of the chosen hyperfine coupling constants are shown in Table 4.1). The goal was to demonstrate the possibility of obtaining a large (on the order of 10%) variation (either an increase or decrease) in activation yield when the magnetic field is varied according to the experiments [57].

In order to determine more precisely the magnetic field effect on cryptochrome activation, one needs to obtain more accurate values of the hyperfine coupling constants for the relevant nuclei in FADH and tryptophan. The results presented below can only show the feasibility of obtaining a significant magnetic field effect in cryptochrome based on estimates for the hyperfine coupling within the radical pair.

### 4.3 Rate Constants for the Electron Transfer Processes in Cryptochrome

For realistic estimates of the reaction rate constants for electron forward transfer, electron back-transfer, and tryptophan deprotonation, a combination of experimental values from the literature [138, 141] and our own theoretical estimates were [36]. The rate constants for the electron transfer process were estimated within the framework of the Marcus theory, that has been outlined in section 3.1.7.

#### 4.3.1 Electron Forward Transfer

As indicated in Fig. 2.10, the rate constants for forward electron transfer  $\text{Trp377} \rightarrow \text{Trp400}$  and  $\text{Trp324} \rightarrow \text{Trp377}$  are denoted by  $k_1$  and  $k_2$ . These transfers correspond to an electron jumping between tryptophans in the direction opposite to that of



the arrows shown in Fig. 2.10, since the arrows actually indicate hole transfer. The rate constants for the reverse electron transfer are denoted by  $(k_1)'$  and  $(k_2)'$ . The electron forward transfer rate constants were experimentally determined for DNA photolyase and were estimated to be about  $10^8 \text{ s}^{-1}$  [138, 141].

The rate constants for the electron transfer process can be calculated with Eq. (3.61). Note that the use of the edge-to-edge distance  $R$  in Eq. (3.61) provides only a rough estimate of the electron tunneling rate constant. The edge-to-edge distance is suitable in the case when the molecules are static, but in a protein at thermal equilibrium, the tryptophans move and rotate, and the average distance between donor and acceptor groups offers a better variable for the spatial dependence of the electron transfer rate. Accordingly, the average distance between tryptophans is substituted in Eq. (3.61)

$$\langle R \rangle = \frac{1}{N_{\text{pairs}}} \sum_{i \in \text{Trp}_1} \sum_{j \in \text{Trp}_2} |\mathbf{r}_i - \mathbf{r}_j| \quad (4.1)$$

for  $R$ , where  $i$  and  $j$  denote the atoms in the first and second tryptophan, respectively, and  $N_{\text{pairs}}$  is the total number of atomic pairs. The average distance between Trp377 and Trp400 calculated from Eq. (4.1) is 7.21 Å, while the average distance between Trp324 and Trp377 is 8.37 Å. With  $\Delta G_0 = -0.2 \text{ eV}$  (see Figs. 2.10 and 3.3) and the generic value  $\lambda = 1.0 \text{ eV}$  for the reorganization energy of electron tunneling processes in proteins [159], one estimates  $k_1 = 4.9 \times 10^8 \text{ s}^{-1}$  and  $k_2 = 9.9 \times 10^7 \text{ s}^{-1}$  for electron transfer from Trp377 to Trp400 and from Trp324 to Trp377 respectively. The value of  $\lambda \approx 1.0 \text{ eV}$  is typical for electron transfer in polar solvent, when no large bond length changes are involved [217].

The value  $\Delta G_0$  is estimated to be negative (see Figs. 2.10 and 3.3) despite differences in the polarities of the tryptophan environments [138]. From inspection of the crystal structure it was suggested [138] that the polarities increase and, hence, the potentials decrease in the order of Trp400, Trp377, Trp324. The value for  $\Delta G_0$  in DNA photolyase is calculated and discussed in [140].

The estimates above for  $k_1$  and  $k_2$  are in good agreement with experimentally determined values [138, 141] and correctly reproduce the order of magnitude of the electron transfer rate constants. To determine these constants the absorption spectrum of the protein was recorded as a function of time. Absorbance changes accompanying formation of the excited state of FADH and subsequent electron transfer were monitored on a picosecond time scale. The recorded spectra were then attributed

to a particular state of the FAD and tryptophan, because in different charge states the molecules absorb light differently. From the changes in the absorption spectrum it was possible to establish the rate constants for the electron transfer process.

For a more accurate evaluation of the rate constants it is necessary to employ a more detailed model which accounts explicitly for the structure and vibrations of the protein. However, such a model [218] is far beyond the scope of the present thesis. Since the estimated rate constants are of the same order of magnitude as the experimentally measured values, the experimentally measured rate constants will be used in calculations. The estimated rate constants  $k_1$  and  $k_2$  are of about the same order of magnitude, supporting the assumption that  $k_1 = k_2$  in the stochastic Liouville equation, Eqs. (3.39)-(3.41).

The rate constants for electron transfer  $\text{Trp400} \rightarrow \text{Trp377}$  and  $\text{Trp377} \rightarrow \text{Trp324}$  can also be estimated through Eq. (3.61). In this case  $\Delta G_0 = 0.2$  eV is employed for both processes. Thus, one estimates  $(k_1)' = 1.6 \times 10^6$  s<sup>-1</sup> and  $(k_2)' = 3.3 \times 10^5$  s<sup>-1</sup> for  $\text{Trp400} \rightarrow \text{Trp377}$  and  $\text{Trp377} \rightarrow \text{Trp324}$  transitions, respectively. These rate constants are significantly smaller than  $k_1$  and  $k_2$  and, accordingly, electron transfer in the reverse direction of the  $\text{Trp400}$ ,  $\text{Trp377}$ ,  $\text{Trp324}$  chain can be neglected.

The physical reason behind the fact that  $k' \ll k$  was discussed in section 3.1.7. The rate constant of the electron transfer process is determined by the free energy of the reaction, which in the case of electron forward transfer is negative (i.e. the product state is energetically more favorable than the initial state), and is positive in the case of electron backward transfer. This implies that the probability for the electron to transfer backward is small and, therefore,  $k' \ll k$ .

### 4.3.2 Electron Back-Transfer

The rate constants for electron back-transfer from FADH to a tryptophan,  $k_1^b$ ,  $k_2^b$ , and  $k_3^b$  (see Fig. 2.10) can also be estimated through Eq. (3.61). For this purpose, one needs to know the distances between the fragments, the reorganization energies, and the driving forces. The characteristic distances  $R_{\text{FADH-Trp400}}$ ,  $R_{\text{FADH-Trp377}}$ , and  $R_{\text{FADH-Trp324}}$  are 6.0, 8.9, and 13.3 Å, respectively. The reorganization energies are expected to increase with the growth of distance between the two fragments and, thus, are chosen as 0.85, 1.0, and 1.4 eV for the pairs  $\text{FADH} + \text{Trp400}$ ,  $\text{FADH} + \text{Trp377}$ , and  $\text{FADH} + \text{Trp324}$ , respectively. The driving forces for these processes can be estimated from the energy diagram in Fig. 2.10.

Since cryptochrome is excited by a blue light photon, the energy difference between the ground and excited states should be about 2.6 eV. The initial electron transfer step, from Trp400 to FADH, proceeds downhill with a driving force of about 0.5 eV [138]. The next two electron transfer steps proceed with a decrease in energy of 0.2 V [138, 140]. Accordingly, the driving energies are  $\Delta G_{0_{\text{FADH-Trp400}}} = -2.1$  eV,  $\Delta G_{0_{\text{FADH-Trp377}}} = -1.9$  eV, and  $\Delta G_{0_{\text{FADH-Trp324}}} = -1.7$  eV. With these driving energies one obtains  $k_1^b = 8.0 \times 10^6$  s<sup>-1</sup>,  $k_2^b = 1.4 \times 10^7$  s<sup>-1</sup>, and  $k_3^b = 8.7 \times 10^6$  s<sup>-1</sup> for the electron back transfers FADH → Trp400, FADH → Trp377, and FADH → Trp324, respectively. The rate constants compare well with each other. For the sake of simplicity the three rate constants will be considered to be equal, assuming a value of  $10^7$  s<sup>-1</sup> (see Table 4.3).

### 4.3.3 Deprotonation Rate

The measured deprotonation rate of Trp324 at pH = 7.4 is  $k_d = 3.3 \times 10^6$  s<sup>-1</sup> [138, 141]. This rate constant can also be estimated, but it depends on the temperature and on the concentration of the external agent which induces deprotonation.

### 4.3.4 Rate Constants of Various Processes in Cryptochrome

The estimated values of the rate constants for various processes considered in the calculation are compiled in Table 4.3. It should be noted that the measured rate constants referenced in the thesis refer to DNA photolyase<sup>2</sup>, not cryptochrome, and could easily be off by an order of magnitude for cryptochrome. However, since accurate data for the rate constants in cryptochrome are not available, the estimated values are used in conjunction with the measured rate constants from photolyase. While the values presented here must be considered as approximate, the fact that magnetic field effects are observed in *Arabidopsis* (which would not be possible for unsuitable cryptochrome rate constants, see discussion below) suggests that the estimated values are likely accurate to within an order of magnitude.

---

<sup>2</sup>DNA photolyase is an enzyme that binds complementary DNA strands and breaks pyrimidine dimers that are typically caused by exposure to ultraviolet light. Pyrimidine dimers occur when a pair of thymine bases or cytosine bases on the same strand of DNA bind together, resulting in a 'bulge' of the DNA structure referred to as a lesion. Photolyase has a high affinity for these lesions in the DNA and will reversibly bind and split the dimer using light-energy. This enzyme only functions as a DNA repair mechanism when visible light is available (preferentially from the violet/blue end of the spectrum). This process is also known as photoreactivation.

Process	Rate constant	Estimate ( $s^{-1}$ )	Measured value ( $s^{-1}$ )
Electron forward transfer	$k_1 = k_2 = k_{et}$	$1 \times 10^8$	$1 \times 10^8$ , [138, 141]
Electron reverse transfer	$(k_1)'$	$1.6 \times 10^6$	-
Electron back-transfer	$(k_2)'$ $k_1^b = k_2^b = k_3^b = k_b$	$3.3 \times 10^5$ $1 \times 10^7$	- -
Tryptophan deprotonation	$k_d$	-	$3.3 \times 10^6$ , [138, 141]
Singlet-triplet interconversion	$\Omega$	$8.3 \times 10^7$	-

Table 4.3: Rate constants of various processes in cryptochrome-1.

## 4.4 Magnetic Field Dependence of Activation Yield

The dynamics of electron spins is governed by the hyperfine interaction with the nuclei of the radical pairs. Due to computational costs it is impossible to account for all nuclei in the system explicitly. Thus, two radical pair models have been considered, each of which includes only selected nuclei from each of the radicals (see chapter 4, section 4.2).

The choice of the radical pair model 1 was inspired by the work of Ahmad *et al.* [57] on magnetic field effects in *Arabidopsis thaliana*, in which it was shown that an external magnetic field can inhibit hypocotyl elongation, a process regulated by cryptochrome. The inhibition of the hypocotyl growth in *Arabidopsis thaliana* plantule is schematically shown in Fig. 4.2. The two plantules in Fig. 4.2 received the same quantity of light, but were subjected to different magnetic fields. The plantule shown in Fig. 4.2a is that which received the weaker magnetic field, while in stronger magnetic field (see Fig. 4.2b) the magnetic field intensified the signal perceived by the plant from light and inhibited the hypocotyky growth.

The results of this work strongly suggest that cryptochrome is responsible for the magnetic field dependence of hypocotyl elongation in *Arabidopsis thaliana*. Radical pair model 1 was used to justify this hypothesis and to show that the external magnetic field can lead to an increase of the activation yield in cryptochrome. For this model, nuclei which have the highest hyperfine coupling constants according to

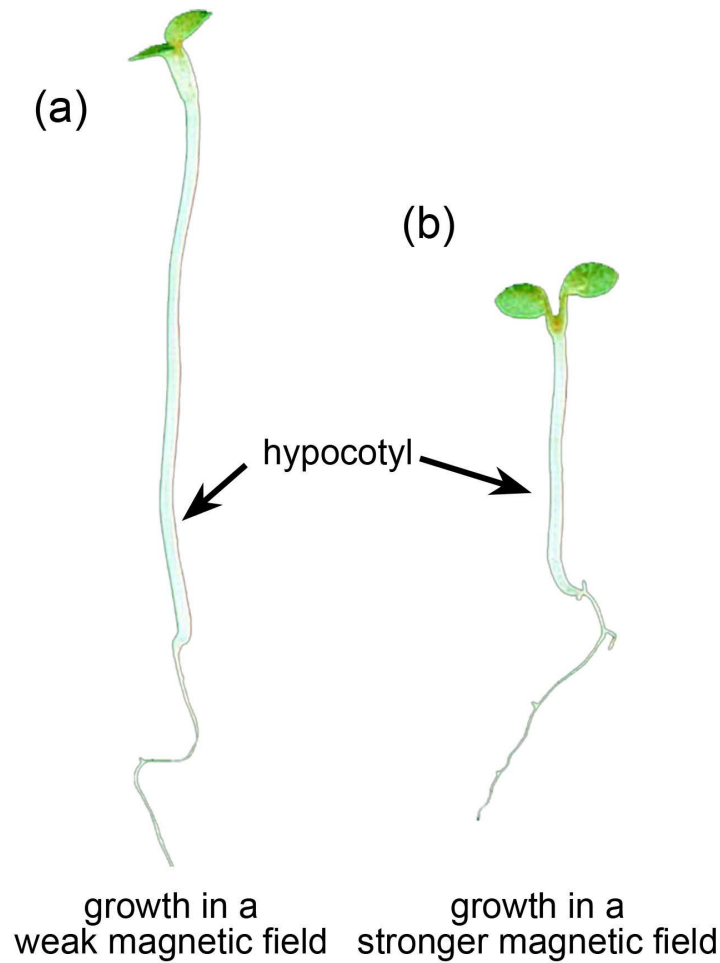


Figure 4.2: Plantule of *Arabidopsis thaliana* drawn according to Ref. [57]. Both plantules received the same quantity of light, but were subjected to different magnetic fields. The plantule with the smaller stem (hypocotyl) (see (a)) is that which received the weaker magnetic field, while in stronger magnetic field (see (b)) the magnetic field intensified the signal perceived by the plant from light and inhibited its growth.

the literature were used. Radical pair model 2 was chosen to show that the activation yield in cryptochrome depends strongly on the hyperfine coupling constants of the nuclei and that changes in their values can lead to rather different behavior of the activation yield. For the purpose of demonstration, some of the experimentally measured hyperfine coupling constants were altered (see Table 4.1).

Figures 4.3 and 4.4 present the magnetic field dependence of the total activation yield  $\bar{Y}(B_0)$  calculated for two chosen radical pair models. The total activation yields

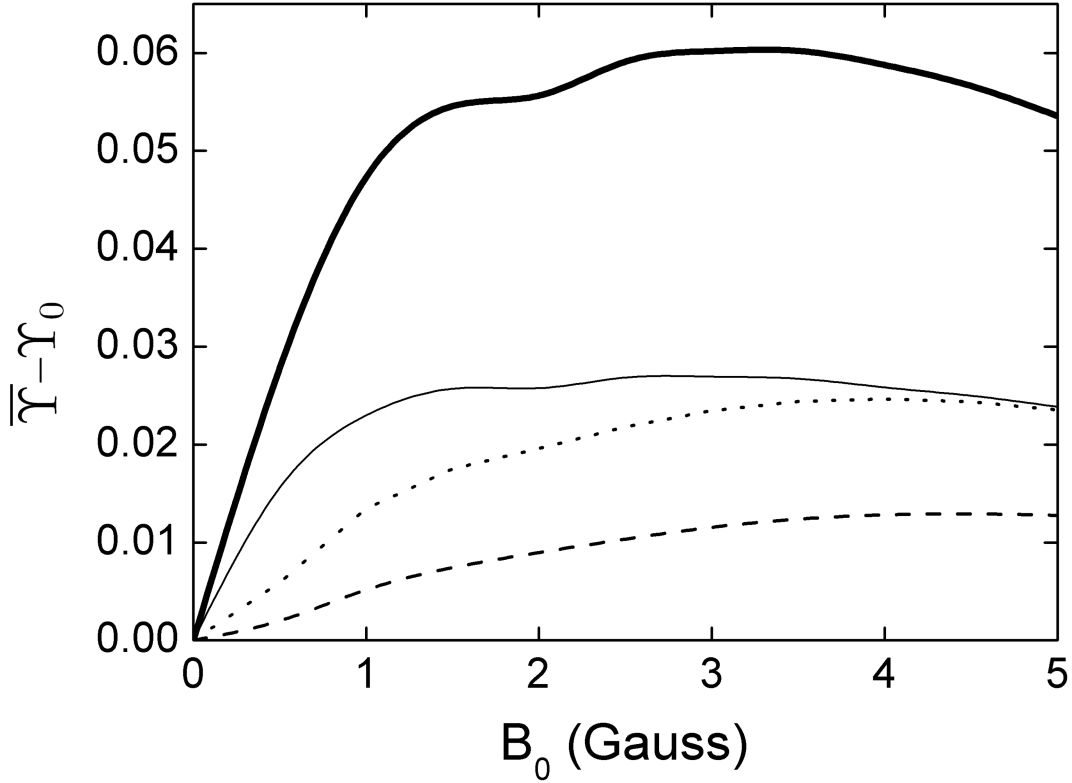


Figure 4.3: Cryptochrome activation yield  $\bar{\Upsilon}(B_0)$  for radical pair model 1. The probability for the formation of FADH + Trp324<sub>dep</sub>, averaged over angles  $\Theta$  and  $\Phi$ , for radical pair model 1, that contains nuclear spins  $N_5$  on FADH and  $H_5$  and  $H_1^\beta$  on the tryptophans, was calculated for different electron back-transfer rate constants: thin solid line,  $k_b = 10^6 \text{ s}^{-1}$ ; thick solid line,  $k_b = 10^7 \text{ s}^{-1}$ ; dotted line,  $k_b = 5 \times 10^7 \text{ s}^{-1}$ ; dashed line,  $k_b = 10^8 \text{ s}^{-1}$ .  $\Upsilon_0$  represents the value of the yield at  $B_0 = 0$ . The values of the activation yield at  $B_0 = 0$  are given in Table 4.4. The maximal difference in yield over the range from 0 to 5 Gauss is approximately +10% for this model.

Rate constant $k_b$ ( $s^{-1}$ )	Radical pair model 1	Radical pair model 2
$10^6$	0.873	0.892
$10^7$	0.425	0.524
$5 \times 10^7$	0.121	0.163
$10^8$	0.058	0.080

Table 4.4: Values of the total activation yield  $\bar{\Upsilon}(B_0)$  for  $B_0 = 0 \text{ G}$  calculated for two radical pair models with different electron back-transfer rate constants.

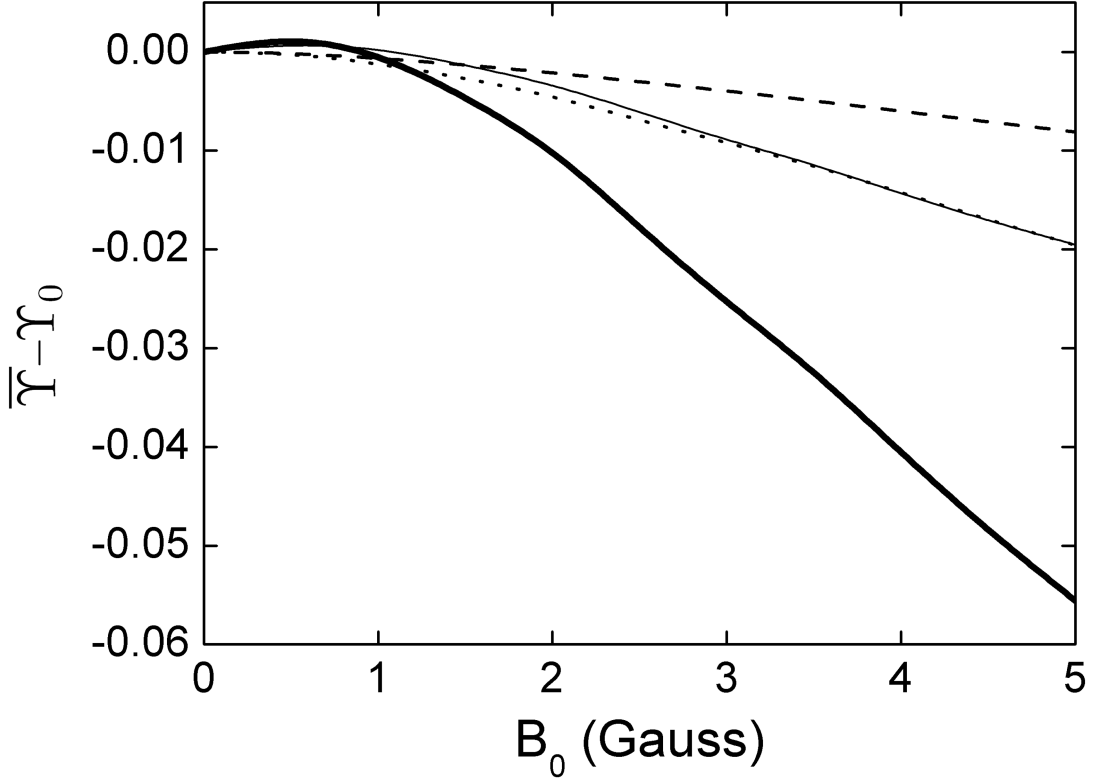


Figure 4.4: Cryptochrome activation yield  $\bar{\Upsilon}(B_0)$  for radical pair model 2. The probability for the formation of FADH + Trp324<sub>dep</sub>, averaged over angles  $\Theta$  and  $\Phi$ , for radical pair model 2, that contains nuclear spins  $N_5$  and  $H_5$  on FADH and  $H_5$  and  $H_1^\beta$  on the tryptophans, was calculated for different electron back-transfer rate constants: thin solid line,  $k_b = 10^6 s^{-1}$ ; thick solid line,  $k_b = 10^7 s^{-1}$ ; dotted line,  $k_b = 5 \times 10^7 s^{-1}$ ; dashed line,  $k_b = 10^8 s^{-1}$ .  $\Upsilon_0$  represents the value of the yield at  $B_0 = 0$ . The values of the activation yield at  $B_0 = 0$  are given in Table 4.4. The maximal difference in yield over the range from 0 to 5 Gauss is approximately -11% for this model.

for  $\bar{\Upsilon}(B_0 = 0)$  are given in Table 4.4. The results in Fig. 4.3 are consistent with the hypothesis that cryptochrome harbors a measurable radical pair effect. The experimental results of Ahmad *et al.* [57] on magnetic field effects in *Arabidopsis thaliana* suggest that cryptochrome spends more time in its signaling state when placed in a field of 5 G than in an earth-strength magnetic field. The activation yield  $\bar{\Upsilon}(B_0)$  presented in Fig. 4.3 is proportional to the time that the protein spends in its signaling state. Fig. 4.3 shows that the activation yield increases with increasing external magnetic field. For an electron back-transfer rate constant of  $10^7 s^{-1}$  (see

solid line in Fig. 4.3), the relative increase of  $\bar{\Upsilon}(B_0)$  at 5 G is about 10%, which is of the same order of magnitude as the plant growth inhibition effect reported in [57]. The relative increase of  $\bar{\Upsilon}$ ,  $\bar{\Upsilon}_{rel}$ , is defined as follows:

$$\bar{\Upsilon}_{rel}(B_0) = \frac{\bar{\Upsilon} - \Upsilon_0}{\Upsilon_0(k_b = 10^7 \text{ s}^{-1})}. \quad (4.2)$$

Of course the 10% effect is rather small, but nevertheless it might be recognized by the living system. This supports the hypothesis that cryptochrome is responsible for the magnetic-field-dependent stem growth in plants. Note, that the activation yield in Fig. 4.3 increases only for low magnetic fields, i.e. 0.5-2 G, and is almost constant for magnetic fields higher than 2 G.

The magnetic field dependence of the activation yield  $\bar{\Upsilon}(B_0)$  for radical pair model 2 is shown in Fig. 4.4. This example shows that the activation yield can decrease with an increase of the external magnetic field. Of the considered electron back-transfer rate constants, the maximal relative decrease occurs for a constant of  $10^7 \text{ s}^{-1}$  and is about 11%. Comparison of model 2 with model 1 shows an increase of total FADH + Trp324<sub>dep</sub> yield with field strength, demonstrating dramatically that the hyperfine coupling constants influence the activation yield behavior in a complex way. Unfortunately, the hyperfine coupling constants are not well known for the nuclei of the FADH and tryptophan in cryptochrome. In order to determine the exact magnetic field response, it will be necessary to obtain experimental information regarding the hyperfine coupling constants of FADH and of each of the three tryptophans in their native environment within cryptochrome. It will also be necessary to greatly extend the present numerical calculation to include a large number of nuclear spins hyperfine-coupled to the unpaired electronic spins.

Figures 4.3 and 4.4 also show the magnetic field dependence of the activation yield  $\bar{\Upsilon}(B_0)$  calculated for different electron back-transfer rate constants. From the estimates performed above, one expects the rate for electron back-transfer to be of the order of  $10^7 \text{ s}^{-1}$ . From Figs. 4.3 and 4.4 it is clear that for this particular value of the electron back-transfer rate constant the magnetic field effect is maximal (see solid lines in Figs. 4.3 and 4.4).

The fact that lower and higher values of the electron back-transfer rate constants lead to less pronounced magnetic field effects on cryptochrome activation has a simple explanation. If the electron back-transfer rate constants ( $k_b$ ) are  $10^6 \text{ s}^{-1}$  or less, then most of the hole density will reach Trp324 and the protein will reach its



signaling state with only minor loss of the hole density. This happens because the rate constants of the electron forward transfer process and the tryptophan deprotonation process are larger than the rate constant of electron back-transfer ( $10^6 \text{ s}^{-1}$ ). The external magnetic field modulates the probability for the radical pair to be in the singlet state of  $\text{FADH} + \text{Trp324}^+$  – the only state in which the electron back-transfer process is possible. If electron back-transfer is slower than the deprotonation  $\text{Trp324}^+ \rightarrow \text{Trp324}_{\text{dep}}$  ( $k_d \approx 3 \times 10^6 \text{ s}^{-1}$ ), the external field can only slightly influence the signaling state of the protein (see solid thin lines in Figs. 4.3 and 4.4).

On the other hand if the electron back-transfer rate constant is larger than  $10^7 \text{ s}^{-1}$ , e.g.  $5 \times 10^7 \text{ s}^{-1}$  or  $10^8 \text{ s}^{-1}$  (dotted and dashed lines in Figs. 4.3 and 4.4), it becomes comparable to the rate constants of forward electron transfer ( $10^8 \text{ s}^{-1}$ ) and with the rate of singlet-triplet interconversion ( $\approx 10^8 \text{ s}^{-1}$ , see Eq. (3.82)). In this case, formation of the  $\text{FADH} + \text{Trp324}^+$  radical pair is impeded and magnetic-field-dependent spin conversion processes will arise to a lesser degree such that the activation yield  $\bar{\Upsilon}(B_0)$  becomes reduced.

## 4.5 Angular Dependence of Activation Yield

In order for a radical-pair-based activation in cryptochrome to function as an inclination compass, the  $\text{FADH} + \text{Trp324}_{\text{dep}}$  yield must exhibit variations with respect to the orientation of cryptochrome relative to an external magnetic field. This orientational dependence could modulate the visual sense of a bird to produce magnetotaxis, as described in [1]. The variation of the total activation yield for the case of radical pair model 1 is shown in Fig. 4.5. The angular dependence of the activation yield depends strongly on the hyperfine coupling constants of the nuclei and, therefore, should be different for radical pair model 2. In the present thesis no differences are discussed and only a single example as an illustration of the possible outcome, namely, for radical pair model 1 is shown.

Figure 4.5 shows that at  $(\Theta = 15^\circ, \Phi = 90^\circ)$  and  $(\Theta = 165^\circ, \Phi = -90^\circ)$  the activation yield has profound minima at all magnetic field strengths. Fig. 4.5 shows also that the activation yield,  $\Upsilon(B_0, \Theta, \Phi)$ , in the  $\Theta, \Phi$ -plane has a maximal ridge near  $\Theta = 90^\circ$  which is most prominent around  $B_0 = 2.5 \text{ G}$  and is less pronounced at higher and lower magnetic field strengths. These minima and the maximal ridge at  $\Theta = 90^\circ$  can be explained if one examines the principal axes of the hyperfine

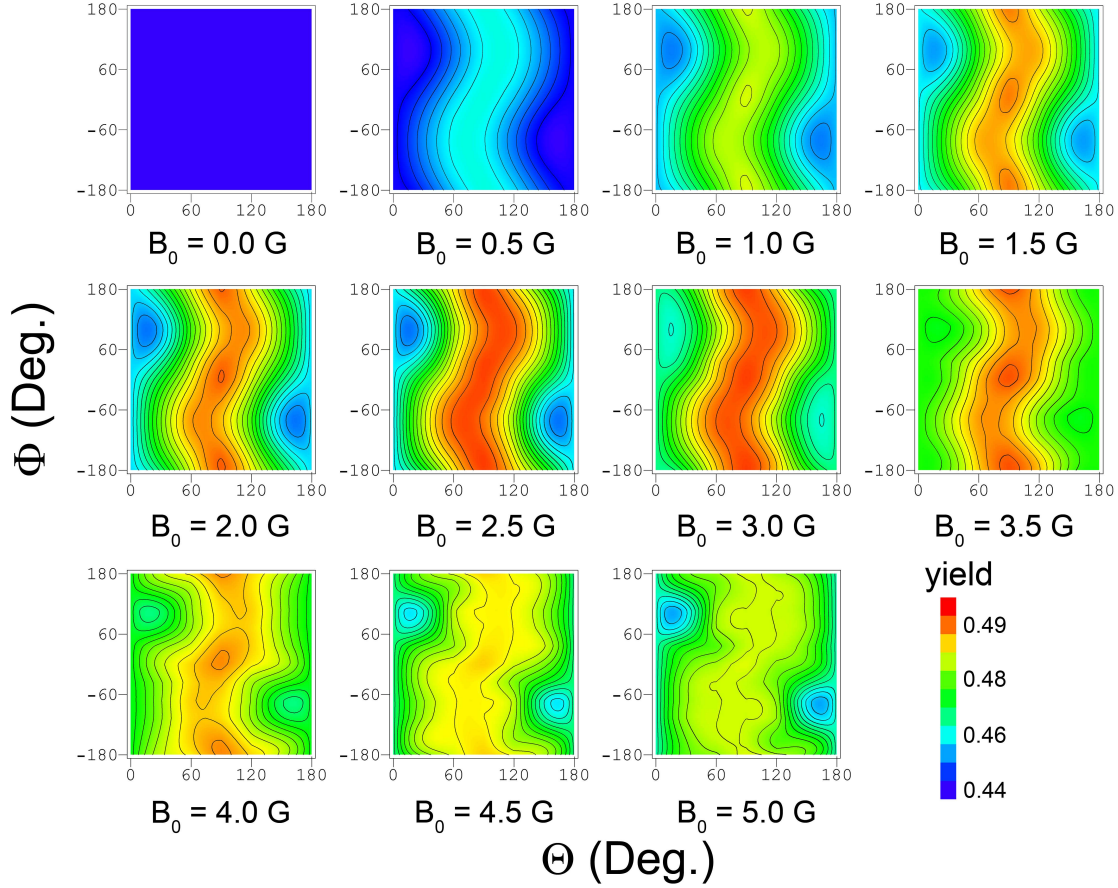


Figure 4.5: Contour plots of the angular dependence of the cryptochrome activation yield. The plots show the FADH + Trp324<sub>dep</sub> yield for radical pair model 1. The yield exhibits a maximal ridge at about  $\theta = 90^\circ$  which is most prominent around  $B_0 = 2.5$  G and fades away at higher and lower magnetic field strengths.

coupling tensors and considers the fact that each nuclear spin contributes an effective local field (see Fig. 3.1)  $\mu_B \vec{I}_i \cdot \hat{A}_i$  to the electron spin precession. The nuclei that contribute to the anisotropic hyperfine coupling are N<sub>5</sub> and H<sub>5</sub> on FADH (see Fig. 3.1), the hyperfine tensors being listed in Table 4.1. The dominant contribution to the hyperfine coupling stems from the principle axes of N<sub>5</sub> and H<sub>5</sub> that happen to both be oriented closely along the  $z$ -axis, deviating from it by  $\Theta = 15^\circ$ ,  $\Phi = 90^\circ$ . N<sub>5</sub> contributes a local field of  $\pm 14$  G (combining isotropic and anisotropic contributions), while H<sub>5</sub> contributes  $\pm 5$  G. These fields are larger than the external field, so that the effect of the external field is minimized in the direction  $\Theta = 15^\circ$ ,  $\Phi = 90^\circ$  (as well as in the opposite direction  $\Theta = 165^\circ$ ,  $\Phi = -90^\circ$ ). This behavior can be seen

clearly in Fig. 4.5.

The effective field contributed by  $N_5$  and  $H_5$  in the  $xy$ -plane, on the other hand, is small enough that an external field of about 2.5 G can effectively modulate the electron spin precession around the combined (nuclear and external) local field (see the semiclassical picture of the radical pair electron spin dynamics in Fig. 3.1).

As explained in detail in [88,89], in the semiclassical picture the electrons precess in the local magnetic field, which is given by  $\vec{B} + \sum_i \vec{I}_i \cdot \hat{A}_i$ , with contributions from the external field  $\vec{B}$  and from the nuclear spins  $\vec{I}_i$ . Nitrogen and hydrogen have nuclear spin 1 and 1/2 respectively, thus  $N_5$  contributes only  $\pm 1$  G in each component of the  $xy$ -plane ( $B_x^{N_5} \approx 3.93 - 4.92 \approx -1$  G;  $B_y^{N_5} \approx 3.93 - 4.98 \approx -1$  G), while  $H_5$  contributes  $\pm 7$  G along the  $x$ -axis ( $B_x^{H_5} \approx \frac{1}{2}(-7.69 - 6.16) \approx -7$  G), and a negligible field along the  $y$ -axis. Therefore, an external field can contribute significantly to the effective local field on FADH in the  $xy$ -plane, leading to the maximal ridge in the orientational dependence as seen in Fig. 4.5.

The projection of the local magnetic field in the FADH radical on the  $xy$ -plane is limited by an ellipse which has principal radii  $b_x = |B_x^{N_5}| + |B_x^{H_5}| + B_0 = 8 + B_0$  G and  $b_y = |B_y^{N_5}| + |B_y^{H_5}| + B_0 = 1 + B_0$  G. The  $x$ - and  $y$ -contributions of the  $N_5$  and  $H_5$  nuclei are 8 G and 1 G, respectively, and  $B_0$  is the contribution of the external magnetic field. The average field created by the  $N_5$  and  $H_5$  nuclei in the  $xy$ -plane is defined as follows:

$$\tilde{B} = \frac{\int_{el.} \sqrt{x^2 + y^2} dx dy}{S_{el.}}, \quad (4.3)$$

where the integration is performed over the area of the ellipse, in which the local magnetic field is changing.  $S_{el.} = \pi b_x b_y$  is the area of this ellipse. The integral in Eq. (4.3) can be computed accordingly:

$$\tilde{B} = \frac{1}{\pi b_x b_y} \int_0^{2\pi} \int_0^{\frac{b_x b_y}{\sqrt{b_y^2 \cos^2 \alpha + b_x^2 \sin^2 \alpha}}} r^2 dr d\alpha = \frac{4b_y \text{EllipticE}\left(1 - \frac{b_x^2}{b_y^2}\right)}{3\pi}. \quad (4.4)$$

Here  $\text{EllipticE}(x)$  is the complete elliptic integral, which is defined as follows:

$$\text{EllipticE}(x) = \int_0^{\pi/2} \sqrt{1 - \frac{\pi}{2} \sin^2(\theta)} d\theta. \quad (4.5)$$

At  $B_0 = 0$  G,  $\tilde{B} = 3.47$  G. This value of  $B_0$  corresponds to the upper left contour plot in Fig. 4.5, which is constant and without angular dependence. The

ridge in the orientational dependence at  $\theta = 90^\circ$  in Fig. 4.5 has its maximal value at  $B_0 = 2.5 - 3.5$  G, which is also close to the field value where  $\bar{\Upsilon}(B_0)$  has its maximum (see Fig. 4.3).

It is important to note that the activation yield is dependent only on the inclination of the external magnetic field and not on its polarity, a feature explained in section 2.2. This can be seen from the contour plots in Fig. 4.5, which obey the symmetry property:

$$\Upsilon(\Theta, \Phi) = \begin{cases} \Upsilon(\pi - \Theta, -\pi + \Phi), & \Phi \geq 0 \\ \Upsilon(\pi - \Theta, \pi + \Phi), & \Phi < 0 \end{cases} \quad (4.6)$$

Small deviations from this condition arise due to interpolation errors of the contour plots. The fact that the activation yield depends only on the inclination of the magnetic field and not its direction, supports the hypothesis that the radical pair mechanism is involved in avian magnetoreception, as migratory birds only possess an inclination compass.

## 4.6 Time Dependence of Singlet and Triplet Populations

The probability  $\text{Tr}[\hat{Q}^S \rho_3(t)]$  arising in Eq. (3.85) and its complement  $\text{Tr}[\hat{Q}^T \rho_3(t)]$  represent the populations for the FADH + Trp324<sup>+</sup> radical pair in the singlet and triplet state, respectively. The time dependence of these quantities provides information on the characteristic time scales of the spin dynamics underlying the radical pair mechanism. From the time evolution of the singlet and triplet populations, it is possible to establish the time needed for the electron hole to reach Trp324, and for FADH + Trp324<sup>+</sup> to assume a maximal singlet or triplet state character, as well as the characteristic time of the entire process, i.e., the time when the population of FADH + Trp324<sup>+</sup> has decayed to zero.

The time dependence of the singlet and triplet populations ( $\text{Tr}[\hat{Q}^S \rho_3(t)]$  and  $\text{Tr}[\hat{Q}^T \rho_3(t)]$ ) for radical pair model 1 are plotted in Fig. 4.6. The populations oscillate about an initial rise and a subsequent exponential decay. The oscillations arise due to the singlet-triplet interconversion, while the decay stems from electron back-transfer and Trp324<sup>+</sup> deprotonation.

From the maxima and minima of the singlet/triplet population one can establish the characteristic time of the singlet-triplet interconversion. The first five maxima

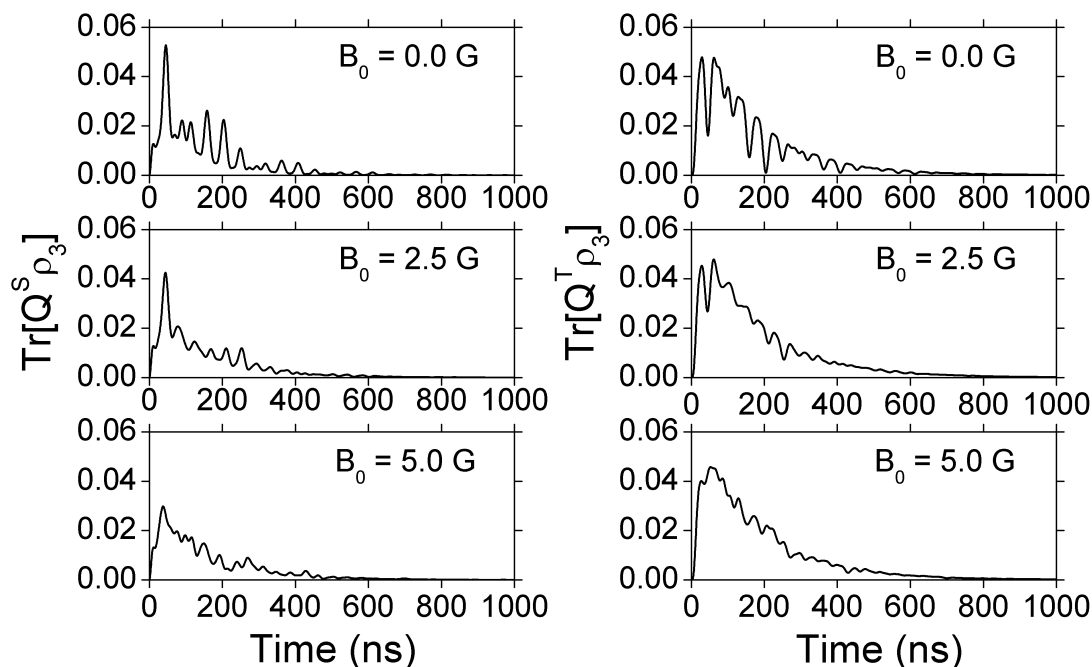


Figure 4.6: Time dependence of singlet and triplet populations. The results shown are those for radical pair model 1, calculated for rate constants  $k_{\text{et}} = 1 \times 10^8 \text{ s}^{-1}$ ,  $k_b = 1 \times 10^7 \text{ s}^{-1}$ , and evaluated at  $\Theta = 0^\circ$ ,  $\Phi = 0^\circ$ .

and minima which arise in the time dependence of the triplet population at an external field of 0 G are compiled in Table 4.5. The time difference between two neighboring maxima and minima corresponds to the time of the interconversion process governed by the hyperfine coupling only. From the data presented in Table 4.5 one finds  $\tau_{T-S} \sim \tau_{S-T} \sim 15 - 25 \text{ ns}$  ( $k_{S-T} = 5 - 6.7 \times 10^7 \text{ s}^{-1}$ ). This estimate is in agreement with the estimate performed earlier (see subsection 3.1.8 and Eq. (3.82)).

The results for the time evolution of the spin populations might be used for the experimental verification of the suggested mechanism. For example, time-resolved ESR techniques could be applied to probe the spin correlation of photoinduced radical pairs in cryptochrome in the same manner as these techniques have been applied to photosynthetic reaction centers [219, 220]).

At 0 G, the singlet and triplet populations reach their first maxima at 45 ns and 29 ns, respectively (see Fig. 4.7). Note that a maximum in the singlet population corresponds to a minimum in the triplet population and vice versa. Thus, at 45 ns the triplet population has a profound minimum (see Fig. 4.6 and Fig. 4.7). The

Maxima (ns)	Minima (ns)	$\Delta\tau$ (ns)
29	45.5	16.5
62(74)	91	29(23.5)
100.5	114.5	14
128.5(139)	158	29.5(24.3)
177.5	204	26.5

Table 4.5: The first five maxima and minima in the time evolution of the triplet population at 0 G.  $\Delta\tau$  gives the time difference between two neighboring maxima and minima. The values in brackets correspond to cases when two close lying maxima arise.

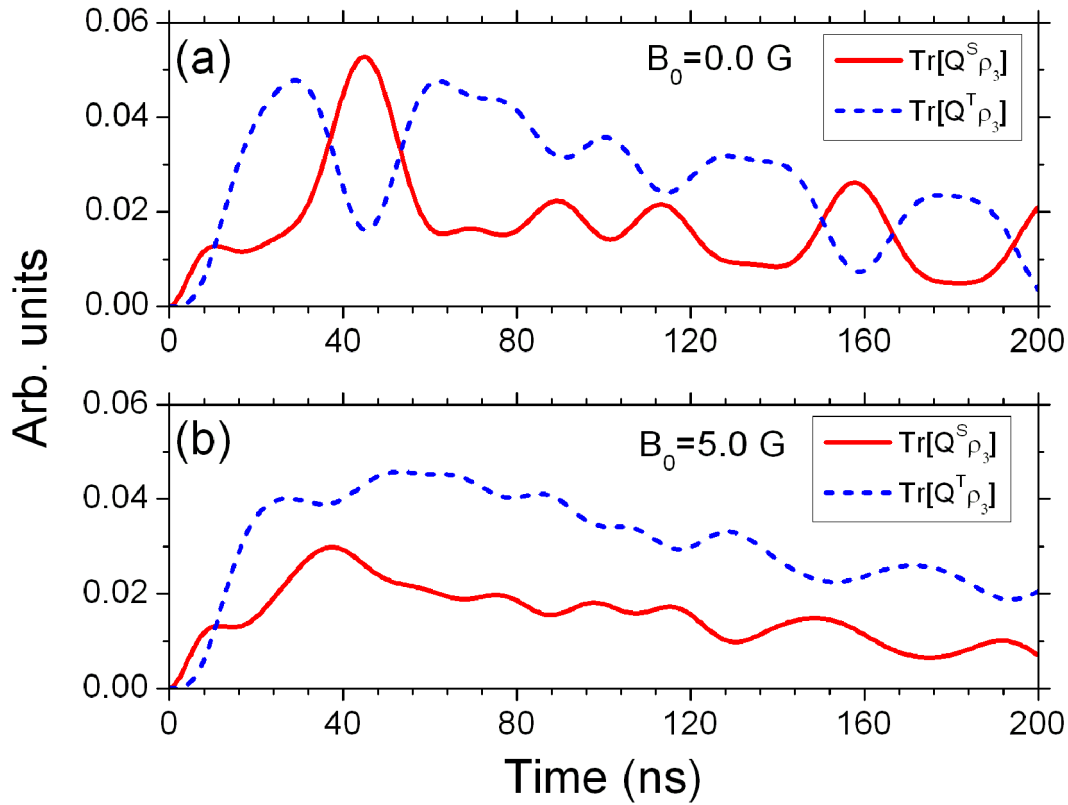


Figure 4.7: Time dependence of singlet and triplet populations. The results shown are those for radical pair model 1, calculated for rate constants  $k_{\text{et}} = 1 \times 10^8 \text{ s}^{-1}$ ,  $k_b = 1 \times 10^7 \text{ s}^{-1}$ , and evaluated at  $\Theta = 0^\circ$ ,  $\Phi = 0^\circ$ . (a) The time evolution of the singlet and triplet population at 0 G; (b) The time evolution of the singlet and triplet population at 5.0 G;

positions of maxima and minima depend on the magnetic field strength; the first maximum for the singlet population is shifted to shorter times with increasing mag-

netic field strength, while the first triplet population maximum is shifted to longer times. At 5 G, the first maximum occurs at 37.5 ns for the singlet population and at 52.5 ns for the triplet population. The triplet population also exhibits a strong second maximum which occurs at 61 ns and 62.5 ns for 0 and 5 G, respectively.

The value of the singlet and triplet populations at these maxima (especially in the singlet population) decreases with increasing magnetic field strength. This fact has a simple explanation. The two maxima in the triplet population come closer to each other with increasing magnetic field, and nearly merge at 5 G. Thus, the value of the population at the minimum between the maxima rises and the magnitude of the maximum in the singlet population decreases.

From Fig. 4.6 it is also possible to estimate the time of the overall radical pair reaction. From this figure it is clear that at  $t \sim 700$  ns, both singlet and triplet populations have decayed to zero.





# Chapter 5

## Iron-Mineral based Magnetoreceptor Model

### 5.1 Introduction

In this section the iron-mineral-based magnetoreception mechanism is discussed. First the potential energy surfaces of the magnetite cluster calculated at different orientations of the external magnetic field are presented and the differences are discussed. From the potential energy surfaces the forces acting on the magnetite cluster are calculated and the differences arising at different orientations of the external magnetic field are shown. In subsection 5.3 all particles in the system are assumed to behave like point-like dipoles, while in subsection 5.5 their size is accounted for. In subsection 5.4 the transducer mechanism of the geomagnetic field is discussed. In subsection 5.6 the magnetic functionality window of the iron-mineral-based magnetoreceptor is discussed. In subsection 5.7 It is demonstrated that the iron-mineral based magnetoreceptor mechanism provides a polarity compass. In subsection 5.8 the magnetoreceptor systems with different number of platelets are discussed. It is demonstrated that magnetoreceptor system with one platelet possesses the properties of an inclination compass, while magnetoreceptor systems with two, three and more platelets have the properties of a polarity compass. In section 5.9 the magnetoreceptor systems with different number of platelets is studied in higher magnetic fields (i.e. higher than the geomagnetic field). In subsection 5.10 several possible roles of the non-magnetic vesicle are suggested. In subsection 5.11 the most important problems, which need further experimental confirmation are outlined.

## 5.2 Magnetic Properties of the Magnetite Platelets and of the Magnetite Cluster

As already discussed in section 2.4.2 the magnetoreceptor unit likely includes ten maghemite platelets and a magnetite cluster (see Fig. 2.14) which consist of ferrimagnetic minerals and thus should have magnetic moments. However there might be units with a different number of platelets, i.e. with five, two, one. As will be shown in section 5.8 that such systems might play a very important role in the magnetoreception process. Therefore an experimental determination of the distribution of magnetoreceptor units with different number of platelets is necessary. First, a magnetoreceptor unit with ten platelets will be considered, while in the later subsections of this chapter magnetoreceptor systems with different number of platelets will be discussed.

The magnetic moments of the platelets and the cluster are quite different altogether: the platelets behave like small permanent magnets while the cluster has an induced magnetic moment. In subsections 3.2.2 and 3.2.3 the expressions for the magnetic moments of the maghemite platelets and the magnetite clusters will be derived.

The magnetization of a ferrimagnet determines its magnetic properties. The magnetization of magnetite and maghemite has a hysteresis shape (see Fig. 3.7) if considered as a function of an external magnetic field (induction) [202, 203]. The hysteresis loop is characterized by the remanent magnetization  $M_r$ , saturation magnetization  $M_s$  and coercive force  $H_c$  (see Fig. 3.7). The hysteresis parameters depend on the temperature and on the size of the particle. The size of the maghemite platelets is about  $1 \mu\text{m}$  and the magnetite cluster consists of magnetite nanoparticles which are 2-5 nm in diameter [46, 47, 60].

The hysteresis parameters for  $1 \mu\text{m}$  maghemite particles at room temperature are:  $M_r = 50 \text{ emu/cm}^3$  [202],  $M_s = 377 \text{ emu/cm}^3$  [203] and  $H_c = 233 \text{ Oe}$ , corresponding to  $B_c = 233 \text{ G}$  [203].

For magnetite nanoparticles (1-10 nm), the hysteresis parameters are  $M_r \approx M_s = 480 \text{ emu/cm}^3$  [25, 203], while  $H_c = 180 - 295 \text{ Oe}$  ( $B_c = 180 - 295 \text{ G}$ ).

The Earth magnetic field has an induction of about 0.5 G, while the typical magnetic field created by the chain of maghemite platelets is 10 G, based on calculations to be, discussed in the next subsection. Note, that the chain-like assembly of the maghemite platelets is energetically the most favorable because in that case

the magnetic moments of the platelets are aligned one after another. The resulting magnetic field in this case is maximal. The magnetite cluster interacts with the external magnetic field and with the magnetic field created by the platelets. If all maghemite platelets would bundle together, then the magnetic moments of individual platelets would be stochastically distributed, leading to a lower magnetic field compared to the case of an ordered chain. Since for maghemite and for magnetite,  $B_c \gg 10$  G, only a narrow region of the magnetization plot in Fig. 3.7 corresponding to the field strengths less than 10 G is used in the system and the magnetization of magnetite and maghemite is almost constant, equal to the remanent saturation magnetization.

Using Eq. (3.90) one can estimate the magnetic moment of the maghemite platelet. With  $M_r^{maghm} = 50$  emu/cm<sup>3</sup> [203],  $l_x = l_z = 1$   $\mu$ m and  $l_y = 0.1$   $\mu$ m one obtains:  $m_i \approx 3.121$  eV/G.

With  $M_r^{magn} = 480$  emu/cm<sup>3</sup> [25,203] and  $r_0 = 2.5$  nm [25,46,47,63] one obtains  $\mu \approx 19.61$   $\mu$ eV/G. Substituting this value into Eq. (3.101) and dividing it by the volume of the magnetite cluster one obtains the volume susceptibility of the cluster  $\chi_v$  (see also Eq. (3.103)), which at 300 K is equal to  $\chi_v = 0.12$  CGS units. Note that this value is in very good agreement with the value used in an earlier investigation [40], and is typical for ferrofluids based on magnetite ( $\chi_v = 0.1$  CGS units). With  $H = 10$  Oe, being the typical value of the local field at the site of the magnetite cluster, one obtains:  $\langle \mathcal{M} \rangle \approx 0.392$  eV/G. Note that this value is about an order of magnitude smaller than the magnetic moment of a single maghemite platelet (see estimates in the previous paragraph).

## 5.3 Interaction of Point-Like Dipoles

### 5.3.1 Potential Energy Surface of the Magnetite Cluster

Figure 5.1 shows the potential energy of the magnetite cluster as a function of coordinates  $x$  and  $y$ , while  $z=0$   $\mu$ m (see Fig. 2.14), calculated at different orientations of the external magnetic field vector. Plots (a), (b) and (c) show the potential energy surfaces calculated for three different orientations of the external magnetic field vector corresponding to alignment along the  $x$ -,  $y$ - and  $z$ - axes of the considered coordinate frame respectively. In this calculation the maghemite platelets and the magnetite cluster are considered as point-like dipoles. However because of their real

dimensions, there exists an excluded region on the potential energy surface, where the magnetite cluster can not be placed. The maghemite platelets in Fig. 5.1 are shown with black rectangles. The gray rectangle in the center of the potential energy surfaces defines the excluded region for the magnetite cluster.

In the calculations, the external magnetic field strength was assumed to be 0.5 G, being a typical value of the earth magnetic field strength. The potential energy surfaces shown in Fig. 5.1 were calculated using Eq. (3.111) with  $w = 1$ , corresponding to the first order of approximation of the magnetic moments of the platelets.

To study the accuracy of the first-order approximation, Fig. 5.2 shows the difference between the potential energy surface of the magnetite cluster calculated with  $w = 1$  and with  $w = 4$ , assuming that the external magnetic field is oriented along the z-axis (see Fig. 2.14). Fig. 5.2 shows that the energy difference between the two approximations is less than 3 meV, being maximal when the energy of the magnetite cluster is less than -1 eV (see Fig. 5.1). Therefore with  $w = 1$  it is possible to calculate the potential energy surface of the magnetite cluster with an error of less than 1 %.

The reason why corrections of higher order do not influence the potential energy surface of the magnetite cluster significantly can be understood if one considers the magnetic moment of the platelets calculated at different orders of successive approximation. The x- and z- components of the magnetic moments of the ten platelets obtained with  $w = 0, 1, 2, 4$  and 10 are compiled in Tab. 5.1, with the external magnetic field oriented along the z-axis. Since the magnetic moment of a platelet rotate only in the (xz)- plane, its y-component is zero. This assumption is governed by the size and the spatial arrangement of the platelets in the dendrite (see discussion in section 2.4.2).

From Tab. 5.1 it is clear that accounting for approximations of higher orders does not change the direction of the magnetic moments significantly. This is because the external magnetic field is of the order of 0.5 G, being significantly lower than the magnetic field created locally by the platelets. Therefore the magnetic moments of the platelets are aligned along the x-axis with only a small deviation in the z-direction (see Tab. 5.1). Comparing the magnetic moments obtained with  $w = 1$  and  $w = 10$ , one can conclude that the first-order approximation describes the magnetic moments of the platelets with a reasonable accuracy (deviation  $\approx 10^{-3}$ ). **In further considerations, the first-order approximation will be used since it describes the essential physics of the system and provides a relatively**

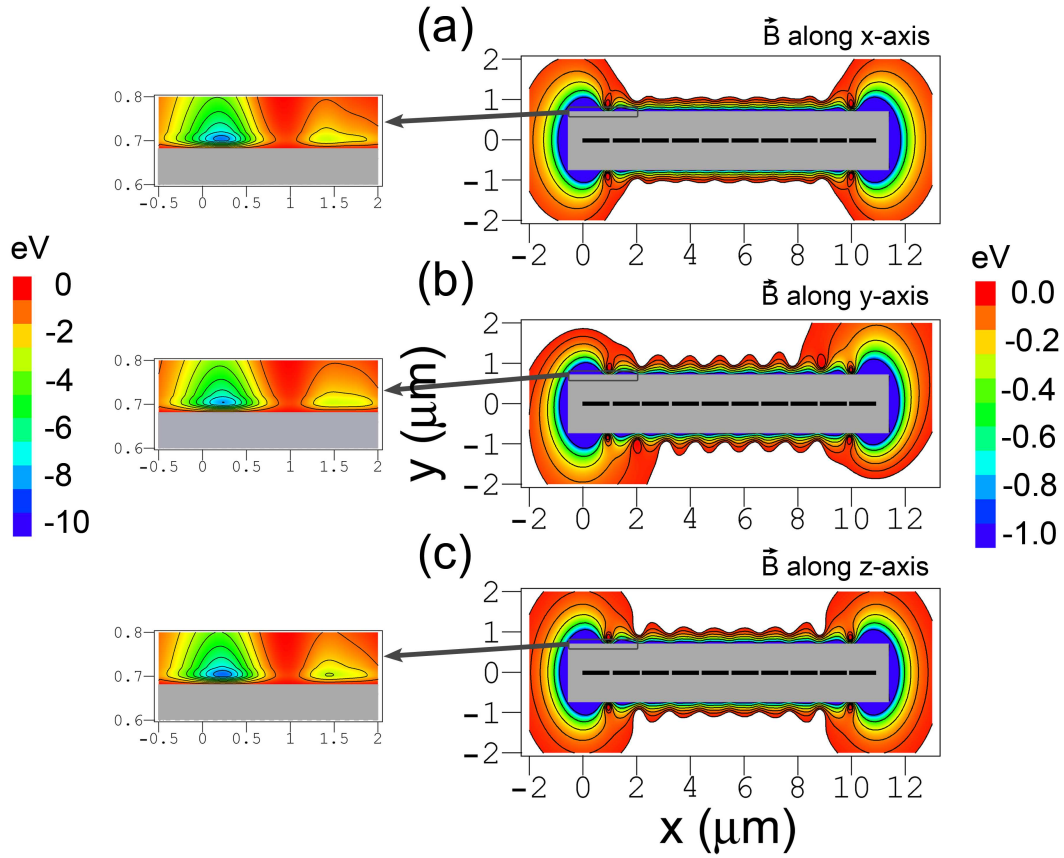


Figure 5.1: Potential energy surfaces of the magnetite cluster calculated in the case when the maghemite platelets and the magnetite cluster are assumed point-like dipoles. The potential energy surfaces are shown as a function of its  $x$  and  $y$  coordinates, while  $z=0 \mu\text{m}$  (see Fig. 2.14) calculated at different orientations of the external magnetic field vector: magnetic field vector aligned along the  $x$ -axis (a); magnetic field vector aligned along the  $y$ -axis (b); magnetic field vector aligned along the  $z$ -axis (c). The maghemite platelets are shown with black rectangles. The gray rectangle in the center of the potential energy surfaces shows the region, where the magnetite cluster can not be placed, due to the finite size of the particles in the system. The energy scale is given in eV right to the contour plots. The equipotential lines are shown for the energies  $-0.03$ ,  $-0.06$ ,  $-0.12$ ,  $-0.24$ ,  $-0.48$  and  $-0.96$  eV. The region of the potential energy surface in the vicinity of the maghemite platelets chain tip is shown at the left of the corresponding surface with greater resolution. The equipotential lines in these contour plots are shown for the energies  $-1$ ,  $-2$ ,  $-3$ ,  $-4$ ,  $-5$ ,  $-6$ ,  $-7$ ,  $-8$  and  $-9$  eV.

**simple analytical expression for the potential energy** (see Eq. (3.111)).

The potential energy surfaces calculated for the  $x$ -,  $y$ - and  $z$ - orientations of the

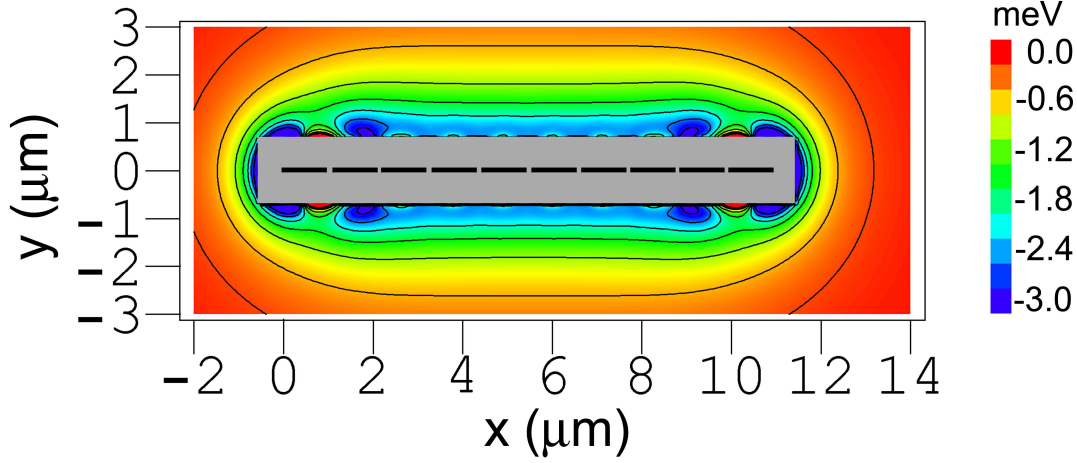


Figure 5.2: The difference between the potential energy of the magnetite cluster calculated in the first and in the fourth orders of approximation using Eq. (3.111). The energy scale is given in meV. The equipotential lines are shown for the energies -0.2, -0.5, -1.0, -1.5, -2.0, -2.5, -3.0 meV. The external magnetic field is directed along the z-axis.

N	Magnetic moment of a platelet $(m_x^{(w)}, m_z^{(w)})$ eV/G				
	$w = 0$	$w = 1$	$w = 2$	$w = 4$	$w = 10$
1	(3.212, 0)	(3.116, 0.173)	(3.119, 0.127)	(3.118, 0.145)	(3.117, 0.150)
2	(3.212, 0)	(3.120, 0.095)	(3.121, 0.031)	(3.121, 0.040)	(3.121, 0.044)
3	(3.212, 0)	(3.120, 0.090)	(3.121, 0.042)	(3.121, 0.056)	(3.121, 0.061)
4	(3.212, 0)	(3.120, 0.088)	(3.121, 0.043)	(3.121, 0.054)	(3.121, 0.058)
5	(3.212, 0)	(3.120, 0.088)	(3.121, 0.043)	(3.121, 0.054)	(3.121, 0.058)
6	(3.212, 0)	(3.120, 0.088)	(3.121, 0.043)	(3.121, 0.054)	(3.121, 0.058)
7	(3.212, 0)	(3.120, 0.088)	(3.121, 0.043)	(3.121, 0.054)	(3.121, 0.058)
8	(3.212, 0)	(3.120, 0.090)	(3.121, 0.042)	(3.121, 0.056)	(3.121, 0.061)
9	(3.212, 0)	(3.120, 0.095)	(3.121, 0.031)	(3.121, 0.040)	(3.121, 0.044)
10	(3.212, 0)	(3.116, 0.173)	(3.119, 0.127)	(3.118, 0.145)	(3.117, 0.150)

Table 5.1: Magnetic moments of the maghemite platelets of the magnetoreceptor unit (see Fig. 2.14) calculated at different orders of successive approximation,  $w$ . The values in the table correspond to the x- and z- components of the magnetic moments are indicated as  $m_x^{(w)}$  and  $m_z^{(w)}$ . The y-component of the magnetic moments  $m_y^{(w)} = 0$  eV/G. The external magnetic field is aligned along the z-axis.

external magnetic field are shown in plots (a), (b) and (c) in Fig. 5.1 respectively. The potential energy surfaces for these three cases are similar, although some differences can be observed. For instance, the potential energy surfaces corresponding to

the x- and z- orientations of the external magnetic field have axial symmetry along the  $y=0 \mu\text{m}$ ,  $z=0 \mu\text{m}$  axis, while the potential energy surface corresponding to the y-orientation of the external magnetic field has point symmetry with respect to the point  $(5.45,0) \mu\text{m}$ . At  $y \approx \pm 0.7 \mu\text{m}$ ,  $z=0 \mu\text{m}$  there are two valleys with several minima whose steepness is determined by the external magnetic field.

Additionally, there are two strong minima at the tips of the platelet chain with energy of about  $-8.5 \text{ eV}$ . This is significantly lower than the energy of the minima in the valleys at  $y \approx \pm 0.7 \mu\text{m}$ , which is  $-2.8 \text{ eV}$  (see plots in the left part of Fig. 5.1). This leads to the conclusion that the spots of the most energetically favorable attachment of the magnetite cluster are at the tips of the maghemite chain. This fact is in agreement with experimental observations [58–61].

### 5.3.2 Forces Acting on the Magnetite Cluster

From the potential energy surface of the magnetite cluster it is possible to calculate the force acting on it. The three force components are shown in Fig. 5.3 as a function of the x-coordinate of the magnetite cluster when  $y=0.8 \mu\text{m}$  and  $z=0 \mu\text{m}$  (see Fig. 2.14). The force components were calculated with Eq. (3.112) for three perpendicular orientations of the external magnetic field. Plots (a), (b) and (c) in Fig. 5.3 correspond to the magnetic field orientation along the x-, y- and z-axes respectively. Solid-thin, dotted and dashed lines in Fig. 5.3 correspond to the x-, y- and z-components of the force vector respectively. Thick lines show the dependence of the force vector magnitude on the x-coordinate of the magnetite cluster.

From Fig. 5.3 it is clear that the largest force acts on the magnetite cluster at the tips of the maghemite platelet chain. Note, that the z-component of the force vector is zero if the external magnetic field is directed along the x- and y-axes. In these cases the magnetic moments of the platelets and of the cluster are found in the (xy)-plane, and therefore the force acting on the cluster in the z-direction is zero. If the external field is directed along the z-axis then the magnetic moments of the platelets and the cluster contain a z-component (see Tab. 5.1), hence a z-component of the force vector exists. This fact is illustrated in Fig. 5.3.

The effect of the external magnetic field on the forces acting on the magnetite cluster can be seen if one considers the differences between the forces at different orientations of the external magnetic field vector. The plots in the left part of Fig. 5.4 show the difference between the force components corresponding to the

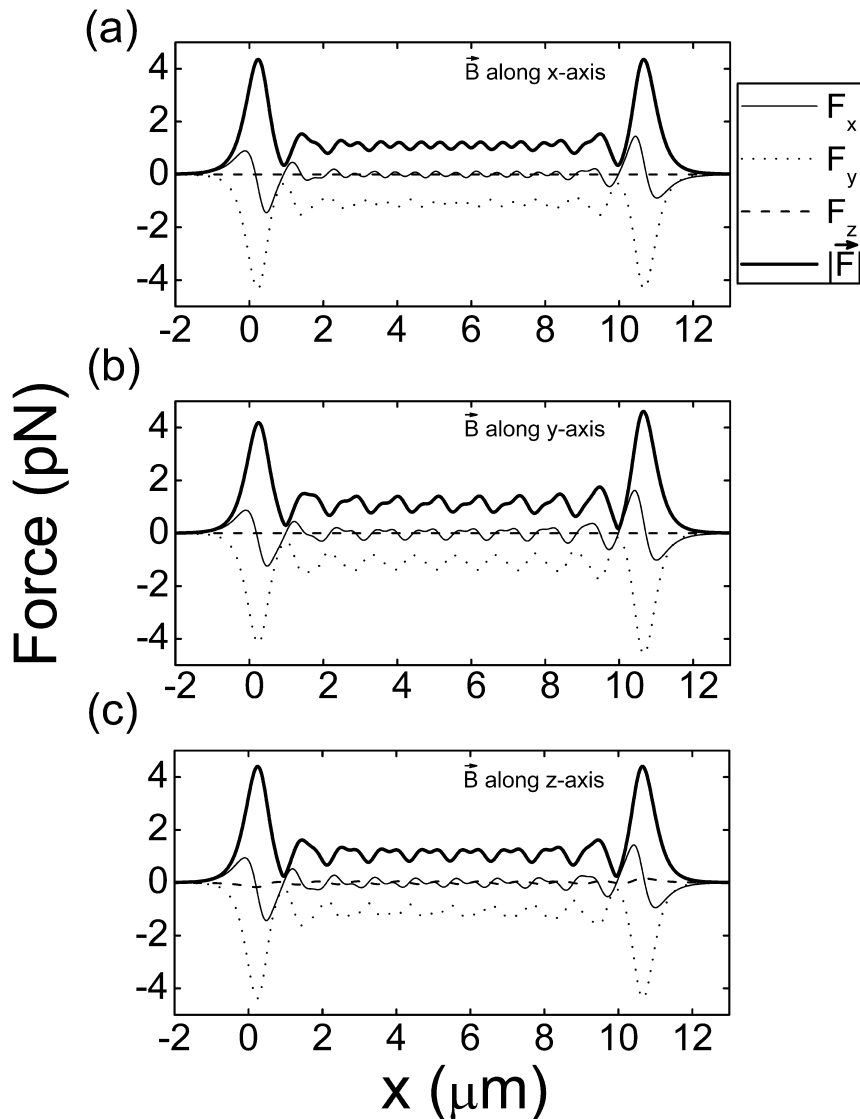


Figure 5.3: Force components acting on the magnetite cluster as a function of the x-coordinate of the magnetite cluster, while the y- and z- coordinates are  $0.8 \mu\text{m}$  and  $0 \mu\text{m}$  respectively (see Fig. 2.14) calculated at different orientations of the external magnetic field vector: plots (a), (b) and (c) correspond to the alignment of the magnetic field vector along the x-, y- and z-axes respectively. The x-, y- and z-components of the force vector are shown with thin-solid, dotted and dashed lines respectively. Thick lines show the dependence of the force vector magnitude on the x-coordinate of the magnetite cluster.

change of external magnetic field orientation from x to z, while the plots in the right part of the figure show the differences between the force components corresponding to the change from x- to y-orientation. Plots (a), (b) and (c) in Fig. 5.4 show the



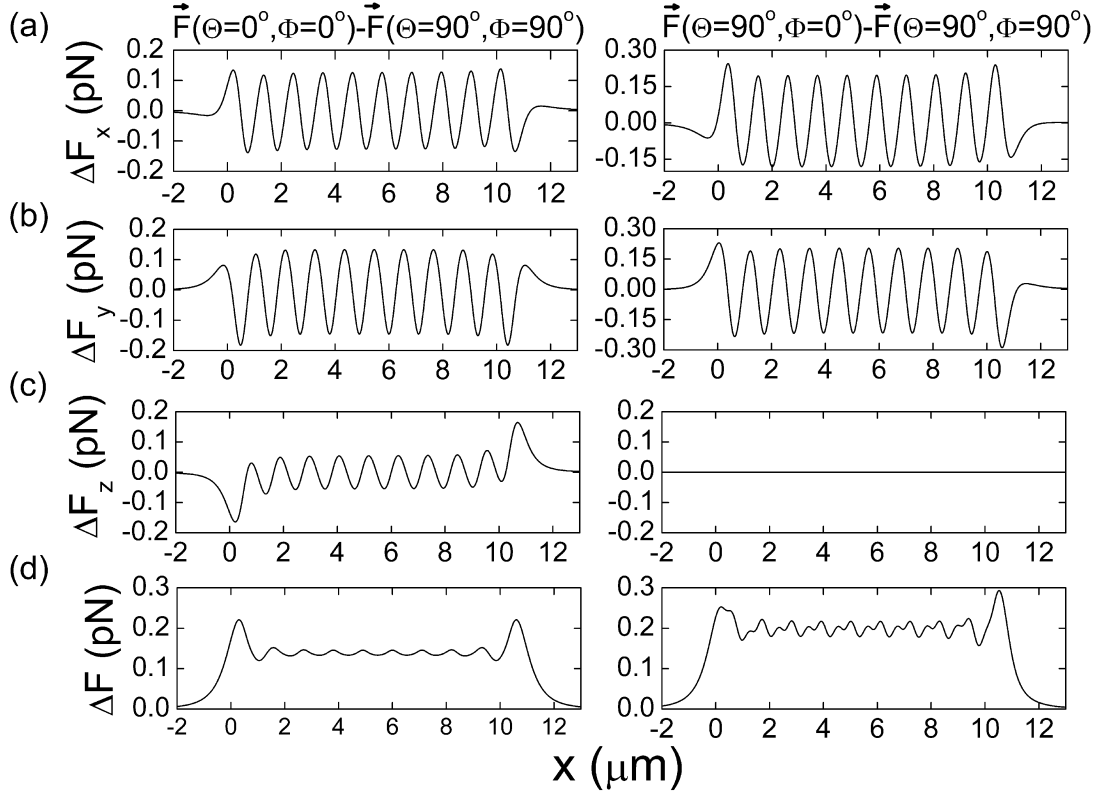


Figure 5.4: Difference in force components acting on the magnetite cluster at different orientations of the external magnetic field vector. The plots in the left part of the figure show the difference between the force components corresponding to the change of external magnetic field orientation from x to z, while plots in the right part of the figure show the differences between the force components corresponding to the change from x- to y-orientation are shown. Plots (a), (b) and (c) show the differences arising in the x-, y- and z-components of the force vector as a function of the x-coordinate of the magnetite cluster. The x-dependence of the magnitude of the force difference vector is shown in plots (d) of the figure. The y- and z-coordinates of the magnetite cluster are  $0.8 \mu\text{m}$  and  $0 \mu\text{m}$  respectively.

differences arising in the x-, y- and z-components of the force vector as a function of the x-coordinate of the magnetite cluster. The difference of force components are defined as follows:

$$\Delta F_x(\Omega_1) = F_x(\Omega_1) - F_x(\Omega_0) \quad (5.1)$$

$$\Delta F_y(\Omega_1) = F_y(\Omega_1) - F_y(\Omega_0) \quad (5.2)$$

$$\Delta F_z(\Omega_1) = F_z(\Omega_1) - F_z(\Omega_0), \quad (5.3)$$

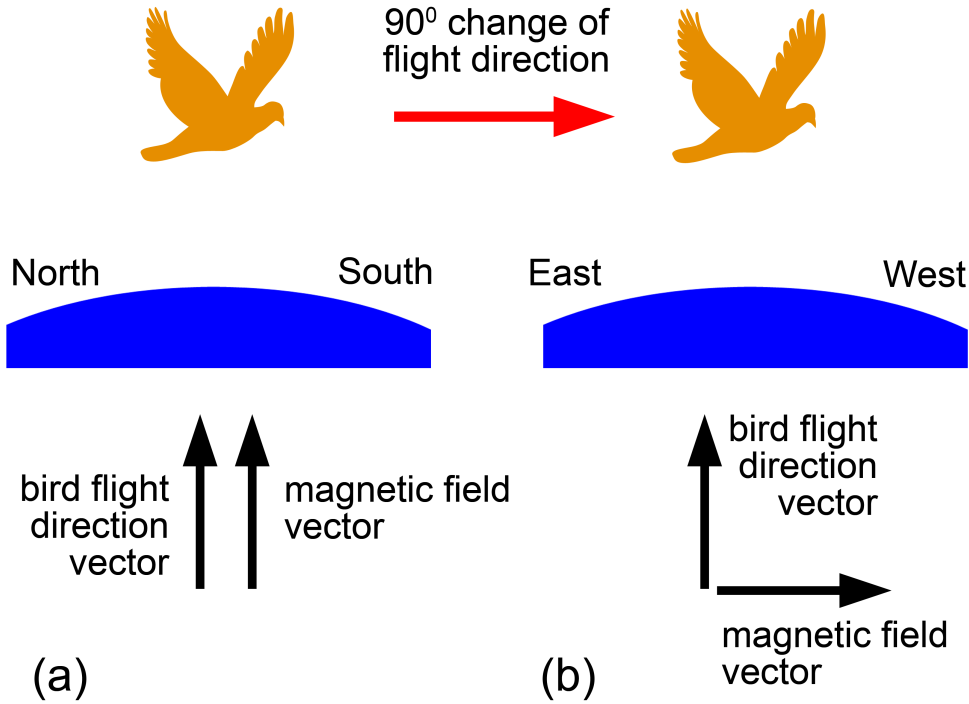


Figure 5.5: Schematic illustration of the 90° change of the direction of the external magnetic field through the magnetoreceptor system. Plot (a): the bird flying from North to South has the magnetoreceptor system (see Fig. 2.14) aligned with the direction of the geomagnetic field. Plot (b): the bird changed its course to East→West causing the geomagnetic field vector to become perpendicular to the magnetoreceptor system.

where  $\Omega_1$  denotes the direction of the external magnetic field, which is characterized either by  $(\Theta = 0^\circ, \Phi = 0^\circ)$  or  $(\Theta = 90^\circ, \Phi = 0^\circ)$ .  $\Omega_0$  denotes the "reference direction", which is characterized by  $(\Theta = 90^\circ, \Phi = 90^\circ)$ . The x-dependence of the magnitude of the force difference vector is shown in plots (d) in Fig. 5.4. The magnitude of the force difference vector is defined as:

$$\Delta F(\Omega_1) = \sqrt{\Delta F_x^2(\Omega_1) + \Delta F_y^2(\Omega_1) + \Delta F_z^2(\Omega_1)} \quad (5.4)$$

Figure 5.4 shows that the 90° change in the direction of the external magnetic field changes the force acting on the magnetite cluster by 0.1-0.2 pN (see plots (d) in Fig. 5.4). In the next section, the influence of this force on the probability of

opening the mechanosensitive ion channels is discussed.

The described 90° change in direction of the external magnetic field arises, for example, if a bird changes its flight route direction from North→South to East→West. A schematic illustration for such behavior is shown in Fig. 5.5

## 5.4 Model for a Transducer Mechanism of the Geomagnetic Field

In this subsection a model for a transducer mechanism of the geomagnetic field based on the magnetite clusters interacting with maghemite platelets and the external field is discussed. Two possible transducer mechanisms are presented, as the connection between the cluster and the membrane is not fully understood. The mechanism presented here need further experimental support. It should be technically feasible to remove the layer of skin with the sensory endings still attached to the afferent nerves and perform gentle distortions that may mimic effects of magnetic fields. This kind of data may hint to the preferential direction and magnitude of the expected dendrite deformations.

Depending on the magnetic field strength, the magnetite cluster can exert forces on the membrane and activate certain mechanosensitive ion channels<sup>1</sup> that modulates the flux of ions into the cell. Gating these channels will alter the membrane potential and produce a receptor potential that can be transmitted to other cells – thus influencing the behavior of the bird. A typical example of a mechanosensitive

---

<sup>1</sup>An ion channel is an integral membrane protein or more typically an assembly of several proteins. Such "multi-subunit" assemblies usually involve a circular arrangement of identical or homologous proteins closely packed around a water-filled pore through the plane of the membrane or lipid bilayer. While some channels permit the passage of ions based solely on charge, the archetypal channel pore is just one or two atoms wide at its narrowest point. It conducts a specific species of ion, such as sodium or potassium, and conveys them through the membrane single file – nearly as quickly as the ions move through free fluid. In some ion channels, passage through the pore is governed by a "gate," which may be opened or closed by chemical or electrical signals, temperature, or mechanical force, depending on the variety of channel. Because "voltage-gated" channels underlie the nerve impulse and because "transmitter-gated" channels mediate conduction across the synapses, channels are especially prominent components of the nervous system. Indeed, most of the offensive and defensive toxins that organisms have evolved for shutting down the nervous systems of predators and prey (e.g., the venoms produced by spiders, scorpions, snakes, fish, bees, sea snails and others) work by plugging ion channel pores. In addition, ion channels figure in a wide variety of biological processes that involve rapid changes in cells, such as cardiac, skeletal, and smooth muscle contraction, epithelial transport of nutrients and ions, T-cell activation and pancreatic beta-cell insulin release. In the search for new drugs, ion channels are a favorite target.

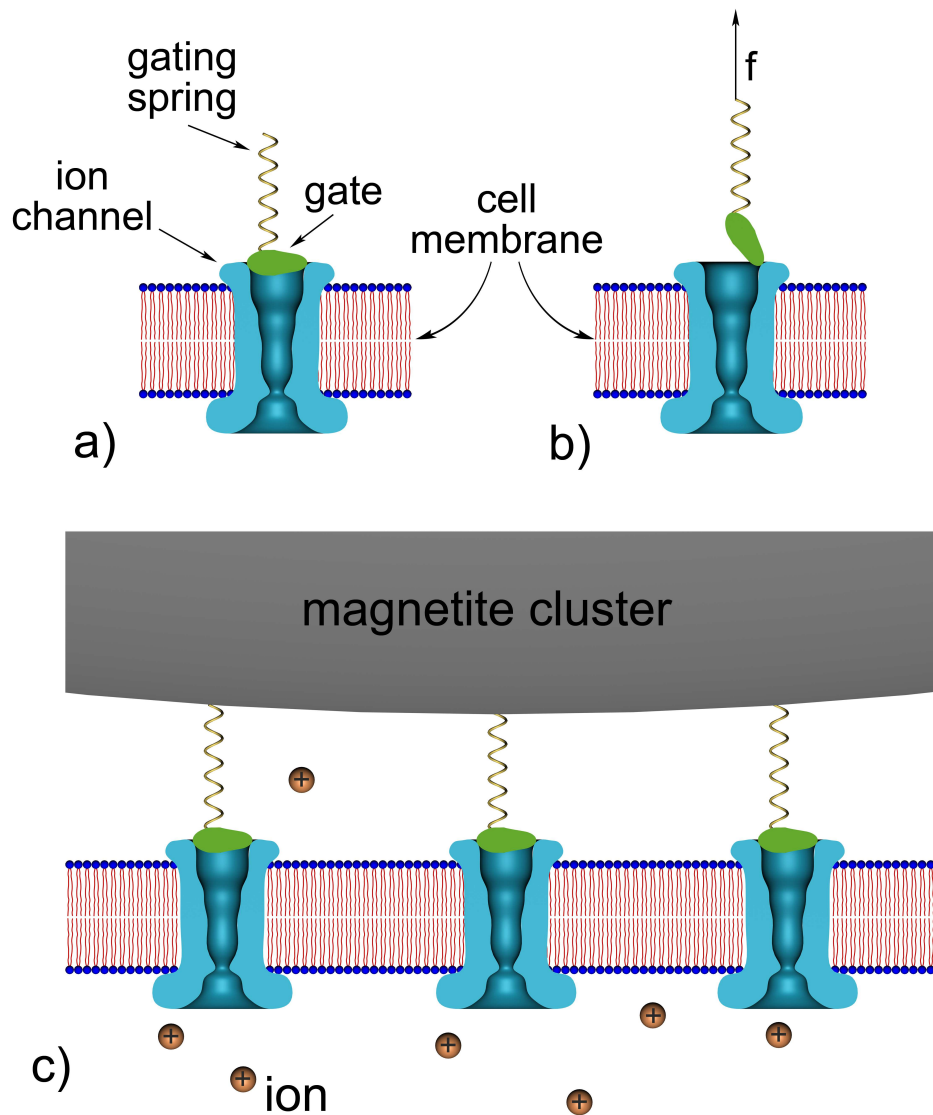


Figure 5.6: Schematic illustration of the gating-spring transducer mechanism of the geomagnetic field. The opening/closing of the mechanosensitive ion channel is regulated by the gate, which is connected to an elastic element, the gating spring. The channel has two conformations, closed (a) and open (b), being in thermal equilibrium. The gating springs are connected to the magnetite cluster (c) which produces an external pull or push on the gates.

ion channel is the transduction channel of a hair cell (for review see Refs. [221–225]). A schematic illustration of an ion channel gated by mechanical force is shown in Fig. 5.6. The channel is assumed to have two conformations: closed (see Fig. 5.6a) and open (see Fig. 5.6b). Because the gate swings through a distance of  $\lambda_0$  upon

opening, an external force  $f$  changes the energy difference between open and closed states and can bias the channel to spend more time in its open state. The gating springs are connected to the magnetite cluster (see Fig. 5.6c) which produces an external pull on the gates. The magnitude of the external force can be estimated. Consider an animal rotating by  $90^\circ$  (see Fig. 5.5), the direction of the earth's magnetic field lines through the sensor changes, causing a force difference of about 0.2 pN (see subsection 5.3) which is transmitted to the membrane.

If the work done in gating the channel is  $\Delta E$  and the equilibrium probability of the open state is  $p_O$ , then according to statistical physics:

$$p_O = \frac{1}{1 + \exp\left(\frac{\Delta E}{kT}\right)}. \quad (5.5)$$

Assuming that the magnetite cluster exerts a pull on the gate then the expression for  $\Delta E$  reads as [226, 227]:

$$\Delta E = \Delta\varepsilon - f\lambda_0, \quad (5.6)$$

here the first term represents the change of the intrinsic energy between the open and the closed states of the channel and the second term shows the work of the external force required for opening the channel.  $\lambda_0$  is the displacement value of the gate. For the mechanosensitive ion channels in hair cells,  $\lambda_0 \approx 4$  nm [222, 226]. Substituting Eq. (5.6) into Eq. (5.5) one obtains the probability for the channel to be open in the presence of an external force:

$$p = \frac{1}{1 + \exp\left(\frac{\Delta\varepsilon - f\lambda_0}{kT}\right)}. \quad (5.7)$$

Thus, the change of the channel opening probability due to the applied force is:

$$\eta = \frac{p - \tilde{p}_O}{\tilde{p}_O} \cdot 100\% = \frac{\exp\left(\frac{\Delta\varepsilon}{kT}\right) \left(\exp\left(\frac{f\lambda_0}{kT}\right) - 1\right)}{\exp\left(\frac{f\lambda_0}{kT}\right) + \exp\left(\frac{\Delta\varepsilon}{kT}\right)} \cdot 100\%, \quad (5.8)$$

where  $\tilde{p}_O$  is the probability for the channel to be open if no external force is applied (i.e.  $f = 0$ ). Usually [226], it is assumed that  $\Delta\varepsilon = 0$ , but in general it is not because the gate can build hydrogen bonds with the membrane, which brake when the gate is opened. Thus  $\Delta\varepsilon > 0$ .

The dependence of the change of channel opening probability,  $\eta$  on  $\Delta\varepsilon$  (thick line) is shown in Fig. 5.7. This curve was obtained for  $f = 0.2$  pN. From Fig. 5.7

and from Eq. (5.8) it follows that the change of the channel opening probability saturates at large values of  $\Delta\varepsilon$ . The limiting value is

$$\eta_{max} = \left( \exp\left(\frac{f\lambda_0}{kT}\right) - 1 \right) \cdot 100\%. \quad (5.9)$$

For the given  $f$ ,  $\lambda_0$  and  $T$ :  $\eta_{max} = 21\%$ , being the maximal possible change of the channel opening probability in the suggested mechanism. If  $\Delta\varepsilon = 0$  then

$$\eta_0 = \frac{\exp\left(\frac{f\lambda_0}{kT}\right) - 1}{1 + \exp\left(\frac{f\lambda_0}{kT}\right)} \cdot 100\%. \quad (5.10)$$

With the given  $f$ ,  $\lambda_0$  and  $T$ :  $\eta_0 = 9.6\%$ . If  $\Delta\varepsilon$  is positive then  $\eta$  is somewhere between  $\eta_0$  and  $\eta_{max}$ .

Another possible transducer mechanism of the geomagnetic field is based on the elastic deformation of the membrane. The deformation mechanism might arise as an addition to the gating mechanism or it could be an alternative to it. It is difficult to specify the precise transducer mechanism because little information is available on the structure which connects the magnetite clusters with the cell membrane.

Let us discuss the deformation mechanism of the channel opening. Figure 5.8a shows the non deformed membrane, while Fig. 5.8b and Fig. 5.8c show the possible membrane deformation caused by either pull (see Fig. 5.8b) or push (see Fig. 5.8c) of the magnetite cluster on the membrane. Both deformation cases are physically identical since the work needed to deform the membrane in both cases is equal. The connections of the magnetite cluster with the membrane are shown schematically with the springs. Note that the ion channel, the membrane and the magnetite cluster in Fig. 5.8 are drawn approximately to the correct scale, while the ions are shown schematically. The non-deformed membrane corresponds to the case of low magnetic field acting on the magnetite cluster (see Fig. 5.8a), while an increase in the magnetic field strength creates a stress situation (see Fig. 5.8b and Fig. 5.8c).

With  $f$  being the force difference and  $\gamma$  being the membrane surface tension coefficient the deformation criteria is given by

$$f\Delta x = \gamma\Delta S, \quad (5.11)$$

where  $\Delta x$  is the displacement of the cluster and  $\Delta S$  is the change in the membrane surface area. Assuming that the membrane deformation has a spherical profile with the same radius as the magnetite cluster one can introduce two deformation

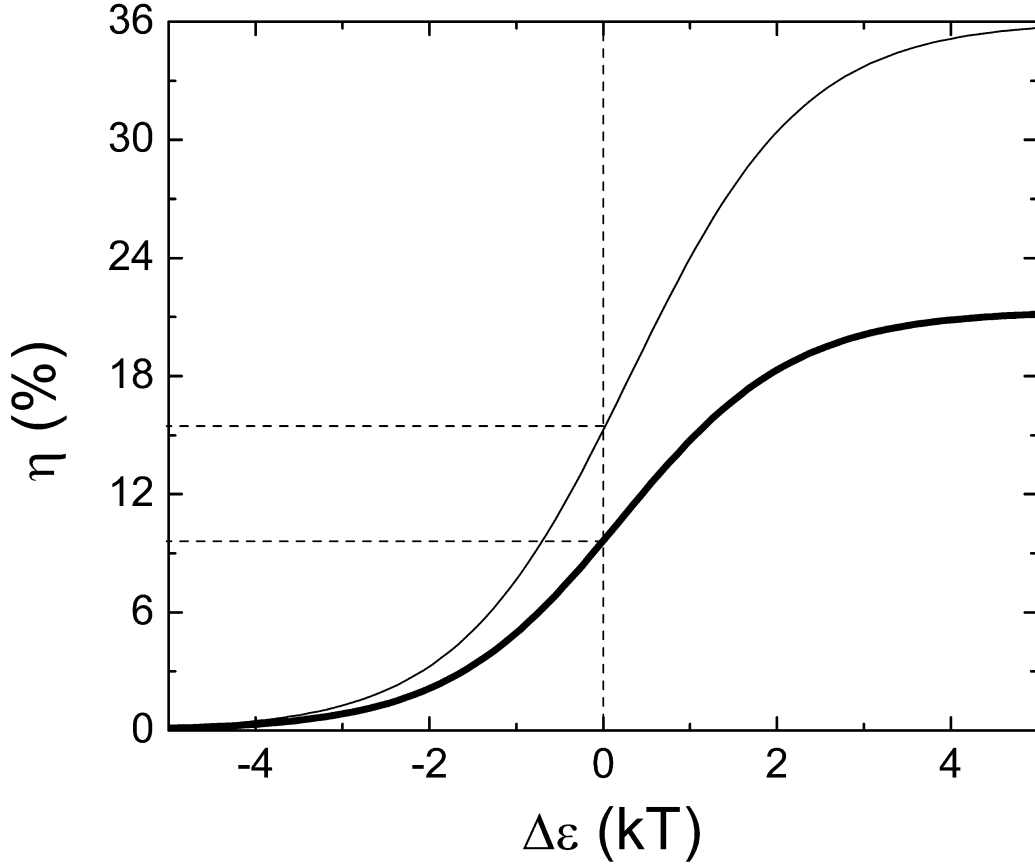


Figure 5.7: Change of the mechanosensitive ion channel opening probability calculated as the function of the intrinsic energy between the open and the closed states of the channel. Thick line corresponds to the gating-spring transducer mechanism and thin line corresponds to the mechanism based on the elastic deformation of the membrane (thin line). The change of channel opening probability for the gating-spring transducer mechanism and for the mechanism based on the elastic deformation of the membrane were calculated using Eq. (5.8) and Eq. (5.20) respectively.

increments:  $\Delta x$  and  $\Delta y$ , which describe the deformation region (see Fig. 5.8b-c and 5.4). The assumption on the deformation radius of the membrane is correct in the vicinity of the point where the force is applied [228]. This is a well known fact from mathematical physics of elastic membrane deformation [228]. From simple geometrical considerations (see Fig. 5.4) it follows that:

$$\Delta y = \sqrt{2R_0\Delta x - \Delta x^2}, \quad (5.12)$$

where  $R_0$  is the radius of the magnetite cluster and  $\Delta y$  is the radius of the defor-

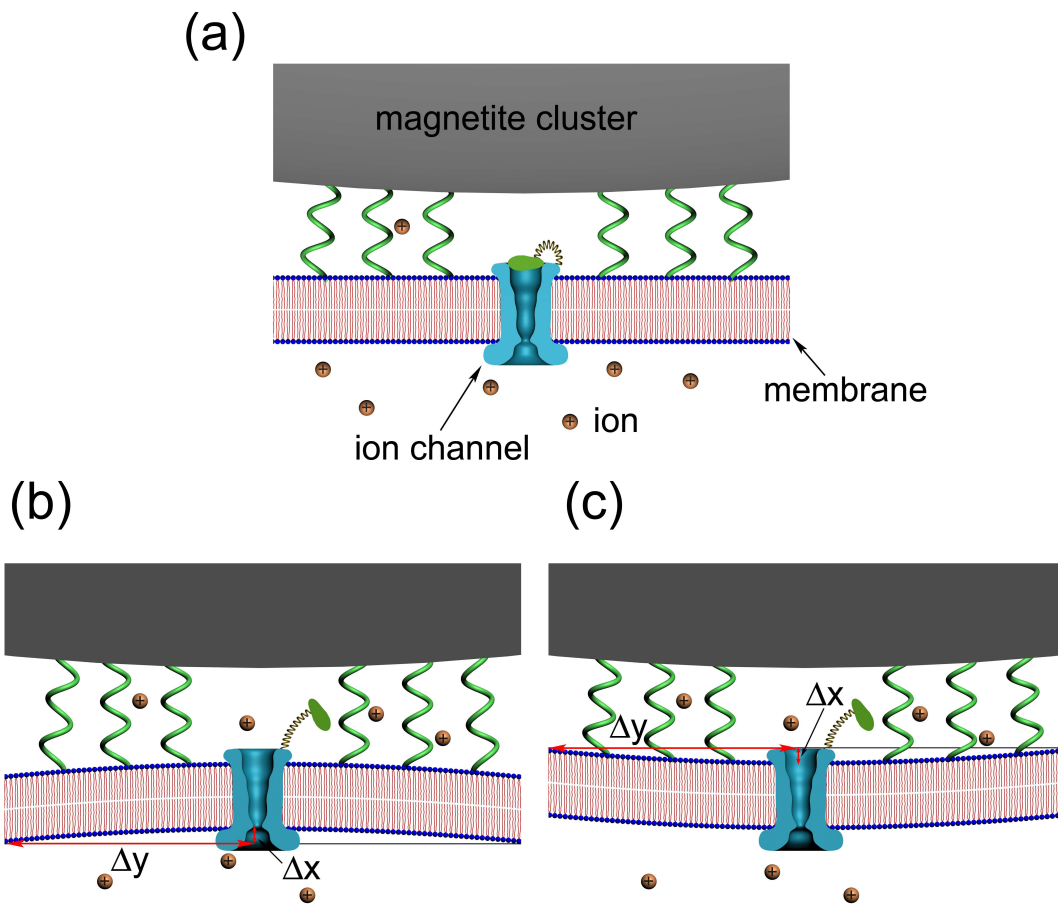


Figure 5.8: Schematic illustration of the transducer mechanism of the geomagnetic field based on the elastic deformation of the membrane. The external magnetic field causes the change in the pressure which the magnetite cluster puts on the cell membrane, causing its deformation. The non-deformed membrane corresponding to the case of low magnetic field is shown in part (a) of the figure. The increase of the magnetic field creates a stress situation leading to the membrane deformation caused by either push (b) or pull (c) of the magnetite cluster on the membrane. The magnetite cluster is shown schematically atop the membrane. The connections of the magnetite cluster with the membrane is schematically shown with the springs. Note that the ion channel, the membrane and the magnetite cluster are drawn approximately in the correct scale, while the ions are shown schematically.

mation zone (see Fig. 5.8b). The magnetite cluster deforms a certain area of the membrane. Let  $S_0$  and  $S_1$  be this area in the normal and stress cases respectively (see Fig. 5.4):



$$S_0 = \pi \Delta y^2 \quad (5.13)$$

$$S_1 = R_0^2 \int_0^{\vartheta_{cr}} \sin \vartheta \int_0^{2\pi} d\vartheta d\varphi = 2\pi R_0^2 [1 - \cos \vartheta_{cr}], \quad (5.14)$$

where  $\vartheta_{cr}$  is defined in Fig. 5.4 as

$$\cos \vartheta_{cr} = \frac{R_0 - \Delta x}{R_0} = \frac{\sqrt{R_0^2 - \Delta y^2}}{R_0}. \quad (5.15)$$

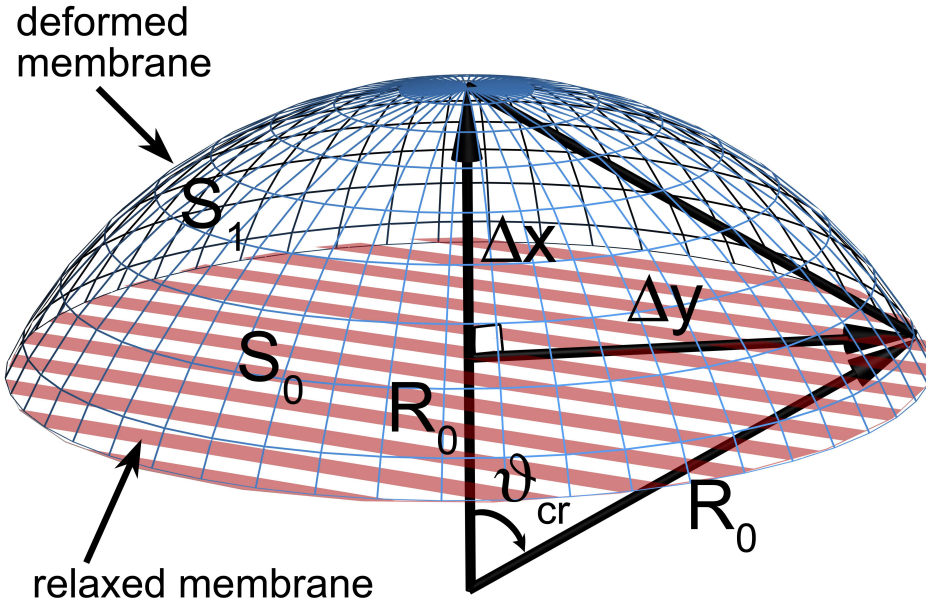


Figure 5.9: Schematic illustration of the membrane deformation caused by the external magnetic field.  $\Delta x$  and  $\Delta y$  are the deformation increments describing the membrane deformation.  $R_0$  is the radius of the deformation,  $S_0$  and  $S_1$  are the areas of the membrane deformation region corresponding to the non-deformed (relaxed) and stress (deformed) cases respectively.

Substituting (5.15) into (5.14) one obtains the final expression for  $S_1$ . The change of membrane area of the deformation is then given by

$$\Delta S = S_1 - S_0 = (2\pi R_0 \Delta x) - (2\pi R_0 \Delta x - \pi \Delta x^2) = \pi \Delta x^2. \quad (5.16)$$

Substituting (5.16) in (5.11) one obtains:

$$\Delta x = \frac{f}{\gamma\pi}, \quad (5.17)$$

with  $\Delta x$  being the characteristic value of membrane deformation. Finally, substituting Eq. (5.17) into Eq. (5.16) one obtains:

$$\Delta S = \frac{f^2}{\pi\gamma^2}. \quad (5.18)$$

Note that  $\Delta x$  and  $\Delta S$  do not depend on the radius of membrane deformation. The work,  $A_{def}$ , on membrane deformation is given by:

$$A_{def} = \gamma\Delta S = \frac{f^2}{\pi\gamma}. \quad (5.19)$$

Thus the change in the channel opening probability caused by the membrane deformation is:

$$\eta^{def} = \frac{p - \tilde{p}_0}{\tilde{p}_0} \cdot 100\% = \frac{\exp\left(\frac{\Delta\varepsilon}{kT}\right) \left( \exp\left(\frac{f^2}{\pi\gamma kT}\right) - 1 \right)}{\exp\left(\frac{f^2}{\pi\gamma kT}\right) + \exp\left(\frac{\Delta\varepsilon}{kT}\right)} \cdot 100\%. \quad (5.20)$$

The dependence of the change of channel opening probability caused by the membrane deformation on  $\Delta\varepsilon$  (thin line) is shown in Fig. 5.7. This curve was obtained for  $f = 0.2$  pN and  $\gamma = 0.01$  dyn/cm =  $10^{-5}$  N/m, which is the typical surface tension coefficient of a membrane [229–237]. The tension of membranes has been extensively studied during the last decades. For a review, see the Refs. [208, 234–241]. The resting tension of chicken neurons was estimated to be  $3 \cdot 10^{-6}$  N/m [235], while in normal molluscan neuron it is  $4 \cdot 10^{-5}$  N/m [236]. The elastic shear modulus of a red blood cell was measured to be  $6.6 \cdot 10^{-6}$  N/m [237]. The differences in the various tension coefficients published earlier (see e.g. Refs. [229–237]) is beyond the scope of this thesis though it will be considered in the future. Therefore, a characteristic value of membrane tension equal to  $10^{-5}$  N/m is used. The maximal value of  $\eta^{def}$  is  $\eta_{max}^{def} = 36\%$ , being 1.7 times greater than in the case of the gate-spring mechanism discussed above. If  $\Delta\varepsilon = 0$  then  $\eta_0^{def} = 15\%$ . Since  $\Delta\varepsilon$  is expected to be positive then  $15\% < \eta^{def} < 36\%$ .

It has been demonstrated that in both of the considered transducer mechanisms the forces which the magnetite cluster exerts on the membrane are sufficient to influence the probability of the mechanosensitive ion channel opening. From the

performed analysis it follows that the change of magnetic force caused by a  $90^\circ$  change of the external geomagnetic field produces a change in the channel opening probability in the range of 15%-30%.

Semm and Beason [49] have suggested that the bird's magnetoreceptor system can respond to a 1% change of the normal geomagnetic field. The change of the geomagnetic field of 0.01 G changes the forces acting on the magnetite cluster by approximately 0.004 pN. This leads to the change of channel opening probability on the order of 0.5 %.

Another important feature of the suggested magnetoreception mechanism that is worth noting, is the so-called **safety-principle**. Experiments of Fleissner *et al.* [58–61, 125] show that the dendrite contains about 10-15 magnetoreceptor units, which have a similar behavior in an external magnetic field. When the dendrite is subject to the external field, the repetition of the magnetoreceptor units increases the functional safety of the whole dendrite magnetoreception process.

## 5.5 Interaction of Dipoles of Finite Size

In this section the size of the iron minerals is taken into consideration in order to account more precisely for the interaction of the magnetite cluster with the chain of maghemite platelets. The aim of this discussion is to strengthen the suggested magnetoreception mechanism which has been shown to be feasible in the model case of interacting point-like dipoles.

### 5.5.1 Potential Energy Surface of the Magnetite Cluster

The potential energy surface of the magnetite cluster is shown in Fig. 5.10 as a function of coordinates  $x$  and  $y$ , while  $z=0 \mu\text{m}$  (see Fig. 2.14). The surfaces shown in plots (a), (b) and (c) in Fig. 5.10 were calculated for the external magnetic field vector oriented along the  $x$ -,  $y$ - and  $z$ -axes respectively. Similarly to Fig. 5.1 – due to the finite size of the magnetite cluster, the excluded region on the potential energy surfaces in Fig. 5.10 is shown with the gray rectangle in the center of the potential energy surfaces. The maghemite platelets are shown in Fig. 5.10 with black rectangles.

The potential energy surfaces shown in Fig. 5.10 were calculated with the use of Eq. (3.124) (see subsection 3.2.5 for details) and are topologically close to the

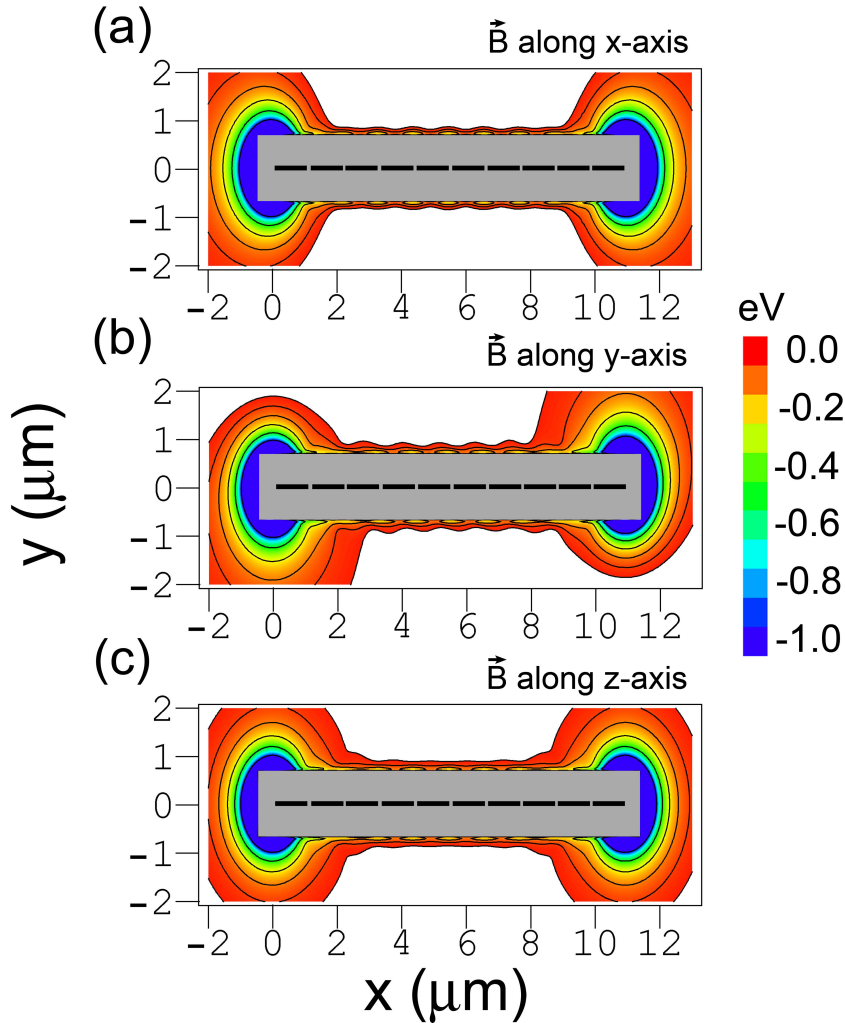


Figure 5.10: Potential energy surfaces of the magnetite cluster calculated in the case when the integration over the volume of the maghemite platelets and of the magnetite cluster is performed (see subsection 3.2.5). The potential energy of the magnetite cluster is plotted as a function of x- and y-coordinates of the magnetite cluster, while  $z=0 \mu\text{m}$  (see Fig. 2.14). The energy is calculated at different orientations of the external magnetic field vector. Plots (a), (b) and (c) correspond to the alignment of the external magnetic field along the x-, y- and z-axes respectively. The maghemite platelets are shown with black rectangles. The gray rectangle in the center of the potential energy surfaces shows the region, where the magnetite cluster can not be placed, due to its finite size. The energy scale is given in eV. The equipotential lines are shown for the energies -0.03, -0.06, -0.12, -0.24, -0.48 and -0.96 eV.

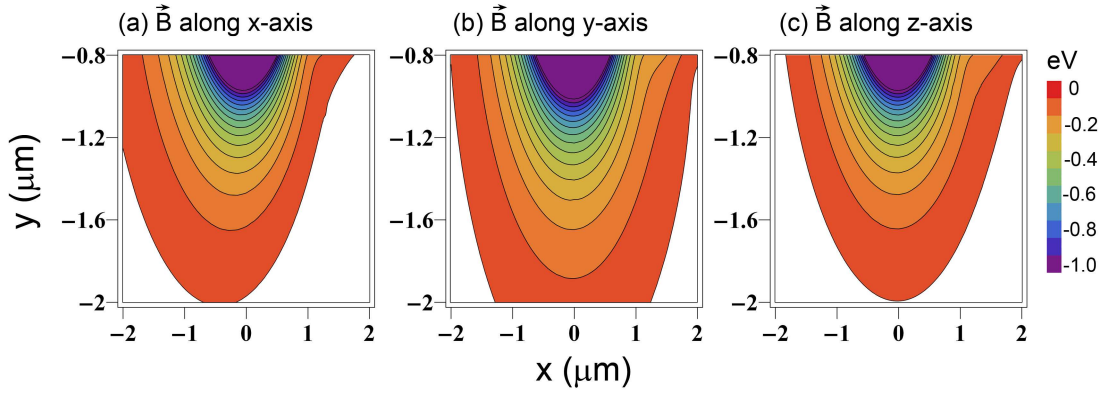


Figure 5.11: The region of the potential energy surface in the vicinity of the maghemite platelets chain tip calculated as a function of x- and y-coordinates of the magnetite cluster, while  $z=0$   $\mu\text{m}$  (see Fig. 2.14). The energy is calculated at different orientations of the external magnetic field vector. Plots (a), (b) and (c) correspond to the alignment of the external magnetic field along the x-, y- and z-axes respectively. The figure shows the small differences in energy, arising due to a  $90^\circ$  change of the direction of the magnetic field.

corresponding potential energy surfaces obtained for the point-like dipoles shown in Fig. 5.1. The potential energy surfaces shown in Fig. 5.10 have two strong minima at the tips of the chain of maghemite platelets, which are also found in the point-like dipole model (see Fig. 5.1). The energies of these minima in Fig. 5.10 are -15.6 eV, being 7.1 eV lower than the corresponding value for the point-like dipoles. The fact that the minima are found in both models proves that the energetically most favorable attachment of the magnetite cluster occurs at the tip of the chain.

Another significant difference between the potential energy surface for the point-like dipoles and dipoles of finite size concerns the valleys at  $y \approx \pm 0.7$   $\mu\text{m}$ ,  $z=0$   $\mu\text{m}$ , which are found for the point-like dipoles but are absent for the dipoles of finite size (see Figs. 5.1 and 5.10). The reason why the valleys vanish is a simple one. The distance between the maghemite platelets is 0.1  $\mu\text{m}$ , while the size of a platelet is 1  $\mu\text{m}$ . The direction of magnetic moments of the platelets do not change much if the direction of the external magnetic field changes (see discussion in subsection 5.3) and therefore the chain of platelets behaves like a solid magnetic bar, that attracts magnetic particles only at its tips.

To stress the differences arising in the potential energy of the magnetite cluster at three principal orientations of the external magnetic field, Fig. 5.11 shows the region

of the potential energy surface in the vicinity of the maghemite platelets chain tip calculated as a function of x- and y-coordinates of the magnetite cluster, while  $z=0$   $\mu\text{m}$ . The surfaces shown in plots (a), (b) and (c) in Fig. 5.11 were calculated for the external magnetic field vector oriented along the x-, y- and z-axes respectively. This figure shows that the changes in the potential energy due to a  $90^\circ$  change of the direction of the magnetic field are relatively small, and are on the order of 0.1 eV.

### 5.5.2 Forces Acting on the Magnetite Cluster

In subsection 5.3, it was shown that an important characteristic that determines the feasibility of the magnetoreception mechanism, is the difference between the forces acting on the magnetite cluster at different orientations of the external magnetic field vector. The force differences calculated for the dipoles of finite size are shown in Fig. 5.12. The plots in the left part of Fig. 5.12 show the differences between the force components arising due to the  $x \rightarrow z$  change of the direction of the external magnetic field vector, while plots in the right part of the figure show the differences between force components arising due to the  $x \rightarrow y$  change. Plots (a), (b) and (c) in Fig. 5.12 show the differences arising in the x-, y- and z-components of the force vector as a function of the x-coordinate of the magnetite cluster. The x-dependence of the magnitude of the force difference vector is shown in plots (d) in Fig. 5.12. In the case of dipoles of finite size, the characteristic change in force caused by the external field of 0.5 G is 0.05-0.1 pN (see plots (d) in Fig. 5.12), which is about two to three times lower than the value obtained for the case of point-like dipoles (see Fig. 5.4).

Thus, substituting  $\Delta F = 0.1$  pN in Eq. (5.8) and Eq. (5.20), one obtains the change in the channel opening probability in the gating-spring transducer mechanism,  $\eta$ , and in the mechanism based on the elastic deformation of the membrane,  $\eta^{def}$ . Thus,  $\eta_0 = 5\%$ ,  $\eta_{max} = 10\%$  and  $\eta_0^{def} = 4\%$ ,  $\eta_{max}^{def} = 8\%$ . Note that the values of  $\eta^{def}$  are smaller than the values of  $\eta$ . This happens because the work performed in the gating-spring transducer mechanism is linearly proportional to the force (see Eq. (5.6)), while the work performed on the membrane deformation is proportional to its second power (see Eq. (5.19)). Therefore the channel opening probability in the mechanism based on the elastic deformation of the membrane decreases faster with decrease of the applied force.

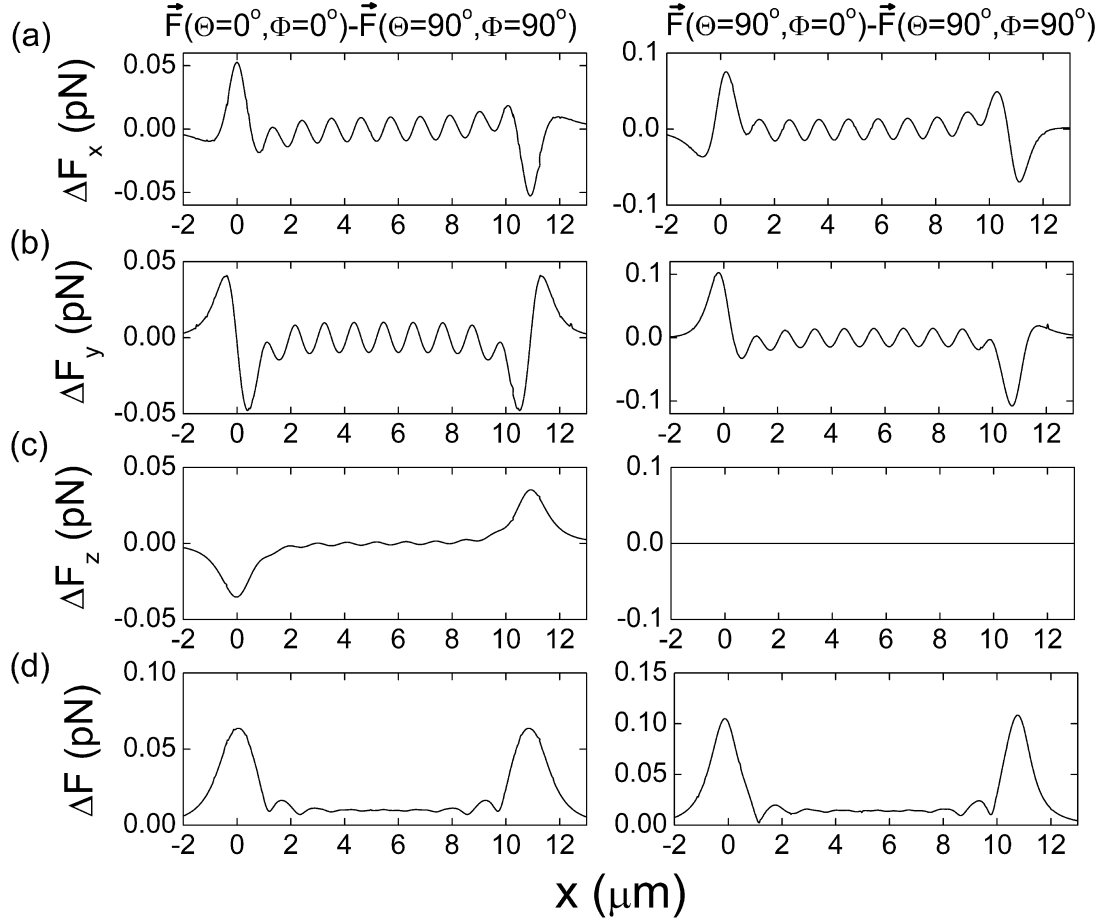


Figure 5.12: Difference in forces acting on the magnetite cluster at different orientations of the external magnetic field vector calculated in the case when the integration over the volume of the maghemite platelets and of the magnetite cluster is performed. Plots in the left part of the figure show the difference between the force components arising due to the  $x \rightarrow z$  change of the direction of the external magnetic field vector, while plots in the right part of the figure show the differences between force components arising due to the  $x \rightarrow y$  change. Plots (a), (b) and (c) show the differences arising in the x-, y- and z-components of the force vector as a function of the x-coordinate of the magnetite cluster. The x-dependence of the magnitude of the force difference vector is shown in plots (d) of the figure. The y- and z-coordinates of the magnetite cluster are  $0.8 \mu\text{m}$  and  $0 \mu\text{m}$  respectively.

Fig. 5.12 shows that away from the tips of the maghemite chain the force differences are significantly smaller than the force differences at its tips (see plots (d) in Fig. 5.12). Note that this is different from the case of point-like dipoles, where the force differences were of about the same order of magnitude along the whole chain of

maghemite platelets (see plots (d) in Fig. 5.4). This happens because in the case of dipoles of finite size there are no valleys on the potential energy surface at  $y \approx \pm 0.7 \mu\text{m}$ ,  $z = 0 \mu\text{m}$ , which are present for the point-like dipoles, causing additional forces on the magnetite cluster in this region.

## 5.6 Magnetic Window of the Iron-Mineral-Based Magnetoreception Mechanism

The behavior studies of avian magnetoreception reveal that birds become disoriented outside a fairly narrow functional window around the local geomagnetic field. It has been demonstrated [15, 75] that the birds become disoriented when the intensity of the local geomagnetic field is reduced or increased by more than 25 %. The functional window of the magnetic compass is presently not fixed, however, it could be adjusted to intensities outside the normal functional range by exposing the birds to these intensities [126].

With Eq. (5.7) it is possible to establish the magnetic field intensities at which the operation of the iron-mineral-based magnetoreceptor mechanism is possible. If the force transmitted to the gate of the mechanosensitive ion channel is sufficiently large, then the channel will always be open and no magnetic field effect could be observed. The magnetic field intensity at which the ion channel opening probability reaches 100 per cent (or is close to 100 per cent) defines the **magnetic window** of operation of the iron-mineral-based magnetoreceptor.

In order to determine the magnetic field strength at which the magnetoreception process is violated, the probability of mechanosensitive ion channel opening,  $p$ , is plotted as a function of the force applied to the gate,  $f$ , calculated using Eq. (5.7) for different values of the intrinsic energy between the open and the closed states of the channel, Fig. 5.13. The solid thick line was obtained for  $\Delta\varepsilon = 0 \text{ kT}$ , while the solid thin line, the dotted and dashed lines correspond to the values of  $\Delta\varepsilon = 1 \text{ kT}$ ,  $\Delta\varepsilon = 2 \text{ kT}$  and  $\Delta\varepsilon = 3 \text{ kT}$  respectively.

The fact that birds becomes disoriented at higher magnetic field strengths might be connected to the probability of the opening of mechanosensitive ion channels in the nerve cell membrane. Indeed, in higher magnetic fields, the forces transmitted to the gates become higher and the probability for the ion channels to be open increases. This fact is clearly illustrated in Fig. 5.13. If the intrinsic energy between the open and the closed states of the channel is zero ( $\Delta\varepsilon = 0$ ) then in the geomagnetic field



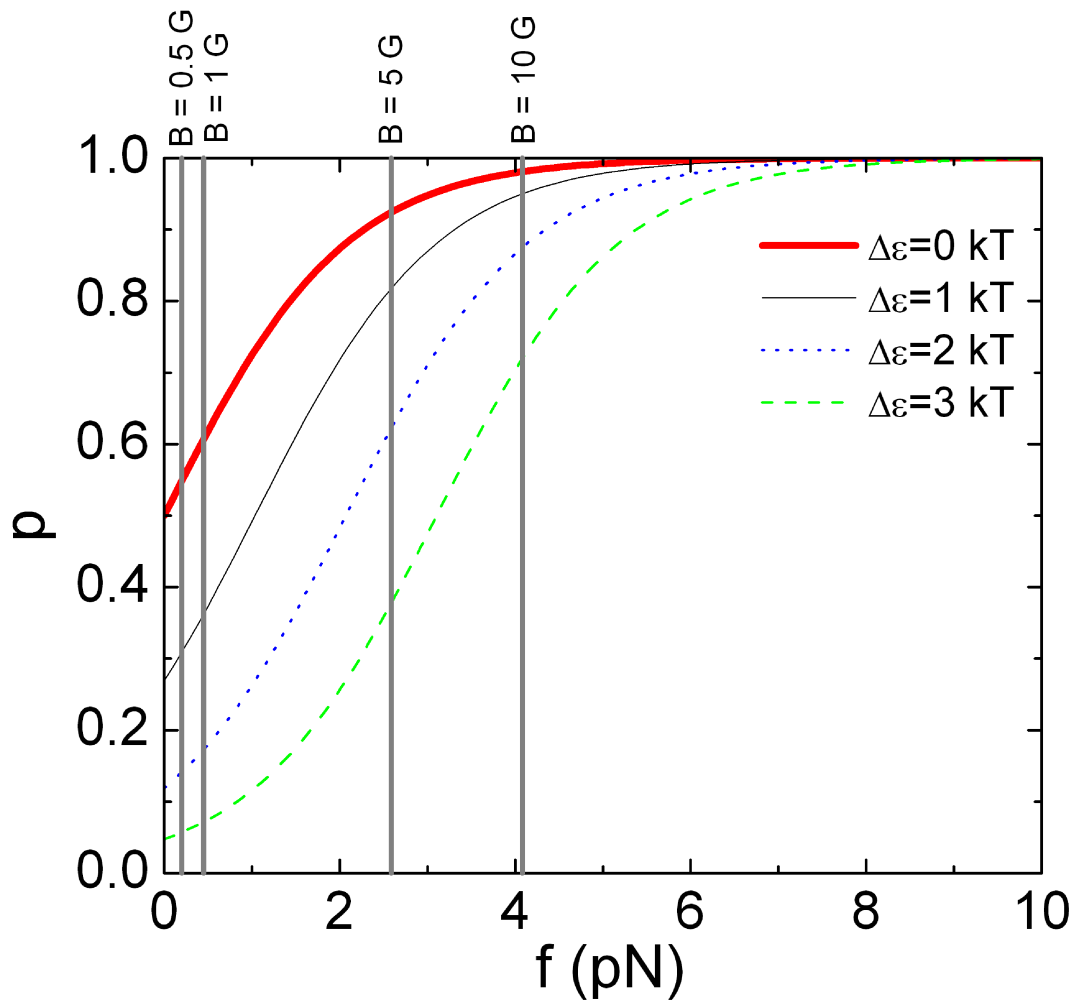


Figure 5.13: Probability of mechanosensitive ion channel opening,  $p$ , as a function of the force applied to the gate,  $f$ , calculated using Eq. (5.7) for different values of the intrinsic energy between the open and the closed states of the channel:  $\Delta\varepsilon = 0$  kT (solid thick line);  $\Delta\varepsilon = 1$  kT (solid thin line);  $\Delta\varepsilon = 2$  kT (dotted line);  $\Delta\varepsilon = 3$  kT (dashed line).  $T = 300$  K. The forces corresponding to the magnetic field strengths of 0.5, 1.0, 5.0 and 10.0 G are indicated with vertical lines.

(0.5 G) 55 % of all ion channels are open. A twofold increase of the intensity of the magnetic field (1 G) changes the probability of the ion channels to be open to 60 % (see Fig. 5.13).

The 1 G magnetic field is of particular interest because recent behavior studies [126] demonstrate that the flight orientation of European robins during the autumn migrational season can be significantly violated if the birds are put in magnetic fields

of 92000 nT = 0.92 G. However, the same studies also showed that birds were able to orient in the correct direction after an hour's pre-exposure in this higher magnetic intensity. The fact that the birds were still able to orient in the increased magnetic field is in qualitative agreement with the present observations. The probability of 60 % for the ion channels to be open is significantly smaller than 100 % when no magnetic field effect is possible. On the other hand, it is higher than the probability of 55 % which corresponds to the normal operation of the magnetoreceptor system. Therefore, if the birds are placed in an increased magnetic field, they first require some time (e.g. 1 hour) to reconfigure their magnetoreceptor system in the new environment. After this reconfiguration time, the birds are able to orient in the increased magnetic field.

If the fact that birds can become disoriented in magnetic fields higher than the earth's magnetic field is connected with the iron-mineral-based magnetoreceptor, then the birds should lose their ability to orient if the magnetic field is sufficiently large. Calculations show that if  $\Delta\varepsilon = 0$ , then in a magnetic field of 5 G, 93 % of the mechanosensitive channels are open, which is very close to the saturation limit of 100 %. At 10 G, the opening probability reaches the value of 98 % (see Fig. 5.13). Thus the field strengths at which the iron-mineral based mechanism should stop its functioning is of the order of 5-10 G. These magnetic intensities are the limiting magnetic field strengths (defining the **magnetic window**) at which the magnetoreception is possible.

Note that in the analysis  $\Delta\varepsilon = 0$ , but in general this might not be the case. The different values of  $\Delta\varepsilon$  will influence the functional window of the magnetoreception mechanism as follows from Fig. 5.13. The value of  $\Delta\varepsilon$  can be determined if the limiting magnetic field strength is known. Experimentalists should perform systematic behavior experiments, similar to [126] at magnetic field intensities ranging from several Gauss up to tenth Gauss in order to verify the suggested theoretical predictions.

## 5.7 The Polarity Compass

It has been experimentally demonstrated [2, 3] that at normal conditions (i.e. geomagnetic field, blue-green light illumination, normal light intensity) birds use the inclination compass to orient.

When the vertical component of the magnetic field is inverted, it has been shown

that birds whose original heading had been North, now prefer South [2, 16, 74–76]. Reversing the horizontal component and inverting the vertical component both alter the axial course of the field lines in the same way; an animal not perceiving the polarity of the magnetic field will not realize any difference. Hence birds reverse their headings in both situations alike (see Fig. 2.4). The experiment which showed the inclination compass in birds were first done by Wiltschko *et al.*, and are described in greater detail in section 2.2.

However exposing a bird to a different condition (i.e. illuminating it with red-light) can drastically change the properties of the compass. For example, a pre-exposure to red light for 1 hr immediately before the critical tests under red light of  $6\text{--}7 \times 10^{15}$  quanta $\cdot$ s $^{-1}\cdot$ m $^{-2}$  enabled European robins to orient in their seasonally appropriate migratory direction in spring as well as in autumn [107] with a polarity compass.

In the previous chapter, it has demonstrated that the radical-pair mechanism in cryptochrome provides the birds with an inclination compass, because the cryptochrome activation yield exhibits characteristic variations with respect to the orientation of the external magnetic field. On the contrary, the iron-mineral-based magnetoreceptor provides the animals with a polarity compass. To illustrate this fact Fig. 5.14 shows the forces acting on the magnetite cluster in the magnetoreceptor unit with ten platelets, introduced in Fig. 2.14. The forces were calculated as a function of angles  $\Theta$  and  $\Phi$  which describe the orientation of the external magnetic field. The field strength used in the calculation was 0.5 G.

Figure 5.14 shows that at  $(\Theta = 90^\circ, \Phi = 21^\circ)$  the force acting on the magnetite cluster is minimal, while at  $(\Theta = 90^\circ, \Phi = -154^\circ)$  it is maximal. The force difference between the maximum and the minimum is 0.44 pN. Figure 5.14 shows that the force acting on the magnetite cluster is symmetric with respect to  $\Theta = 90^\circ$ , and thus it satisfies the following symmetry property:

$$f(\Theta, \Phi) = f(\pi - \Theta, \Phi). \quad (5.21)$$

This condition, Eq. (5.21), is a mathematical formulation of the polarity compass, which describes the inversion of the vertical component of the magnetic field. Indeed, the polarity compass should not be influenced when only the vertical component of the magnetic field is inverted (see Fig. 2.4a, top left plot and Fig. 2.4a, bottom right plot).

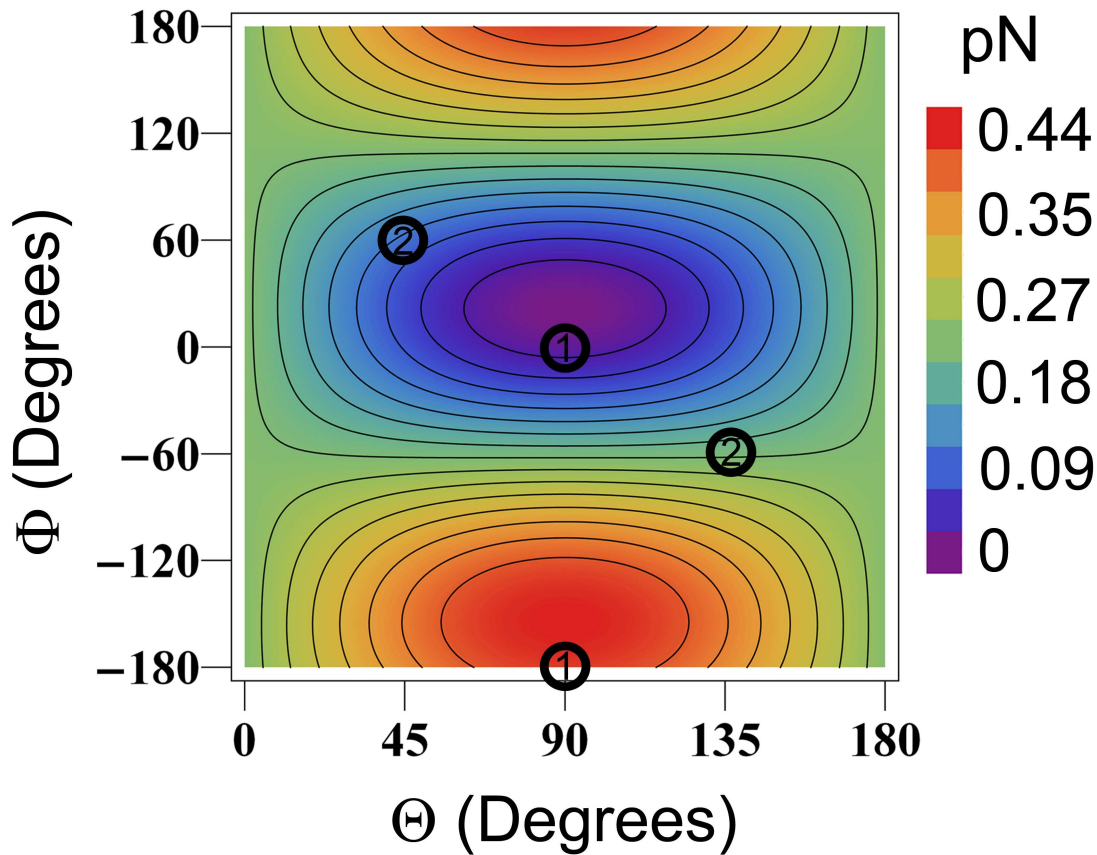


Figure 5.14: Forces acting on the magnetite cluster in magnetoreceptor unit introduced in Fig. 2.14 in the geomagnetic field of 0.5 G calculated as a function of angles  $\Theta$  and  $\Phi$ , describing the orientation of the external magnetic field (see Fig. 2.14). The forces are counted from the minimal value at  $(\Theta = 90^\circ, \Phi = 21^\circ)$  and are given in pN. In the calculation the magnetite cluster is located at  $x=0.3 \mu\text{m}$ ,  $y=0.8 \mu\text{m}$ ,  $z=0 \mu\text{m}$ , being its favorable attachment position (see Fig. 5.4). The figure shows that the force-profile satisfies the polarity compass condition Eq. (5.21), and does not satisfy the inclination compass condition Eq. (5.22). To illustrate this fact two pairs of points which should transform into each other according to Eq. (5.22) are indicated in the contour plot.

The symmetry relation Eq. (5.21) is schematically illustrated in Fig. 5.15, where a part of the magnetoreceptor unit, Fig. 2.14, is shown. The coordinate frame is also indicated in the figure. Since in the coordinate frame considered, the magnetite cluster moves in the (xy)-plane, then this plane is the plane of symmetry for the whole structure. Thus, mirroring of the external magnetic field vector with respect to the (xy)-plane has no influence on the force acting on the magnetite cluster.

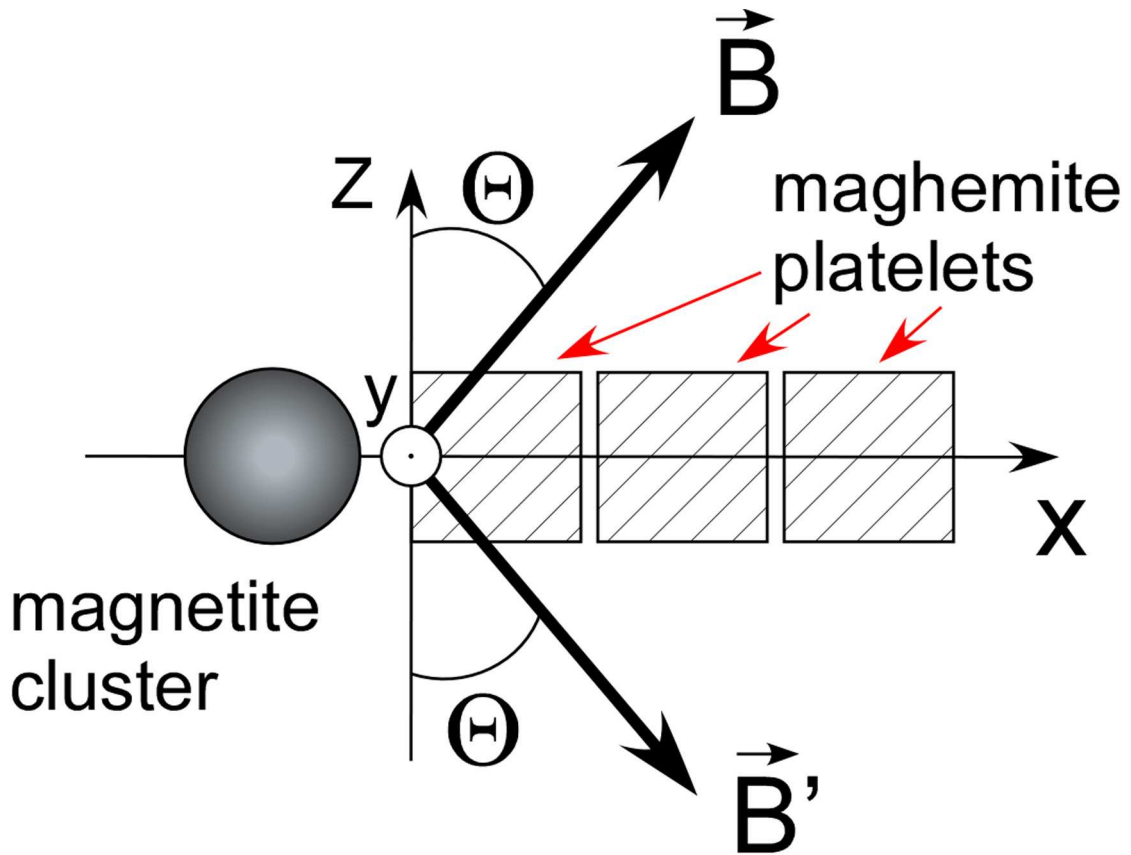


Figure 5.15: Schematic illustration of magnetoreceptor unit symmetry with respect to the inversion of the vertical component of the magnetic field. Since in the coordinate frame considered the magnetite cluster moves in the  $(xy)$ -plane, then this plane is the plane of symmetry for the magnetoreceptor unit. Thus, mirroring of the external magnetic field vector ( $\vec{B} \rightarrow \vec{B}'$ ) in respect to this plane has no influence on forces which act on the magnetite cluster. The symmetry condition is mathematically described by Eq. (5.21), and corresponds to the polarity compass, introduced in section 2.2.

An inclination compass in the iron-mineral-based magnetoreceptor is only possible if the system satisfies the following symmetry condition:

$$f(\Theta, \Phi) = \begin{cases} f(\pi - \Theta, -\pi + \Phi), & \Phi \geq 0 \\ f(\pi - \Theta, \pi + \Phi), & \Phi < 0 \end{cases} \quad (5.22)$$

This condition is similar to the condition of the inclination compass introduced in Eq. (4.6), in section 4.5. Figure 5.14 shows that the forces acting on the magnetite cluster do not satisfy the symmetry relation, Eq. (5.22). To illustrate this fact,

two pairs of points on the contour plot in Fig. 5.14 are marked. If the system is an inclination compass, the forces at the sites of the points with the same labeling should be identical, but they are obviously not.

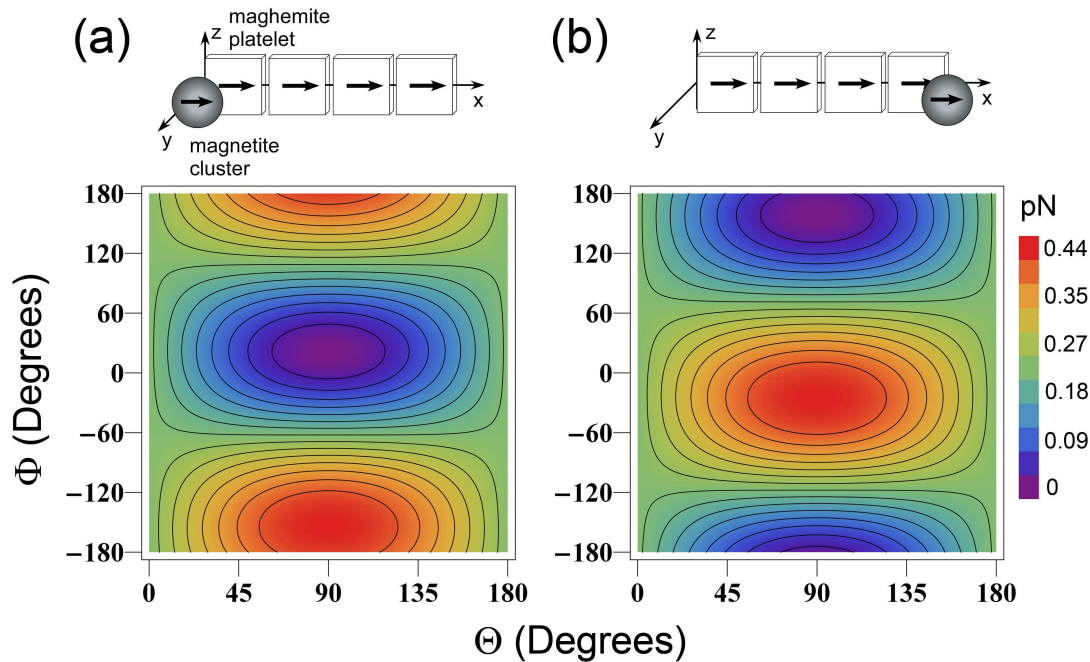


Figure 5.16: Forces acting on the magnetite cluster in a magnetoreceptor system consisting of ten platelet calculated as a function of angles  $\Theta$  and  $\Phi$  in the geomagnetic field of 0.5 G. In this calculation the magnetite cluster is located at (a)  $x=0.3 \mu\text{m}$ ,  $y=0.8 \mu\text{m}$ ,  $z=0 \mu\text{m}$  and (b)  $x=10.6 \mu\text{m}$ ,  $y=0.8 \mu\text{m}$ ,  $z=0 \mu\text{m}$ , corresponding to its two favorable attachment positions at the tips of the chain (see Fig. 5.4). The localization of the magnetite cluster is schematically shown atop the corresponding plot. The magnetic moments of the particles are shown to stress the difference between the two systems. For illustrative purpose only four platelets are shown, while ten platelets were used in the calculation. The forces are counted from the minimal value and are given in pN.

The favorable attachment position of the magnetite cluster is at the tips of the maghemite platelets chain, as follows from Fig. 5.4. However the "beginning" and the "ending" of the chain are not equivalent because the relative orientation of the magnetic moments of the maghemite platelets and of the magnetite cluster are different. This fact is illustrated in Fig. 5.16, where the localization of the magnetite cluster and the maghemite platelets are shown and their magnetic moments are

indicated. Figure 5.16a shows the magnetite cluster located at the beginning of the chain, while Fig. 5.16b shows the magnetite cluster at the end of the chain. The dependence of forces acting on the magnetite cluster on angles  $\Theta$  and  $\Phi$  in the geomagnetic field of 0.5 G is shown below the corresponding image.

The position of the magnetite cluster at the beginning and the end of the chain are characterized by its x-coordinate, and are  $0.3 \mu\text{m}$  and  $10.6 \mu\text{m}$  respectively. Figure 5.16a shows that if the magnetite cluster is found at the beginning of chain, then the dependence of force on angles  $\Theta$  and  $\Phi$  has a prominent minimum and maximum at  $(\Theta = 90^\circ, \Phi = 23.6^\circ)$  and  $(\Theta = 90^\circ, \Phi = -156.7^\circ)$  respectively, while Fig. 5.16b shows that if the magnetite cluster is found at the end of the chain the minimum and maximum are shifted towards  $(\Theta = 90^\circ, \Phi = 156.4^\circ)$  and  $(\Theta = 90^\circ, \Phi = -23.3^\circ)$  respectively. This fact is important because the probability of opening of ion channels in the membrane is directly related to the forces which act on the magnetite cluster (see discussion in section 5.4). It is natural to expect that in a dendrite, there should be magnetoreceptor units with magnetite cluster at both the beginning and the end of the chain. This however should be clarified experimentally. Note that both dependencies of forces shown in Fig. 5.16 satisfy the polarity compass condition Eq. (5.21).

The fact that birds acquire a polarity compass in red light leads to the hypothesis that the magnetoreceptor system functions differently than under the blue-light illumination. If the magnetic sense in birds involves two magnetoreceptors (cryptochromes in the eye and iron-mineral-receptor in the beak), then the cryptochrome-based receptor will be disabled in the red light because the protein will not be excited (see discussion in chapter 4) and only the iron-mineral-based magnetoreceptor remains. This fact is in a good agreement with the results presented.

## 5.8 Magnetoreceptor Unit with Different Number of Platelets

Every dendrite has about 10-15 magnetoreceptor units, as suggested by experimental observations [60] which act in a similar manner in the external magnetic field. However, it is still not clear if all units are identical, or if they are composed of different number of platelets. It is also important to understand how the magnetoreceptor units are distributed around the vesicle (see Fig. 2.12): symmetrically or not. Several possible distributions are shown in Fig. 5.17. Figure 5.17a illustrates an

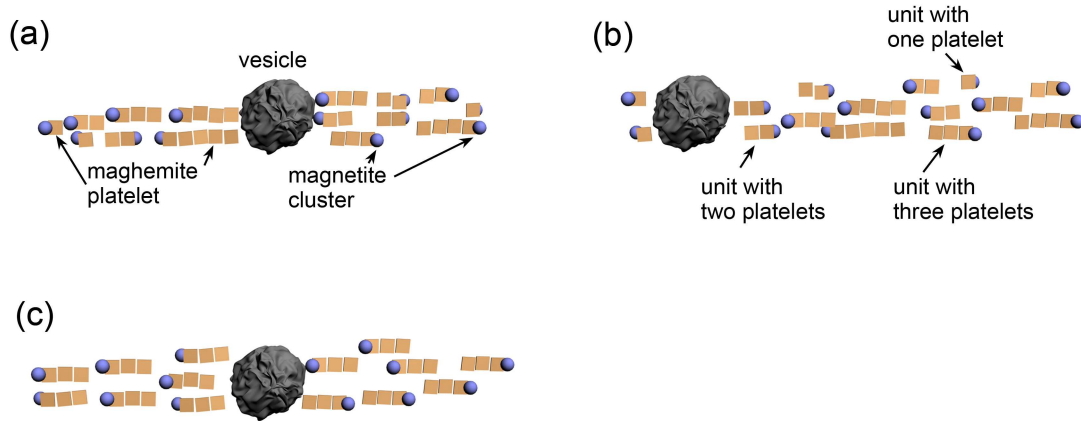


Figure 5.17: Possible localization of iron minerals within a dendrite (see Fig. 2.12). (a) chains of maghemite platelets of different length are distributed almost symmetrically around the vesicle; (b) the majority of magnetoreceptor units of different length are located to one side from the vesicle; (c) all magnetoreceptor units have the same number of platelets. The magnetite cluster, the maghemite platelets and the vesicle are indicated in the figure.

almost symmetrical distribution of magnetoreceptor units of different length around the vesicle (i.e. the number of magnetoreceptor units to the left and to the right from the vesicle is close). Figure 5.17b shows an asymmetric distribution of platelets of different length (note, that some magnetoreceptor units have one platelets, some have two, etc). The case when all magnetoreceptor units have the same number of platelets is shown in Figure 5.17c. Figure 5.17 is an illustration of possible distributions of iron-mineral particles in the dendrite. The distribution of the iron-mineral based magnetoreceptors should be considered experimentally, and the spatial location of the maghemite platelets should be measured. Such an investigation is important because the number of platelets in the magnetoreception unit determines the forces which act on the magnetite cluster.

The forces acting on the magnetite cluster in a magnetoreceptor unit consisting of one, two, three and ten platelets calculated as a function of angles  $\Theta$  and  $\Phi$  are shown in Fig. 5.18a-d respectively. In this calculation, the field strength was assumed to be 0.5 G. Figure 5.18a shows that the forces acting on the magnetite cluster in a magnetoreceptor unit with one platelet are significantly different from other cases. The differences can be understood if one considers the direction of the



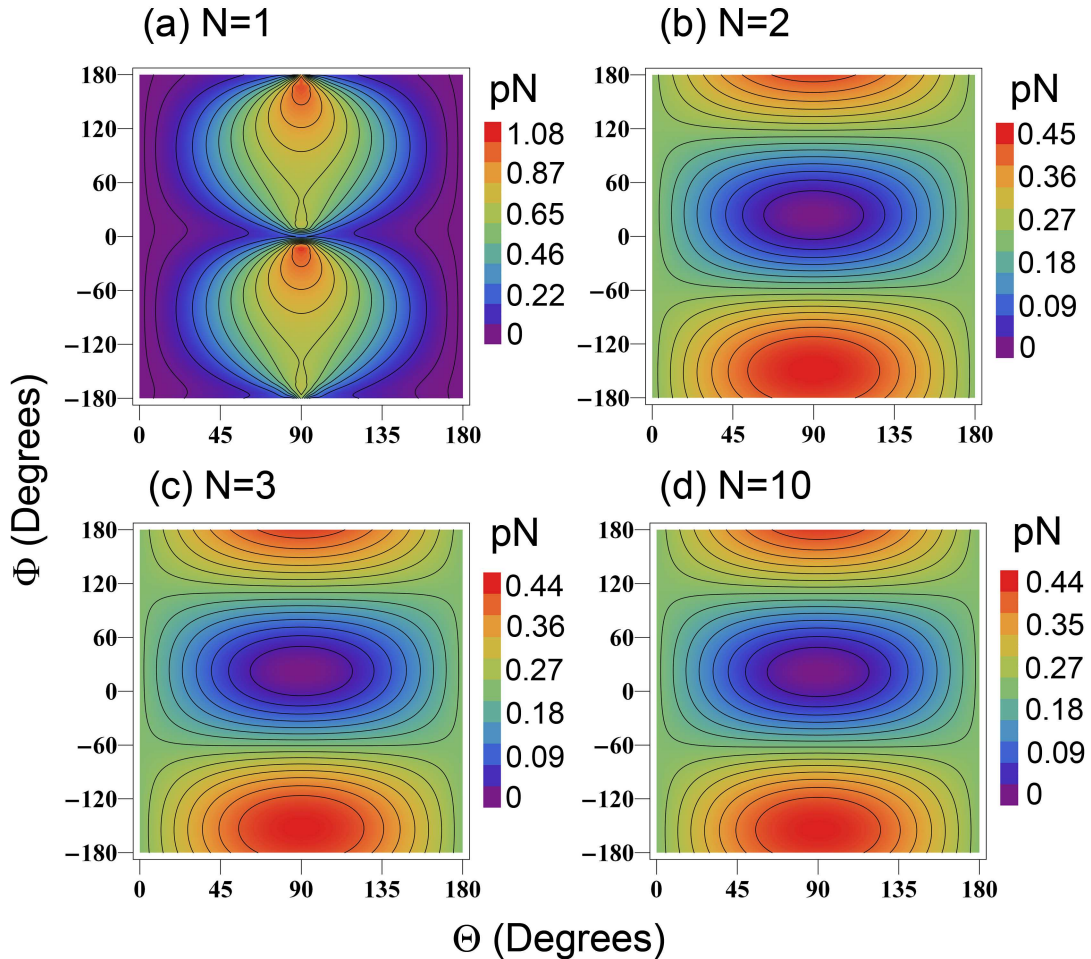
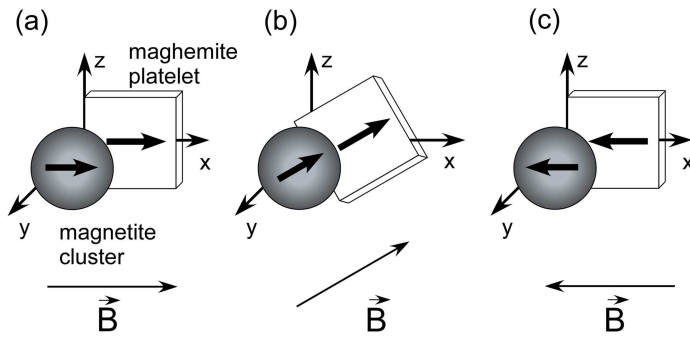


Figure 5.18: Forces acting on the magnetite cluster in the geomagnetic field of 0.5 G calculated as a function of angles  $\Theta$  and  $\Phi$ , describing the orientation of the external magnetic field (see Fig. 2.14). The forces were calculated for a magnetoreceptor system, containing one maghemite platelet (a), two maghemite platelets (b), three maghemite platelets (c) and ten maghemite platelets (d). The position of the maghemite cluster is  $x=0.3 \mu\text{m}$ ,  $y=0.8 \mu\text{m}$ ,  $z=0 \mu\text{m}$ . The forces are counted from the minimal value and are given in pN.

magnetic moments of the platelets at different orientations of the external magnetic field (see Fig. 5.19).

In the magnetoreceptor system with one platelet (see Fig. 5.19a), the magnetic moment of the platelet will be governed by the (xz)-projection of the external magnetic field. This happens because the platelet can rotate in the (xz)-plane of the considered coordinate frame in order to minimize its energy – which is, to a large

### 1-platelet system



### 2-platelet system

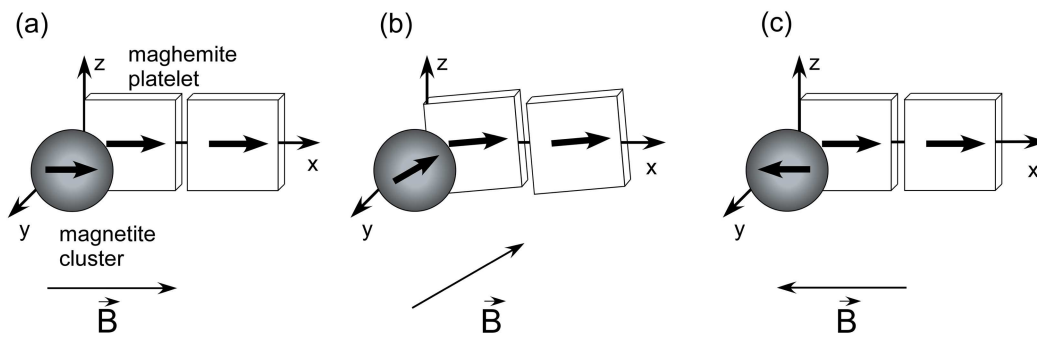


Figure 5.19: Magnetoreceptor system consisting of one platelet (a) and two platelets (b) at different orientations of the external magnetic field. In the model considered the platelets can rotate in the (xz)-plane depending on the orientation of the external magnetic field (see discussion in section 2.4.2). If the magnetoreceptor system has one platelet then its magnetic moment will align along the external field (see (a)). If the magnetoreceptor unit has two or more platelets then due to the interaction between them the external magnetic field of 0.5 G has minor effect on the direction of the magnetic moments of the platelets (see (b)).

extent, determined by the external magnetic field. Figure 5.19a illustrates this fact.

If the magnetoreceptor unit consists of two or more platelets (see Fig. 5.19b) then the energy of each platelet is determined by the external magnetic field and by the interaction between the platelets. Calculations show that the interaction energy of a platelet with geomagnetic field is about ten times smaller than with other platelets. Therefore an external magnetic field of 0.5 G has minor effect on the direction of the magnetic moments of the platelets. Figure 5.19b shows that a 30° change of

the direction of the magnetic field results in a  $2\text{-}4^\circ$  tilt of the platelet. A similar behavior is expected for the system with three, four, etc platelets. This fact leads to significant modification of forces acting on the cluster (see Fig. 5.18b-d).

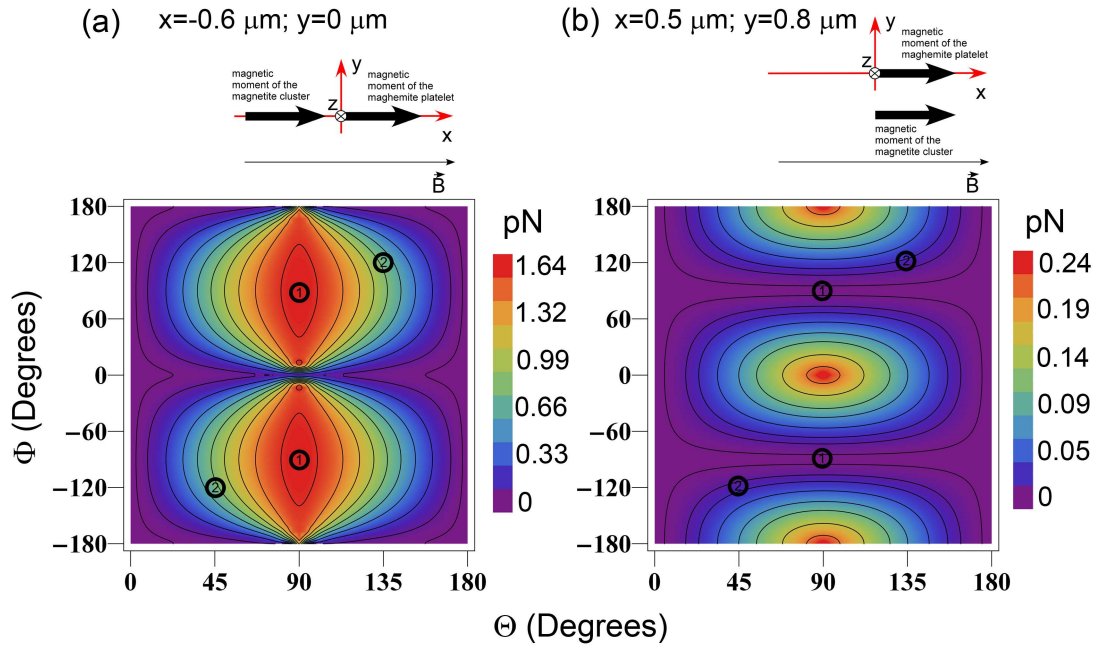


Figure 5.20: Forces acting on the magnetite cluster in a magnetoreceptor system consisting of one platelet calculated as a function of angles  $\Theta$  and  $\Phi$  in the geomagnetic field of 0.5 G. In this calculation the magnetite cluster is located at  $x = -0.6 \mu\text{m}$ ,  $y = 0.0 \mu\text{m}$ ,  $z = 0 \mu\text{m}$  (a) and  $x = 0.5 \mu\text{m}$ ,  $y = 0.8 \mu\text{m}$ ,  $z = 0 \mu\text{m}$  (b), corresponding to the two possible symmetrical arrangement of the magnetic moments of the maghemite platelet and of the magnetite cluster which are schematically shown atop of the corresponding plot. The forces are counted from the minimal value and are given in pN. Two pairs of points illustrating that the force pattern obey the inclination compass condition Eq. (5.22) are indicated.

Figure 5.18b-d show the dependence of forces acting on the magnetite cluster in a magnetoreceptor unit consisting of two, three and ten platelets calculated as a function of angles  $\Theta$  and  $\Phi$ . The comparison of these dependencies shows that the forces acting on the magnetite cluster in a magnetoreceptor unit (with two, three or ten platelets) are almost identical. This fact has a simple explanation. In the calculation the magnetite cluster was assumed to be located at  $x = 0.3 \mu\text{m}$ ,  $y = 0.8 \mu\text{m}$ ,  $z = 0 \mu\text{m}$ , corresponding to its favorable attachment position (see Fig. 5.4). Thus the distance from the center of the cluster to the center of the first two platelets are

0.82  $\mu\text{m}$  and 1.53  $\mu\text{m}$  respectively, while the distance to the third platelet is 2.53  $\mu\text{m}$ . Since the energy of the platelet-cluster interaction decreases as  $1/R^3$ , where  $R$  is the distance between the platelet and the cluster, then in the weak magnetic field (0.5 G) the interaction between the magnetite cluster and the third platelet becomes negligible. The interaction with other platelets is even smaller.

Beside the difference in forces which act on the magnetite cluster in a magnetoreceptor unit with one platelet it is important to note that the force-pattern shown in Fig. 5.19a almost satisfies the inclination compass condition described by Eq. (5.22) in contrast to the force patterns shown in Fig. 5.19b-d. The two maxima in Fig. 5.19a are slightly asymmetric in respect to the point  $(\Theta = 90^\circ, \Phi = 0^\circ)$  and therefore the inclination compass condition Eq. (5.22) is violated. This happens because the magnetite cluster in Fig. 5.19a has the coordinates  $x=0.3 \mu\text{m}$ ,  $y=0.8 \mu\text{m}$ ,  $z=0 \mu\text{m}$  and thus the points on the surface Fig. 5.19a with coordinates  $(\Theta = 90^\circ, \Phi)$  and  $(\Theta = 90^\circ, -\pi + \Phi)$  are not equivalent.

The inclination compass condition Eq. (5.22) is satisfied in a one-platelet magnetoreceptor unit if the maghemite platelet and the magnetite cluster are arranged one after another or are located side by side, so that the angle between the radius vector connecting them and their magnetic moments is either  $0^\circ$  or  $90^\circ$ . The arrangement of magnetic moments, corresponding to these two cases, and the dependence of the interaction force on angles  $\Theta$  and  $\Phi$  is schematically shown in Figs. 5.20a and 5.20b respectively. In order to stress that, the force dependencies in Figs. 5.20a and 5.20b obey the inclination compass condition Eq. (5.22) two pairs of points which are transformed into each other according to this condition are indicated.

Note however, that when the cluster and the platelet are aligned one after another then the change of forces caused by a  $90^\circ$  change of the direction of the magnetic field is almost an order of magnitude larger than in the case of a ten-platelet magnetoreceptor unit (see Fig 5.14 and Fig. 5.20a). This happens because in the case of a single-platelet magnetoreceptor unit, the direction of the magnetic moment of the platelet is determined mainly by the external magnetic field, and thus it can rotate freely and align in a way that the interaction between the maghemite platelet and the magnetite cluster is at its strongest. If several platelets are aligned one after another then the interaction between the platelets is much stronger than the interaction with the external magnetic field and the direction of the magnetic moments is almost fixed (see discussion above). Thus, the change in the force acting on the magnetite cluster caused by a  $90^\circ$  change will be mainly determined by the direc-

tion of the magnetic moment of the magnetite cluster, resulting in a much weaker interaction.

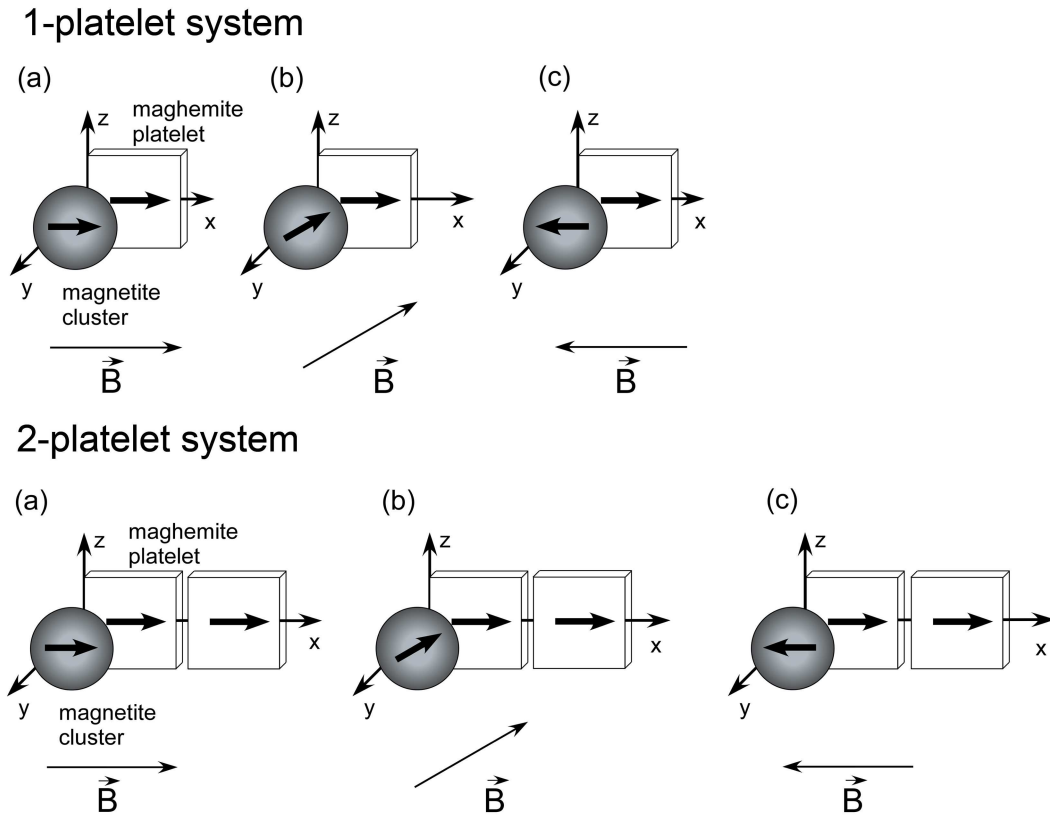


Figure 5.21: Magnetoreceptor system consisting of one platelet (a) and two platelets (b) at different orientations of the external magnetic field. Here the platelets are fixed and can not rotate. Their magnetic moments are assumed to be aligned along the x-axis of the chosen coordinate frame. Thus, the external magnetic field influences only the direction of the magnetic moment of the magnetite cluster, which is also indicated.

The finding that a one-platelet magnetoreceptor unit provides an inclination compass leads to the conclusion that probably, not all magnetoreceptor units in the beak are identical and have the form introduced in Fig. 2.14. It might be that some of the units contain 5-10 platelets, as discussed, but some have only a single platelet, providing the bird with an inclination compass. This fact is very important because it might explain why birds have the inclination compass and should be considered experimentally in the nearest future.

Another important observation is that, since in a one-platelet magnetoreceptor

the forces acting on the magnetite cluster are an order of magnitude higher than in a ten-platelet magnetoreceptor unit. Thus a one-platelet magnetoreceptor system can respond to small variations of the external magnetic field (i.e. 1 or several per cent) in a much more efficient way than a ten-platelet magnetoreceptor unit does and can therefore be responsible for birds disorientation at magnetic anomalies [82,242,243].

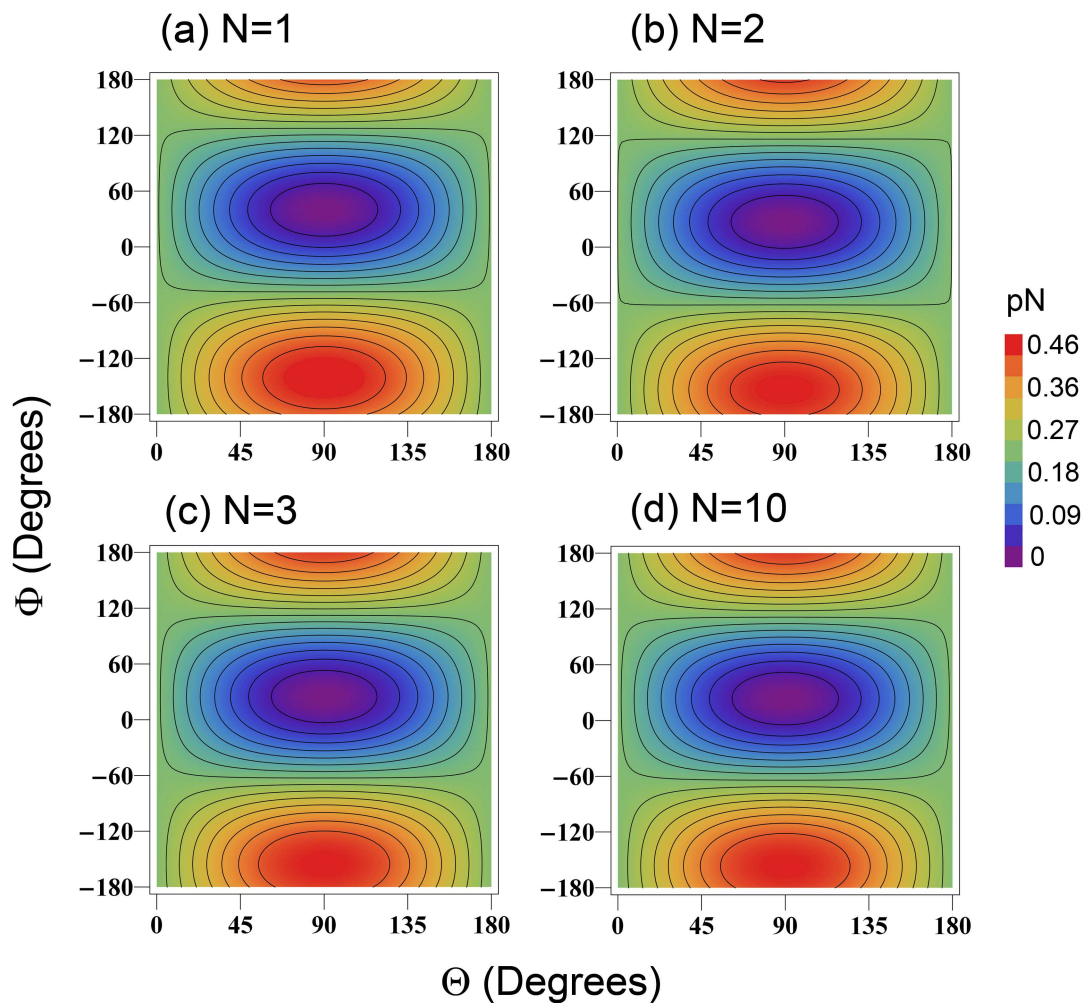


Figure 5.22: Forces acting on the magnetite cluster in the geomagnetic field of 0.5 G calculated as a function of angles  $\Theta$  and  $\Phi$ . The forces were calculated for a magnetoreceptor system, containing one maghemite platelet (a), two maghemite platelets (b), three maghemite platelets (c) and ten maghemite platelets (d), assuming that the platelets are fixed in space and could not rotate. The magnetite cluster is located at  $x=0.3 \mu\text{m}$ ,  $y=0.8 \mu\text{m}$ ,  $z=0 \mu\text{m}$ . The forces are counted from the minimal value and are given in pN.

The inclination compass in the iron-mineral-based magnetoreceptor is only possible if the platelets can rotate, which is a reasonable assumption as discussed in section 2.4.2, but which still needs experimental proof. If the platelets are fixed then the external magnetic field influences only the magnetic moment of the magnetite cluster. The magnetoreceptor system consisting of one platelet and two platelets at different orientations of the external magnetic field are shown in Figs. 5.21a-b respectively. In both cases the change of force acting on the magnetite cluster arises due to the different orientations of the magnetic moment of the cluster. The forces acting on the magnetite cluster in a magnetoreceptor unit consisting of one, two, three and ten platelets calculated as a function of angles  $\Theta$  and  $\Phi$  are shown in Fig. 5.22a-d respectively. In this calculation the field strength is 0.5 G.

Figure 5.22 shows that for magnetoreceptor units with one, two, three and ten platelets the dependencies of force on angles  $\Theta$  and  $\Phi$  are very close to each other with minor differences which are on the order of interpolation error of the contour plots. This happens because the magnetite cluster, located at the tip of the maghemite platelets chain, interacts effectively only with several platelets, since the energy of the platelet-cluster interaction decreases as the third power of distance between the platelet and the cluster.

Figure 5.22 clearly demonstrates that if the platelets are fixed then the inclination compass in a one-platelet magnetoreceptor system becomes a polarity one. This follows from Fig. 5.22a which satisfies the symmetry condition Eq. (5.21), describing the polarity compass.

## 5.9 Magnetoreceptor Unit in Higher Magnetic Fields

The force, acting on the magnetite cluster significantly changes with increase in the intensity of the magnetic field. Figure 5.23a-d shows the forces acting on the magnetite cluster in magnetoreceptor unit consisting of one, two, three and ten platelets respectively in the magnetic field of 10 G, calculated as a function of angles  $\Theta$  and  $\Phi$ . The dependence of force shown in Fig. 5.23a is similar to the dependence shown in Fig. 5.18a, which describes the interaction of a magnetite cluster and a maghemite platelet in a one-platelet magnetoreceptor system. The principal difference between these two plots is in the magnitude of force which acts on the cluster: the changes in force arising in the geomagnetic field of 0.5 G are on

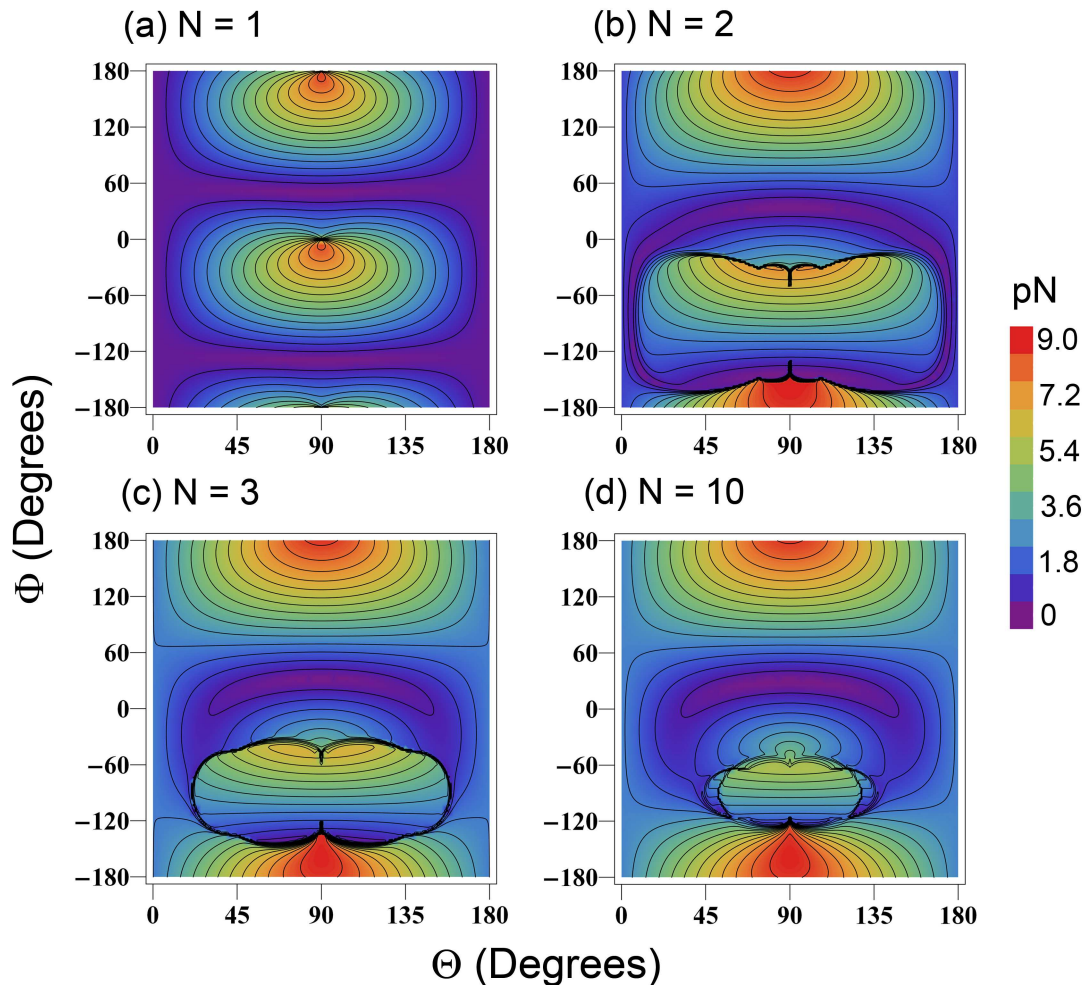


Figure 5.23: Increasing the intensity of the magnetic field significantly changes the forces acting on the magnetite cluster. The figure shows the forces acting on the magnetite cluster in the magnetic field of 10 G calculated as a function of angles  $\Theta$  and  $\Phi$ . The forces were calculated for a magnetoreceptor system, containing one platelet (a), two platelets (b), three maghemite (c) and ten platelets (d). The position of the maghemite cluster is  $x=0.3 \mu\text{m}$ ,  $y=0.8 \mu\text{m}$ ,  $z=0 \mu\text{m}$ . The forces are counted from the minimal value and are given in pN.

the order of 0.4 pN, while in a 10 G field it is 9 pN. However, the general trend of the force on angles  $\Theta$  and  $\Phi$  in both cases are similar.

The dependencies of forces shown in Fig. 5.23b-d differ strongly from the corresponding plots presented in Fig. 5.18b-d. Figures 5.23b-d show that at higher magnetic fields the magnetoreceptor units with two and more platelets possess a



pronounced irregularity at  $\Phi \sim -120^\circ \dots -60^\circ$ . The nature of this irregularity can be understood if one considers the direction of magnetic moments of the platelets. Figure 5.24 illustrates the spatial orientation of magnetic moments in the magnetoreceptor system at three different orientations of the external magnetic field.

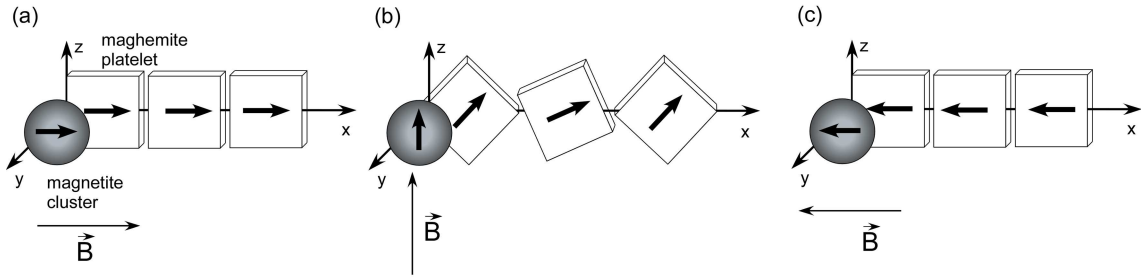


Figure 5.24: Magnetoreception system consisting of three particles at different orientation of the external magnetic field of 10 G. (a) External magnetic field is directed along the x-axis of the considered coordinate frame; (b) External magnetic field is directed along the z-axis; (c) External magnetic field is directed in the direction opposite to the direction of the x-axis.

If the external magnetic field is directed along the x-axis of the considered coordinate frame (see Fig. 5.24a), or is close to it, then the magnetic moments of the maghemite platelets are aligned preferably along the x-axis. A  $90^\circ$  change in the direction of the magnetic field, corresponding to the alignment along the z-axis of the coordinate frame, leads to a significant reorientation of the platelets (see Fig. 5.24b). In this case, the first and the third platelet are tilted on  $46^\circ$  while the second platelet is tilted on  $24^\circ$ . Finally, if the external magnetic field is directed in the direction opposite to the direction of the x-axis then the platelets make a  $180^\circ$  turn and their magnetic moments point in the direction opposite to the direction of the x-axis (see Fig. 5.24c). This fact explains the peculiarity in Fig. 5.23b-d. Indeed, in the weak magnetic field (e.g. 0.5 G) the magnetic moments of the platelets can not be reversed, because of the strong interplatelet interaction. Thus in the weak magnetic field the platelets are always preferably directed along the x-axis. In the magnetic field of 10 G, the interplatelet interaction becomes weaker than the interaction with external magnetic field and therefore the magnetic moments of the platelets can be reversed.

The critical magnetic field at which the magnetic moments can be reversed can

be easily estimated. Assume a two platelet system, each having a magnetic moment  $\vec{m}$  directed along the x-axis, and let the distance between them to be  $\vec{r}_0$ , then the field created by one platelet at the site of a nearby platelet reads as

$$\vec{H} = \frac{3\vec{r}_0(\vec{m}\vec{r}_0) - \vec{m}r_0^2}{r_0^5} = \frac{2\vec{m}}{r_0^3}. \quad (5.23)$$

with  $m \approx 3.121$  eV/G (see estimates in the section 5.2) and  $r_0 \approx 1.1$   $\mu\text{m}$ , one obtains  $|\vec{H}| \approx 7.5$  Oe, corresponding to the magnetic induction of 7.5 G. This estimate shows that if the projection of the external magnetic field on the x-axis is negative and greater than 7.5 G in magnitude the maghemite platelets can turn and align their magnetic moments with respect to the field lines (see Fig. 5.24c). Thus, the irregularity regions in Fig. 5.23b-d corresponds to the angles when the projection of the external magnetic field is greater than the field created by the platelets.

Note that if a magnetoreceptor unit has more than two platelets, the critical field should become larger than 7.5 G, because the magnetic field created at a site of a given platelet increases due to the contributions produced by the distant platelets. This fact reduces the irregularity region in Fig. 5.23b-d with increase in the number of platelets in the magnetoreceptor system.

It is also worth noting that in strong magnetic field (i.e. 10 G) the magnetite cluster effectively interacts with a larger number of maghemite platelets than in the weak magnetic field. Figure 5.23c shows the dependence of the forces acting on the cluster as a function of angles  $\Theta$  and  $\Phi$  calculated for a three-platelet magnetoreceptor unit. This plot reproduces the general features of the plot shown in Fig. 5.23d, corresponding to the ten-platelet system, with some minor differences. This fact leads to the conclusion that in the field of 10 G, the magnetite cluster effectively interacts with four-five platelets.

## 5.10 Role of the Non-Magnetic Vesicle

As discussed in section 2.4.2, dendrites contain maghemite platelets, magnetite clusters and a non-magnetic vesicle. In the previous sections it has been shown that the maghemite platelets and the magnetite clusters play an important role in the magnetoreception mechanism. However, the role of the non-magnetic vesicle is still a matter of discussion since insufficient experimental information is presently available.

In the latest experiment by Fleissner *et al.* [125] it was demonstrated that the vesicle might be located in the center of the dendrite and is probably covered by some non-crystalline iron-substance. The diameter of the vesicle was estimated to be about 3-5  $\mu\text{m}$  [58–60, 125].

Since the vesicle is found in the dendrite, it should play a certain role in the magnetoreception process of birds and therefore two hypotheses which might explain how the vesicle is involved in this phenomenon are suggested.

The first possible function of the vesicle is the *divider-function*. Indeed, from the potential energy surfaces Fig. 5.1 and Fig. 5.10, it follows that the force acting on the magnetite clusters rapidly increases if the distance between the platelets and the cluster decreases. Hence, without the non-magnetic vesicle, the magnetite clusters are free to stick anywhere on the chain of the maghemite platelets – in which case, no further magnetic field effects will be possible. Therefore, one possible role of the vesicle might be to prevent the clusters from getting close to the chain of maghemite platelets. With a size of about 5  $\mu\text{m}$  it keeps the walls of the cell membrane far apart, acting as a divider and protecting the dendrite from collapse.

In addition to the divider-function, the vesicle might be some sort of *iron-reservoir* that provides iron for the maghemite platelets and magnetite cluster formation. This idea is inspired by experimental findings [58–60, 125], showing that the vesicle seems to be covered with some non-magnetic iron material. However, at present it is still not clear how the magnetite clusters and the maghemite platelets emerge in the beak of birds and how the size of the magnetoreceptor unit evolves with age. It might be the case that dendrites of young birds contain no magnetic platelets or clusters, and that these might appear at a later age when crystallization of iron in the vesicle has occurred. To verify this assumption, one has to perform experiments on birds of different ages and determine how the vesicle, maghemite platelets and magnetite clusters change/grow with the age of the animal.

## 5.11 Further Steps for Experimental Verification

This subsection gives an overview of possible experiments which are necessary in order to check various assumptions of the theory and to make the suggested iron-mineral based magnetoreceptor mechanism more quantitative. The experiments in this section are listed in order to show that there are many-more open question in addition to those discussed in the present thesis and thus, need a careful consideration

in the future.

- The spatial localization of iron minerals should be checked in an independent experiment without disturbing the structure of the dendrite. This should give an important insight on the structure of the magnetoreceptor system.
- The nature of the magnetic moments of the particles should be clarified and the magnetization parameters of magnetite and maghemite should be measured.
- It is natural to expect that magnetoreceptor units in the dendrite have different number of platelets. The distribution function of platelets in the dendrite is not known but is very important because the number of platelets in the magnetoreception unit determines the forces acting on the magnetite cluster.
- It might be that some of the magnetoreceptor units contain 5-10 platelets, but some have only a single platelet providing the bird with an inclination compass. This fact is very important because it might explain why birds have the inclination compass and thus should be carefully considered by experimentalists.
- Another important issue of the magnetoreceptor unit which needs an experimental verification is the position of the magnetite cluster at the beginning of the maghemite platelet chain or at its end (see Fig. 5.16). The position of the cluster has an impact on forces which act on it and therefore influences the probability of opening of the ion channels in the membrane.
- An important question, which is not fully understood, is how the maghemite platelets are fixed in the dendrite. Are they absolutely fixed, or can they rotate? If the platelets can rotate, then how? These questions need a further experimental verifications. So far there have been some arguments [58–60,125] that the platelets are fixed, however, they are not very convincing. Therefore the question of platelet fixation should be carefully considered. Additionally it is very unlikely that the particles are stiffly bound in space and cannot move. It is much likely that the platelets can rotate around their principal axis, as assumed in the thesis. However it should be checked whether this is true or not. Another possibility for the platelet chain is to rotate as a rigid object. In this way, if it is connected to the membrane, it can also influence the probability of the opening/closing of the ion channels.

- 
- The connection of the magnetite cluster to the membrane should also be studied in a separate experiment, in order to verify the experimental observations suggested in [58–60, 125].
  - Test should be performed on birds in magnetic field significantly higher than the Earth magnetic field, i.e. 5-10 G, in order to determine the magnetic window, outside of which birds cannot perceive the magnetic field.
  - At present it is still not clear how the magnetite clusters and the maghemite platelets emerge in the beak of birds and how the size of the magnetoreceptor unit evolves with age. It might be the case that dendrites of young birds contain no magnetic platelets or clusters, and that these might appear at a later age when crystallization of iron in the vesicle has occurred. To verify this assumption, one has to perform experiments on birds of different ages and determine how the vesicle, maghemite platelets and magnetite clusters change/grow with the age of the animal.
  - The magnetic properties of the vesicle should also be elaborated.



# Chapter 6

## Conclusion

This work is devoted to the description of mechanisms that might be responsible for avian magnetoreception. Two possible theoretical concepts underlying this phenomenon have been formulated and their functioning have been shown to exist in realistic geomagnetic fields.

It has been suggested that animal magnetoreception is mediated by the blue light receptor protein, cryptochrome, which was recently found localized in the retinas of migratory birds [64]. It was shown that such a magnetic field sensing mechanism can explain many long-observed properties of avian magnetoreception [1–6, 36] and of a recently-observed magnetic field effect in plants [57].

The active site of cryptochrome binds internally the chromophore flavin adenine dinucleotide (FAD) (see Figs. 2.8 and 4.1). One of the goals of this thesis was to investigate the possibility that a weak external magnetic field could alter the photoreduction of the FAD cofactor in cryptochrome via a radical pair mechanism. In this mechanism the FADH cofactor of cryptochrome and three of the protein's tryptophans are involved in a dominant electron transfer pathway. Changes in the cryptochrome's FAD reduction activity alter the protein's ability to autophosphorylate [143, 144], this in turn alters the protein's signaling behavior. The results of calculations on cryptochrome's photoreduction pathway demonstrate the possibility of cryptochrome's activation to exhibit a dependence on magnetic field strength and orientation. The results also support the hypothesis that a radical pair mechanism in cryptochrome is responsible for the magnetic field effects observed in *Arabidopsis thaliana* [57]. Although the extension of the findings to a cryptochrome-based magnetic sensor in animals involves several factors (see [5, 36] for a review), the demonstrated results suggest that such a mechanism is clearly possible.

Unfortunately, lack of sufficient information regarding isotropic and anisotropic hyperfine coupling in cryptochrome hinders one from drawing conclusions about the precise magnetic field effects in cryptochrome – limiting the present investigation to a study of feasibility. When more experimental data regarding the hyperfine coupling and reaction rate constants in cryptochrome become available, the present investigation can be extended to a quantitative description.

The second magnetoreception mechanism studied in the present thesis is the iron-mineral-based magnetoreceptor mechanism. The mechanism is based on the experimental findings of Fleissner *et al.* [60,61], which proved the existence of two types of magnetic minerals in the beak of birds, namely the maghemite platelets and magnetite clusters.

It was shown that in a weak external magnetic field (i.e. comparable with the geomagnetic fields) the magnetite clusters will experience an attractive (repulsive) force leading to their displacement. This induces a primary receptor potential via strain-sensitive membrane channels and could lead to a certain orientational effect of a bird. Note, however that this mechanism is very different from the magnetite-based magnetoreception mechanism suggested by other authors [40–44, 62] as it involves two different types of iron-minerals (magnetite and maghemite).

Based on the analysis of forces that act on the magnetite particles, (arising from the external magnetic field and from the maghemite platelets) it was demonstrated that the iron-mineral system can be considered as a magnetoreceptor unit with distinct orientational properties. It was shown as well that – depending on the orientation of the external magnetic field – the pressure on the cell membrane can change significantly, leading to different nerve signals. These signals are thought to be delivered to the brain and to cause a certain orientational behavior of the bird. Two transducer mechanisms of the geomagnetic field which are based on opening/closing of mechanosensitive ion channels were suggested and analyzed, and the probability of the channel opening was investigated.

The iron-mineral-based magnetoreceptor has been analyzed at different external magnetic field strengths and the magnetic field intensities at which the suggested mechanism stops functioning were established. These magnetic field intensities determine the **magnetic window** of the iron-mineral-based magnetoreceptor mechanism. The experimental conditions at which the magnetoreception mechanism is violated have also been outlined and their experimental proof is needed.

Additionally the feasibility of **polarity** and **inclination compass** in the sug-



gested magnetoreceptor system has been analyzed from different points of view. It was demonstrated that at the conditions which correspond to the experimentally observed structures the magnetoreceptor system is a polarity compass, but at certain conditions it can become an inclination compass. This fact was not discussed elsewhere and is very important because birds use inclination compass for their navigation. Thus, the mentioned observation is solely a theoretical prediction. The experimentalists should check if the inclination-compass conditions described in the thesis are possible in the bird's beak.

The feasibility of the iron-mineral based magnetoreception mechanism has been demonstrated quantitatively. However, many questions remain open and in need of further investigation. For example the role of the big non-magnetic vesicle found in the dendrite is still not clear and needs further experimental investigation. To answer this question, one should perform experiments on birds of different ages and determine how the vesicle, maghemite platelets and magnetite clusters change/grow with the age of an animal. The precise spatial structure of the dendrite is also an open question. It would be interesting to perform experiments similar to [60, 61] but without disturbing the dendrite (e.g. by computer tomography or X-ray analysis) in order to confirm the spatial location of the maghemite platelets and the magnetite clusters precisely. **The connection of the magnetite clusters to the cell membrane should also be studied in a more careful and systematic way.** Another problem concerns the influence of oscillating magnetic (and electrical) fields on the magnetoreception mechanism. The analysis of field frequencies at which magnetoreception is violated can be used to suggest certain experimental conditions for probing the magnetoreception mechanism in birds.

The analysis performed in this work supports the hypothesis that birds possibly have two magnetic field receptors: one located in the eye and the second located in the beak. Both receptors may supplement each other and enhance the effect of the weak geomagnetic field on birds. **One possibility might be that the nervous signals induced in the beak and in the eye modulate each other leading to an enhanced effective signal to be sent to the brain of the animal.** To understand if this is the case, it is necessary to study the nervous system of the bird and clarify which nervous signals can be produced due to the described magnetoreception systems. Another possibility for the two mechanisms to operate together is inspired by recent electrophysiological and histological studies, which suggest that, in birds, a radical pair mechanism located in the right eye provides

directional information for a compass, while a magnetite-based mechanism located in the upper beak records magnetic intensity, thus providing positional information [6]. These hypotheses should be studied both experimentally and theoretically.

The suggested magnetoreception mechanisms were investigated specifically in birds, however the same mechanisms might also be responsible for magnetosensation in other animals like fishes [46], salamanders [17–20] bees [21–25] and others. Unfortunately, lack of sufficient information about magnetic particles in these species hinders one from drawing conclusions about their precise magnetoreception mechanism. Therefore, when more experimental data regarding the magnetic particles in animals become available the present investigation can be extended to a more general description.

# Acknowledgments

Although only my name appears on the cover of this dissertation, a great many people have contributed to its production. I owe my gratitude to all those people who have made this dissertation possible and because of whom my graduate experience has been one that I will cherish forever.

The research on which this dissertation reports has been conducted during the years 2004 to 2007 while employed at the Frankfurt international Graduate School for Science at the Frankfurt Institute for Advanced Studies (FIAS). First and foremost I thank Prof. Dr. h. c. mult. Walter Greiner and Prof. Dr. Klaus Schulten for the uncounted enlightening talks we had during this time. The strong interest in the progress of this work that they took at all times. Their valuable comments and constructive criticism, expressed in a straight – forward but friendly manner, not only helped me gain new insights but also motivated me time and time again. I am glad to have worked with them and grateful for having been their student.

While working on my dissertation, I profited a lot from the many opportunities to present and discuss my work-in-progress in various meetings at the Frankfurt Institute for Advanced Studies. My special gratitude goes to the members of the MesoBioNano Science Group, especially to Prof. Dr. Andrey Solov'yov, Dr. Andrey Korol, Dr. Oleg Obolensky, Dr. Elsa Henriques and Mr. Alexander Yakubovich. I also want to express my gratitude to Ms. Danielle Chandler, who is a member of the Theoretical and Computational Biophysics Group (Urbana/Champaign, Illinois, USA) and contributed a lot to the presented results.

Special thanks go to Profs. Gerta and Günther Fleissner for many helpful discussions and valuable comments on the data presented in this thesis. They introduced me to their experimental works and helped to understand many biological aspects of the study.

I am very greatfull to Ms. Adilah Hussein and Ms. Stephanie Lo for their help in the proofreading of this manuscript. I also acknowledge Dr. Andrey Korol for

reading the theoretical part of the thesis and for his critical commentaries.

I would also like to acknowledge Dr. Irina Solovyeva and Mr. Matthias Hempel for helping me with the German Zusammenfassung.

The possibility to perform complex computer simulations at the Frankfurt Center for Scientific Computing is gratefully acknowledged.

I want to thank Ms. Vita Levitan for the moral support, patience and understanding during the whole period of writing the thesis. I am also very thankful to Vita for the careful reading of the manuscript, her critical remarks and help in improving the contents of the dissertation.

Most importantly, none of this would have been possible without the love and patience of my family. Especially I want to mention my parents Andrey and Irina, my sister Elena, my grandmothers Aza and Ljubov, my grandfather Vladimir, my aunt Elena and my uncle Vladimir, my cousins Anna, Ljubov and Nadezda. My family has been a constant source of love, concern, support and strength all these years. I would like to express my heart-felt gratitude to my family.

# Appendix A: Direct Product of Matrices

The Direct Product (also called as Kronecker product) of matrices plays a central role in mathematics and in applications found in engineering and theoretical physics. These applications are signal processing, statistical physics, quantum groups, quantum computers and others. In the problem discussed in the present thesis the direct product formalism is necessary for the construction of the spin Hamiltonian discussed in chapter 3, in section 3.1.2.

In this appendix section the general ideas of the direct product algebra are outlined and a spin Hamiltonian of a simple few-spin system is constructed.

Mathematically speaking, the direct product of a matrix  $A$  (which has the dimensions  $m \times n$ ) and a matrix  $B$  (which has the dimensions  $p \times q$ ) is a  $(mp) \times (nq)$  matrix with elements defined by

$$c_{\alpha\beta} = a_{ij}b_{kl} \quad (1)$$

where

$$\alpha = p(i - 1) + k \quad (2)$$

$$\beta = q(j - 1) + l \quad (3)$$

For example, the matrix direct product of the  $2 \times 2$  matrix  $A$  and the  $3 \times 2$  matrix  $B$  is given by the following  $6 \times 4$  matrix,

$$A \otimes B = \begin{pmatrix} a_{11}B & a_{12}B \\ a_{21}B & a_{22}B \end{pmatrix} = \begin{pmatrix} a_{11}b_{11} & a_{11}b_{12} & a_{12}b_{11} & a_{12}b_{12} \\ a_{11}b_{21} & a_{11}b_{22} & a_{12}b_{21} & a_{12}b_{22} \\ a_{11}b_{31} & a_{11}b_{32} & a_{12}b_{31} & a_{12}b_{32} \\ a_{21}b_{11} & a_{21}b_{12} & a_{22}b_{11} & a_{22}b_{12} \\ a_{21}b_{21} & a_{21}b_{22} & a_{22}b_{21} & a_{22}b_{22} \\ a_{21}b_{31} & a_{21}b_{32} & a_{22}b_{31} & a_{22}b_{32} \end{pmatrix}. \quad (4)$$

Let us consider a physical example: the interaction of a three spin 1/2-particles, where two particles represent electrons, and one particle represents a nucleus. This model system represents a simple radical pair with one nucleus. It has been discussed for example in Refs. [1, 179, 244].

Let  $\hat{H}_1$  be the Hamiltonian of a single electron and  $\hat{H}_2$  be the Hamiltonian of the other electron and of the nucleus. Then the Hamiltonian matrix of the entire system is defined as:

$$\hat{H} = \hat{H}_1 \otimes \begin{pmatrix} 1 & 0 & 0 & 0 \\ 0 & 1 & 0 & 0 \\ 0 & 0 & 1 & 0 \\ 0 & 0 & 0 & 1 \end{pmatrix} + \begin{pmatrix} 1 & 0 \\ 0 & 1 \end{pmatrix} \otimes \hat{H}_2, \quad (5)$$

where

$$\hat{H}_1 = \mu_B \vec{B} \hat{g} \vec{S}_1 = \mu_B g \left[ B_x \left( \frac{1}{2} \sigma_x \right) + B_y \left( \frac{1}{2} \sigma_y \right) + B_z \left( \frac{1}{2} \sigma_z \right) \right]. \quad (6)$$

Here  $\vec{B}$  is the external magnetic induction vector and  $\vec{S}_1$  describes the spin of the electron.  $\sigma_x$ ,  $\sigma_y$  and  $\sigma_z$  are the Pauli matrices defined in Eq. (3.9).  $\hat{g}$  is the g-tensor, and  $g$  is the g-factor. The g-factor for free electron, has the value close to two:  $g_e = 2.0023193$ . Thus, for the sake of simplicity let us assume that  $g = 2$ . Substituting Eqs. (3.9) in Eq. (6) one obtains:

$$\hat{H}_1 = \mu_B \begin{pmatrix} B_z & B_x - iB_y \\ B_x + iB_y & -B_z \end{pmatrix}. \quad (7)$$

$\hat{H}_2$  is defined as follows:

$$\hat{H}_2 = \mu_B \vec{B} \hat{g} \vec{S}_2 + \mu_B \vec{I}_1 \hat{A} \vec{S}_2, \quad (8)$$

where  $\hat{A}$  is the hyperfine coupling tensor for the nucleus. For the sake of simplicity let us assume that it has only isotropic part. Then, in the appropriate coordinate frame it can be brought to its diagonal form:

$$\hat{A} = \begin{pmatrix} A_{xx} & 0 & 0 \\ 0 & A_{yy} & 0 \\ 0 & 0 & A_{zz} \end{pmatrix}. \quad (9)$$

Substituting Eq. (9) into Eq. (8) one obtains:

$$\begin{aligned} \hat{H}_2 = & \mu_B \left( B_x \sigma_x \otimes \begin{pmatrix} 1 & 0 \\ 0 & 1 \end{pmatrix} + B_y \sigma_y \otimes \begin{pmatrix} 1 & 0 \\ 0 & 1 \end{pmatrix} + B_z \sigma_z \otimes \begin{pmatrix} 1 & 0 \\ 0 & 1 \end{pmatrix} \right) + \\ & + \frac{\mu_B}{2} (A_{xx} \sigma_x \otimes \sigma_x + A_{yy} \sigma_y \otimes \sigma_y + A_{zz} \sigma_z \otimes \sigma_z). \end{aligned} \quad (10)$$

With the definition of the direct product Eq. (4) the direct products in Eq. (10) can be calculated accordingly:

$$\sigma_x \otimes \begin{pmatrix} 1 & 0 \\ 0 & 1 \end{pmatrix} = \begin{pmatrix} 0 & 1 \\ 1 & 0 \end{pmatrix} \otimes \begin{pmatrix} 1 & 0 \\ 0 & 1 \end{pmatrix} = \begin{pmatrix} 0 & 0 & 1 & 0 \\ 0 & 0 & 0 & 1 \\ 1 & 0 & 0 & 0 \\ 0 & 1 & 0 & 0 \end{pmatrix} \quad (11)$$

$$\sigma_y \otimes \begin{pmatrix} 1 & 0 \\ 0 & 1 \end{pmatrix} = \begin{pmatrix} 0 & -i \\ i & 0 \end{pmatrix} \otimes \begin{pmatrix} 1 & 0 \\ 0 & 1 \end{pmatrix} = \begin{pmatrix} 0 & 0 & -i & 0 \\ 0 & 0 & 0 & -i \\ i & 0 & 0 & 0 \\ 0 & i & 0 & 0 \end{pmatrix} \quad (12)$$

$$\sigma_z \otimes \begin{pmatrix} 1 & 0 \\ 0 & 1 \end{pmatrix} = \begin{pmatrix} 1 & 0 \\ 0 & -1 \end{pmatrix} \otimes \begin{pmatrix} 1 & 0 \\ 0 & 1 \end{pmatrix} = \begin{pmatrix} 1 & 0 & 0 & 0 \\ 0 & 1 & 0 & 0 \\ 0 & 0 & -1 & 0 \\ 0 & 0 & 0 & -1 \end{pmatrix} \quad (13)$$

The direct products in the second term in Eq. (10) read as:

$$\sigma_x \otimes \sigma_x = \begin{pmatrix} 0 & 1 \\ 1 & 0 \end{pmatrix} \otimes \begin{pmatrix} 0 & 1 \\ 1 & 0 \end{pmatrix} = \begin{pmatrix} 0 & 0 & 0 & 1 \\ 0 & 0 & 1 & 0 \\ 0 & 1 & 0 & 0 \\ 1 & 0 & 0 & 0 \end{pmatrix} \quad (14)$$

$$\sigma_y \otimes \sigma_y = \begin{pmatrix} 0 & -i \\ i & 0 \end{pmatrix} \otimes \begin{pmatrix} 0 & -i \\ i & 0 \end{pmatrix} = \begin{pmatrix} 0 & 0 & 0 & -1 \\ 0 & 0 & 1 & 0 \\ 0 & 1 & 0 & 0 \\ -1 & 0 & 0 & 0 \end{pmatrix} \quad (15)$$

$$\sigma_z \otimes \sigma_z = \begin{pmatrix} 1 & 0 \\ 0 & -1 \end{pmatrix} \otimes \begin{pmatrix} 1 & 0 \\ 0 & -1 \end{pmatrix} = \begin{pmatrix} 1 & 0 & 0 & 0 \\ 0 & -1 & 0 & 0 \\ 0 & 0 & -1 & 0 \\ 0 & 0 & 0 & 1 \end{pmatrix}. \quad (16)$$

Substituting Eqs. (11)-(16) into Eq. (10) one obtains:

$$\begin{aligned}
\hat{H}_2 &= \mu_B \begin{pmatrix} B_z & 0 & B_x - iB_y & 0 \\ 0 & B_z & 0 & B_x - iB_y \\ B_x + iB_y & 0 & -B_z & 0 \\ 0 & B_x + iB_y & 0 & -B_z \end{pmatrix} + \\
&+ \frac{\mu_B}{4} \begin{pmatrix} A_{zz} & 0 & 0 & A_{xx} - A_{yy} \\ 0 & -A_{zz} & A_{xx} + A_{yy} & 0 \\ 0 & A_{xx} + A_{yy} & -A_{zz} & 0 \\ A_{xx} - A_{yy} & 0 & 0 & A_{zz} \end{pmatrix} = \\
&= \frac{\mu_B}{2} \begin{pmatrix} 2B_z + \frac{A_{zz}}{2} & 0 & 2(B_x - iB_y) & \frac{A_{xx} - A_{yy}}{2} \\ 0 & 2B_z - \frac{A_{zz}}{2} & \frac{A_{xx} + A_{yy}}{2} & 2(B_x - iB_y) \\ 2(B_x + iB_y) & \frac{A_{xx} + A_{yy}}{2} & -2B_z - \frac{A_{zz}}{2} & 0 \\ \frac{A_{xx} - A_{yy}}{2} & 2(B_x + iB_y) & 0 & -2B_z + \frac{A_{zz}}{2} \end{pmatrix}.
\end{aligned} \tag{17}$$

With Eqs. (7) and (18) one can determine the summands in Eq. (5):

$$\begin{aligned}
\hat{H}_1 \otimes \begin{pmatrix} 1 & 0 & 0 & 0 \\ 0 & 1 & 0 & 0 \\ 0 & 0 & 1 & 0 \\ 0 & 0 & 0 & 1 \end{pmatrix} &= \mu_B \begin{pmatrix} B_z & B_x - iB_y \\ B_x + iB_y & -B_z \end{pmatrix} \otimes \begin{pmatrix} 1 & 0 & 0 & 0 \\ 0 & 1 & 0 & 0 \\ 0 & 0 & 1 & 0 \\ 0 & 0 & 0 & 1 \end{pmatrix} = \\
\mu_B \begin{pmatrix} B_z & 0 & 0 & 0 & B_x - & & & & \\ & & & & iB_y & 0 & 0 & 0 & \\ 0 & B_z & 0 & 0 & 0 & B_x - & & & \\ & & & & & iB_y & 0 & 0 & \\ 0 & 0 & B_z & 0 & 0 & 0 & B_x - & & \\ & & & & & & iB_y & 0 & \\ 0 & 0 & 0 & B_z & 0 & 0 & 0 & B_x - & \\ & & & & & & & iB_y & \\ B_x + & & & & & & & & \\ iB_y & 0 & 0 & 0 & -B_z & 0 & 0 & 0 & \\ 0 & B_x + & & & & & & & \\ & iB_y & 0 & 0 & 0 & -B_z & 0 & 0 & \\ 0 & 0 & B_x + & & & & & & \\ & & iB_y & 0 & 0 & 0 & -B_z & 0 & \\ 0 & 0 & 0 & B_x + & & & & & \\ & & & iB_y & 0 & 0 & 0 & -B_z & \end{pmatrix}
\end{aligned} \tag{18}$$



$$\begin{aligned}
 & \begin{pmatrix} 1 & 0 \\ 0 & 1 \end{pmatrix} \otimes \hat{H}_2 = \frac{\mu_B}{2} \begin{pmatrix} 1 & 0 \\ 0 & 1 \end{pmatrix} \otimes \begin{pmatrix} 2B_z + \frac{A_{zz}}{2} & 0 \\ 2(B_x + iB_y) & 2(B_x - iB_y) \end{pmatrix} = \\
 & = \mu_B \begin{pmatrix} B_z + \frac{A_{zz}}{4} & 0 & B_x - iB_y & \frac{A_{xx} - A_{yy}}{4} & 0 & 0 & 0 & 0 \\ 0 & B_z - \frac{A_{zz}}{4} & \frac{A_{xx} + A_{yy}}{4} & B_x - iB_y & 0 & 0 & 0 & 0 \\ B_x + iB_y & \frac{A_{xx} + A_{yy}}{4} & -B_z - \frac{A_{zz}}{4} & 0 & 0 & 0 & 0 & 0 \\ \frac{A_{xx} - A_{yy}}{4} & B_x + iB_y & 0 & -B_z + \frac{A_{zz}}{4} & 0 & 0 & 0 & 0 \\ 0 & 0 & 0 & 0 & B_z + \frac{A_{zz}}{4} & 0 & B_x - iB_y & \frac{A_{xx} - A_{yy}}{4} \\ 0 & 0 & 0 & 0 & 0 & B_z - \frac{A_{zz}}{4} & \frac{A_{xx} + A_{yy}}{4} & B_x - iB_y \\ 0 & 0 & 0 & 0 & B_x + iB_y & \frac{A_{xx} + A_{yy}}{4} & -B_z - \frac{A_{zz}}{4} & 0 \\ 0 & 0 & 0 & 0 & \frac{A_{xx} - A_{yy}}{4} & B_x + iB_y & 0 & -B_z + \frac{A_{zz}}{4} \end{pmatrix} \quad (19)
 \end{aligned}$$

Substituting Eq. (18) and Eq. (19) in Eq. (5) one obtains the final expression for the Hamiltonian:

$$\hat{H} = \mu_B \begin{pmatrix} 2B_z + \frac{A_{zz}}{4} & 0 & B_x - iB_y & \frac{A_{xx} - A_{yy}}{4} & B_x - iB_y & 0 & 0 & 0 \\ 0 & 2B_z - \frac{A_{zz}}{4} & \frac{A_{xx} + A_{yy}}{4} & B_x - iB_y & 0 & B_x - iB_y & 0 & 0 \\ B_x + iB_y & \frac{A_{xx} + A_{yy}}{4} & -\frac{A_{zz}}{4} & 0 & 0 & 0 & 0 & 0 \\ B_x + iB_y & 0 & 0 & \frac{A_{zz}}{4} & 0 & 0 & B_x - iB_y & 0 \\ 0 & B_x + iB_y & 0 & 0 & 0 & 0 & 0 & B_x - iB_y \\ 0 & 0 & B_x + iB_y & 0 & 0 & 0 & \frac{A_{xx} + A_{yy}}{4} & B_x - iB_y \\ 0 & 0 & 0 & B_x + iB_y & 0 & -\frac{A_{zz}}{4} & \frac{A_{xx} + A_{yy}}{4} & 0 \\ 0 & 0 & 0 & B_x + iB_y & 0 & \frac{A_{xx} - A_{yy}}{4} & -2B_z - \frac{A_{zz}}{4} & -2B_z + \frac{A_{zz}}{4} \end{pmatrix} \quad (20)$$

In this appendix section it was demonstrated how the spin-Hamiltonian matrix can be constructed. The Hamiltonian,  $\hat{H}$ , in Eq. (3.48) can be constructed in a similar way. Its analytic expression becomes somewhat lengthy because of the larger number of nuclei and because of the anisotropic part of the hyperfine interaction, which was omitted in the discussed example.

# Appendix B: Physical Units

## Length Relations

The units of length in the SI system of units are metres (m) and in the CGS system of units it is centimeters (cm). However, in the problems discussed in the thesis other units of length were used (i.e. micrometer ( $\mu\text{m}$ ) and nanometer (nm)). The relation between these units reads as follows:

$$1 \text{ m} = 10^2 \text{ cm} = 10^6 \mu\text{m} = 10^9 \text{ nm}$$

## Energy Relations

There are many different units for expressing energy. Here only those which are most closely related to the subject of the dissertation are reviewed. In the SI system of units, the energy unit is Joule (J), named after James Prescott Joule for his work on the relationship between heat, electricity and mechanical work:

$$1 \text{ J} = 1 \frac{\text{kg} \cdot \text{m}^2}{\text{s}^2}.$$

In the dissertation several other units of energy were used: electron volt (eV), milli-electron volt (meV), kilocalorie/mole (kcal/mol) and ergs (erg). These units can be expressed in units of Joule as follows:

$$\begin{aligned} 1 \text{ eV} &= 1.602 \cdot 10^{-19} \text{ J} = 1000 \text{ meV} = 23.045 \frac{\text{kcal}}{\text{mol}} = 1.602 \cdot 10^{-12} \text{ erg} \\ 1 \frac{\text{kcal}}{\text{mol}} &= 4.339 \cdot 10^{-2} \text{ eV} = 6.952 \cdot 10^{-22} \text{ J} \\ 1 \text{ J} &= 10^7 \text{ erg.} \end{aligned}$$

## Magnetic Field Units, Magnetization

The SI unit of magnetic flux density (or magnetic induction) is tesla (symbol T). It defines the intensity (density) of a magnetic field. The tesla is equal to one weber per square meter and was defined in 1960 in honor of inventor, scientist and electrical engineer Nikola Tesla.

$$1 \text{ T} = 1 \frac{\text{V} \cdot \text{s}}{\text{m}^2} = 1 \frac{\text{N}}{\text{A} \cdot \text{m}} = 1 \frac{\text{Wb}}{\text{m}^2} = 1 \frac{\text{kg}}{\text{A} \cdot \text{s}^2}$$

1 Tesla is equivalent to 10,000 gauss (G), used in CGS system, or  $10^9$  gammas ( $\gamma$ ), used in geophysics. Thus,

$$\begin{aligned} 1 \gamma &= 10^{-9} \text{ T} \\ 1 \text{ G} &= 10^{-4} \text{ T}. \end{aligned}$$

The unit of magnetizing force (magnetic field strength) in the CGS electromagnetic system is Oersted (Oe). To convert Oe to the SI system of units the following relation can be used:

$$1 \text{ Oe} = \frac{1000}{4\pi} \frac{\text{A}}{\text{m}} = 79.58 \frac{\text{A}}{\text{m}}.$$

*In vacuo* the magnetic field of one Oersted corresponds to the magnetic induction of one Gauss.

Magnetization is a property of some materials (e.g. magnets) that describes to what extent they are affected by magnetic fields, and also determines the magnetic field that the material itself creates. Magnetization is defined as the amount of magnetic moment per unit volume. The units of magnetization in the SI system of units are A/m. In the CGS system of units it is emu (electromagnetic unit) per unit volume. The units can be converted according to the following equation:

$$1 \frac{\text{emu}}{\text{cm}^3} = 10^3 \frac{\text{A}}{\text{m}}.$$

## Magnetic Moment

The magnetic moment or magnetic dipole moment is a measure of the strength of a magnetic source. In the CGS system of units the measure for the magnetic moment

is emu (electromagnetic unit), while in the SI system of units it is  $\text{A}\cdot\text{m}^2$ . Both units are related as follows:

$$1 \text{ emu} = 10^{-3} \text{ A} \cdot \text{m}^2$$

For a grain of volume  $V$  ( $\text{cm}^3$ ) and saturation magnetization  $M_s$  ( $\text{emu}/\text{cm}^3$ ), the units of the magnetic moment  $\vec{\mu} = V \cdot M_s$  are:

$$1 \text{ emu} = 1 \frac{\text{erg}}{\text{G}} = 10^{-3} \frac{\text{J}}{\text{T}} = 6.242 \times 10^{11} \frac{\text{eV}}{\text{G}}.$$

## Magnetic Susceptibility

The volume susceptibility is a dimensionless quantity. It can be measured in the CGS and SI systems of units. The conversion between the two systems is governed by the following equation

$$\chi_v^{(\text{CGS})} = 4\pi\chi_v^{(\text{SI})}.$$

## Light Intensity Units

Irradiance is a radiometry term for the power of electromagnetic radiation at a surface, per unit area. "Irradiance" is used when the electromagnetic radiation is incident on the surface. The SI units for this quantity is watts per square metre ( $\text{W}/\text{m}^2$ ), while the CGS units are ergs per square centimeter per second ( $\text{erg}\cdot\text{cm}^{-2}\cdot\text{s}^{-1}$ , which is often used in astronomy). These quantities are sometimes called intensity, but this usage leads to confusion with radiant intensity, which has different units.

All of these quantities characterize the total amount of radiation present, at all frequencies. It is also common to consider each frequency in the spectrum separately. This can be achieved by dividing the Irradiance by the energy of one quanta  $h\nu$ , where  $h$  is the Planck constant and  $\nu$  is the light-frequency. then the corresponding units for irradiance in the SI system of units are  $\text{quanta}\cdot\text{s}^{-1}\text{m}^{-2}$ .



# Bibliography

- [1] Ritz, T., S. Adem, and K. Schulten. 2000. A model for photoreceptor-based magnetoreception in birds. *Biophys. J.* 78:707–718.
- [2] Wiltschko, W. and R. Wiltschko. 2002. Magnetic compass orientation in birds and its physiological basis. *Naturwissenschaften.* 89:445–452.
- [3] Wiltschko, W. and R. Wiltschko. 2005. Magnetic orientation and magnetoreception in birds and other animals. *J. Comp. Physiol. A.* 191:675–693.
- [4] Beason, R. C. 2005. Mechanisms of magnetic orientation in birds. *Integr. Comp. Biol.* 45:565–573.
- [5] Mouritsen, H. and T. Ritz. 2005. Magnetoreception and its use in bird navigation. *Curr. Opin. Neurobiol.* 15:406–414.
- [6] Wiltschko, R. and W. Wiltschko. 2006. Magnetoreception. *BioEssays.* 28:157–168.
- [7] Schmidt-Koenig, K. 1990. The sun compass. *Experientia.* 46:336–342.
- [8] Able, K. 1982. Skylight polarization patterns at dusk influence migratory orientation in birds. *Nature.* 299:550–551.
- [9] Moore, F. 1987. Sunset and the orientation behaviour of migrating birds. *Biol. Rev.* 62:65–86.
- [10] Helbig, A. 1991. Dusk orientation of migratory European robins, *erithacus rubecula*: the role of sun-related directional information. *Anim. Behav.* 41:313–322.
- [11] Sauer, E. 1957. Die sternorientierung nachtlich ziehender Grasmucken, *sylvia atricapilla, borin and curruca*. *Z. Tierpsychol.* 14:20–70.

- 
- [12] Emlen, S. 1970. Celestial rotation: its importance in the development of migratory orientation. *Science*. 170:1198–1201.
- [13] Merkel, F. and W. Wiltschko. 1965. Magnetismus und Richtungsfinden zugunruhiger Rotkehlchen, *erithacus rubecula*. *Vogelwarte*. 23:71–77.
- [14] Wiltschko, W. and F. Merkel. 1966. Orientierung zugunruhiger Rotkehlchen im statischen magnetfeld. *Verh. dt. Zool. Ges.* 59:362–367.
- [15] Wiltschko, W. 1968. Über den Einfluss Statischer Magnetfelder auf die zugorientierung der Rotkehlchen, *erithacus rubecula*. *Z. Tierpsychol.* 25:537–558.
- [16] Wiltschko, W. and R. Wiltschko. 1972. Magnetic compass of European robins. *Science*. 176:62–64.
- [17] Lohmann, K., S. Cain, S. Dodge, and C. Lohmann. 2001. Regional magnetic fields as navigational markers for sea turtles. *Science*. 294:364–366.
- [18] Lohmann, K., C. Lohmann, L. Erhart, D. Bagley, and T. Swing. 2004. Geomagnetic map used in sea-turtle navigation. *Nature*. 428:909–910.
- [19] Phillips, J., M. Freake, and S. Borland. 2002. Behavioral titration of magnetic map coordinates. *J. Comp. Physiol. A*. 188:157–160.
- [20] Phillips, J. and S. Borland. 1992. Behavioral evidence for use of a light-dependent magnetoreception mechanism by a vertebrate. *Nature*. 359:142–144.
- [21] Gould, J., J. Kirschvink, and K. Deffeyes. 1978. Bees have magnetic remanence. *Science*. 201:1026–1028.
- [22] Kirschvink, J. 1982. Birds, Bees and Magnetism : A new look at the old problem of magnetoreception. *Trends in Neurosciences*. 5:160–167.
- [23] Hsu, C.-Y. and C.-W. Li. 1994. Magnetoreception in Honeybees. *Science*. 265:95–97.
- [24] Nichol, H., M. Locke, J. L. Kirschvink, M. M. Walker, M. H. Nesson, C.-Y. Hsu, and C.-W. Li. 1995. Honeybees and magnetoreception. *Science*. 269:1888–1890.



- 
- [25] Schiff, H. and G. Canal. 1992. The magnetic and electric fields induced by superparamagnetic magnetite in Honeybees. *Biol. Cyber.* 69:7–17.
- [26] Blakemore, R. 1975. Magnetotactic Bacteria. *Science.* 190:377–379.
- [27] Frankel, R. B., R. P. Blakemore, and R. S. Wolfe. 1979. Magnetite in freshwater magnetotactic Bacteria. *Science.* 203:1355–1356.
- [28] Gorby, Y. A., T. J. Beveridge, and R. P. Blakemore. 1988. Characterization of the bacterial magnetosome membrane. *J. Bacteriol.* 170:834–841.
- [29] Wiltschko, W., R. Wiltschko, and U. Munro. 2000. Light-dependent magnetoreception in birds: the effect of intensity of 565-nm green light. *Naturwissenschaften.* 87:366–369.
- [30] Wiltschko, W. and R. Wiltschko. 1981. Disorientation of inexperienced young pigeons after transportation in total darkness. *Nature.* 291:433–434.
- [31] Wiltschko, W. and R. Wiltschko. 1998. Pigeon homing: effect of various wavelengths of light during displacement. *Naturwissenschaften.* 85:164–167.
- [32] Wiltschko, W. and R. Wiltschko. 2001. Light-dependent magnetoreception in birds: The behaviour of European robins, *Erithacus rubecula*, under monochromatic light of various wavelengths and intensities. *J. Exp. Biol.* 204:3295–3302.
- [33] Semm, P. and C. Demaine. 1986. Neurophysiological properties of magnetic cells in the pigeon’s visual system. *J. Comp. Physiol. A.* 159:619–625.
- [34] Schulten, K. and A. Windemuth. 1986. Model for a physiological magnetic compass. In G. Maret, N. Boccara, and J. Kiepenheuer, editors, *Biophysical Effects of Steady Magnetic Fields*, volume 11 of *Proceedings in Physics*. Springer, Berlin, pages 99–106.
- [35] Cintolesi, F., T. Ritz, C. Kay, C. Timmel, and P. Hore. 2003. Anisotropic recombination of an immobilized photoinduced radical pair in a 50 microTesla magnetic field: a model avian photomagnetoceptor. *Chem. Phys.* 294:707–718.

- [36] Solov'yov, I. A., D. Chandler, and K. Schulten. 2007. Magnetic field effects in *arabidopsis thaliana* Cryptochrome-1. *Biophys. J.* 92:2711–2726.
- [37] Solov'yov, I. A. and W. Greiner. 2007. Possible mechanism of avian orientation in magnetic field. *Biophys. J.* 93.
- [38] Solov'yov, I. and W. Greiner. 2007. A first attempt to model the mechanism of magnetoreception in birds. *Submitted to New. J. Phys.*
- [39] Solov'yov, I. and W. Greiner. 2007. Towards an understanding of the mechanism of magnetoreception in birds. [[arXiv.org: 0704.1763v1](https://arxiv.org/abs/0704.1763v1) [*physics.bio-ph*] 13 Apr 2007].
- [40] Davila, A. F., M. Winklhofer, V. P. Shcherbakov, and N. Petersen. 2005. Magnetic pulse affects a putative magnetoreceptor mechanism. *Biophys. J.* 89:56–63.
- [41] Winklhofer, M. 2004. Vom magnetischen Bakterium zur Brieftaube. *Physik unserer Zeit.* 35:120–127.
- [42] Kirschvink, J. L., M. M. Walker, and C. E. Diebel. 2001. Magnetite-based magnetoreception. *Curr. Opin. Neurobiol.* 11:462–467.
- [43] Kirschvink, J. and J. Gould. 1981. Biogenic magnetite as a basis for magnetic field detection in animals. *Biosystems.* 13:181–201.
- [44] Johnsen, S. and K. J. Lohmann. 2005. The physics and neurobiology of magnetoreception. *Neuroscience.* 6:703–712.
- [45] Shcherbakov, V. and M. Winklhofer. 1999. The osmotic magnetometer: a new model for magnetite-based magnetoreceptors in animals. *Europ. Biophys. J.* 28:380–392.
- [46] Winklhofer, M. 1999. *Modelle hypothetischer Magnetfeldrezeptoren auf der Grundlage biogenen Magnetits.* Verlag Merie Leidorf GmbH, Rahden/Westfallen. ISBN 3-89646-015-3.
- [47] Davila, A. F. 2005. *Detection and Function of Biogenic Magnetite.* Dissertation, Ludwig Maximilians Universität München, Deutschland.

- [48] von Middendorff, A. 1859. Die Isepiptesen Rußlands. *Mem Acad. Sci. St. Petersbourg VI Ser.* 8:1–43.
- [49] Semm, P. and R. Beason. 1990. Responses to small magnetic variations by the trigeminal system of the Bobolink. *Brain Res. Bull.* 25:735–740.
- [50] Semm, P. and R. Beason. 1990. Sensory basis of bird orientation. *Experientia.* 46:372–378.
- [51] Wiltschko, R. and W. Wiltschko. 1995. *Magnetic Orientation in Animals.* Berlin, Heidelberg, New York: Springer Verlag.
- [52] Munro, U., J. Munro, and J. Phillips. 1997. Evidence for a magnetite-based navigational “map” in birds. *Naturwissenschaften.* 84:26–28.
- [53] Lohmann, J. and S. Johnson. 2000. The neurobiology of magnetoreception in vertebrate animals. *Trends Neurosci.* 23:153–159.
- [54] Lin, C. and T. Todo. 2005. The cryptochromes. *Gen. Biol.* 6:220.1 – 220.9.
- [55] Partch, C. L. and A. Sancar. 2005. Cryptochromes and circadian photoreception in animals. *Meth. Enzym.* 393:726–745.
- [56] Christie, J. M. and W. R. Briggs. 2001. Blue light sensing in higher plants. *J. Biol. Chem.* 276:11457–11460.
- [57] Ahmad, M., P. Galland, T. Ritz, R. Wiltschko, and W. Wiltschko. 2007. Magnetic intensity affects cryptochrome-dependent responses in *Arabidopsis thaliana*. *Planta.* 225:615–624.
- [58] Fleissner, G., E. Holtkamp-Rötzler, M. Hanzlik, M. Winklhofer, G. Fleissner, N. Petersen, and W. Wiltschko. 2003. Ultrastructural analysis of a putative magnetoreceptor in the beak of homing pigeons. *J. Comparat. Neurol.* 458:350–360.
- [59] Stahl, B., G. Fleissner, G. Falkenberg, and G. Fleissner. 2006. Magnetite nanoparticles alone are not able to explain iron mineral-based magnetoreception in homing pigeons. In A. Kyriakopoulos, B. Michalke, A. Grabert, and D. Behne, editors, *Proceedings of the 4-th Fall Conference on Metalloproteins and Metalloidproteins.* Herbert Utz Verlag: München, pages 63–68.

- [60] Fleissner, G., B. Stahl, P. Thalau, G. Falkenberg, and G. Fleissner. 2007. A novel concept of Fe-mineral based magnetoreception: Histological and physicochemical data from the upper beak of homing pigeons. *Naturwissenschaften*. 94:631–642.
- [61] Stahl, B., G. Fleissner, G. Falkenberg, and G. Fleissner. 2007. Micromagnetic aspects of magnetoreception of homing pigeons based on iron minerals. In *Proceedings of the XAFS13*, volume 882. American Institute of Physics, pages 755–757.
- [62] Kirschvink, J. 1992. Comment on "constraints on biological effects of weak extremely-low-frequency electromagnetic fields". *Phys. Rev. A*. 46:2178–2186.
- [63] Hunt, C., B. Moskowitz, and S. Banerjee. 1995. Magnetic properties of rocks and minerals. *Rock Physics and Phase Relations, A Handbook of Physical Constants, AGU Reference Shelf 3*:189–204.
- [64] Cashmore, A. R., J. A. Jarillo, Y.-J. Wu, and D. Liu. 1999. Cryptochromes: Blue light receptors for plants and animals. *Science*. 284:760–765.
- [65] Pecharroman, C., T. Gonzalez-Carreno, and J. Iglesias. 1995. The infrared dielectric properties of maghemite,  $\gamma\text{-Fe}_2\text{O}_3$ , from reflectance measurement on pressed powders sample: a) idealized. *Physics and Chemistry of Minerals*. 22:21–29.
- [66] Downs, R. and M. Hall-Wallace. 2003. The american mineralogist crystal structure database. *Am. Mineral*. 88:247–250.
- [67] Shmakov, A., G. Kryukova, S. Tsybulya, A. Chuvilin, and L. Solovyeva. 1995. Vacancy ordering in  $\gamma\text{-Fe}_2\text{O}_3$ : Synchrotron x-ray powder diffraction and high-resolution electron microscopy studies. *Journal of Applied Crystallography*. 28:141–145.
- [68] Villars, P. and L. Calvert. 1985. *Pearson's handbook of crystallographic data for intermetallic phases*. Metals Park, Ohio.
- [69] Skiles, D. 1985. *Magnetite Biomineralization and Magnetoreception in Organisms: a New Biomagnetism*, chapter The geomagnetic field: its nature,

- history, and biological relevance. New York, London: Plenum Press, pages 43–102.
- [70] Bloxham, J. and D. Gubbins. 1989. The evolution of the earth's magnetic field. *Sci. Am.* 261:68–75.
- [71] 2005-03-13. Geomagnetism, north magnetic pole. *Natural Resources Canada*.
- [72] Tenforde, T. 1995. *Electromagnetic Fields: Biological Interactions and Mechanisms*, chapter Spectrum and intensity of environmental electromagnetic fields from natural and man-made sources. Washington DC: American Chemical Society, pages 13–35.
- [73] Rodda, G. 1984. The orientation and navigation of juvenile alligators: evidence of magnetic sensitivity. *J. Comp. Physiol. A.* 154:649–658.
- [74] Wiltschko, W. and R. Wiltschko. 1996. Magnetic orientation in birds. *J. Exp. Biol.* 199:29–38.
- [75] Wiltschko, W. 1978. *Animal migration, navigation, and homing*, chapter Further analysis of the magnetic compass of migratory birds. Springer, Berlin, Heidelberg, New York, pages 302–310.
- [76] Akesson, S., J. Morin, R. Muheim, and U. Ottosson. 2001. Avian orientation at steep angles of inclination: experiments with migratory white-crowned sparrows at the magnetic north pole. *Proc. R. Soc. Lond. B. (Biol. Sci.)*. 268:1907–1913.
- [77] Marhold, S., H. Burda, and W. Wiltschko. 1997. A magnetic polarity compass for direction finding in a subterranean mammal. *Naturwissenschaften*. 84:421–423.
- [78] Lohmann, K., N. Pentcheff, G. Nevitt, G. Stetten, R. Zimmer-Faust, and et al. 1995. Magnetic orientation of spiny lobsters in the ocean: experiments with underseas coil systems. *J. Exp. Biol.* 198:2041–2048.
- [79] Phillips, J. 1986. Two magnetoreception pathways in a migratory salamander. *Science*. 233:765–767.

- [80] Light, P., M. Salmon, and K. Lohmann. 1993. Geomagnetic orientation of loggerhead sea turtles: evidence for an inclination compass. *J. Exp. Biol.* 182:1–10.
- [81] Boles, L. and K. Lohmann. 2003. True navigation and magnetic map in spiny lobsters. *Nature.* 421:60–63.
- [82] Walcott, C. 1978. *Animal Migration, Navigation and Homing*, chapter Anomalies in the earth's magnetic field increase the scatter of pigeons' vanishing bearings. Berlin, Heidelberg, New York: Springer Verlag, pages 143–151.
- [83] Beck, W. and W. Wiltschko. 1988. *Acta XIX Congr Int Ornithol Vol II. ed.*, chapter Magnetic factors control the migratory direction of Pied Flycatchers, (*Ficedula hypoleuca* Pallas). Ottawa: University of Ottawa Press, pages 1955–1962.
- [84] Wiltschko, W. and R. Wiltschko. 1992. Migratory orientation: magnetic compass orientation of Garden warblers (*sylvia borin*) after a simulated crossing of the magnetic equator. *Ethology.* 91:70–79.
- [85] Fransson, T., S. Jakobsson, P. Johansson, C. Kullberg, J. Lind, and A. Vallin. 2001. Magnetic cues trigger extensive refuelling. *Nature.* 414:35–36.
- [86] Leask, M. 1977. Physiochemical mechanism for magnetic field detection by migratory birds and homing pigeons. *Nature.* 267:144–145.
- [87] Schulten, K., C. E. Swenberg, and A. Weller. 1978. A biomagnetic sensory mechanism based on magnetic field modulated coherent electron spin motion. *Z. Phys. Chem.* NF111:1–5.
- [88] Schulten, K. 1982. Magnetic field effects in chemistry and biology. In J. Treusch, editor, *Festkörperprobleme*, volume 22. Vieweg, Braunschweig, pages 61–83.
- [89] Schulten, K. and P. G. Wolynes. 1978. Semiclassical description of electron spin motion in radicals including the effect of electron hopping. *J. Chem. Phys.* 68:3292–3297.
- [90] Schulten, K. and A. Weller. 1978. Exploring fast electron transfer processes by magnetic fields. *Biophys. J.* 24:295–305.

- [91] Schulten, K. 1986. Magnetic field effects on radical pair processes in chemistry and biology. In J. H. Bernhard, editor, *Biological Effects of Static and Extremely Low Frequency Magnetic Fields*. MMV Medizin Verlag, Munich, pages 133–140.
- [92] Timmel, C. R., U. Till, B. Brocklehurst, K. Mclauchlan, and P. Hore. 1998. Effects of weak magnetic fields on free radical recombination reactions. *Mol. Phys.* 95:71–89.
- [93] Schulten, K., H. Staerk, A. Weller, H.-J. Werner, and B. Nickel. 1976. Magnetic field dependence of the geminate recombination of radical ion pairs in polar solvents. *Z. Phys. Chem.* NF101:371–390.
- [94] Schulten, K. 1984. Ensemble averaged spin pair dynamics of doublet and triplet molecules. *J. Chem. Phys.* 80:3668–3679.
- [95] O’Dea, A. R., A. F. Curtis, N. J. B. Green, C. R. Timmel, and P. Hore. 2005. Influence of dipolar interactions on radical pair recombination reactions subject to weak magnetic fields. *J. Phys. Chem. A.* 109:869–973.
- [96] Wiltschko, W., J. Traudt, O. Güntürkün, H. Prior, and R. Wiltschko. 2002. Lateralization of magnetic compass orientation in a migratory bird. *Nature.* 419:467–470.
- [97] Bailey, M., N. Chong, J. Xiong, and V. Cassone. 2002. Chickens’ cry2: molecular analysis of an avian cryptochrome in retinal and pineal photoreceptors. *FEBS Letters.* 513:169–174.
- [98] Möller, A., S. Sagasser, B. Schierwater, and W. Wiltschko. 2003. Retinal photopigments as possible transducers for the avian magnetic compass. *Vogelwarte.* 42:52.
- [99] Semm, P., D. Nohr, C. Demaine, and W. Wiltschko. 1984. Neural basis of the magnetic compass: interactions of visual, magnetic and vestibular inputs in the pigeon’s brain. *J. Comp. Physiol. A.* 155:283–288.
- [100] Wiltschko, W., U. Munro, H. Ford, and R. Wiltschko. 1993. Red light disrupts magnetic orientation of migratory birds. *Nature.* 364:525–527.

- [101] Wiltschko, W. and R. Wiltschko. 1995. Migratory orientation of European robins is affected by the wavelength of light as well as by a magnetic pulse. *J. Comp. Physiol. A.* 177:363–369.
- [102] Wiltschko, W. and R. Wiltschko. 1999. The effect of yellow and blue light on magnetic compass orientation in European robins, *erithacus rubecula*. *J. Comp. Physiol. A.* 184:295–299.
- [103] Munro, U., J. Munro, J. Phillips, and W. Wiltschko. 1997. Effect of wavelength of light and pulse magnetization on different magnetoreception systems in a migratory bird. *Austral. J. Zool.* 45:189–198.
- [104] Rappl, R., R. Wiltschko, P. Weindler, P. Berthold, and W. Wiltschko. 2000. Orientation behaviour of Garden warblers, *sylvia borin*, under monochromatic light of various wavelengths. *Auk.* 117:256–260.
- [105] Wiltschko, W., R. Wiltschko, and U. Munro. 2000. Light-dependent magnetoreception in birds: does directional information change with light intensity? *Naturwissenschaften.* 87:36–40.
- [106] Wiltschko, W., U. Munro, H. Ford, and R. Wiltschko. 2003. Magnetic orientation in birds: non-compass responses under monochromatic light of increased intensity. *Proc. R. Soc. Lond. B.* 270:2133–2140.
- [107] Wiltschko, W., A. Möller, M. Gesson, C. Noll, and R. Wiltschko. 2004. Light-dependent magnetoreception in birds: analysis of the behaviour under red light after pre-exposure to red light. *The Journal of Experimental Biology.* 207:1193–1202.
- [108] Walcott, C., J. Gould, and J. Kirschvink. 1979. Pigeons have magnets. *Science.* 205:1027–1028.
- [109] Beason, R. and J. Nichols. 1984. Magnetic orientation and magnetically sensitive material in a transequatorial migratory bird. *Nature.* 309:151–153.
- [110] Beason, R. and W. Brennan. 1986. Natural and induced magnetization in the Bobolink, *dolichonyx oryzivorus* (Aves: Icteridae). *J. Exp. Biol.* 125:49–56.
- [111] Edwards, H., G. Schnell, R. DuBois, and V. Hutchison. 1992. Natural and induced remanent magnetism in birds. *Auk.* 109:43–56.



- [112] Hanzlik, M., C. Heunemann, E. Holtkamp-Rötzler, M. Winklhofer, N. Petersen, and G. Fleissner. 2000. Superparamagnetic magnetite in the upper beak tissue of homing pigeons. *BioMetals*. 13:325–331.
- [113] Winklhofer, M., E. Holtkamp-Rötzler, M. Hanzlik, G. Fleissner, and N. Petersen. 2001. Clusters of superparamagnetic magnetite particles in the upper-beak skin of homing pigeons: evidence of a magnetoreceptor? *Europ. J. Mineral.* 13:659–669.
- [114] Williams, M. and J. Wild. 2001. Trigeminally innervated iron-containing structures in the beak of homing pigeons, and other birds. *Brain Res.* 889:243–246.
- [115] Yorke, E. 1985. *Magnetite Biomineralization and Magnetoreception in Organisms: a New Biomagnetism*, chapter Energetics and sensitivity considerations of ferromagnetic magnetoreceptors. New York, London: Plenum Press, pages 233–242.
- [116] Edmonds, D. 1992. A magnetic null detector as the migrating bird's compass. *Proc. R. Soc. Lond. B.* 249:27–31.
- [117] Walker, M., T. Dennis, and J. Kirschvink. 2002. The magnetic sense and its use in long-distance navigation by animals. *Curr. Opin. Neurobiol.* 12:735–744.
- [118] Kirschvink, J. and M. Walker. 1985. *Magnetite Biomineralization and Magnetoreception in Organisms: a New Biomagnetism*, chapter Particle-size considerations for magnetite-based magnetoreceptors. New York, London: Plenum Press, pages 243–254.
- [119] Wiltschko, W., U. Munro, R. Beason, H. Ford, and R. Wiltschko. 1994. A magnetic pulse leads to a temporary deflection in the orientation of migratory birds. *Experientia.* 50:679–700.
- [120] Beason, R., N. Dussourd, and M. Deutschlander. 1995. Behavioural evidence for the use of magnetic material in magnetoreception by a migratory bird. *J. Exp. Biol.* 198:141–146.
- [121] Beason, R. and P. Semm. 1996. Does the avian ophthalmic nerve carry magnetic navigational information? *J. Exp. Biol.* 199:1241–1244.

- [122] Wiltschko, W., U. Munro, H. Ford, and R. Wiltschko. 1998. Effect of a magnetic pulse on the orientation of silvereyes, *zoosterops l. lateralis*, during spring migration. *J. Exp. Biol.* 201:3257–3261.
- [123] Wiltschko, W., U. Munro, R. Wiltschko, and J. Kirschvink. 2002. Magnetite-based magnetoreception in birds: the effect of a biasing field and a pulse on migratory behavior. *J. Exp. Biol.* 205:3031–3037.
- [124] Beason, R. and P. Semm. 1987. Magnetic responses of the trigeminal nerve system of the Bobolink, *dolichonyx oryzivorus*. *Neurosc. Lett.* 80:229–234.
- [125] Stahl, B., G. Fleissner, G. Falkenberg, and G. Fleissner. 2007. Cross-species unveiling of a putative avian magnetoreceptor. *DESY Annual Report*:1269–1270.
- [126] Wiltschko, W., K. Stapput, P. Thalau, and R. Wiltschko. 2006. Avian magnetic compass: Fast adjustment to intensities outside the normal functional window. *Naturwissenschaften.* 93:300–304.
- [127] Ritz, T., P. Thalau, J. B. Phillips, R. Wiltschko, and W. Wiltschko. 2004. Resonance effects indicate a radical-pair mechanism for avian magnetic compass. *Nature.* 429:177–180.
- [128] Thalau, P., T. Ritz, K. Stapput, R. Wiltschko, and W. Wiltschko. 2005. Magnetic compass orientation of migratory birds in the presence of a 1.315 MHz oscillating field. *Naturwissenschaften.* 92:86–90.
- [129] Canfield, J. M., R. L. Belford, P. G. Debrunner, and K. Schulten. 1994. A perturbation theory treatment of oscillating magnetic fields in the radical pair mechanism. *Chem. Phys.* 182:1–18.
- [130] Canfield, J. M., R. L. Belford, P. G. Debrunner, and K. Schulten. 1995. A perturbation treatment of oscillating magnetic fields in the radical pair mechanism using the Liouville equation. *Chem. Phys.* 195:59–69.
- [131] Mouritsen, H., U. Janssen-Bienhold, M. Liedvogel, G. Feenders, J. Stalleicken, P. Dirks, and R. Weiler. 2004. Cryptochromes and neuronal-activity markers colocalize in the retina of migratory birds during magnetic orientation. *Proc. Natl. Acad. Sci. USA.* 101:14294–14299.

- [132] Möller, A., S. Sagasser, W. Wiltschko, and B. Schierwater. 2004. Retinal cryptochrome in a migratory passerine bird: A possible transducer for the avian magnetic compass. *Naturwissenschaften*. 91:585–588.
- [133] Schulten, K. 1977. Quantum mechanical propensity rules for the transfer of angular momentum in three-atom reactions. *Ber. Bunsenges. Phys. Chem.* 81:166–168.
- [134] Ahmad, M. and A. R. Cashmore. 1996. Seeing blue: The discovery of cryptochrome. *Plant Mol. Biol.* 30:851–861.
- [135] Sancar, A. 2003. Structure and function of DNA photolyase and cryptochrome blue-light photoreceptors. *Chem. Rev.* 103:2203–2237.
- [136] Lin, C. and D. Shalitin. 2003. Cryptochrome structure and signal transduction. *Annu. Rev. Plant Biol.* 54:469–496.
- [137] Byrdin, M., A. P. Eker, M. H. Vos, and K. Brettel. 2003. Dissection of the triple tryptophan electron transfer chain in *E. coli* DNA photolyase. *Proc. Natl. Acad. Sci. USA*. 100:8676–8681.
- [138] Byrdin, M., V. Sartor, A. P. Eker, M. H. Vos, C. Aubert, K. Brettel, and P. Mathis. 2004. Intraprotein electron transfer and proton dynamics during photoactivation in DNA photolyase from *E. coli*: Review and new insights from an “inverse” deuterium isotope effect. *Biochim. Biophys. Acta*. 1655:64–70.
- [139] Cheung, M., I. Daizadeh, A. Stuchebrukhov, and P. Heelis. 1999. Pathways of electron transfer in *E. coli* DNA photolyase - Trp306 to FADH. *Biophys. J.* 76:1241–1249.
- [140] Popovic, D. M., A. Zmirić, S. D. Zarić, and E.-W. Knapp. 2002. Energetics of radical transfer in DNA photolyase. *J. Am. Chem. Soc.* 124:3775–3782.
- [141] Aubert, C., M. H. Vos, P. Mathis, A. P. Eker, and K. Brettel. 2000. Intraprotein radical transfer during photoactivation of DNA photolyase. *Nature*. 405:586–590.

- [142] Shalitin, D., X. Yu, M. Maymon, T. Mockler, and C. Lin. 2003. Blue light-dependent *in vivo* and *in vitro* phosphorylation of *Arabidopsis* cryptochrome 1. *The Plant Cell*. 15:2421–2429.
- [143] Bouly, J.-P., B. Giovani, A. Djamei, M. Mueller, A. Zeugner, E. A. Dudkin, A. Batschauer, and M. Ahmad. 2003. Novel ATP-binding and autophosphorylation activity associated with *Arabidopsis* and human cryptochrome-1. *Eur. J. Biochem.* 270:2921–2928.
- [144] Zeugner, A., M. Byrdin, J.-P. Bouly, N. Bakrim, B. Giovani, K. Brettel, and M. Ahmad. 2005. Light-induced electron transfer in *Arabidopsis* cryptochrome-1 correlates with *in-vivo* function. *J. Biol. Chem.* 280:19437–19440.
- [145] Giovanni, B., M. Byrdin, M. Ahmad, and K. Brettel. 2003. Light-induced electronic transfer in a cryptochrome blue-light photoreceptor. *Nat. Struct. Biol.* 10:489–490.
- [146] Kottke, T., A. Batschauer, M. Ahmad, and J. Heberle. 2006. Blue-light-induced changes in *Arabidopsis* cryptochrome 1 probed by FTIR difference spectroscopy. *Biochemistry*. 45:2472–2479.
- [147] Altschul, S. F., W. Gish, W. Miller, E. W. Myers, and D. J. Lipman. 1990. Basic local alignment search tool. *J. Mol. Biol.* 215:403–410.
- [148] Kaptein, R. and L. Oosterhoff. 1969. Chemically induced dynamic nuclear polarization II : (relation with anomalous ESR spectra). *Chem. Phys. Lett.* 4:195–197.
- [149] Kaptein, R. and L. Oosterhoff. 1969. Chemically induced dynamic nuclear polarization III (anomalous multiplets of radical coupling and disproportionation products). *Chem. Phys. Lett.* 4:214–216.
- [150] Closs, G. 1969. Mechanism explaining nuclear spin polarizations in radical combination reactions. *J. Am. Chem. Soc.* 91:4552–4554.
- [151] Closs, G. and A. Trifunac. 1970. Theory of chemically induced nuclear spin polarization. III. effect of isotropic g shifts in the components of radical pairs with one hyperfine interaction. *J. Am. Chem. Soc.* 92:2183–2184.

- [152] Closs, G. and A. Trifunac. 1970. Theory of chemically induced nuclear spin polarization. V. comparison of coupling reactions in singlet and triplet derived radical pairs and of radicals not generated in pairs. *J. Am. Chem. Soc.* 92:2186–2187.
- [153] Marcus, R. and N. Sutin. 1985. Electron transfer in chemistry and biology. *Biochim. Biophys. Acta.* 811:265–322.
- [154] Marcus, R. 1956. On the theory of oxidation-reduction reactions involving electron transfer. I. *J. Chem. Phys.* 24:966–978.
- [155] Marcus, R. 1965. On the theory of electron-transfer reactions. VI. Unified treatment of homogeneous and electrode reactions. *J. Chem. Phys.* 43:679–701.
- [156] Hopfield, J. 1974. Electron transfer between biological molecules by thermally activated tunneling. *Proc. Natl. Acad. Sci. USA.* 71:3640–3644.
- [157] Moser, C., J. Keske, K. Warncke, R. Farid, and P. Dutton. 1992. Nature of biological electron transfer. *Nature.* 355:796–802.
- [158] Bertran, D., J. Onuchic, J. Winkler, and H. Gray. 1992. Electron-tunneling pathways in proteins. *Science.* 258:1740–1741.
- [159] Page, C., C. Moser, X. Chen, and P. Dutton. 1999. Natural engineering principles of electron tunneling in biological oxidation-reduction. *Nature.* 402:47–52.
- [160] Dutton, M. and P. Dutton. 1989. Temperature and  $\Delta G^\circ$  dependence of the electron-transfer from  $\text{BPh}^-$  to  $\text{Q}_A$  in reaction center protein from *Rhodobacter sphaeroides* with different quinones as  $\text{Q}_A$ . *J. Am. Chem. Soc.* 111:3400–3412.
- [161] Blättler, C., F. Jent, and H. Paul. 1990. A novel radical-triplet pair mechanism for chemically induced electron polarization (CIDEP) of free radicals in solution. *Chem. Phys. Lett.* 166:375–380.
- [162] Chaney, E. and M. Forbes. 2003. Dynamics of spin-correlated radical pairs in non-ionic surfactant solutions. *J. Phys. Chem. B.* 107:4464–4469.
- [163] Dinse, K.-P. 2002. Photo-induced dissociation reactions in solution: A challenge for fourier-transform EPR. *RIKEN Review.* 44:113–115.

- [164] Schulten, Z. and K. Schulten. 1977. The generation, diffusion, spin motion, and recombination of radical pairs in solution in the nanosecond time domain. *J. Chem. Phys.* 66:4616–4634.
- [165] Boxer, S., C. Chidsey, and M. Roelofs. 1982. Dependence of the yield of a radical-pair reaction in the solid state on orientation in a magnetic field. *J. Am. Chem. Soc.* 104:2614–2675.
- [166] Yakimchenko, O. and Y. Lebedev. 1978. Radical pairs in the study of elementary chemical reactions in solid organic substances. *Rus. Chem. Rev.* 47:531–548.
- [167] Werner, H.-J., K. Schulten, and A. Weller. 1978. Electron transfer and spin exchange contributions to the magnetic field dependence of the primary photochemical reaction of bacterial photosynthesis. *Biochim. Biophys. Acta.* 502:255–268.
- [168] Shankar, R. 1994. *Principles of Quantum Mechanics*. New York: Plenum Press.
- [169] Landau, L. and E. Lifshitz. 1981. *Quantum Mechanics: Non-Relativistic Theory*. Elsevier Butterworth-Heinemann.
- [170] Greiner, W. 2000. *Quantum Mechanics: An Introduction*. Springer: Berlin, Heidelberg, New York.
- [171] Greiner, W. 1989. *Quantum Mechanics: Special Chapters*. Springer: Berlin, Heidelberg, New York.
- [172] Tsentalovich, Y. P., O. B. Morozova, N. I. Avdievich, G. S. Ananchenko, A. V. Yurkovskaya, J. D. Ball, and M. D. Forbes. 1997. Influence of molecular structure on the rate of intersystem crossing in flexible biradicals. *J. Phys. Chem. A.* 101:8809–8816.
- [173] Levitt, M. H. 2001. *Spin Dynamics – Basics of Nuclear Magnetic Resonance*. Wiley and Sons.
- [174] Vega, A. and D. Fiat. 1974. The stochastic liouville equation and the approach to thermal equilibrium. *Pure and Applied Chemistry.* 40:181–192.

- [175] Tanimura, Y. 2006. Stochastic liouville, langevin, fokker-planck, and master equation. *J. Phys. Soc. Jpn.* 75:082001–(1–39).
- [176] Shushin, A. 2004. Anomalous relaxation in quantum systems and the non-markovian stochastic liouville equation. *J. Phys. Soc. Jpn.*:1–18. ArXiv:cond-mat/0409578v2.
- [177] Kubo, R. 1963. Stochastic Liouville equations. *J. Math. Phys.* 4:174–183.
- [178] Kubo, R., M. Toda, and N. Hashitsume. 2003. *Statistical Physics II: Nonequilibrium Statistical Mechanics*. Springer.
- [179] Timmel, C., F. Cintolesi, B. Brocklehurst, and P. Hore. 2001. Model calculations of magnetic field effects on the recombination reactions of radicals with anisotropic hyperfine interactions. *Chem. Phys. Lett.* 334:387–395.
- [180] Fermi, E. 1950. *Nuclear Physics*. University of Chicago Press.
- [181] Marcus, R. 1957. On the theory of oxidation-reduction reactions involving electron transfer. II. Applications to data on the rates of isotopic exchange reactions. *J. Chem. Phys.* 26:867–871.
- [182] Closs, G., L. Calcaterra, N. Green, K. Penfield, and J. Miller. 1986. Distance, stereoelectronic effects, and the marcus inverted region in intramolecular electron transfer in organic radical anions. *J. Phys. Chem.* 90:3673–3683.
- [183] Dakhnovskii, Y., R. Doolen, and J. Simon. 1994. Electron transfer in the marcus inverted region: Experiment and adiabatic tunneling mechanism. *J. Phys. Chem.* 101:6640.
- [184] Davis, W., W. Svec, M. Ratner, and M. Wasielewski. 1998. Molecularwire behaviour in p-phenylenevinylene oligomers. *Nature.* 396:60.
- [185] Ratner, M. and J. Jortner, editors. 1997. *Molecular Electronics*. Blackwells, Oxford.
- [186] Devault, D. 1980. Quantum mechanical tunneling in biological systems. *Quart. Rev. Biophys.* 13:387–594.

- [187] Smalley, J., S. Feldberg, C. Chidsey, M. Linford, M. Newton, and Y. Liu. 1995. The kinetics of electron-transfer through ferrocene-terminated alkenethiol monolayers on gold. *J. Phys. Chem.* 99:13141–13149.
- [188] Moser, C. and P. Dutton. 1992. Engineering protein structure for electron transfer function in photosynthetic reaction centres. *Biochim. Biophys. Acta.* 1101:171–176.
- [189] Venturoli, G., F. Drepper, J. Williams, J. Allen, X. Lin, and P. Mathis. 1998. Effects of temperature and  $\Delta G^\circ$  on electron transfer from cytochrome  $c_2$  to the photosynthetic reaction center of the purple bacterium *Rhodobacter sphaeroides*. *Biophys. J.* 74:3226–3240.
- [190] Salikhov, K. 2000. *10 Lectures on Spin Chemistry (in Russian)*. Kazan: Unipress. ISBN 5-900044-69-6.
- [191] Haavik, C., S. Stolen, H. Fjellvag, M. Hanfland, and D. Hausermann. 2000. Equation of state of magnetite and its high-pressure modification: Thermodynamics of the Fe-O system at high pressure sample at  $p = 0$ . *Am. Mineral.* 85:514–523.
- [192] Fleet, M. 1986. The structure of magnetite: Symmetry of cubic spinels. *Journal of Solid State Chemistry.* 62:75–82.
- [193] Greiner, W., L. Neise, and H. Stöcker. 1997. *Thermodynamics and Statistical Mechanics*. Springer: Berlin, Heidelberg, New York.
- [194] Landau, L. D. and E. M. Lifshitz. 2000. *Statistical Physics*. Elsevier Butterworth-Heinemann.
- [195] Kittel, C. 2004. *Introduction to Solid State Physics*. Wiley.
- [196] Pauthenet, R. and L. Bochirol. 1951. Spontaneous magnetization of some ferrites. *J. Phys. Radium.* 12:249–251.
- [197] Miyamoto, Y. and S. Chikazumi. 1988. Crystal symmetry of magnetite in low temperature phase deduced from magnetoelectric measurement. *J. Phys. Soc. Jpn.* 57:2040–2050.



- [198] Verwey, E. 1939. Electronic conduction of magnetite ( $\text{Fe}_3\text{O}_4$ ) and its transition point at low-temperature. *Nature*. 44:327–328.
- [199] Gleitzer, C. 1997. Electrical properties of anhydrous iron oxides. *Key Eng. Mat.* 125-126:355–418.
- [200] Néel, L. 1949. Théorie du trainage magnétique des ferromagnétiques en grains fins avec applications aux terres cuites. *Ann. Geophys.* 5:99–136.
- [201] Banerjee, S. and B. Moskowitz. 1985. *Magnetite Biomineralization and Magnetoreception in Organisms: a New Biomagnetism*, chapter Ferrimagnetic properties of magnetite. New York, London: Plenum Press, pages 17–41.
- [202] Horák, D., F. Lednický, E. Petrovský, and A. Kapička. 2004. Magnetic characteristics of ferrimagnetic microspheres prepared by dispersion polymerization. *Macromolecular Materials and Engineering*. 289:341–348.
- [203] Mathé, V. and F. Lèveque. 2005. Trace magnetic minerals to detect redox boundaries and drainage effects in a marshland soil in western France. *Eur. Journ. Soil Sci.* 56:737–751.
- [204] Wohlfarth, E. 1958. Relation between different modes of acquisition of the remanent magnetization of ferromagnetic particles. *J. Appl. Phys.* 35:595–596.
- [205] Dunlop, D. and Ö. Özdemir. 1997. *Rock Magnetism*. Fundamentals and Frontiers. Cambridge University Press.
- [206] Day, R., M. Fuller, and V. Schmidt. 1977. Hysteresis properties of titanomagnetites: Grain-size and compositional dependence. *Phys. Earth Planet. Int.* 13:260–267.
- [207] Wasilewski, P. 1973. Magnetic hysteresis in natural materials. *Earth Planet. Sci. Lett.* 20:67–72.
- [208] Evans, M. and F. Heller. 2003. *Environmental Magnetism: Principles and applications of enviromagnetics*. Academic Press, Oxford.
- [209] Thompson, R., J. Bloemendal, J. Dearing, F. Oldfield, T. Rummery, J. Stober, and G. Turner. 1980. Environmental applications of magntic measurements. *Science*. 207:481–486.

- [210] Stacey, F. and S. Banerjee. 1974. *The physical principles of rock magnetism*. Elsevier, Amsterdam.
- [211] Dana, J. D. 1985. *Manual of Mineralogy*. John Wiley and Sons Inc. ISBN 0471805807.
- [212] Greiner, W. 1998. *Classical Electrodynamics*. Springer-Verlag, New York, Berlin, Heidelberg.
- [213] Landau, L. and E. Lifshitz. 1965. *The Classical Theory of Fields*. London Pergamon.
- [214] Kay, C. W. M., R. Feicht, K. Schulz, P. Sadewater, A. Sancar, A. Bacher, K. Möbius, G. Richter, and S. Weber. 1999. EPR, ENDOR, and TRIPLE resonance spectroscopy of the neutral flavin radical in *E. coli* DNA photolyase. *Biochemistry*. 38:16740–16748.
- [215] Lendzian, F., M. Sahlin, F. MacMillan, R. Bittl, R. Fiege, S. Pötsch, B.-M. Sjöbert, A. Gräslund, W. Lubitz, and G. Lassmann. 1996. Electronic structure of neutral tryptophan radicals in ribonucleotide reductase studied by EPR and ENDOR spectroscopy. *J. Am. Chem. Soc.* 118:8111–8120.
- [216] Himo, F. and L. A. Eriksson. 1997. Theoretical study of model tryptophan radicals and radical cations: Comparison with experimental data of DNA photolyase, cytochrome c peroxidase, and ribonucleotide reductase. *J. Phys. Chem. B*. 101:9811–9819.
- [217] Sjödin, M., S. Styring, B. Akermark, L. Sun, and L. Hammarström. 2002. The mechanism for proton-coupled electron transfer from tyrosine in a model complex and comparisons with YZ oxidation in photosystem II. *Phil. Trans. R. Soc. Lond. B*. 357:1471–1479.
- [218] Balabin, I. A. and J. N. Onuchic. 2000. Dynamically controlled protein tunneling paths in photosynthetic reaction centers. *Science*. 290:114–117.
- [219] Kothe, G., S. Weber, R. Bittl, and E. Ohmes. 1991. Transient EPR of light-induced radical pairs in plant photosystem I: observation of quantum beats. *Chem. Phys. Lett.* 186:474–480.

- [220] Lubitz, W. 2004. EPR in photosynthesis. In B. Gilbert, M. Davies, and D. Murphy, editors, *Electron Paramagnetic Resonance*, volume 19. Royal Society of Chemistry, pages 174–242.
- [221] Sotomayor, M., D. P. Corey, and K. Schulten. 2005. In search of the hair-cell gating spring: Elastic properties of ankyrin and cadherin repeats. *Science*. 13:669–682.
- [222] Hudspeth, A. J., Y. Choe, A. Mehta, and P. Martin. 2000. Putting ion channels to work: Mechanoelectrical transduction, adaptation and amplification by hair cells. *Proc. Natl. Acad. Sci. USA*. 97:11765–11772.
- [223] Howard, J. and A. J. Hudspeth. 1988. Compliance of the hair bundle associated with gating of mechanoelectrical transduction channels in the bullfrog’s saccular hair cell. *Neuron*. 1:189–199.
- [224] Markin, V. S. and A. Hudspeth. 1995. Gating-spring models of mechanoelectrical transduction by hair cells of the internal ear. *Annual Reviews*. 24:59–83.
- [225] Hamill, O. P. and B. Martinac. 2001. Molecular basis of mechanotransduction in living cells. *Physiol. Rev*. 81:685–740.
- [226] Corey, D. P. and J. Howard. 1994. Models for ion channel gating with compliant states. *Biophys. J*. 66:1254–1257.
- [227] Sachs, F. and H. Lecar. 1991. Stochastic models for mechanical transduction. *Biophys. J*. 59:1143–1145.
- [228] Courant, R. and D. Hilbert. 1962. *Methods of Mathematical Physics*. Interscience (Wiley) New York.
- [229] Gullingsrud, J. and K. Schulten. 2004. Lipid bilayer pressure profiles and mechanosensitive channel gating. *Biophys. J*. 86:3496–3509.
- [230] Marrink, S. and A. Mark. 2001. Effect of undulations on surface tension in simulated bilayers. *Journal of Physical Chemistry B*. 105:6122–6127.
- [231] Charras, G. T., B. A. Williams, S. M. Sims, and M. A. Horton. 2004. Estimating the sensitivity of mechanosensitive ion channels to membrane strain and tension. *Biophys. J*. 87:2870–2884.

- [232] Turner, M. S. and P. Sens. 2004. Gating-by-tilt of mechanically sensitive membrane channels. *Phys. Rev. Lett.* 93:118103–1–118103–4.
- [233] Sheetz, M. and J. Dai. 1996. Modulation of membrane dynamics and cell motility by membrane tension. *Trends Cell. Biol.* 6:85–89.
- [234] Morris, C. and U. Homann. 2001. Cell surface area regulation and membrane tension. *J. Membr. Biol.* 179:79–102.
- [235] Hochmuth, R. M., J.-Y. Shao, J. Dai, and M. P. Sheetz. 1996. Deformation and flow of membrane into tethers extracted from neuronal growth cones. *Biophys. J.* 70:358–369.
- [236] Dai, J., M. P. Sheetz, X. Wan, and C. E. Morris. 1998. Membrane tension in swelling and shrinking molluscan neurons. *J. Neurosci.* 18:6681–6692.
- [237] Waugh, R. and E. Evans. 1979. Thermoelasticity of red blood cell membrane. *Biophys. J.* 26:115–131.
- [238] Nichol, J. and O. Hutter. 1996. Tensile strength and dilatational elasticity of giant sarcolemmal vesicles shed from rabbit muscle. *J. Physiol.* 493:187–198.
- [239] Evans, E. and R. Waugh. 1977. Osmotic correction to elastic area compressibility measurements on red cell membrane. *Biophys. J.* 20:307–313.
- [240] Heinrich, V., K. Ritchie, N. Mohandas, and E. Evans. 2001. Elastic thickness compressibility of the red cell membrane. *Biophys. J.* 81:1452–1463.
- [241] Evans, E., R. Waugh, and L. Melnik. 1976. Elastic area compressibility modulus of red cell membrane. *Biophys. J.* 16:585–595.
- [242] Lednor, A. and C. Walcott. 1988. Orientation of homing pigeons at magnetic anomalies. *Beh. Ecol. Sociobiol.* 130:3–8.
- [243] Alerstam, T. 1987. Bird migration across a strong magnetic anomaly. *J. Exp. Biol.* 130:63–86.
- [244] Doktorov, A., M. Hansen, and J. B. Pedersen. 2006. Recombination yield of geminate radical pairs in low magnetic fields – a green’s function method. *Chemical Physics.* 328:333–337.

# Biography (Lebenslauf)

**Name** Ilya Andreevich Solov'yov  
**Address** Frankfurt International Graduate School for Science  
at Frankfurt Institute for Advanced Studies (FIAS)  
Johann Wolfgang Goethe – University  
Max – von – Laue Str. 1  
60438 Frankfurt am Main, Germany  
**Tel. Nr.** +49 (069) 79847502  
**E-mail** ilia@fias.uni-frankfurt.de  
**Date of Birth** 10 November 1983  
**Place of Birth** Leningrad/St. Petersburg, USSR/Russia

## Education

1990–1992 Elsa-Brandström school, Frankfurt am Main, Germany  
1992–1998 Gymnasium No 192, St. Petersburg, Russia  
in 1995 Elm-Wood School, London, England  
1998–2000 Lyceum "Physical-technical school"  
at the A.F. Ioffe Physical-Technical Institute,  
Academy of Sciences of Russia, St. Petersburg, Russia  
2000–2006 Physical-Technical Department of  
St. Petersburg State Polytechnical University, Russia  
2001–2002 Course T (study department for technical and mathematical  
natural sciences) in Studienkolleg, Frankfurt am Main, Germany  
2002–2004 Physics Department of Johann Wolfgang Goethe-University,  
Frankfurt am Main, Germany  
2004–2007 PhD at the Frankfurt International Graduate School for Science  
at Frankfurt Institute for Advanced Studies of  
Johann Wolfgang Goethe-University, Frankfurt am Main, Germany

**Degrees and Academic Qualifications**

- 2000 School-leaving certificate, St. Petersburg, Russia
- 2002 Certificate about Diploma pre examinations (Vordiplom) in Physics average note: ⟨excellent⟩, Frankfurt am Main, Germany
- 2004 Diploma in Physics at the Johann-Wolfgang Goethe University average note ⟨excellent⟩, Frankfurt am Main, Germany supervisors: Prof. Dr. h. c. mult. Walter Greiner, Prof. Dr. Andrey V. Solov'yov
- 2004 Bachelor of Sciences in Physics with honor, St. Petersburg State Technical University, St. Petersburg, Russia supervisor: Prof. Dr. Andrey V. Solov'yov
- 2006 Master of Sciences in Physics with honor, St. Petersburg State Technical University, St. Petersburg, Russia supervisor: Prof. Dr. Andrey V. Solov'yov

**Awards**

- 2000 Third degree diploma in Regional State Physics Olympiad, St. Petersburg, Russia
- 2003-2004 Scholarship award in the "Studienstiftung des deutschen Volkes", Germany
- 2003 Laureate of the ISSEP contest "Student of the Year 2003", St. Petersburg, Russia
- 2004 Laureate of the ISSEP contest "Student of the Year 2004", St. Petersburg, Russia
- 2006 Philipp Siedler-Wissenschaftspreis 2005/2006 for the best Diploma, Frankfurt am Main, Germany

# List of Publications

## Manuscripts

1. I. A. Solov'yov, "*Structure and properties of metallic and noble gas clusters*", Master of Science thesis, St. Petersburg State Polytechnical University, St.Petersburg, Russia, pp. 1-171 (2006) (in Russian).
2. I. A. Solov'yov, "*Modeling of Lennard-Jones Clusters*", Bachelor of Science thesis, St. Petersburg State Polytechnical University, St.Petersburg, Russia, pp. 1-54 (2004) (in Russian).
3. I. A. Solov'yov, "*Ab Initio and Model Description of Atomic Clusters*", Diploma thesis, Johann Wolfgang Goethe-University, Frankfurt am Main, Germany, pp. 1-171 (2004).

## Journal Publications

1. I.A. Solov'yov, A.V. Yakubovich, A.V. Solov'yov and W. Greiner, " *$\alpha$ -helix $\leftrightarrow$  random coil phase transition: analysis of ab initio theory predictions*", Submitted to The European Physical Journal D (2007); [arXiv.org: 0704.3085v1 [physics.bio-ph] 23 Apr 2007].
2. A.V. Yakubovich, I.A. Solov'yov, A.V. Solov'yov and W. Greiner, "*Ab initio theory of helix $\leftrightarrow$ coil phase transition*", Submitted to The European Physical Journal D (2007); [arXiv.org: 0704.3079v1 [physics.bio-ph] 23 Apr 2007].
3. I.A. Solov'yov, and W. Greiner. "*Towards an understanding of the mechanism of magnetoreception in birds*" [arXiv.org: 0704.1763v1 [physics.bio-ph] 13 Apr 2007].

4. I.A. Solov'yov, D.E. Chandler, and K. Schulten. "*Magnetic Field Effects in Arabidopsis thaliana Cryptochrome-1*", Biophysical Journal, **92**, 2711-2726 (2007).
5. I.A. Solov'yov, and W. Greiner. "*A first attempt to model the mechanism of magnetoreception in birds*", Submitted to The New Journal of Physics (2007).
6. I.A. Solov'yov, and W. Greiner. "*Theoretical analysis of an iron mineral-based magnetoreceptor model in birds*", Biophysical Journal, **93** (2007).
7. I.A. Solov'yov, A.V. Yakubovich, A.V. Solov'yov, and W. Greiner. "*Two center multipole expansion method: application to macromolecular systems*", Physical Review E, **75**, 051912-(1-9) (2007); [arXiv.org: 0704.1672v1 [physics.-bio-ph], 12 Apr 2007].
8. A.V. Yakubovich, I.A. Solov'yov, A.V. Solov'yov, and W. Greiner. "*Ab initio description of phase transitions in finite bio-nano-systems*", Europhysicsnews, **38**, 10 (2007).
9. A. Lyalin, I.A. Solov'yov, A.V. Solov'yov, and W. Greiner. "*Interplay of electronic and geometry shell effects in properties of neutral and charged Sr-clusters*", Physical Review A, **75**, 053201-(1-13), (2007).
10. A.V. Yakubovich, I.A. Solov'yov, A.V. Solov'yov and W. Greiner. "*Phase transition in polypeptides: a step towards the understanding of protein folding*", European Physical Journal D, **40**, 363-367 (2006), **Highlight Paper**.
11. I.A. Solov'yov, A.V. Yakubovich, A.V. Solov'yov and W. Greiner. "*On the fragmentation of biomolecules: fragmentation of alanine dipeptide along the polypeptide chain*", Journal of Experimental and Theoretical Physics, **103**, 463-471 (2006). Original Russian Text, published in Zhurnal Eksperimental'noi i Teoreticheskoi Fiziki, **130**, 534-543 (2006).
12. A.V. Yakubovich, I. A. Solov'yov, A.V. Solov'yov and W.Greiner. "*Conformational changes in glycine tri- and hexapeptide*", European Physical Journal D **39**, 23-34 (2006).
13. I.A. Solov'yov, A.V. Yakubovich, A.V. Solov'yov and W. Greiner. "*Ab initio study of alanine polypeptide chain twisting*", Physical Review E **73**, 021916(1-10) (2006).



14. A.V. Yakubovich, I.A. Solov'yov, A.V. Solov'yov and W. Greiner. "*Conformations of glycine polypeptides*", Khimicheskaja Fizika (Chemical Physics (in Russian)) **25**, 11-23 (2006).
15. I.A. Solov'yov, A.V. Yakubovich, A.V. Solov'yov and W. Greiner. "*Potential energy surface for alanine polypeptide chains*", Journal of Experimental and Theoretical Physics, **102**, 314-326 (2006). Original Russian Text, published in Zhurnal Eksperimental'noi i Teoreticheskoi Fiziki, **129**, 356-370 (2006).
16. O.I. Obolensky, I.A. Solov'yov, A. V. Solov'yov, W. Greiner, "*Fusion and fission of small metal clusters: Recent advances*", Computing Letters (CoLe) **1**, 313-318 (2005).
17. A.G. Lyalin, O.I. Obolensky, I.A. Solov'yov, A.V. Solov'yov and W. Greiner, "*Molecular dynamics simulations of cluster fission and fusion processes*". Physica Scripta **T110**, 319-324 (2004).
18. I.A. Solov'yov, A.V. Solov'yov and W. Greiner, "*Fusion process of Lennard-Jones clusters: global minima and magic numbers formation*". International Journal of Modern Physics E, **13**, 697-736 (2004).
19. I.A. Solov'yov, A.V. Solov'yov and W. Greiner, "*Optical response of small magnesium clusters*". Journal of Physics B: Atomic, Molecular and Optical Physics **37**, L137-L145 (2004).
20. A. Lyalin, O. Obolensky, A.V. Solov'yov, I.A. Solov'yov and W. Greiner, "*Rearrangement of cluster structure during fission processes*". Journal of Physics B: Atomic, Molecular and Optical Physics **37**, L7-L13 (2004).
21. A.G. Lyalin, A. Matveentzev, I.A. Solov'yov, A.V. Solov'yov and W. Greiner, "*On the applicability of deformed jellium model to the description of metal clusters*", The European Physical Journal D **24**, 15-18 (2003)
22. A. Lyalin, I.A. Solov'yov, A.V. Solov'yov and W. Greiner, "*Evolution of electronic and ionic structure of Mg-clusters with increase in cluster size*". Physical Review A **67**, 063203-(1-13) (2003).
23. I.A. Solov'yov, "*Calculation and comparison of atomic cluster systems*". Okno v Mikromir (in Russian), **2**, 26(1-4) (2003).

24. I.A. Solov'yov, A. Koshelev, A. Shutovich, A.V. Solov'yov and W. Greiner, "*Cluster growing process and a sequence of magic numbers*". Physical Review Letters **90**, 053401(1-4) (2003).
25. A. Matveentsev, A. Lyalin, I.A. Solov'yov, A.V. Solov'yov and W. Greiner, "*On the applicability of jellium model to the description of alkali clusters*". International Journal of Modern Physics E **12**, 81-107 (2003).
26. I.A. Solov'yov A.V. Solov'yov and W. Greiner, "*Structure and properties of small sodium clusters*". Physical Review A **65**, 053203(1-19) (2002).

## Invited contributions to books and invited commentaries

1. I.A. Solov'yov, A.V. Solov'yov, W. Greiner, "*Cluster Fusion Algorithm: Application to Lennard-Jones Clusters*". In: Chemical Physics: New Research. ed. A.N. Linke, pp. 89-127 (New York, Nova Science Publishers Inc, 2006, ISBN: 1-60021-026-0).
2. O.I. Obolensky, I.A. Solov'yov, A.V. Solov'yov, W. Greiner, "*Determination of atomic cluster structure with cluster fusion algorithm*". In: Advances in Computational Methods in Science and Engineering 2005, **4A**, eds. Th. Simos, G. Maroulis, pp. 1022-1025, (The Netherlands, Brill Academic Publishers, 2005).
3. A. Lyalin, O. Obolensky, I.A. Solov'yov, A.V. Solov'yov and W. Greiner, "*Metal cluster fission; jellium model and molecular dynamics simulations*". In: Latest Advances in Atomic Cluster Collisions: Fission, Fusion, Electron, Ion and Photon Impact, ed. A.V. Solov'yov and J.-P. Connerade, pp.157-168, (Singapore, World Scientific Press, 2004).
4. I.A. Solov'yov, A.V. Solov'yov and W. Greiner, "*Photoabsorption of small sodium and magnesium clusters*". In: Latest Advances in Atomic Cluster Collisions: Fission, Fusion, Electron, Ion and Photon Impact, ed. A.V. Solov'yov and J.-P. Connerade, pp. 113-124, (Singapore, World Scientific Press, 2004).
5. I.A. Solov'yov, A.G. Lyalin, A.V. Solov'yov and W. Greiner, "*Ab initio calculations and modelling of atomic cluster structure*". In: Latest Advances

- 
- in Atomic Cluster Collisions: Fission, Fusion, Electron, Ion and Photon Impact, ed. A.V. Solov'yov and J.-P. Connerade, pp. 51-65, (Singapore, World Scientific Press, 2004).
6. I.A. Solov'yov, A. Koshelev, A. Shutovich, A.V. Solov'yov and W. Greiner, "*Formation of global energy minimim structures in the growth process of Lennard-Jones clusters*". In: From the Atomic to the Nano-Scale, eds. J.H. McGuire and C.T. Whelan, pp. 184-194, (Old Dominion University, American Institute of Physics, 2003).